Lehrstuhl für Hochfrequenztechnik
Fakultät für Elektrotechnik und Informationstechnik
Technische Universität München

Discrete Mode Matching Method for Conformal Multilayered Structures with Anisotropic Substrates

Veenu Kamra

Vollständiger Abdruck der von der Fakultät für Elektrotechnik und Informationstechnik der Technischen Universität München zur Erlangung des akademischen Grades eines

Doktor-Ingenieurs (Dr.-Ing.)

genehmigten Dissertation.

Vorsitzender:
Prof. Dr.-Ing. Norbert Hanik

Prüfende der Dissertation:
1. Prof. Dr.-Ing. Thomas Eibert
2. Prof. Dr.-Ing. Marcos V. T. Heckler,
   Federal University of Pampa, Brazil

Die Dissertation wurde am 30.09.2019 bei der Technischen Universität München eingereicht und durch die Fakultät für Elektrotechnik und Informationstechnik am 02.03.2020 angenommen.

Acknowledgements

First of all, I would like to thank God for giving me grace and wisdom to accomplish the presented work. Further, I would like to convey my deep sense of gratitude to my supervisor, Prof. Dr.-Ing Thomas Eibert for showing kind interest in my work and giving me valuable cooperation in carrying out this thesis. It is a great pleasure to work under his supervision. I would like to thank Prof. Marcos V. T. Heckler for his support in understanding the basics of the topic in early stage and also for being my second reviewer.

It is a great opportunity to complete my research work at Institute of Communications and Navigation, German Aerospace Center (DLR), Oberpfaffenhofen. I specially thank Dr.-Ing. Achim Dreher, leader of antennas group at DLR, for providing me an opportunity to conduct this work. His continuous support and motivation at every stage of my research encouraged me to give my best efforts. I would like to thank my office roommate Dr.-Ing Andreas Winterstein for his time to time guidance in several issues, which was instrumental in making this dissertation work a success.

I would like to thank my colleagues at Navigation Department in DLR, Dr.-Ing. Lukasz A. Greda, Anja Grosch, Dr.-Ing. Simona Circiu, Dr.-Ing. Michael Felux, Friederike Fohlmeister, Dr. Stefano Caizzone, Wahid Elmarissi and former colleague Dr.-Ing. Kazeem Yinusa for their friendship and providing me pleasant and productive working environment. Also, I express my appreciation to the department secretary Monika Eiber for always helping me with bureaucratic issues and business trips.

I also thank my M.Tech. supervisor Prof. M.V. Kartikeyan who first encouraged me to go to Germany for my master thesis and then doctoral thesis.

I thank my parents for their unconditional love and support, and for always encouraging me with their best wishes. I also want to express my gratitude to my two lovely sisters, Komal and Kashish, for always being there for me and giving me reasons to laugh hard and my parents in-law for their support and blessings.

Finally, I wish to express my deepest thanks to my husband Nitish Tripathi for his never losing trust and confidence on me, even in my toughest time and become source of inspiration. I also thank him for productive proofreading of the thesis.

Gilching, June 2020
Veenu Kamra

Contents

Abstract

The discrete mode matching (DMM) method has been proven to be an efficient numerical method to analyze multilayered structures with thin dielectric layers for microwave and optical technologies. The main contribution of this thesis is to extend the method to structures which consist of anisotropic or isotropic, homogeneous or inhomogeneous dielectric layers, or metamaterials. We consider both electric and magnetic anisotropies in the material. There are several numerical techniques available to analyze electromagnetic problems with arbitrary shape and different material properties. All techniques have their advantages and disadvantages. By doing an extensive literature review, we see that they need a lot of computational effort, time and memory space to deal with multilayered structures.

To ease the calculation, we model the multilayered structures by using the full-wave equivalent circuit (FWEC) theory. We derive the mathematical formulation in Cartesian, cylindrical or elliptical coordinate systems. The derivation is well suited for the analysis of planar as well as conformal structures. We analyze planar and cylindrical structures, which are modeled in their respective principal coordinate system, using a spectral domain formulation, while for quasi-planar and quasi-cylindrical structures, we use a spatial domain formulation from the beginning of the analysis. We analyze elliptical structures using both cylindrical and elliptical coordinate systems in the spatial domain. We also analyze structures that consist of inhomogeneous dielectric layers or where material properties are not constant throughout the layer.

We use a generalized relation of the field components which can be represented by a full-wave hybrid matrix for each dielectric layer. Then, we obtain the Green's function using the FWEC of the structure. We need to do only one-dimensional (1D) discretization to analyze transmission lines which we consider to be infinite in the propagation direction. For patch antennas, we need to discretize the structure in two dimensions which are tangential to the interfaces between the dielectric layers and take an analytical solution in the remaining direction perpendicular to the interfaces. We bound the computational domain by using two or four lateral boundary walls for 1D discretization and 2D discretization, respectively. Lateral walls can be natural walls, i.e., electric and magnetic walls, or absorbing boundary conditions (ABCs) for radiating or open structures.

In order to validate the proposed formulation, we analyze various commonly used multilayered structures such as waveguides, microstrip lines and microstrip patch antennas. We compare the results obtained from the DMM with those found in open literature and/or obtained from commercial softwares. We achieve very good agreement between the results with only few discretization lines. The DMM calculation takes very little time and uses low memory storage due to the discretization in only one or two dimensions.

Kurzfassung

Die Discrete Mode Matching ist eine bewährte Methode zur Analyse von mehrlagigen Strukturen mit dünnen dielektrischen Lagen, wie sie in der Mikrowellentechnik und Optik eingesetzt werden. Der Hauptbeitrag dieser Dissertation ist die Erweiterung dieser Methode auf Strukturen, die aus anisotropen oder isotropen, homogenen oder inhomogenen dielektrischen Lagen sowie Metamaterialien bestehen. Es werden sowohl elektrische als auch magnetische Anisotropien im Material betrachtet. Zur Analyse von elektromagnetischen Problemen mit beliebigen Formen und Materialeigenschaften existieren verschiedene numerische Techniken. Mittels einer umfassenden Literaturübersicht wird gezeigt, dass diese Techniken großen Rechenaufwand sowie viel Zeit und Arbeitsspeicher benötigen, um mit mehrlagigen Strukturen umzugehen.

Um die Berechnung zu vereinfachen, werden die mehrlagigen Strukturen mit Hilfe der full-wave equivalent circuit (FWEC) Theorie modelliert. Die mathematische Formulierung wird in kartesischen, zylindrischen und sphärischen Koordinaten hergeleitet und ist für die Analyse von planaren sowie konformen Strukturen geeignet. Planare und zylindrische Strukturen, die im jeweiligen Hauptachsensystem modelliert wurden, werden mittels Frequenzbereichsformulierung analysiert. Für quasi-planare und quasi-zylindrische Strukturen hingegen wird die Raumbereichsformulierung von Beginn der Analyse an verwendet. Elliptische Strukturen werden sowohl mittels zylindrischer als auch elliptischer Koordinatensysteme im Raumbereich analysiert. Außerdem werden Strukturen untersucht, die aus inhomogenen dielektrischen Schichten bestehen oder bei denen die Materialeigenschaften in der Schicht nicht konstant sind.

Es wird eine generalisierte Relation der Feldkomponenten verwendet, die mit Hilfe einer Vollwellen-Hybridmatrix für jede dielektrische Schicht dargestellt wird. Hieraus wird nun mittels der FWEC der Struktur die dyadische Green'sche Funktion hergeleitet. Für die Analyse von Wellenleiter, die in Übertragungsrichtung als unendlich lang angenommen werden, ist nur eine eindimensionale Diskretisierung erforderlich. Bei Patchantennen hingegen ist eine Diskretisierung in zwei Dimensionen, die tangential zu den Randflächen der dielektrischen Schichten verlaufen, notwendig. Für die verbleibende Dimension, die senkrecht zu den Randflächen verläuft, wird die analytische Lösung verwendet. Der berechnete Raum ist, bei eindimensionaler Diskretisierung durch zwei, bei zweidimensionaler Diskretisierung durch vier seitliche Wände begrenzt. Die seitlichen Wände können dabei natürliche Begrenzungen sein, also elektrische oder magnetische Wände, oder Absorptionsbedingungen für strahlende oder offene Strukturen herstellen.

Um die vorgeschlagene Formulierung zu validieren, werden verschiedene, häufig anzutreffende mehrlagige Strukturen wie Wellenleiter, Mikrostreifenleiter und Streifenleiter-Patchantennen untersucht. Dabei werden die mittels DMM erzielten Ergebnisse mit solchen aus der offenen Literatur und/oder von kommerziell erhältlicher Simulationssoftware verglichen. Selbst mit wenigen Diskretisierungslinien ist eine sehr gute Übereinstimmung zwischen den Ergebnissen zu beobachten. Durch die Diskretisierung in nur einer oder zwei Dimensionen benötigt die Berechnung mittels DMM dabei deutlich weniger Zeit und Arbeitsspeicher.

1 Introduction

Printed antennas and microstrips are the basic components of satellite and terminal antennas in satellite navigation and communication systems [Caizzone, 2017; Liu et al., 2016; Dietrich et al., 1998]. In the open literature, it is possible to find developments in the microstrip antenna technology [Pozar and Schaubert, 1995]. Microstrip antennas have various advantages in terms of polarization diversity, flexible input impedance, very low profile and small size, and are mechanically rugged [Pozar and Schaubert, 1995; Garg et al., 2001; Balanis, 1997]. Due to this, they are highly used for research and industrial applications. Microstrip antennas have several applications in defence and commercial sectors, for example mobile satellite communications and global positioning system (GPS) [Huang, 1995].

The focus of the present work is to deal with multilayered structures consisting of different kinds of dielectric layers which can be used as substrate for microstrip antennas and medium for transmission lines. The dielectric media can be homogeneous or non-homogeneous, isotropic or anisotropic, and can consist of conventional materials or metamaterials. The dielectric layers can be planar or conformal. Conformal structures find applications in satellite [Yinusa et al., 2018; Karahan et al., 2015] and mobile [Talbi et al., 2018] communication, on aircrafts and vehicles. The physical structure should be flexible enough so that they can adapt the shape of the interface where they are installed on.

When electrical and/or magnetic properties of a medium depend on the directions of the field vectors, then the medium is known as anisotropic. Currently, different anisotropic materials are widely used in integrated optics and microwave engineering. The technological advancements are making the production of substrates and dielectric anisotropic films, and filling of anisotropic material increasingly convenient. This shows the necessity of better characterizing the anisotropic media and producing more realistic models for the components that use them. For this reason we make use of anisotropic materials rather than isotropic. The dielectric media can be either electric anisotropic or magnetic anisotropic or both. The field relations can be written in the form of

$$\vec{D} = \varepsilon_0 \bar{\bar{\varepsilon}}_r \cdot \vec{E}, \tag{1.1}$$

$$\vec{B} = \mu_0 \bar{\bar{\mu}}_r \cdot \vec{H}, \tag{1.2}$$

where $\bar{\bar{\varepsilon}}_r$ and $\bar{\bar{\mu}}_r$ are relative permittivity and permeability tensors of rank two. They can be represented as

$$\bar{\bar{\nu}}_r = \begin{pmatrix} \nu_{11} & \nu_{12} & \nu_{13} \\ \nu_{21} & \nu_{22} & \nu_{23} \\ \nu_{31} & \nu_{32} & \nu_{33} \end{pmatrix}, \qquad \nu = \varepsilon, \mu. \tag{1.3}$$

The permittivity and permeability tensors can be diagonalized by using a suitable coordinate system, i.e., the principal axes:

$$\bar{\bar{\varepsilon}}_r = \begin{pmatrix} \varepsilon_1 & 0 & 0 \\ 0 & \varepsilon_2 & 0 \\ 0 & 0 & \varepsilon_3 \end{pmatrix}, \tag{1.4}$$

$$\bar{\bar{\mu}}_r = \begin{pmatrix} \mu_1 & 0 & 0 \\ 0 & \mu_2 & 0 \\ 0 & 0 & \mu_3 \end{pmatrix}. \tag{1.5}$$

If all three diagonal elements of the tensors are equal, then the medium is isotropic and both tensors become scalar ε_r, μ_r. If two of the three diagonal elements are equal and the other one is different, then the medium is known as uniaxial anisotropic medium. The axis with the different element is known as the optical axis. If all three diagonal elements are different, then the medium is known as biaxial anisotropic medium.

There are also engineered materials, i.e., metamaterials, widely used in research. They enable us to manipulate the permittivity and the permeability of the materials. Left-handed (LH) metamaterials are materials which exhibit a negative value for the refractive index over some frequency range. An LH metamaterial allows us to control the direction of the emission from radiating sources. It can increase the radiated power of an antenna in a particular direction [Wu et al., 2005]. Metamaterials are basically a broader class of materials than left-handed media. These artificial materials can provide a basis for further miniaturization of microwave antennas having efficient power and acceptable bandwidth. Because of smaller antenna elements, it is possible to make better use of the available space for space-constrained cases, i.e., in satellite navigation and airplanes. A detailed study about metamaterials is given by Caloz and Itoh [2006].

There are several numerical techniques for the analysis of complex multilayered microwave/optical structures such as the method of moments (MoM) [Harrington, 1968; Wei et al., 1984; Sullivan and Schaubert, 1986; Pozar, 1983], the finite-element method (FEM) [Courant, 1943; Lee et al., 1997; Hiptmair, 1999], the finite-difference time domain (FDTD) [Yee, 1966; Ko and Mittra, 1991; Lee et al., 1992], etc. These techniques are very common in the field of computational electromagnetics [Itoh, 1989]. MoM is based on the solution of an integral equation in spatial or spectral domain. It has been proven to be a very accurate numerical technique. It is also widely used with the spatial domain Green's function for multilayered substrates [Chen et al., 2012]. In FEM, a system of equations is obtained by applying a variational formulation. It provides high flexibility for modeling conformal structures using suitable mesh generation. FDTD uses Maxwell's equations in differential form and was originally introduced by Yee [1966]. It approximates all space and time differential operators by finite difference expressions. It also uses 3D meshes to discretize the structure. It has been developed significantly with time by numerous authors [Taflove, 2007]. The number of mesh elements is higher in FDTD than in MoM, while the former one is more suitable for complex structures.

There are also commercial softwares which are built on some of these numerical methods. For example, the main solver of the ANSYS high-frequency structure simulator (HFSS) is based on FEM, but it also uses MoM and the patented ANSYS domain decomposition

method (DDM). The time-domain solver of CST Microwave Studio (CST MWS) is based on the finite integration technique (FIT) [Weiland, 1977; Clemens and Weiland, 2002], the frequency domain solver on FEM, and the integral equation solver on MoM and multilevel fast multipole method (MLFMM) [Coifman et al., 1993; Eibert, 2005]. The FIT transforms Maxwell's equations, in their integral form, to a linear system of equations. It can handle arbitrary shaped and complex structures in more accurate manner. MLFMM is a fast integral method which overcomes the computational complexity of method of moments (MoM). Altair's FEKO uses MoM, FDTD, FEM and MLFMM. The Momentum 3D planar EM simulator supports arbitrary multi-layered geometries and uses spectral domain MoM to analyze complex structures. It is integrated in various platforms, e.g., RFPro, Advanced Design System (ADS), Genesys and Cadence Virtuoso. Another full-wave electromagnetic simulator, i.e., IE3D is also based on MoM. When we deal with multilayered structures then some of the above mentioned techniques are not a good option, specially when the structures consist of several very thin dielectric layers like glue. FEM and FDTD require a lot of computational effort to perform the simulations and large memory for the 3D meshes and integral equation methods require complex mathematical formulations [Heckler, 2010].

There is another finite difference technique that can deal with multilayers easily, namely the method of lines (MoL) [Pregla, 2008]. It has the advantage that we need to discretize the structure only in one or two coordinate directions while we use the analytical solution in the remaining directions. Thus, we save a lot of computational time and effort compared to other numerical schemes. However, MoL depends on approximation of the differential operators and calculating the eigenvalues of the corresponding matrices which introduce errors in the computation.

1.1 The Discrete Mode Matching Method

24 years ago, a method has been developed for the simple full-wave analysis of patches and microstrips in stratified structures, known as the discrete mode matching (DMM) method [Dreher and Rother, 1995]. It was originally developed to overcome the disadvantage of the MoL. The DMM method depends on the exact eigenvalues of waveguide modes which reduce the computational effort due to unnecessary approximations. The convergence of the normalized propagation constants, computed with the MoL, of the fundamental and higher-order modes of a partially filled waveguide to their exact analytical values with respect to the discretization distance is discussed in [Dreher and Rother, 1995].

A lot of work has been done for planar and quasi planar cases and also for cylindrical and quasi-cylindrical cases [Dreher, 1996; Dreher and Ioffe, 2000; Ioffe et al., 2003; Heckler and Dreher, 2007b; Heckler, 2010]. It has been proven to be an efficient spectral or spatial domain numerical method for the full-wave analysis of microwave structures such as waveguides, striplines and microstrip antennas. For the present thesis, we extend the DMM method to analyze structures with anisotropic materials and metamaterials. We analyze various multilayered microstrip structures in different coordinate systems.

The formulation employs the full-wave equivalent circuit (FWEC) to derive the Green's function. The general wave solution is applied within each dielectric layer to calculate the field components at its interfaces. Therefore, each electric layer can be represented with a hybrid matrix. The FWEC consists of these hybrid blocks denoting the dielectric layers present in the multilayered structure. The formulation is well suited for numerical computations. The DMM method uses sampling of the field components in one or two

dimensions and takes the analytical solutions in the remaining direction perpendicular to the dielectric layers. For this reason only two or four lateral boundaries are used to bound the computational domain. It reduces the computational effort and the memory requirement due to the semi-analytical approach. The tangential field components are matched at discrete sampling points along the interfaces. This procedure can lead us to form the system of equations for the multilayered structure.

Unlike MoL, in the DMM we do not discretize the Helmholtz equation, but we use exact wave numbers as eigenvalues which are dependent on the lateral boundary conditions. The method uses 1D discretization for transmission line structures and 2D discretization for radiating structures unlike 3D meshes used by FEM and FDTD. The computational domain can be bounded with electric walls (E-walls), magnetic walls (H-walls) or absorbing boundary conditions (ABCs) for open or radiating structures.

DMM avoids the initial discretization and transformation process for calculating spectral domain Green's function when layers are homogeneous and constant with respect to position in the desired coordinate system. There is a need to convert the spectral domain Green's function into spatial domain to locate metallization in the interfaces. If there is any change in the shape of the layers with respect to the regular coordinate system, then only we need to use the spatial domain Green's function from the beginning to define the shape of the layer.

In moment method (MoM), the most common way is to set up an electric or magnetic field integral equation for the layered structure involving the dyadic Green's function. Then to solve this equation, suitable basis and weighting functions of the full- or sub-domain type have to be defined for the currents on the strips and/or the magnetic currents in the (small) slots. The solution requires the calculation of multi-dimensional integrals and the discussion of a proper branch cut and integration path in the complex domain. In DMM this complicated process is replaced by a simple multiplication with transformation matrices. The efficiency of MoM strongly depends on the choice of basis and weighting functions as well as on the integration methods. While in DMM, with the use of a suitable discretization scheme we can reach high level of accuracy within a small number of discretization lines [Heckler and Dreher, 2016].

1.2 Outline of the Thesis

In the previous work with DMM, it was assumed that all the layers are homogeneous and isotropic. Depending on the applications, the dielectric structures can be composed of several different types of substrates. The main objective of this dissertation is to further develop the DMM method for the analysis of conformal structures with numerous anisotropic layers or with metamaterials. Here we aim to better characterize the structures and efficiently model them. Structures such as waveguides, microstrip lines or striplines, and microstrip antennas are used for the demonstration of the method.

Chapter 2: In this chapter, we initialize the extension of the DMM to analyze planar structures having uniaxial electric or/and magnetic anisotropy. We start by solving Maxwell's equations in a Cartesian coordinate system to develop the formulation for DMM to obtain the spectral domain Green's function. First, we analyze a planar two-layer waveguide and a microstrip line to find the propagation constants of the guiding structures. For the analysis of structures with metallization, we use one dimensional (1D) discretization. Further, we also investigate the structures with metallization on different interfaces.

Chapter 3: We then extend the DMM theory to the analysis of microstrip antennas which demands the extension of the discretization scheme in a two dimensional (2D) domain. We do the computations for the structures in spectral domain. Initially we analyze a stripline resonator then it is fed with a transmission line in order to predict the antenna characteristics, i.e., the input impedance (Z_{in}) and radiation pattern. We also analyze a microstrip antenna having metamaterial as a substrate. Validation of the theory developed is undertaken by comparison with results from commercially available software, results from other techniques or/and measured data.

Chapter 4: This chapter extends the formulation of full-wave equivalent circuit to deal with biaxial anisotropy in the dielectric layers. The DMM method is applied to analyze quasi-planar structures, where the interface of the dielectric layers is not according to the Cartesian coordinate system. The slope of the interface varies with the horizontal direction. Therefore, we do the computation in spatial domain to analyze the quasi-planar nature.

Chapter 5: We extend the DMM method to analyze cylindrical and quasi-cylindrical structures. We generate the formulation for the full-wave equivalent circuit and determine the Green's function in a cylindrical coordinate system. Again we consider waveguides, microstrips and patch antennas to validate the theory with the other numerical techniques. Both spectral domain and spatial domain analysis are explained for cylindrical and quasi-cylindrical structures, respectively.

Chapter 6: This chapter deals with the extension to analyze planar multilayered structures with inhomogeneous dielectric layers. We derive the hybrid matrix elements for the dielectric layer whose materials properties are dependent on space parameters. Channel waveguides or rib waveguides are commonly used in the optical domain. Therefore, we use these examples to demonstrate the technique and verify with the open literature.

Chapter 7: In the last phase, we deal with an elliptical coordinate system to generate the formulation. We extend the discrete mode matching method to analyze elliptical fibers or transmission lines with elliptical dielectric layers. To demonstrate the technique, we analyze waveguides and compare the results with the data obtained by the other authors and by commercial software. We also compare the results from this formulation with the formulation explained in Chapter 5 with cylindrical coordinate system.

Chapter 8: Finally, we conclude this thesis and summarize the findings. We also outline possible future research directions.

2 Analysis of Planar Transmission Lines with Uniaxial Anisotropy

Microstrip transmission lines are widely used in navigation and communication systems. Substrates with uniaxial media are often integrated for various microwave and optical applications. Thanks to the technological advancements, it is becoming more and more easy to produce anisotropic films and substrates. Hence, there is a need to better characterize the anisotropic medium and to develop efficient numerical techniques to model multilayered transmission lines.

In the case of uniaxial anisotropic materials, there is only one direction of wave propagation along which the velocity of propagation has a constant value, independent of the orientation of the electric displacement vector $\vec{D}$ or magnetic flux density $\vec{B}$. This direction is called optical axis of the material. Basically, there are two types of waves that are propagating in the uniaxially anisotropic medium, one represents ordinary waves which are not dependent on the direction of the wave propagation and the other represents extraordinary waves which are dependent on the angle between the direction of the wave vector and the optical axis. If the ordinary wave travels faster than the extraordinary one then it is a positive uniaxial crystal, otherwise it is a negative uniaxial crystal [Zhang and Li, 1998].

Several numerical techniques and commercial software tools are available to analyze planar microwave structures such as waveguides, microstrip lines and antennas [Itoh, 1989]. Also, significant work has been done by several authors using different approaches for considering anisotropy in the material [Pregla, 2008; Krowne, 1986; Mesa et al., 1998]. In this chapter, the focus is on multilayered planar structures having numerous interfaces and arbitrarily thin anisotropic layers as shown in Fig. 2.1. Some predicted the characteristics of the microtrip lines using different methods, such as potential theory [Kretch and Collin, 1987; Hsu, 2001] and calculation of equivalent isotropic substrate [Verma et al., 2014].

The most complicated task while analyzing the structure is to set up the system matrix. It is possible to derive the system equation or Green's function by using a full-wave equivalent circuit (FWEC), where each dielectric layer is represented by a hybrid matrix (Fig. 2.2). This hybrid matrix relates all the tangential field components at the interfaces. The current sources represent metallizations between the layers, and shorts or admittances are used for closed or open top and bottom layers. This equivalent circuit was already applied successfully for the analytical and numerical analysis of transmission lines and microstrip antennas in different coordinate systems [Dreher and Pregla, 1993; Thiel and Dreher, 2002; Dreher and Ioffe, 2000; Heckler and Dreher, 2006].

This chapter first describes the derivation of the hybrid-matrix elements for uniaxial anisotropic dielectric layers. The FWEC is then used to characterize the structure with anisotropic dielectric layers and to determine the system equation in spectral domain. We demonstrate the application of the extended equivalent circuit by analyzing a simple stratified microwave structure like a waveguide. In the following sections, we explain the discrete mode matching (DMM) method to analyze multilayered striplines with planar dielectric layers having uniaxial anisotropy. Then, we compare the numerical results with those ob-

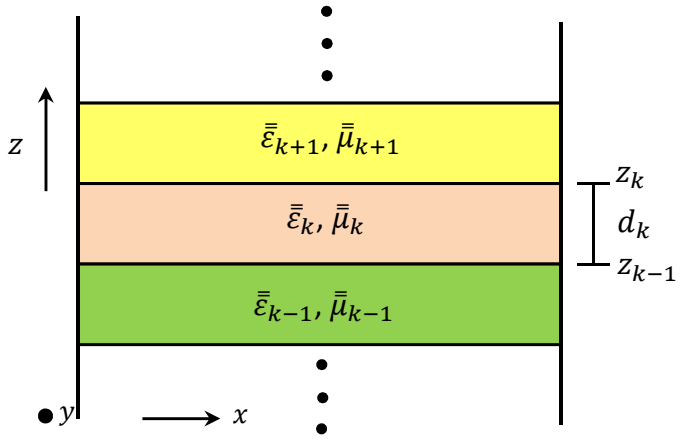

Figure 2.1: Planar microwave structure with anisotropic stratified dielectric.

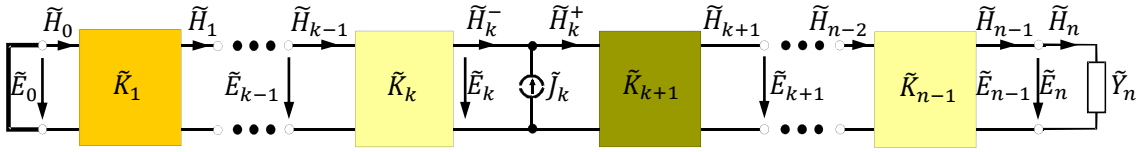

Figure 2.2: Full-wave equivalent circuit of a general planar microwave structure with stratified dielectric.

tained from commercial software and/or open literature. This chapter is based on the papers [Kamra and Dreher, 2017, 2018c,d].

2.1 Formulation for the Full-Wave Equivalent Circuit

In this section, we discuss the electromagnetic equations describing the full-wave equivalent circuit of the multilayered uniaxial anisotropic structure.

2.1.1 Field Relations

To characterize the anisotropic medium, the analysis starts from the permittivity ($\bar{\bar{\varepsilon}} = \varepsilon_0 \bar{\bar{\varepsilon}}_r$) and permeability ($\bar{\bar{\mu}} = \mu_0 \bar{\bar{\mu}}_r$) tensors with optical axis in z-direction, where

$$\bar{\bar{\varepsilon}}_r = \begin{pmatrix} \varepsilon_x & 0 & 0 \\ 0 & \varepsilon_x & 0 \\ 0 & 0 & \varepsilon_z \end{pmatrix}, \quad \bar{\bar{\mu}}_r = \begin{pmatrix} \mu_x & 0 & 0 \\ 0 & \mu_x & 0 \\ 0 & 0 & \mu_z \end{pmatrix}. \tag{2.1}$$

We write the Maxwell's equations in the space frequency domain and for a source-free and homogeneous medium in their differential form by

$$\nabla \times \vec{E}(x,y,z) = -j\omega\mu_0 \bar{\bar{\mu}}_r \cdot \vec{H}(x,y,z), \tag{2.2a}$$

$$\nabla \times \vec{H}(x,y,z) = j\omega\varepsilon_0 \bar{\bar{\varepsilon}}_r \cdot \vec{E}(x,y,z), \tag{2.2b}$$

where $\vec{E}$ and $\vec{H}$ are electric and magnetic field vectors, ω is the angular frequency, μ_0 is the free-space permeability and ε_0 is the free-space permittivity. In rectangular coordinates,

we write

$$\vec{E}(x,y,z) = E_x(x,y,z)\hat{x} + E_y(x,y,z)\hat{y} + E_z(x,y,z)\hat{z}, \tag{2.3}$$

with $\hat{x}$, $\hat{y}$ and $\hat{z}$ denoting the unit vectors along x, y and z coordinates, respectively. We suppress the time dependence $\exp(j\omega t)$ throughout this thesis. To simplify the analysis, space variables are normalized by the free space wave number k_0 $(= \omega\sqrt{\varepsilon_0\mu_0})$ and $\eta_0\vec{H}$ is replaced by $\vec{H}$, where $\eta_0 = \sqrt{\mu_0/\varepsilon_0}$, is the intrinsic impedance of the free space. So in the extended form, Faraday's law (2.2a) gives the field relations as

$$\frac{\partial}{\partial y}E_z - \frac{\partial}{\partial z}E_y = -j\mu_x H_x, \tag{2.4a}$$

$$\frac{\partial}{\partial z}E_x - \frac{\partial}{\partial x}E_z = -j\mu_x H_y, \tag{2.4b}$$

$$\frac{\partial}{\partial x}E_y - \frac{\partial}{\partial y}E_x = -j\mu_z H_z. \tag{2.4c}$$

Next on taking Ampere's law (2.2b), the expressions are

$$\frac{\partial}{\partial y}H_z - \frac{\partial}{\partial z}H_y = j\varepsilon_x E_x, \tag{2.5a}$$

$$\frac{\partial}{\partial z}H_x - \frac{\partial}{\partial x}H_z = j\varepsilon_x E_y, \tag{2.5b}$$

$$\frac{\partial}{\partial x}H_y - \frac{\partial}{\partial y}H_x = j\varepsilon_z E_z. \tag{2.5c}$$

As the optical axis is in z-direction, we can take E_z and H_z as two independent field components. Therefore on rearranging (2.4)-(2.5), the other field components can be calculated using the relation

$$(\frac{\partial^2}{\partial z^2} + \varepsilon_x\mu_x)\begin{bmatrix} E_x \\ H_x \\ E_y \\ H_y \end{bmatrix} = \begin{bmatrix} \frac{\partial}{\partial x}\frac{\partial}{\partial z} & -j\mu_x\frac{\partial}{\partial y} \\ j\varepsilon_x\frac{\partial}{\partial y} & \frac{\partial}{\partial x}\frac{\partial}{\partial z} \\ \frac{\partial}{\partial y}\frac{\partial}{\partial z} & j\mu_x\frac{\partial}{\partial x} \\ -j\varepsilon_x\frac{\partial}{\partial x} & \frac{\partial}{\partial y}\frac{\partial}{\partial z} \end{bmatrix}\begin{bmatrix} E_z \\ H_z \end{bmatrix}. \tag{2.6}$$

Similarly, for the case of optical axis in x- or y-direction, the independent field components will be E_x, H_x and E_y, H_y, respectively. The whole analysis procedure will be the same as shown here for the case of z-optical axis.

2.1.2 Interface Condition

Now consider a stratified dielectric in z-direction as shown in Fig. 2.1, in which an arbitrary layer k is bounded by the interfaces $k-1$ and k. We write the source-free Helmholtz equation in the form

$$\left(\frac{\partial^2}{\partial x^2} + \frac{\partial^2}{\partial y^2} + \frac{\partial^2}{\partial z^2} + K^2\right)\psi(x,y,z) = 0, \tag{2.7}$$

where ψ represents two independent field components, i.e., E_z, H_z and K represents propagation constant of the medium. We assume the propagation in y-direction and the cross-section does not vary in this direction. Therefore, we write

$$\psi(x,y,z) = \psi(x,z)e^{-jk_y y}. \tag{2.8}$$

After introducing (2.8) in (2.7) and taking the derivative with respect to y, we get

$$\left(\frac{\partial^2}{\partial x^2}+\frac{\partial^2}{\partial z^2}-k_y^2+K^2\right)\psi(x,z)=0. \tag{2.9}$$

Using Fourier transformation, we can write the differential equation (2.9) with derivatives with respect to one coordinate only. We can write the relation between the spatial and spectral domain field component as

$$\psi(x,z)=\frac{1}{2\pi}\int_{-\infty}^{+\infty}\tau_x(k_x x)\tilde{\psi}(k_x,z)dk_x, \tag{2.10}$$

where k_x is the spectral variable along x-direction. On transforming (2.9) into the spectral domain, it leads to the ordinary differential equation

$$\left(\frac{\partial^2}{\partial z^2}-k_z^2\right)\tilde{\psi}(k_x,z)=0, \tag{2.11}$$

with $k_z^2=k_x^2-(K^2-k_y^2)$.

In contrast to isotropic media, it must be taken into account that in the uniaxial anisotropic case the propagation constant K has two roots. One represents TE waves (ordinary waves) and the other represents TM waves (extraordinary waves). Therefore, the dispersion relation for the E_z or TM mode is obtained as

$$k_{ze}=\sqrt{\frac{\varepsilon_x}{\varepsilon_z}(-\mu_x\varepsilon_z+k_x^2+k_y^2)}, \tag{2.12}$$

and for the H_z or TE mode as

$$k_{zh}=\sqrt{\frac{\mu_x}{\mu_z}(-\mu_z\varepsilon_x+k_x^2+k_y^2)}. \tag{2.13}$$

Then the solution of (2.11) within an arbitrary layer k can be written in the form

$$\tilde{E}_{z_k}=A_k e^{k_{ze_k}z}+B_k e^{-k_{ze_k}z}, \tag{2.14a}$$

$$\tilde{H}_{z_k}=C_k e^{k_{zh_k}z}+D_k e^{-k_{zh_k}z}. \tag{2.14b}$$

Depending on the roots for $\tilde{E}_z$ and $\tilde{H}_z$, the transverse field components can be written in spectral domain as

$$\tilde{E}_x=-\frac{jk_x\varepsilon_z}{\varepsilon_x k_s^2}\frac{\partial}{\partial z}\tilde{E}_z-\frac{k_y\mu_z}{k_s^2}\tilde{H}_z \tag{2.15a}$$

$$\tilde{E}_y=-\frac{jk_y\varepsilon_z}{\varepsilon_x k_s^2}\frac{\partial}{\partial z}\tilde{E}_z+\frac{k_x\mu_z}{k_s^2}\tilde{H}_z \tag{2.15b}$$

$$\tilde{H}_x=\frac{k_y\varepsilon_z}{k_s^2}\tilde{E}_z-\frac{jk_x\mu_z}{\mu_x k_s^2}\frac{\partial}{\partial z}\tilde{H}_z \tag{2.15c}$$

$$\tilde{H}_y=-\frac{k_x\varepsilon_z}{k_s^2}\tilde{E}_z-\frac{jk_y\mu_z}{\mu_x k_s^2}\frac{\partial}{\partial z}\tilde{H}_z \tag{2.15d}$$

where $k_s = \sqrt{k_x^2 + k_y^2}$. On using (2.14) and (2.15), the transverse field components can be rewritten as

$$\begin{bmatrix} \tilde{E}_{x_k} \\ \tilde{H}_{x_k} \\ \tilde{E}_{y_k} \\ \tilde{H}_{y_k} \end{bmatrix} = \begin{bmatrix} \tilde{Q}_{x_k}^A & \tilde{Q}_{x_k}^B & \tilde{Q}_{x_k}^C & \tilde{Q}_{x_k}^D \\ \tilde{G}_{x_k}^A & \tilde{G}_{x_k}^B & \tilde{G}_{x_k}^C & \tilde{G}_{x_k}^D \\ \tilde{Q}_{y_k}^A & \tilde{Q}_{y_k}^B & \tilde{Q}_{y_k}^C & \tilde{Q}_{y_k}^D \\ \tilde{G}_{y_k}^A & \tilde{G}_{y_k}^B & \tilde{G}_{y_k}^C & \tilde{G}_{y_k}^D \end{bmatrix} \begin{bmatrix} A_k \\ B_k \\ C_k \\ D_k \end{bmatrix}. \tag{2.16}$$

Now to obtain the relation between the tangential fields at the interfaces $k-1$ (bottom) and k (top) bounding the layer k, we write in matrix form

$$\widetilde{\boldsymbol{E}}_k = \begin{bmatrix} \tilde{E}_{x_k} \\ \tilde{E}_{y_k} \end{bmatrix}, \ \widetilde{\boldsymbol{H}}_k = \begin{bmatrix} -\tilde{H}_{y_k} \\ \tilde{H}_{x_k} \end{bmatrix}, \ \boldsymbol{F} = \begin{bmatrix} A_k \\ B_k \\ C_k \\ D_k \end{bmatrix}, \tag{2.17}$$

and

$$\begin{bmatrix} \widetilde{\boldsymbol{E}}_{k-1} \\ \widetilde{\boldsymbol{H}}_{k-1} \end{bmatrix} = \widetilde{\boldsymbol{M}}_{k-1} \boldsymbol{F}, \tag{2.18}$$

$$\begin{bmatrix} \widetilde{\boldsymbol{E}}_{k} \\ \widetilde{\boldsymbol{H}}_{k} \end{bmatrix} = \widetilde{\boldsymbol{M}}_{k} \boldsymbol{F}, \tag{2.19}$$

$$\widetilde{\boldsymbol{M}}_k = \begin{bmatrix} \tilde{Q}_{x_k}^A & \tilde{Q}_{x_k}^B & \tilde{Q}_{x_k}^C & \tilde{Q}_{x_k}^D \\ \tilde{Q}_{y_k}^A & \tilde{Q}_{y_k}^B & \tilde{Q}_{y_k}^C & \tilde{Q}_{y_k}^D \\ -\tilde{G}_{y_k}^A & -\tilde{G}_{y_k}^B & -\tilde{G}_{y_k}^C & -\tilde{G}_{y_k}^D \\ \tilde{G}_{x_k}^A & \tilde{G}_{x_k}^B & \tilde{G}_{x_k}^C & \tilde{G}_{x_k}^D \end{bmatrix}, \tag{2.20}$$

with

$$\tilde{Q}_x^A = -j\varepsilon_z k_x k_{ze} e^{k_{ze}z}/(\varepsilon_x k_s^2), \ \tilde{Q}_x^B = j\varepsilon_z k_x k_{ze} e^{-k_{ze}z}/(\varepsilon_x k_s^2),$$
$$\tilde{Q}_x^C = -\mu_z k_y e^{k_{zh}z}/(k_s^2), \ \tilde{Q}_x^D = -\mu_z k_y e^{-k_{zh}z}/(k_s^2),$$
$$\tilde{Q}_y^A = -j\varepsilon_z k_y k_{ze} e^{k_{ze}z}/(\varepsilon_x k_s^2), \ \tilde{Q}_y^B = j\varepsilon_z k_y k_{ze} e^{-k_{ze}z}/(\varepsilon_x k_s^2),$$
$$\tilde{Q}_y^C = \mu_z k_x e^{k_{zh}z}/(k_s^2), \ \tilde{Q}_y^D = \mu_z k_x e^{-k_{zh}z}/(k_s^2),$$
$$\tilde{G}_x^A = \varepsilon_z k_y e^{k_{ze}z}/(k_s^2), \ \tilde{G}_x^B = \varepsilon_z k_y e^{-k_{ze}z}/(k_s^2),$$
$$\tilde{G}_x^C = -j\mu_z k_x k_{zh} e^{k_{zh}z}/(\mu_x k_s^2), \ \tilde{G}_x^D = j\mu_z k_x k_{zh} e^{-k_{zh}z}/(\mu_x k_s^2),$$
$$\tilde{G}_y^A = -\varepsilon_z k_x e^{k_{ze}z}/(k_s^2), \ \tilde{G}_y^B = -\varepsilon_z k_x e^{-k_{ze}z}/(k_s^2),$$
$$\tilde{G}_y^C = -j\mu_z k_y k_{zh} e^{k_{zh}z}/(\mu_x k_s^2), \ \tilde{G}_y^D = j\mu_z k_y k_{zh} e^{-k_{zh}z}/(\mu_x k_s^2).$$

On eliminating the unknown column matrix $\boldsymbol{F}$ from (2.18) and (2.19), we get the relation for the field components at the interfaces of layer k with normalized thickness d_k in matrix form as

$$\begin{bmatrix} \widetilde{\boldsymbol{E}}_{k-1} \\ \widetilde{\boldsymbol{H}}_{k-1} \end{bmatrix} = \widetilde{\boldsymbol{K}}_k \begin{bmatrix} \widetilde{\boldsymbol{E}}_k \\ \widetilde{\boldsymbol{H}}_k \end{bmatrix}, \tag{2.21}$$

with the hybrid matrix

$$\widetilde{\boldsymbol{K}}_k = \widetilde{\boldsymbol{M}}_{k-1} \widetilde{\boldsymbol{M}}_k^{-1} = \begin{bmatrix} \widetilde{\boldsymbol{V}}_k & \widetilde{\boldsymbol{Z}}_k \\ \widetilde{\boldsymbol{Y}}_k & \widetilde{\boldsymbol{B}}_k \end{bmatrix}. \tag{2.22}$$

Multiple layers can be taken into account by simple matrix multiplication.

For the outer unbounded layer (n), the solution of (2.11) can be written in the form

$$\tilde{E}_{z_n} = B_n e^{-k_{ze_n} z}, \tag{2.23a}$$

$$\tilde{H}_{z_n} = D_n e^{-k_{zh_n} z}. \tag{2.23b}$$

The transverse field components can be rewritten as

$$\begin{bmatrix} \tilde{E}_{x_n} \\ \tilde{H}_{x_n} \\ \tilde{E}_{y_n} \\ \tilde{H}_{y_n} \end{bmatrix} = \begin{bmatrix} \tilde{Q}^B_{x_n} & \tilde{Q}^D_{x_n} \\ \tilde{G}^B_{x_n} & \tilde{G}^D_{x_n} \\ \tilde{Q}^B_{y_n} & \tilde{Q}^D_{y_n} \\ \tilde{G}^B_{y_n} & \tilde{G}^D_{y_n} \end{bmatrix} \begin{bmatrix} B_n \\ D_n \end{bmatrix}. \tag{2.24}$$

We can find the admittance using the relation

$$\widetilde{\boldsymbol{Y}}_n = \widetilde{\boldsymbol{M}}_{H_n} \widetilde{\boldsymbol{M}}_{E_n}^{-1}, \tag{2.25}$$

where

$$\widetilde{\boldsymbol{M}}_{H_n} = \begin{bmatrix} -\tilde{G}^B_{y_n} & -\tilde{G}^D_{y_n} \\ \tilde{G}^B_{x_n} & \tilde{G}^D_{x_n} \end{bmatrix}, \tag{2.26}$$

and

$$\widetilde{\boldsymbol{M}}_{E_n} = \begin{bmatrix} \tilde{Q}^B_{x_n} & \tilde{Q}^D_{x_n} \\ \tilde{Q}^B_{y_n} & \tilde{Q}^D_{y_n} \end{bmatrix}. \tag{2.27}$$

2.1.3 System Equation

We can set up the system equation on using the theory of full-wave equivalent circuit (FWEC) which consists of hybrid matrices ($\widetilde{\boldsymbol{K}}_k$) as shown in Fig. 2.2. We can get the admittance (or impedance) of the structure by using simple network analysis technique. The innermost layer of the planar structures is usually grounded and the outermost layer can be terminated with admittance $\widetilde{\boldsymbol{Y}}_n$ (if it is open), or can be enclosed with a perfect conductor. When there is no metallization in the interfaces of the layers, then in order to simplify the formulation all the inner layers can be modeled by successive matrix multiplication. Therefore, we get the equivalent hybrid matrix as

$$\widetilde{\boldsymbol{K}}_{eq} = \prod_{k=1}^{n-1} \widetilde{\boldsymbol{K}}_k, \tag{2.28}$$

representing all the cascaded $\widetilde{\boldsymbol{K}}_k$ matrices.

Next we should apply the continuity equations at the interface k to match the fields. The continuity equations can be written as

$$(\widetilde{\boldsymbol{E}}_k^+ - \widetilde{\boldsymbol{E}}_k^-) = 0 \tag{2.29}$$

and

$$(\widetilde{\boldsymbol{H}}_k^+ - \widetilde{\boldsymbol{H}}_k^-) = \widetilde{\boldsymbol{J}}_k. \tag{2.30}$$

Here "+" and "-" signs represent fields right above and below the k^{th} interface, respectively, and

$$\widetilde{\boldsymbol{J}}_k = \begin{bmatrix} \tilde{J}_x \\ \tilde{J}_y \end{bmatrix} \tag{2.31}$$

represents the column matrix of current densities present on the interface k. System equation gives the relation between the currents on the strip and the tangential electric field components on the interfaces. Thus, we can obtain the system equation in the spectral domain

$$\begin{bmatrix} \tilde{G}_{xx} & \tilde{G}_{xy} \\ \tilde{G}_{yx} & \tilde{G}_{yy} \end{bmatrix} \begin{bmatrix} \tilde{J}_x \\ J_y \end{bmatrix} = \begin{bmatrix} \tilde{E}_x \\ \tilde{E}_y \end{bmatrix} \quad \text{or} \quad \widetilde{\boldsymbol{G}}\widetilde{\boldsymbol{J}} = \widetilde{\boldsymbol{E}}, \tag{2.32}$$

$$\text{or } \widetilde{\boldsymbol{L}}\widetilde{\boldsymbol{E}} = \widetilde{\boldsymbol{J}}, \tag{2.33}$$

where $\widetilde{\boldsymbol{G}}$ represents the matrix consisting of elements in terms of Green's function (impedance form) of the structure, $\widetilde{\boldsymbol{L}}$(or $\widetilde{\boldsymbol{G}}^{-1}$) gives the admittance matrix of the structure and $\widetilde{\boldsymbol{J}}$ and $\widetilde{\boldsymbol{E}}$ represent column matrices with tangential surface current density and electric field intensity on the interfaces, respectively.

2.2 Analysis of Two-Layer Waveguide

To validate the previous formulation, we have analyzed a two-layer waveguide filled with anisotropic dielectric material stratified in z-direction. For this purpose, we have used unrotated uniaxial anisotropic material whose optical axis is in z-direction. The basic geometry with $a = 12.7$ mm, $d_1 = 0.1a$, $d_2 = 0.9a$, $\varepsilon_{r1} = (9.4,9.4,11.6)$ and $\varepsilon_{r2} = 1$) is shown in Fig. 2.3.

There are no currents on the interface, therefore $\widetilde{\boldsymbol{J}} = 0$. Fig. 2.4 gives the corresponding equivalent circuit from which we can simply obtain the system equation as

$$\widetilde{\boldsymbol{L}}\widetilde{\boldsymbol{E}} = 0, \text{ where } \widetilde{\boldsymbol{L}} = \widetilde{\boldsymbol{Z}}_1^{-1}\widetilde{\boldsymbol{V}}_1 + \widetilde{\boldsymbol{B}}_2\widetilde{\boldsymbol{Z}}_2^{-1} \tag{2.34}$$

with

$$\widetilde{\boldsymbol{K}}_1 = \begin{bmatrix} \widetilde{\boldsymbol{V}}_1 & \widetilde{\boldsymbol{Z}}_1 \\ \widetilde{\boldsymbol{Y}}_1 & \widetilde{\boldsymbol{B}}_1 \end{bmatrix} \text{ and } \widetilde{\boldsymbol{K}}_2 = \begin{bmatrix} \widetilde{\boldsymbol{V}}_2 & \widetilde{\boldsymbol{Z}}_2 \\ \widetilde{\boldsymbol{Y}}_2 & \widetilde{\boldsymbol{B}}_2 \end{bmatrix}. \tag{2.35}$$

The first term of the admittance ($\widetilde{\boldsymbol{Z}}_1^{-1}\widetilde{\boldsymbol{V}}_1$) denotes the admittance of the grounded bottom layer and the second term ($\widetilde{\boldsymbol{B}}_2\widetilde{\boldsymbol{Z}}_2^{-1}$) denotes the admittance of the closed top layer. The propagation constant can be found on solving the indirect eigenvalue problem

$$\det(\widetilde{\boldsymbol{L}}) = 0. \tag{2.36}$$

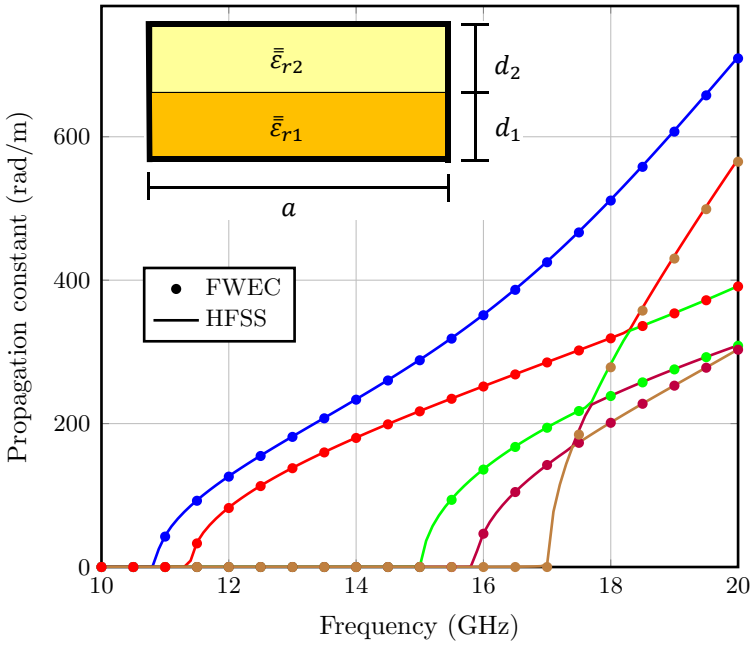

Figure 2.3: Dispersion curve for the 5 lowest order modes of a two-layer waveguide filled with anisotropic material.

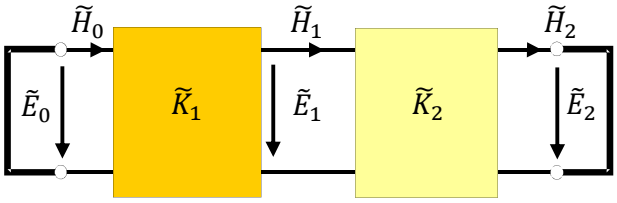

Figure 2.4: Equivalent circuit for a 2-layer waveguide.

Fig. 2.3 depicts the propagation constant k_y for the five lowest-order modes of the waveguide as a function of frequency and shows the comparison between the results obtained from our code written in MATLAB using FWEC and the commercial software ANSYS HFSS. We have obtained a very good agreement between the results and have found the difference of $\approx 0.2\%$.

2.3 Analysis of Multilayered Structures with Metallization

2.3.1 System Equation

The general method to form the system equation for structures with metallization in several interfaces is well explained in [Dreher, 1995]. From (2.21) and (2.22), we can write the equations

$$\widetilde{\boldsymbol{H}}_{k-1} = (\widetilde{\boldsymbol{Y}}_k - \widetilde{\boldsymbol{B}}_k \widetilde{\boldsymbol{Z}}_k^{-1} \widetilde{\boldsymbol{V}}_k)\widetilde{\boldsymbol{E}}_k + \widetilde{\boldsymbol{B}}_k \widetilde{\boldsymbol{Z}}_k^{-1} \widetilde{\boldsymbol{E}}_{k-1}, \tag{2.37}$$

$$\widetilde{\boldsymbol{H}}_k = \widetilde{\boldsymbol{Z}}_k^{-1} \widetilde{\boldsymbol{E}}_{k-1} - \widetilde{\boldsymbol{Z}}_k^{-1} \widetilde{\boldsymbol{V}}_k \widetilde{\boldsymbol{E}}_k. \tag{2.38}$$

By using FWEC of the structure (Fig. 2.2), and (2.37) and (2.38), we obtain

$$\widetilde{\boldsymbol{H}}_k^+ = (\widetilde{\boldsymbol{Y}}_{k+1} - \widetilde{\boldsymbol{B}}_{k+1}\widetilde{\boldsymbol{Z}}_{k+1}^{-1}\widetilde{\boldsymbol{V}}_{k+1})\widetilde{\boldsymbol{E}}_{k+1} + \widetilde{\boldsymbol{B}}_{k+1}\widetilde{\boldsymbol{Z}}_{k+1}^{-1}\widetilde{\boldsymbol{E}}_k, \tag{2.39}$$

$$\widetilde{\boldsymbol{H}}_k^- = \widetilde{\boldsymbol{Z}}_k^{-1}\widetilde{\boldsymbol{E}}_{k-1} - \widetilde{\boldsymbol{Z}}_k^{-1}\widetilde{\boldsymbol{V}}_k\widetilde{\boldsymbol{E}}_k. \tag{2.40}$$

Now, using (2.30), (2.39) and (2.40), we obtain the relation between the current densities present in the interface k with the electric fields present in the interfaces $k-1$, k and $k-1$ as

$$\widetilde{\boldsymbol{J}}_k = \widetilde{\boldsymbol{L}}_{k,k-1}\widetilde{\boldsymbol{E}}_{k-1} + \widetilde{\boldsymbol{L}}_{k,k}\widetilde{\boldsymbol{E}}_k + \widetilde{\boldsymbol{L}}_{k,k+1}\widetilde{\boldsymbol{E}}_{k+1}, \tag{2.41}$$

where

$$\begin{aligned} \widetilde{\boldsymbol{L}}_{k,k-1} &= -\widetilde{\boldsymbol{Z}}_k^{-1} \\ \widetilde{\boldsymbol{L}}_{k,k} &= \widetilde{\boldsymbol{B}}_{k+1}\widetilde{\boldsymbol{Z}}_{k+1}^{-1} + \widetilde{\boldsymbol{Z}}_k^{-1}\widetilde{\boldsymbol{V}}_k \\ \widetilde{\boldsymbol{L}}_{k,k+1} &= \widetilde{\boldsymbol{Y}}_{k+1} - \widetilde{\boldsymbol{B}}_{k+1}\widetilde{\boldsymbol{Z}}_{k+1}^{-1}\widetilde{\boldsymbol{V}}_{k+1}. \end{aligned} \tag{2.42}$$

We can represent the system matrix for the structure with M metallized interfaces by

$$\begin{bmatrix} \widetilde{\boldsymbol{J}}_1 \\ \widetilde{\boldsymbol{J}}_2 \\ \widetilde{\boldsymbol{J}}_3 \\ \vdots \\ \widetilde{\boldsymbol{J}}_{M-1} \\ \widetilde{\boldsymbol{J}}_M \end{bmatrix} = \begin{bmatrix} \widetilde{\boldsymbol{L}}_{11} & \widetilde{\boldsymbol{L}}_{12} & \boldsymbol{0} & \boldsymbol{0} & \cdots & \boldsymbol{0} \\ \widetilde{\boldsymbol{L}}_{21} & \widetilde{\boldsymbol{L}}_{22} & \widetilde{\boldsymbol{L}}_{23} & \boldsymbol{0} & \cdots & \boldsymbol{0} \\ \boldsymbol{0} & \widetilde{\boldsymbol{L}}_{32} & \widetilde{\boldsymbol{L}}_{33} & \widetilde{\boldsymbol{L}}_{34} & \cdots & \boldsymbol{0} \\ \vdots & \cdots & \ddots & \ddots & \cdots & \vdots \\ \boldsymbol{0} & \cdots & \boldsymbol{0} & \widetilde{\boldsymbol{L}}_{M-1,M-2} & \widetilde{\boldsymbol{L}}_{M-1,M-1} & \widetilde{\boldsymbol{L}}_{M-1,M} \\ \boldsymbol{0} & \cdots & \boldsymbol{0} & \boldsymbol{0} & \widetilde{\boldsymbol{L}}_{M,M-1} & \widetilde{\boldsymbol{L}}_{M,M} \end{bmatrix} \begin{bmatrix} \widetilde{\boldsymbol{E}}_1 \\ \widetilde{\boldsymbol{E}}_2 \\ \widetilde{\boldsymbol{E}}_3 \\ \vdots \\ \widetilde{\boldsymbol{E}}_{M-1} \\ \widetilde{\boldsymbol{E}}_M \end{bmatrix} \tag{2.43}$$

or

$$\widetilde{\boldsymbol{J}} = \widetilde{\boldsymbol{L}}\widetilde{\boldsymbol{E}} \tag{2.44}$$

where matrix $\widetilde{\boldsymbol{L}}$ represents the admittance matrix of the system. The elements $\widetilde{\boldsymbol{L}}_{11}$ and $\widetilde{\boldsymbol{L}}_{MM}$ should include the lower and upper terminations. The admittances for lower and upper layers are well defined in the Appendix A. When the outer layer is unbounded, we can write

$$\widetilde{\boldsymbol{L}}_{M,M} = \widetilde{\boldsymbol{Y}}_n + \widetilde{\boldsymbol{Z}}_M^{-1}\widetilde{\boldsymbol{V}}_M. \tag{2.45}$$

2.3.2 The Discrete Mode Matching Method

The general cross-sectional view of the multilayered microwave structure is depicted in Fig. 2.5. Here, we consider several microstrip lines in the interfaces of the anisotropic dielectric layers (optical axis in z-direction). For the present analysis, the structure is stratified in z-direction and the wave propagation ($\exp(-jk_y y)$) is assumed in y-direction. The analysis begins with the Helmholtz's equation, normalized by the free space wave number k_0,

$$\left(\frac{\partial^2}{\partial x^2} + \frac{\partial}{\partial z^2} + \varepsilon_d\right)\psi_k = 0, \qquad \varepsilon_d = K^2 - k_y^2. \tag{2.46}$$

Here, ψ represents the independent field components E_z or H_z and K the propagation constant in any arbitrary layer k.

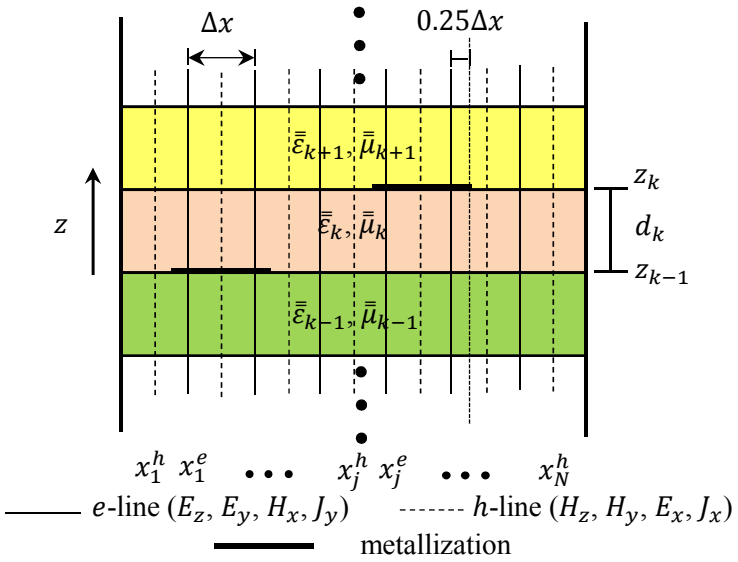

Figure 2.5: Discretized multilayered microwave structure with metallization in the interfaces.

We assume the structure to be infinite in the propagation direction, so we use just 1D discretization along x for the analysis of multilayered microstrip lines as shown in Fig. 2.5. The field components are sampled at N equidistant points x_j between the lateral walls. We do the discretization with two line systems as shown in the figure, e-lines show the position of E_z and h-lines show the position of H_z field components. Using separate line systems have several advantages, for example, we can easily fulfill the lateral boundary conditions (electric- or magnetic-wall) by putting these lines on suitable positions. The two line systems are shifted from each other with uniform distance [Heckler, 2010; Pregla, 2008]. From (2.6), we can see that we need H_z and the derivative of E_z on the same position to calculate the value of E_x. Similarly, we need E_z and the derivative of H_z on the same position to calculate the value of H_x. This can only be done with shifted discretization scheme. Here, we adapt equidistant discretization because the finite difference method yields the derivative in the middle of the lines.

We take the modal expansion of the field components according to the lateral boundary conditions. To satisfy the sampling theorem, we must include the same number of modes in the expansion of the series as the number of lines taken for the discretization [Ioffe and Dreher, 1999; Dreher and Rother, 1995]. Therefore, the transformation equation of the field components having N modes discretized by N samples is given by

$$\psi_j(x_j, z) = \sum_{i=1}^{N} \tau_x(k_{xi} x_j) \tilde{\psi}_i(k_{xi}, z) \qquad \text{or} \qquad \boldsymbol{\psi} = \boldsymbol{T}\widetilde{\boldsymbol{\psi}}. \tag{2.47}$$

Here $\widetilde{\boldsymbol{\psi}}$ represents the column matrix of field component in spectral domain containing all the modal values, $\boldsymbol{\psi}$ represents the column matrix of field component in spatial domain and $\boldsymbol{T}$ is the transformation matrix containing the exact eigensolutions $\tau_x(k_{xi}x_j)$ of the Helmholtz equation (Fourier series elements) which are dependent on the lateral boundary conditions. Table 2.1 summarizes the eigenvalues k_{xi} which are the wave numbers in x-direction and corresponding wave functions for different boundary conditions. In the table, a defines the distance between the lateral walls. The edge parameter, i.e., the distance

Table 2.1: Eigensolutions of the Helmholtz equation for different boundary combinations

Boundary combination (left/right)	τ_{xi}^e	τ_{xi}^h	k_{xi}
E-wall/E-wall	$-j\sin(k_{xi}x^e)$	$\cos(k_{xi}x^h)$	$\frac{i\pi}{a}$
H-wall/H-wall	$\cos(k_{xi}x^e)$	$-j\sin(k_{xi}x^h)$	$\frac{i\pi}{a}$
H-wall/E-wall	$\cos(k_{xi}x^e)$	$-j\sin(k_{xi}x^h)$	$\frac{(i-\frac{1}{2})\pi}{a}$

between the edge of the metallization and the e-line is taken to be $0.25\Delta x$. Heckler [2010] has discussed in detail the edge conditions and suitable line placement for the efficient computation. Appendix D also summarizes the discretization scheme in case of symmetry present in the structures.

From (2.47), we write in matrix form that

$$\boldsymbol{E}_z = \boldsymbol{T}_e \widetilde{\boldsymbol{E}} z, \tag{2.48}$$

$$\boldsymbol{H}_z = \boldsymbol{T}_h \widetilde{\boldsymbol{H}} z, \tag{2.49}$$

with $\boldsymbol{T}_e$ and $\boldsymbol{T}_h$ representing transformation matrices for e- and h-lines with τ_{xi}^e and τ_{xi}^h as the eigensolutions, respectively. We can easily identify the locations of other field components with the help of the field relations (2.6). Fig. 2.5 describes the positions of all the field components. Therefore, the transformation of other field components from the spectral domain into the spatial domain in matrix form can be summarized as

$$\boldsymbol{E}_x = \boldsymbol{T}_h \widetilde{\boldsymbol{E}}_x, \tag{2.50}$$

$$\boldsymbol{E}_y = \boldsymbol{T}_e \widetilde{\boldsymbol{E}}_y, \tag{2.51}$$

$$\boldsymbol{H}_x = \boldsymbol{T}_e \widetilde{\boldsymbol{H}}_x, \tag{2.52}$$

$$\boldsymbol{H}_y = \boldsymbol{T}_h \widetilde{\boldsymbol{H}}_y. \tag{2.53}$$

On using the continuity equation of magnetic fields on the interface, we get the locations of current densities ((2.30)-(2.31)). In matrix notation for the inverse transformation, it comes out

$$\boldsymbol{J}_x = \boldsymbol{T}_h \widetilde{\boldsymbol{J}}_x, \tag{2.54}$$

$$\boldsymbol{J}_y = \boldsymbol{T}_e \widetilde{\boldsymbol{J}}_y. \tag{2.55}$$

Therefore, on transforming field components and current densities in (2.32) into the spatial domain, we get

$$\begin{bmatrix} \boldsymbol{G}_{xx} & \boldsymbol{G}_{xy} \\ \boldsymbol{G}_{yx} & \boldsymbol{G}_{yy} \end{bmatrix} \begin{bmatrix} \boldsymbol{J}_x \\ \boldsymbol{J}_y \end{bmatrix} = \begin{bmatrix} \boldsymbol{E}_x \\ \boldsymbol{E}_y \end{bmatrix} \quad \text{or} \quad \boldsymbol{G}\boldsymbol{J} = \boldsymbol{E}, \tag{2.56}$$

where

$$\begin{bmatrix} \boldsymbol{G}_{xx} & \boldsymbol{G}_{xy} \\ \boldsymbol{G}_{yx} & \boldsymbol{G}_{yy} \end{bmatrix} = \begin{bmatrix} \boldsymbol{T}_h & 0 \\ 0 & \boldsymbol{T}_e \end{bmatrix} \begin{bmatrix} \widetilde{\boldsymbol{G}}_{xx} & \widetilde{\boldsymbol{G}}_{xy} \\ \widetilde{\boldsymbol{G}}_{yx} & \widetilde{\boldsymbol{G}}_{yy} \end{bmatrix} \begin{bmatrix} \boldsymbol{T}_h^{-1} & 0 \\ 0 & \boldsymbol{T}_e^{-1} \end{bmatrix}. \tag{2.57}$$

The boundary conditions state that the tangential electric field components must vanish on the metallizations and the electric currents outside that region. After applying these conditions, we obtain a reduced matrix as

$$\boldsymbol{G}_{\mathrm{red}}\boldsymbol{J}_{\mathrm{red}} = 0 \qquad \text{or} \qquad \boldsymbol{L}_{\mathrm{red}}\boldsymbol{E}_{\mathrm{red}} = 0. \tag{2.58}$$

$\boldsymbol{J}_{\mathrm{red}}$ contains the surface current density components located on the metallizations, while $\boldsymbol{E}_{\mathrm{red}}$ contains the field components located outside the metallization. It can be solved as an indirect eigenvalue problem

$$\det(\boldsymbol{G}_{\mathrm{red}}) = 0 \qquad \text{or} \qquad \det(\boldsymbol{L}_{\mathrm{red}}) = 0, \tag{2.59}$$

to find the propagation constants for the microstrip line structures.

2.4 Numerical Results

This section deals with the various applications of the formulation discussed in the previous sections of the chapter.

2.4.1 Dispersion Curve: Shielded Microstrip Line

To verify the above mentioned approach, first we have analyzed a shielded microstrip line. Here, we have considered the uniaxial electric anisotropy in the dielectric layers with optical axis in the z-direction. The basic geometry of the structure is presented in the inset of Fig. 2.6, where $w = 1.27$ mm, $a = 10w$, $d_1 = w$, $d_2 = a\text{-}d_1$, $\bar{\bar{\varepsilon}}_{r1}$ = (9.4,9.4,11.6) and $\bar{\bar{\varepsilon}}_{r2}$ = (1,1,1). We have considered only half of the structure with 4 e-lines on the strip for analysis due to symmetry. Fig. 2.7 shows the full-wave equivalent circuit used for the analysis. The system equation can thus be obtained as

$$\left(\widetilde{\boldsymbol{Z}}_1^{-1}\widetilde{\boldsymbol{V}}_1 + \widetilde{\boldsymbol{B}}_2\widetilde{\boldsymbol{Z}}_2^{-1}\right)\widetilde{\boldsymbol{E}}_1 = \widetilde{\boldsymbol{J}}_1, \tag{2.60}$$

where $\widetilde{\boldsymbol{J}}_1$ gives the currents on the interface, i.e., on the strip. The wave functions are described in Table 2.1 which should be used for expansion in (2.47) along with (2.14). The results presented in Fig. 2.6 show the propagation constant k_y for the two lowest-order modes with respect to a wide frequency range. It can be realized that the results obtained from DMM and ANSYS HFSS agree very well. They are also in good agreement with the open literature [Mao, 2007].

Figure 2.8 shows the convergence of the propagation constant of the first mode at 10 GHz with increasing number of e-lines in discretization direction. The exact eigenvalues are taken directly according to the sampling theorem, which states that the number of modes should be equal to the number of sampling points. The typical convergence curves do not apply to the canonical structures, i.e., when the dielectric interfaces follow the coordinate axes, without metallization. We do not need any discretization and use exact eigenvalues for analytical solutions using FWEC, for example, the two-layer waveguide in Fig. 2.3. There the approximation is only given by the root-finding algorithm.

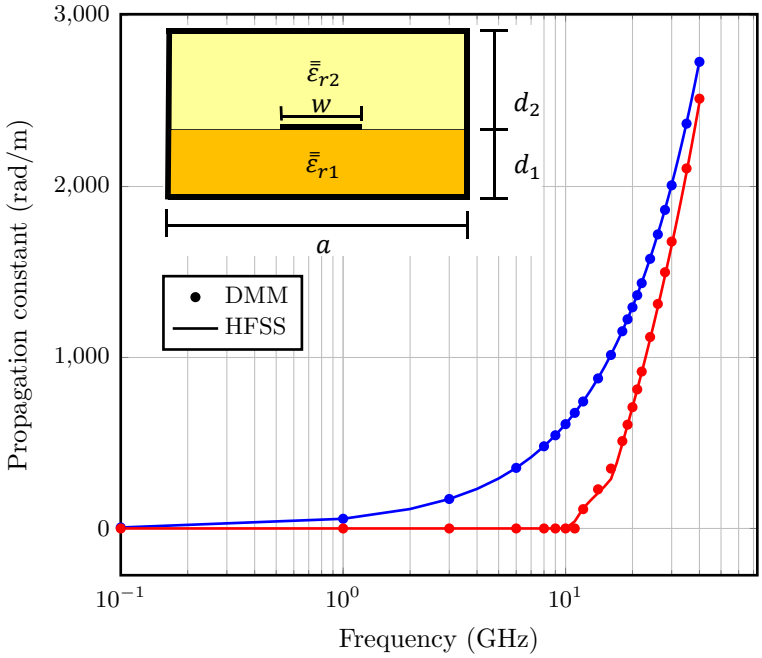

Figure 2.6: Dispersion curve for the lowest 2 modes of a shielded microstrip line filled with anisotropic material.

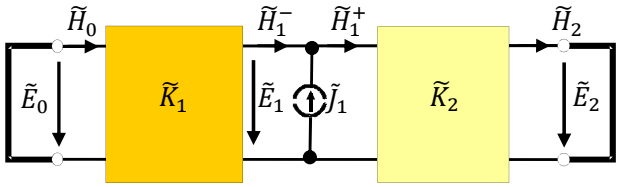

Figure 2.7: Full-wave equivalent circuit for a shielded microstrip line.

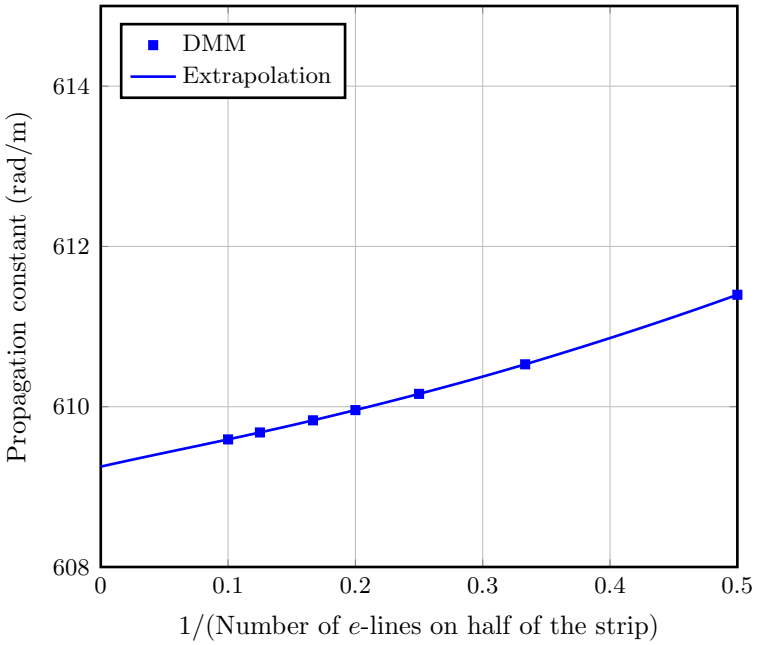

Figure 2.8: Convergence behavior of propagation constant for microstrip line.

2.4.2 Dispersion Curve: Multilayered Microstrip Line

Then we have considered a multilayered structure with four striplines at different interfaces, as shown in Fig. 2.9. The cross-section of the structure is with $a = 19.93$ mm, $d_1 = 1.2$ mm, $d_2 = 1.0$ mm, $d_3 = 0.7$ mm, $d_4 = 1.5$ mm, $w_1 = 1.3$ mm, $w_2 = 1.79$ mm, $w_3 = 1.79$ mm, $w_4 = 2.28$ mm, $s_1 = 8.56$ mm, $s_2 = 7.54$ mm, $s_3 = 1.79$ mm and $s_4 = 9.07$ mm. The material parameters used for the analysis are $\bar{\bar{\varepsilon}}_{r1} = 2.3$ or (2.3, 2.3, 2.2), $\bar{\bar{\varepsilon}}_{r2} = 8.875$ or (8.875, 8.875, 8.5), $\bar{\bar{\varepsilon}}_{r3} = 5$ or (5, 5, 4.8), $\bar{\bar{\varepsilon}}_{r4} = 12$ or (12,12,10.8), $\varepsilon_{r5} = 1$ and $\mu_{r1} = \mu_{r2} = \mu_{r3} = \mu_{r4} = \mu_{r5} = 1$. There are five layers in the structure with four interfaces, thus we build the system matrix of the structure according to (2.43) as

$$\begin{bmatrix} \widetilde{\boldsymbol{J}}_1 \\ \widetilde{\boldsymbol{J}}_2 \\ \widetilde{\boldsymbol{J}}_3 \\ \widetilde{\boldsymbol{J}}_4 \end{bmatrix} = \begin{bmatrix} \widetilde{\boldsymbol{L}}_{11} & \widetilde{\boldsymbol{L}}_{12} & \boldsymbol{0} & \boldsymbol{0} \\ \widetilde{\boldsymbol{L}}_{21} & \widetilde{\boldsymbol{L}}_{22} & \widetilde{\boldsymbol{L}}_{23} & \boldsymbol{0} \\ \boldsymbol{0} & \widetilde{\boldsymbol{L}}_{32} & \widetilde{\boldsymbol{L}}_{33} & \widetilde{\boldsymbol{L}}_{34} \\ \boldsymbol{0} & \boldsymbol{0} & \widetilde{\boldsymbol{L}}_{43} & \widetilde{\boldsymbol{L}}_{44} \end{bmatrix} \begin{bmatrix} \widetilde{\boldsymbol{E}}_1 \\ \widetilde{\boldsymbol{E}}_2 \\ \widetilde{\boldsymbol{E}}_3 \\ \widetilde{\boldsymbol{E}}_4 \end{bmatrix}, \tag{2.61}$$

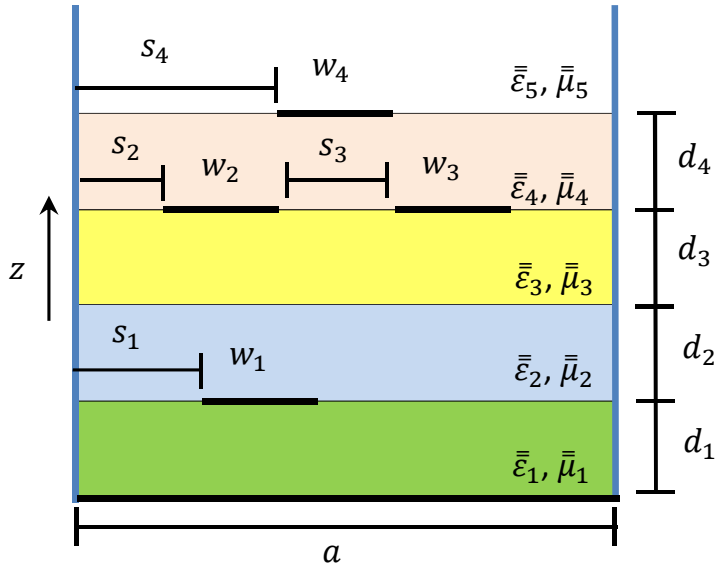

Figure 2.9: Multilayered microstrip structure.

where

$$
\begin{aligned}
\widetilde{\boldsymbol{L}}_{11} &= \widetilde{\boldsymbol{B}}_2\widetilde{\boldsymbol{Z}}_2^{-1} + \widetilde{\boldsymbol{Z}}_1^{-1}\widetilde{\boldsymbol{V}}_1 \\
\widetilde{\boldsymbol{L}}_{12} &= \widetilde{\boldsymbol{Y}}_2 - \widetilde{\boldsymbol{B}}_2\widetilde{\boldsymbol{Z}}_2^{-1}\widetilde{\boldsymbol{V}}_2 \\
\widetilde{\boldsymbol{L}}_{21} &= -\widetilde{\boldsymbol{Z}}_2^{-1} \\
\widetilde{\boldsymbol{L}}_{22} &= \widetilde{\boldsymbol{B}}_3\widetilde{\boldsymbol{Z}}_3^{-1} + \widetilde{\boldsymbol{Z}}_2^{-1}\widetilde{\boldsymbol{V}}_2 \\
\widetilde{\boldsymbol{L}}_{23} &= \widetilde{\boldsymbol{Y}}_3 - \widetilde{\boldsymbol{B}}_3\widetilde{\boldsymbol{Z}}_3^{-1}\widetilde{\boldsymbol{V}}_3 \\
\widetilde{\boldsymbol{L}}_{32} &= -\widetilde{\boldsymbol{Z}}_3^{-1} \\
\widetilde{\boldsymbol{L}}_{33} &= \widetilde{\boldsymbol{B}}_4\widetilde{\boldsymbol{Z}}_4^{-1} + \widetilde{\boldsymbol{Z}}_3^{-1}\widetilde{\boldsymbol{V}}_3 \\
\widetilde{\boldsymbol{L}}_{34} &= \widetilde{\boldsymbol{Y}}_4 - \widetilde{\boldsymbol{B}}_4\widetilde{\boldsymbol{Z}}_4^{-1}\widetilde{\boldsymbol{V}}_4 \\
\widetilde{\boldsymbol{L}}_{43} &= -\widetilde{\boldsymbol{Z}}_4^{-1} \\
\widetilde{\boldsymbol{L}}_{44} &= \widetilde{\boldsymbol{Y}}_5 + \widetilde{\boldsymbol{Z}}_4^{-1}\widetilde{\boldsymbol{V}}_4.
\end{aligned}
\tag{2.62}
$$

We have presented the results for the propagation constant, normalized with k_0, as a function of frequency for both isotropic and anisotropic dielectric layers in Fig. 2.10. For the analysis we have used only 5 e-lines to discretize the top strip (w_4) of the structure. We have bounded the structure by electric walls in the x-direction and have left it open from the top. The computed results are in good agreement with the prediction in [Dreher, 1996] for the isotropic case and with ANSYS HFSS for both the isotropic and the anisotropic cases. The simulation with HFSS under port mode calculation at 5 GHz took 1 second while at 100 GHz took 8.5 minutes. The computation time varied between 1 to 3 seconds with DMM depending on the time to find the roots.

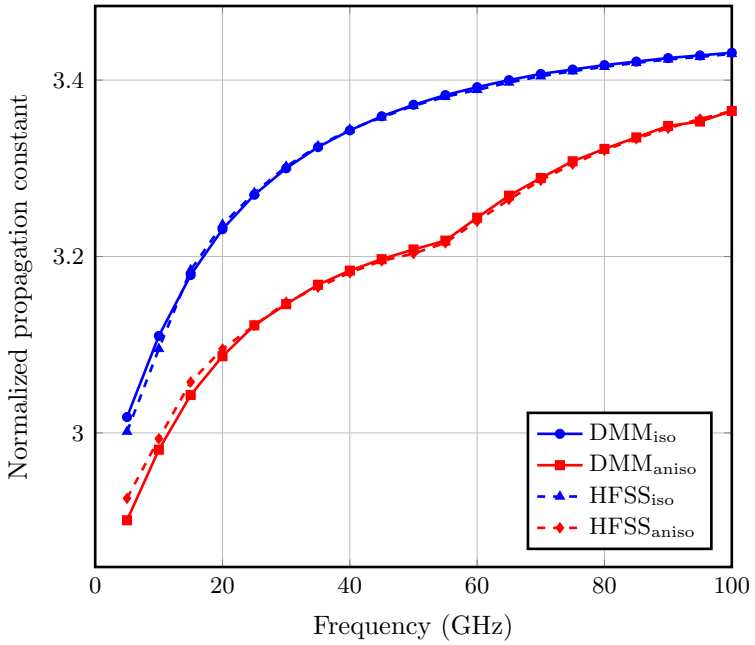

Figure 2.10: Dispersion curve of the multilayered stripline.

2.4.3 Dispersion Curve: Coplanar Waveguide

Next, we have analyzed a shielded coplanar waveguide to further demonstrate the method. The anisotropic substrate has the electric dielectric constant $\bar{\bar{\varepsilon}}_{r1} = (13, 13, 10.3)$ and $\varepsilon_{r2} = 1$. We have applied the similar procedure to compute the dispersion curve for the coplanar waveguide. Fig. 2.11 shows the basic geometry and the computed normalized propagation constant (k_y). We have done the analysis for the two cases shown in the figure. The results agree well with those given in [Hsu, 2001] (till 20 GHz) and those computed from ANSYS HFSS.

2.4.4 Characteristic Impedance

Let us take the case of a coplanar waveguide for calculating the characteristic impedance. We need the propagating power and the total current flowing on the central strip. The power from the transmission line can be computed from the electromagnetic field components using the equations given in [Dreher and Pregla, 1993]. The power component in propagating y-direction is given by

$$P_y = E_z H_x^* - E_x H_z^*. \tag{2.63}$$

To get the power propagation in the cross-section of the structure, we need to find the z-dependence of the field components along the corresponding discretization lines within the dielectric layers. The methodology is given by Dreher and Pregla [1993] and summarized in Appendix A for convenience.

Now we have discrete sampling points in the cross-section of the structure. Therefore we get the power density only at specific points in the cross-section. To calculate the total

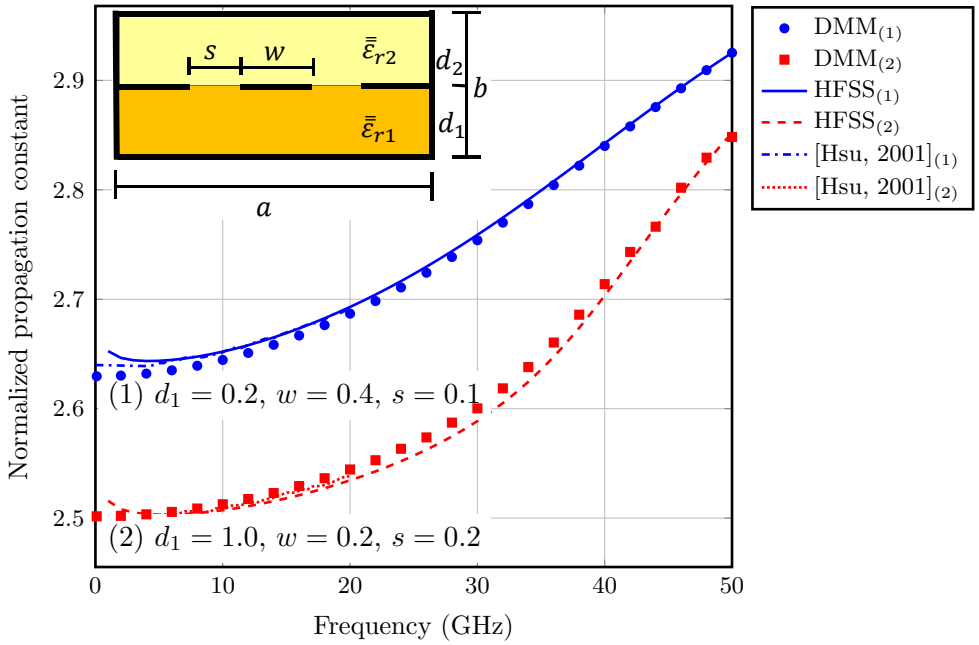

Figure 2.11: Dispersion curve for the coplanar waveguide ($a = 2$, $d_2 = 1$ and $\varepsilon_{r2} = 1$) (all dimensions in mm).

power propagating in the transmission line, we write

$$P_y = \sum_{j,l}^{N,L} (\Re\{\vec{E} \times \vec{H}^*\}_{j,l} \cdot \hat{y}) \Delta x \Delta z. \tag{2.64}$$

Here, N and L represent the number of samples in x- and z-directions, respectively, and the term $\Delta x \Delta z$ denotes a certain area of cross-section given by the discretization distance. Two-dimensional representation of power propagation in y-direction on half of the cross-section of the waveguide is presented in Fig. 2.12.

Similarly, we have currents from the system equation only at specific samples in x-direction. Therefore the total current on the central strip can be computed from

$$I_y = \sum_{j}^{N_c} J_{yj} \Delta x, \tag{2.65}$$

where N_c denotes the samples on the central strip. Consequently, the total characteristic impedance can be found using

$$Z_0 = \frac{P_y}{I_y^2}. \tag{2.66}$$

Fig. 2.13 shows the computed values for the characteristic impedance against frequency, which are closely related with the results in [Hsu, 2001] (till 20 GHz) and with those obtained from ANSYS HFSS.

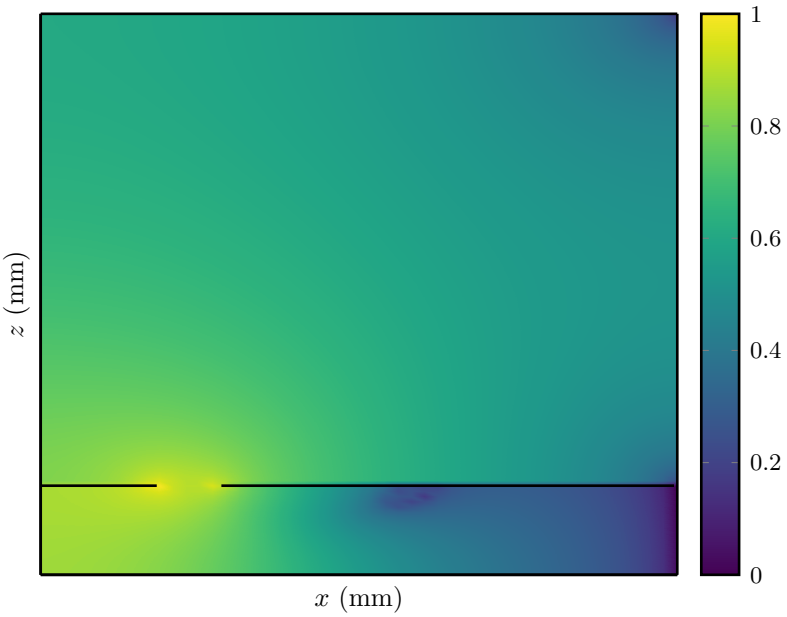

Figure 2.12: Power propagation in coplanar waveguide at 6 GHz for case (1).

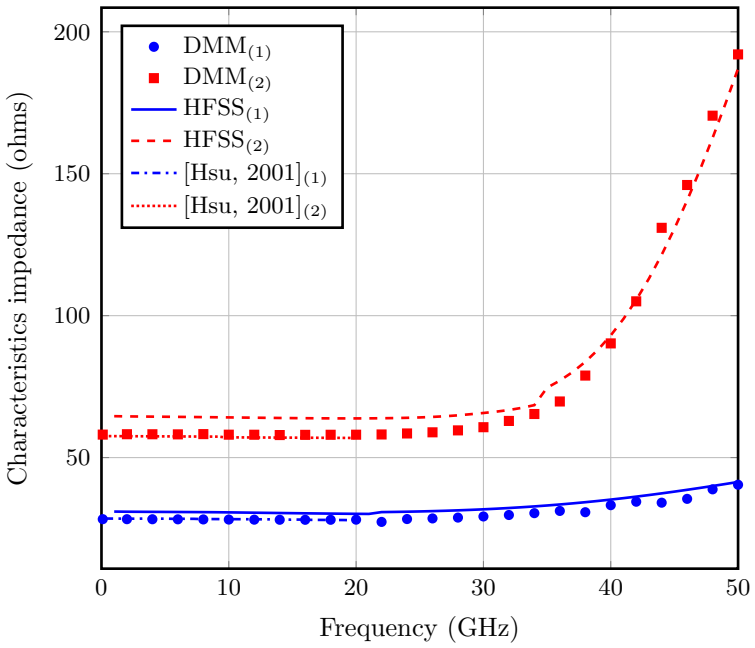

Figure 2.13: Characteristic impedance for coplanar waveguide.

3 Analysis of Planar Microstrip Antennas on Multilayered Substrate

In the previous chapter, applications of the DMM method with 1D discretization were analyzed. Here, we will discuss the extension of the DMM to 2D discretization, e.g., analysis of microstrip patch antennas. Printed antennas are widely used in satellite navigation and communication systems. The properties of the antennas are strongly dependent on the substrate material. The main focus of this chapter is on the characterization of microstrip antennas with 1) uniaxial anisotropic substrate, and 2) metamaterial substrate.

Significant work has been done for analyzing microstrip patch antennas with uniaxial media using method of moments [Krowne, 1986; Pozar, 1987; Hassad et al., 2014; Wong et al., 1993]. Green's function in spectral domain is used in [Krowne, 1986; Hassad et al., 2014] to analyze patch antennas. They discuss the effect of anisotropy on the antenna resonance.

Also, there has been growing interest in the study of metamaterials both theoretically and experimentally. Metamaterials are artificial materials synthesized by embedding specific inclusions, for example, periodic structures, in the host media and have unusual properties which are not readily available in nature. Some of these materials exhibit either negative permittivity or negative permeability. If both permittivity and permeability of such materials are negative at the same frequency, then the composite possesses an effective negative index of refraction and is referred to as a lefthanded (LH) metamaterial. The first theoretical study was done by Veselago [1968], then after several years the first LH material was proposed by Smith et al. [2000].

The dispersive properties of the substrate also change due to the presence of metallic structures in the material [Enoch et al., 2002; Weng et al., 2008], which gives rise to metamaterial substrate. The unusual properties of the metamaterials, such as negative refractive index, huge chirality, magnetic conductivity, directive emission and etc., play a pivotal role in antenna design, which can provide better performance and more flexibility.

The DMM employs discretization in two dimensions for radiating structures, which reduces memory requirement and computation time in comparison to the 3D meshes used in FEM and FDTD. It makes use of the full-wave equivalent circuit (FWEC) in spectral domain, which is well explained in the previous chapter. In this method, the used eigenvalues of the waveguide modes are exact and dependent on the four lateral boundary conditions. We employ absorbing boundary conditions (ABCs) in both horizontal directions, which are artificial boundaries to bound the computational domain. In the procedure, the Green's function is calculated to obtain the system equation of the structure.

In the following sections of the chapter, first we deal with the patch antennas with uniaxial anisotropic substrate and then with the metamaterial based microstrip antennas to achieve multi-band properties in the antenna. Based on that, we demonstrate the accuracy of the DMM method by comparing the results with the open literature as far as available. Some results have been presented in the conferences [Kamra and Dreher, 2018a,b].

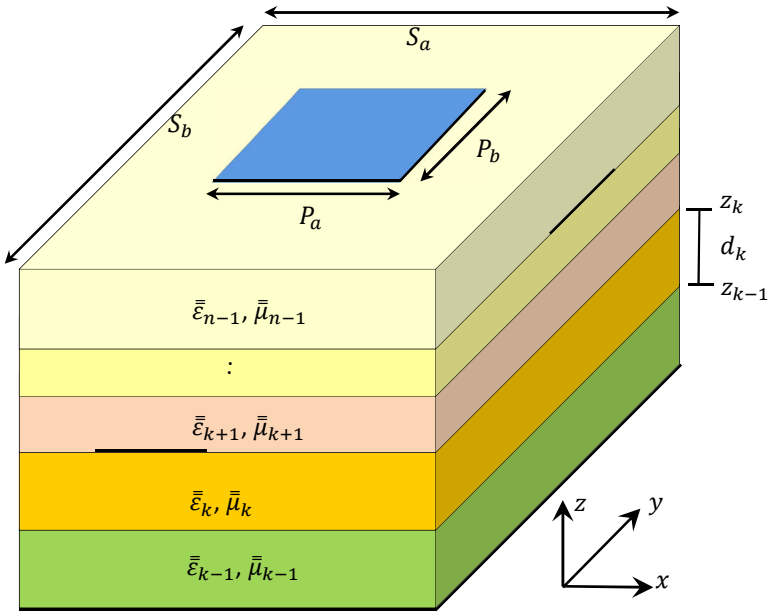

Figure 3.1: Multilayered structure with metallizations.

3.1 Formulation for the 2D discretization

3.1.1 Fourier Transformation and Discretization

We consider an arbitrary planar multilayered structure with metallizations in the interfaces, as shown in Fig. 3.1, in which the layer k is bounded by the interfaces $k-1$ and k. In the presented structure, we do the stacking of the layers in z-direction. On using inverse Fourier transformation, we can relate the field components in spectral and spatial domain by

$$\psi(x,y,z) = \frac{1}{4\pi^2}\int_{-\infty}^{+\infty}\int_{-\infty}^{+\infty}\tilde{\psi}(k_x,k_y,z)e^{jk_x x}e^{jk_y y}dk_x dk_y, \tag{3.1}$$

where $\psi = E_z$, Hz and k_x and k_y are the spectral variables in x- and y-directions, respectively. However, (3.1) is valid for unbounded structures along x and y. We consider the structure under analysis to be bounded in both directions, therefore the modes which exist in the structure are limited and are dependent on the boundaries used to enclose the computational domain. Consequently, the fields in spatial domain can be represented as

$$\psi(x,y,z) = \sum_{i}^{N_x}\sum_{l}^{N_y}\tau_x(k_{xi},x)\tau_y(k_{yl},y)\tilde{\psi}(k_{xi},k_{yl},z), \tag{3.2}$$

where k_{xi} and k_{yl} are the eigenvalues, and $\tau_x(k_{xi},x)$ and $\tau_y(k_{yl},y)$ represent eigensolutions. N_x and N_y are the number of modes included in the modal expansion in x- and y-directions, respectively. According to the Nyquist theorem, the number of lines used for the discretization should be the same as the number of modes used for the expansion. In the present method, we bound the radiating structure with absorbing boundary conditions and discretize it as shown in Fig. 3.2.

Since E_z and H_z are the two independent field components, we conclude that the e-lines are related to the points in the structure where E_z is computed, whereas h-lines are related

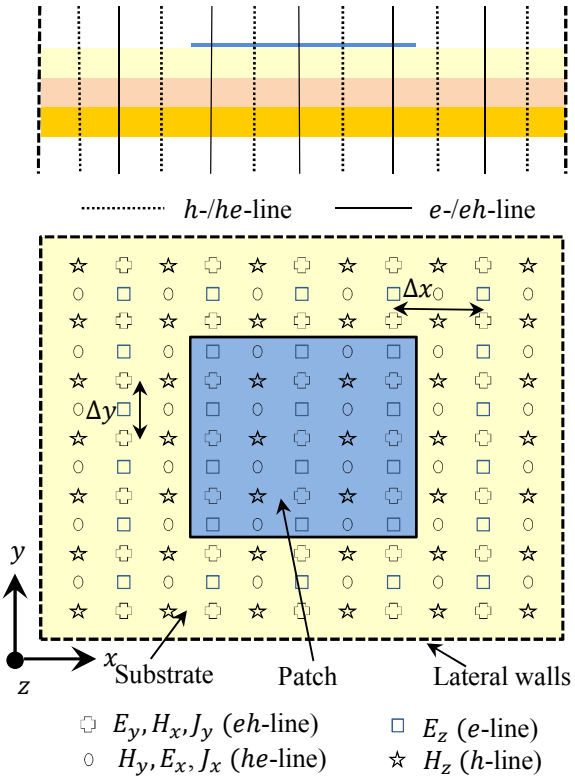

Figure 3.2: Patch discretization.

to the H_z field component. Therefore, from (3.2), we can write the field components in matrix notation as

$$\boldsymbol{E}_z = \boldsymbol{T}_{ee}\widetilde{\boldsymbol{E}}_z, \tag{3.3}$$

$$\boldsymbol{H}_z = \boldsymbol{T}_{hh}\widetilde{\boldsymbol{H}}_z. \tag{3.4}$$

For the case of unrotated uniaxial anisotropic media, we can find the other tangential field components using (2.6). Fig. 3.2 shows the location of all the field components on different positions shifted by half discretization distance ($\Delta x/2$ or $\Delta y/2$). After sampling the fields, we relate the remaining field and current components in spatial domain to their components in spectral domain in matrix notation by

$$\boldsymbol{E}_x = \boldsymbol{T}_{he}\widetilde{\boldsymbol{E}}_x, \tag{3.5}$$

$$\boldsymbol{H}_x = \boldsymbol{T}_{eh}\widetilde{\boldsymbol{H}}_x, \tag{3.6}$$

$$\boldsymbol{E}_y = \boldsymbol{T}_{eh}\widetilde{\boldsymbol{E}}_y, \tag{3.7}$$

$$\boldsymbol{H}_y = \boldsymbol{T}_{he}\widetilde{\boldsymbol{H}}_y, \tag{3.8}$$

$$\boldsymbol{J}_x = \boldsymbol{T}_{he}\widetilde{\boldsymbol{J}}_x, \tag{3.9}$$

$$\boldsymbol{J}_y = \boldsymbol{T}_{eh}\widetilde{\boldsymbol{J}}_y. \tag{3.10}$$

Here $\boldsymbol{T}_{\chi\chi}$ is the transformation matrix whose elements can be computed as

$$\tau_{\chi\chi} = \tau_x^{\chi}(k_{xi}, x)\tau_y^{\chi}(k_{yl}, y), \text{ where } \chi = e, h. \tag{3.11}$$

For $\psi = E_z$, τ_x^e and τ_y^e both follow the same solutions as given in Table 2.1. Similarly for $\psi = H_z$, τ_x^h and τ_y^h both follow the same solutions.

On using the inverse Fourier transformation of (2.32) with the help of (3.5)–(3.10), it will result in the form

$$\begin{bmatrix} \boldsymbol{G}_{xx} & \boldsymbol{G}_{xy} \\ \boldsymbol{G}_{yx} & \boldsymbol{G}_{yy} \end{bmatrix} \begin{bmatrix} \boldsymbol{J}_x \\ \boldsymbol{J}_y \end{bmatrix} = \begin{bmatrix} \boldsymbol{E}_x \\ \boldsymbol{E}_y \end{bmatrix} \tag{3.12}$$

where

$$\begin{bmatrix} \boldsymbol{G}_{xx} & \boldsymbol{G}_{xy} \\ \boldsymbol{G}_{yx} & \boldsymbol{G}_{yy} \end{bmatrix} = \begin{bmatrix} \boldsymbol{T}_{he} & 0 \\ 0 & \boldsymbol{T}_{eh} \end{bmatrix} \begin{bmatrix} \widetilde{\boldsymbol{G}}_{xx} & \widetilde{\boldsymbol{G}}_{xy} \\ \widetilde{\boldsymbol{G}}_{yx} & \widetilde{\boldsymbol{G}}_{yy} \end{bmatrix} \begin{bmatrix} \boldsymbol{T}_{he}^{-1} & 0 \\ 0 & \boldsymbol{T}_{eh}^{-1} \end{bmatrix}. \tag{3.13}$$

3.1.2 Use of Absorbing Boundary Conditions

When the structure is radiating, absorbing boundary conditions (ABCs) in the structure should be implemented to bound the computational domain. For planar structures we have ABCs both in x- and y-directions. First, we start the analysis by placing an ABC-wall in x-direction at $x = -a/2$ and $x = +a/2$. The present formulation makes use of the Higdon's operator [Higdon, 1987] in the calculation of ABCs which is well described by Ioffe and Dreher [1999]. We can write the operator in the form

$$\prod_{p=1}^{n_p} \Big(\frac{\partial}{\partial x} \pm j\sqrt{\varepsilon_m \mu_m}\cos(\theta_p) \Big) \psi = 0, \tag{3.14}$$

where n_p is the number of angles where perfect absorption exists, θ_p is the angle of incidence, ε_m represents relative permittivity and μ_m represents relative permeability of the medium at the placement of ABC-wall. As we are using multilayered anisotropic structures, therefore we consider average value of the material parameters of all dielectric layers, i.e., product of permeability and permittivity. We take

$$\varepsilon_m \mu_m = \frac{\varepsilon_{r1}\mu_{r1} + \varepsilon_{r2}\mu_{r2} + \ldots + \varepsilon_{rn}\mu_{rn}}{n}, \tag{3.15a}$$

$$\text{where } \varepsilon_{rk}\mu_{rk} = \frac{\varepsilon_{x_k}\mu_{x_k} + \varepsilon_{y_k}\mu_{y_k} + \varepsilon_{z_k}\mu_{z_k}}{3} \tag{3.15b}$$

with scalar values. We take the mean of the diagonal elements of the material tensors to remove the tensor effect.

The general field solution from the Helmholtz equation is given as

$$\psi = A_x e^{jk_{xi}x} + B_x e^{-jk_{xi}x}. \tag{3.16}$$

By solving (3.14) with (3.16) at the boundaries, we get the final characteristic equation as

$$e^{jk_{xi}a} \frac{\prod_{k=1}^{p} \left(k_{xi} - \sqrt{\varepsilon_m \mu_m}\cos(\theta_k) \right)}{\prod_{k=1}^{p} \left(k_{xi} + \sqrt{\varepsilon_m \mu_m}\cos(\theta_k) \right)} = \pm 1 = \frac{A_x}{B_x}. \tag{3.17}$$

The eigenvalues k_{xi} can be calculated on solving (3.17) by putting $A_x = \pm B_x$. When we consider $A_x = +B_x$ in (3.17), then the field response will be

$$\psi = 2\cos(k_{xi}x), \tag{3.18}$$

Table 3.1: Eigensolutions of the Helmholtz equation for different boundary combinations with ABCs

Boundary combination (left/right)	τ_{xi}^{e}	τ_{xi}^{h}	k_{xi}
ABC/ABC	$-j\sin(k_{xi}x^{e})$ $\cos(k_{x(i+1)}x^{e})$ $\vdots$ (alternating)	$\cos(k_{xi}x^{h})$ $-j\sin(k_{x(i+1)}x^{h})$ $\vdots$ (alternating)	k_{xi} satisfying B_x=-A_x $k_{x(i+1)}$ satisfying B_x=+A_x $\vdots$ (alternating)
E-wall/ABC	$-j\sin(k_{xi}x^{e})$	$\cos(k_{xi}x^{h})$	k_{xi} satisfying B_x=-A_x
H-wall/ABC	$\cos(k_{xi}x^{e})$	$-j\sin(k_{xi}x^{h})$	k_{xi} satisfying B_x=+A_x

and when $A_x = -B_x$, then

$$\psi = -2j\sin(k_{xi}x). \tag{3.19}$$

Table 3.1 summarizes the eigenvalues and eigensolutions to be used on placing ABC walls to limit the computational domain.

3.2 Numerical Results

After obtaining the system equation, we should impose the boundary conditions on the structure which force the tangential electric field components to vanish on the metallizations and the electric currents outside that region. Therefore, we obtain a reduced system of equations from (3.12) as

$$\boldsymbol{G}_{\text{red}}\boldsymbol{J}_{\text{red}} = 0 \qquad \text{or} \qquad \boldsymbol{L}_{\text{red}}\boldsymbol{E}_{\text{red}} = 0. \tag{3.20}$$

We can solve it as indirect eigenvalue problem to find the resonant frequency of the microstrip antenna. $\boldsymbol{G}_{\text{red}}$ and $\boldsymbol{J}_{\text{red}}$ contain the elements which are calculated at the discretization points located only on the patch (metallization), whereas $\boldsymbol{L}_{\text{red}}$ and $\boldsymbol{E}_{\text{red}}$ contain the elements calculated outside the patch. We can use root-finding algorithms to find the complex root when $\det(\boldsymbol{G}_{\text{red}}) = 0$ or $\det(\boldsymbol{L}_{\text{red}}) = 0$. The real part ($f_r$) of the root gives us the resonant frequency and the imaginary part (f_i) represents the losses in the antenna caused by radiation. As this method calculates the eigenmodes, so no external excitation is required to find the resonant frequency.

3.2.1 Patch Antenna with Uniaxial Anisotropic Substrate

3.2.1.1 Resonant Frequency

First, we have analyzed a single-layered microstrip patch antenna. We have grounded the substrate from bottom and left open at top. With these terminations, we can represent the

Table 3.2: Comparison of resonant frequencies and bandwidth for a rectangular microstrip patch on a substrate with $\varepsilon_x = 13.0$, $\varepsilon_z = 10.2$, $\mu_x = \mu_z = 1$

Input parameters (mm)			Resonant frequency (GHz)					Bandwidth (%)	
			Measured	Calculated					
P_a	P_b	d	[1]	[1]	[2]	[3]	DMM	[1]	DMM
30	20	1.27	2.264	2.268	2.261	2.284	2.2521	0.6	0.4
15	9.5	1.27	4.495	4.520	4.355	4.599	4.4862	1.4	0.9
30	19	2.54	2.242	2.260	2.177	2.299	2.2431	1.2	0.9

[1]=[Pozar, 1987], [2]=[Aouabdia et al., 2011], [3]=[Hassad et al., 2014]

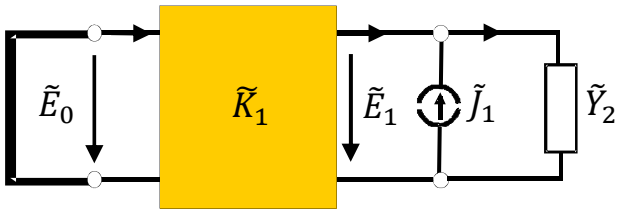

Figure 3.3: Full-wave equivalent circuit for a microstrip patch antenna.

FWEC for the analyzed antenna with Fig. 3.3. Therefore, we obtain the system equation

$$(\widetilde{\boldsymbol{Z}}_1^{-1}\widetilde{\boldsymbol{V}}_1 + \widetilde{\boldsymbol{Y}}_2)^{-1}\widetilde{\boldsymbol{E}}_1 = \widetilde{\boldsymbol{J}}_1, \tag{3.21}$$

where $\widetilde{\boldsymbol{Z}}_1^{-1}\widetilde{\boldsymbol{V}}_1$ denotes the admittance of the layer with closed bottom, $\widetilde{\boldsymbol{Y}}_2$ denotes the admittance of the open top, $\widetilde{\boldsymbol{E}}_1$ denotes the tangential electric field and $\widetilde{\boldsymbol{J}}_1$ the tangential surface current density on the metallized interface. Table 3.2 presents the comparison between the results of the resonant frequency (f') and the bandwidth ($2f''/f'$) using different methods. We have done the computations on considering just one quarter of the patch because of symmetry and put the ABC walls along the substrate with a length of $4P_a$ in x-direction and $6P_b$ in y-direction. For the presented DMM results, we have used 8 e-lines in x- and y-directions both on quarter of the patch.

Fig. 3.4 and 3.5 show the convergence of the computations with increment in the number of lines used for the discretization of the structure for Case 1 in Table 3.2. We have used extrapolation of discretization in x-direction to get the predictions. We can see from the figure that the results do not vary much between 6 and 8 e-lines in y-direction on the patch. Therefore, we have done the analysis till only 8 e-lines along y. We have concluded from the figure that only a few discretization lines are sufficient to lead us close to the results presented in [Pozar, 1987].

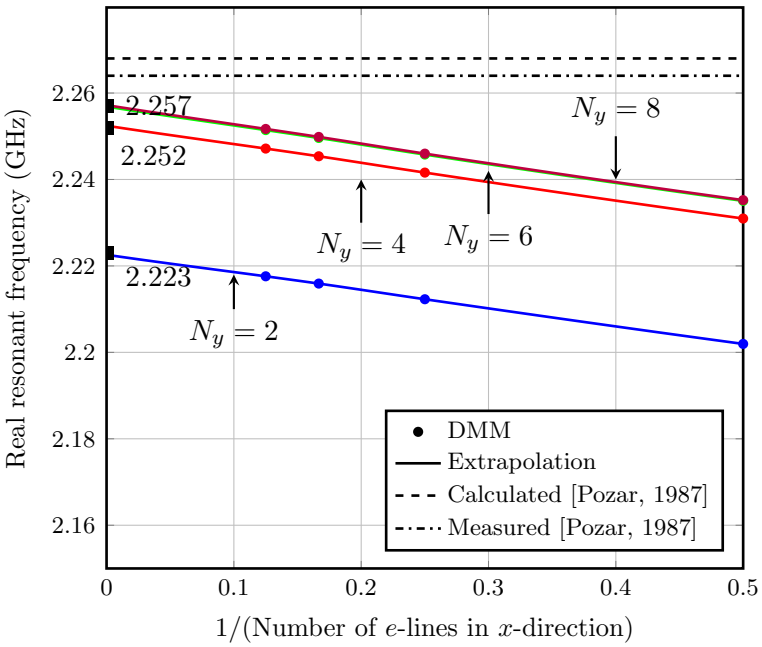

Figure 3.4: Convergence of the DMM computations on the real part of the resonant frequency vs. discretization points in x-direction on the patch.

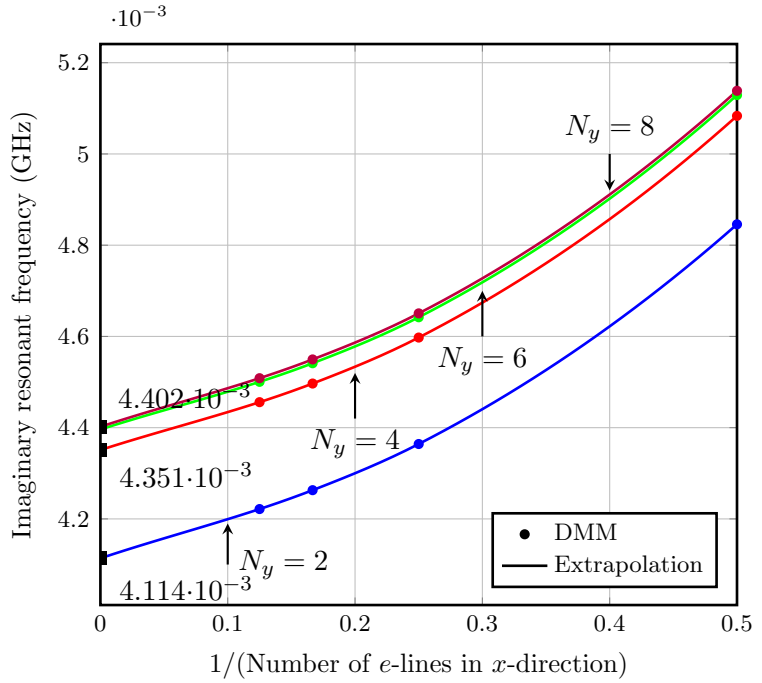

Figure 3.5: Convergence of the DMM computations on the imagninary part of the resonant frequency vs. discretization points in x-direction on the patch.

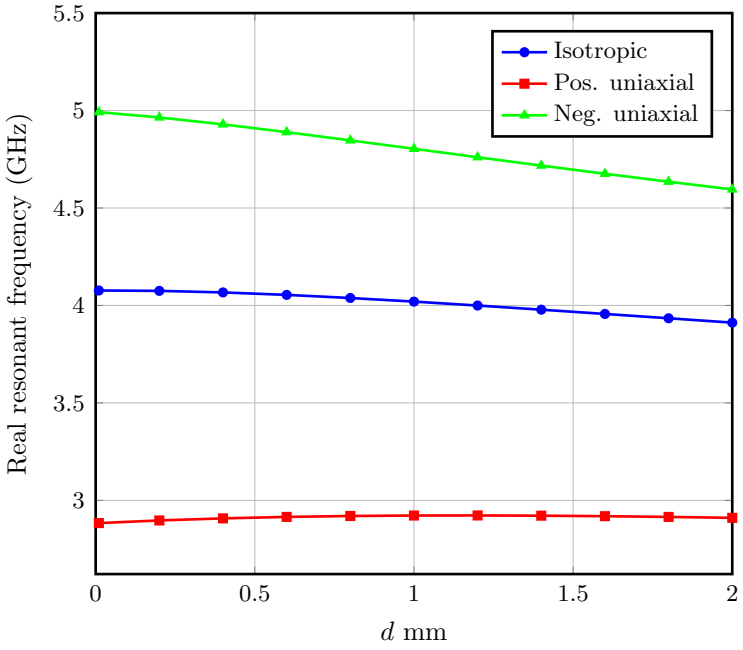

(a) Real part of the resonant frequency.

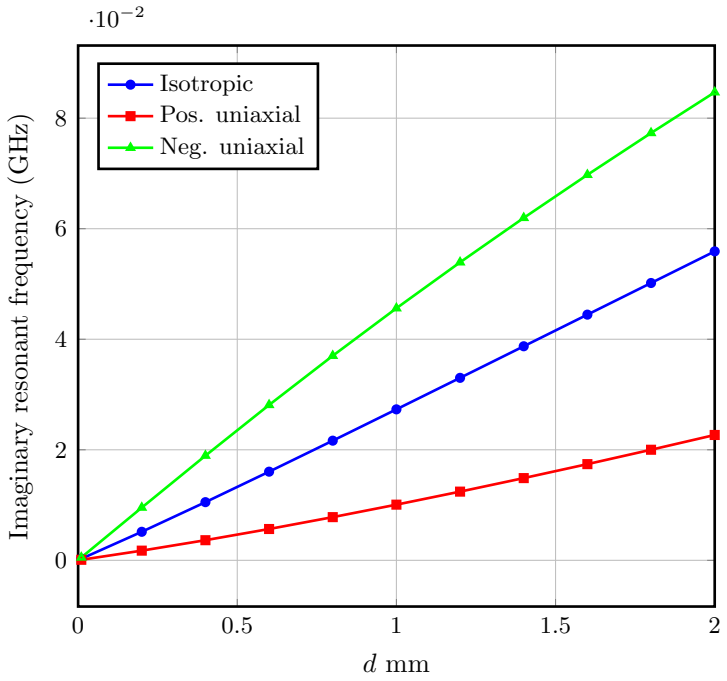

(b) Imaginary part of the resonant frequency.

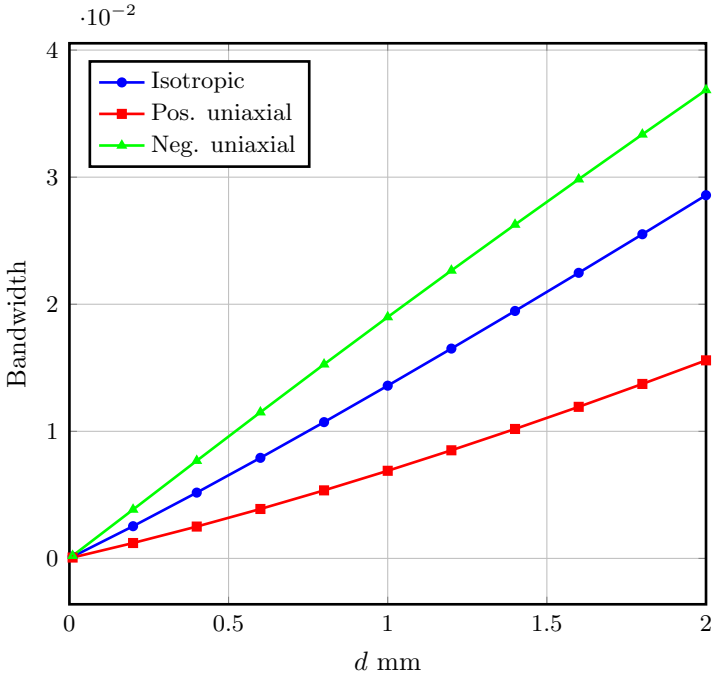

(c) Bandwidth.

Figure 3.6: Resonant frequency and bandwidth versus substrate thickness (electric anisotropic material).

Next, Fig. 3.6 and 3.7 show the real part of the resonant frequency (f'), the imaginary part (f'') of the resonant frequency and the bandwidth ($2f''/f'$) of the microstrip patch antenna on uniaxial electric and uniaxial magnetic anisotropic substrate, respectively. The material parameters used for the electric anisotropic substrate in Fig. 3.6 are $\varepsilon_x = \varepsilon_z = 2.43$ (for isotropic), $\varepsilon_x = 2.43$, $\varepsilon_z = 1.62$ (negative uniaxial), $\varepsilon_x = 2.43$, $\varepsilon_z = 4.86$ (positive uniaxial) and $\mu_x = \mu_z = 1$. The material properties used for the magnetic anisotropic substrate in Fig. 3.7 are $\mu_x = \mu_z = 2.4$ (for isotropic), $\mu_x = 4.8$, $\mu_z = 2.4$ (negative uniaxial), $\mu_x = 1.2$, $\mu_z = 2.4$ (positive uniaxial) and $\varepsilon_x = \varepsilon_z = 1$. The figures compare the results for isotropic, negative uniaxial anisotropic and positive uniaxial anisotropic substrates with $P_a = 19$ mm, $P_b = 22.9$ mm, $S_a = 4P_a$ and $S_b = 4P_b$. They also show the influence of substrate thickness on the resonant frequency and bandwidth. The responses are in good agreement with the open literature [Hassad et al., 2014]. We have used only 4 e-lines in the x- and y-directions both on a quarter of the patch to obtain the shown results.

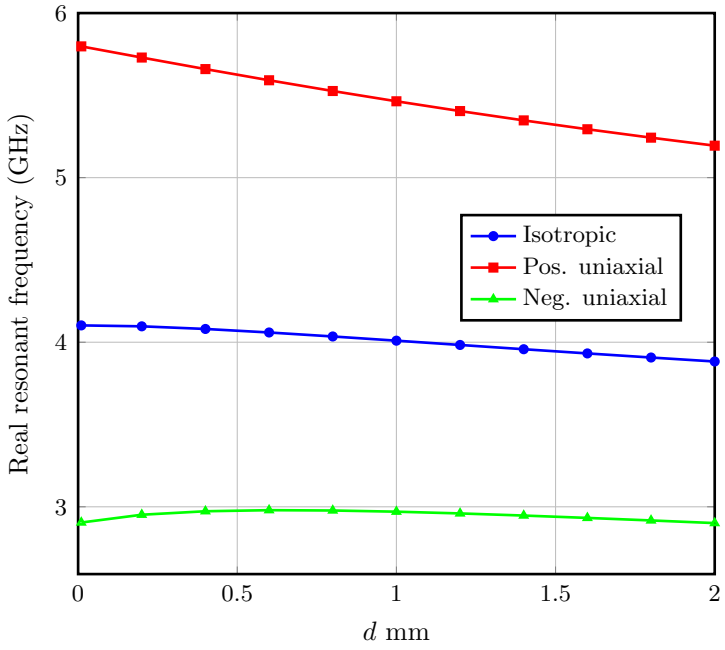

(a) Real part of the resonant frequency.

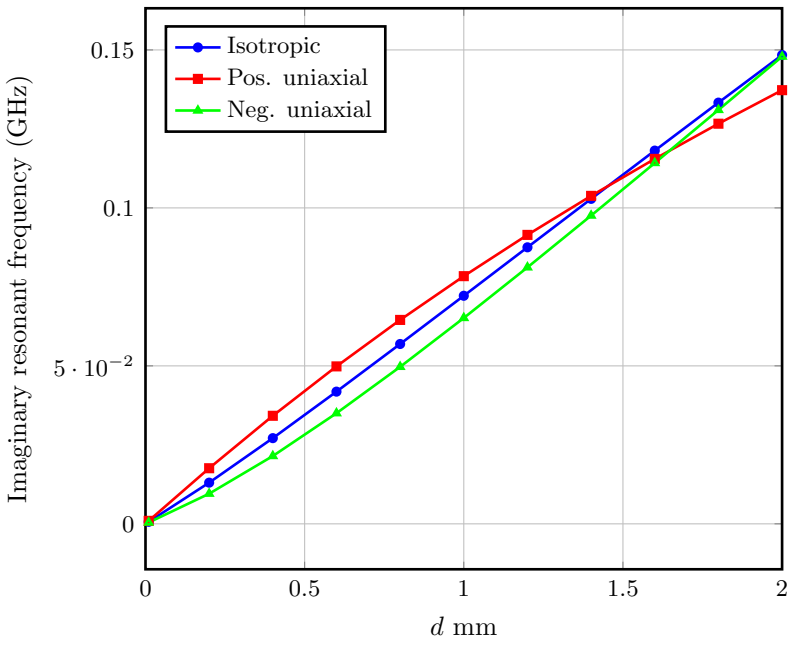

(b) Imaginary part of the resonant frequency.

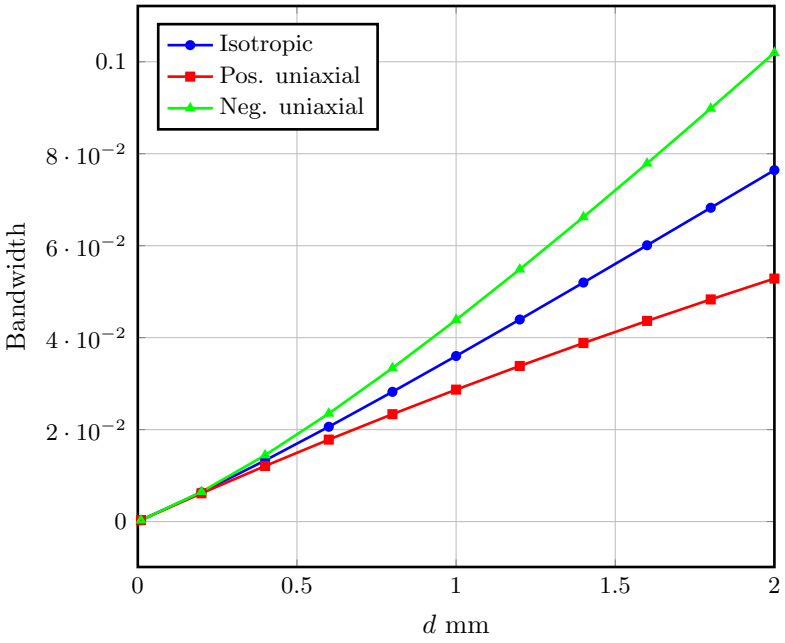

(c) Bandwidth.

Figure 3.7: Resonant frequency and bandwidth versus substrate thickness (magnetic anisotropic material).

3.2.1.2 Radiation Pattern

The presented formulation computes the current densities on the points of discretization on the metallizations. This is done by calculating the eigenvector of the square matrix $\boldsymbol{G}_{\text{red}}$. Afterwards, we compute the current components in spectral domain using

$$\tilde{J}_x = J_x \exp^{j(k_x x\prime + k_y y\prime)}, \tag{3.22}$$

$$\tilde{J}_y = J_y \exp^{j(k_x x\prime + k_y y\prime)}, \tag{3.23}$$

where $(x\prime, y\prime)$ denotes the location of the current point and J_x and J_y denotes the surface current densities in spatial domain. We consider each current element point to be a Hertzian dipole and use them to find the tangential electric fields using (2.32). For this, we calculate the Green's function with respect to stationary values of the wave numbers. Therefore, we represent the electric fields produced by dipoles, in spectral domain, by

$$\begin{bmatrix} \tilde{E}_x \\ \tilde{E}_y \end{bmatrix} = \begin{bmatrix} \tilde{G}_{xx} & \tilde{G}_{xy} \\ \tilde{G}_{yx} & \tilde{G}_{yy} \end{bmatrix} \begin{bmatrix} J_x \exp^{j(k_x x\prime + k_y y\prime)} \\ J_y \exp^{j(k_x x\prime + k_y y\prime)} \end{bmatrix}, \tag{3.24}$$

where

$$k_x = \cos\phi \sin\theta, \tag{3.25}$$

$$k_y = \sin\phi \sin\theta, \tag{3.26}$$

with ϕ and θ representing the spherical coordinates.

We obtain the far field radiation pattern on summation of the fields radiated by each radiator. We do it with the help of the method of stationary phase (MSP) described in

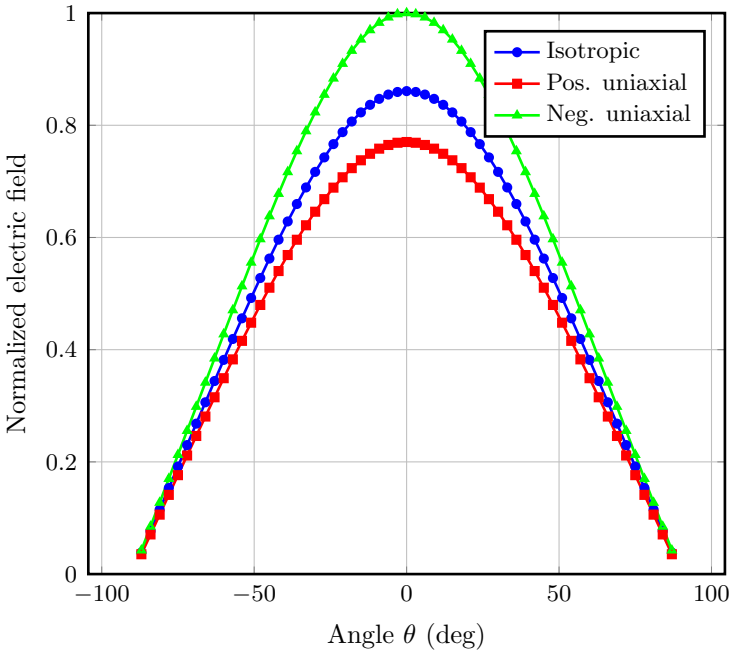

Figure 3.8: Radiation pattern (E-plane) for antenna electric anisotropic substrate.

[Collin and Zucker, 1969] which gives the relation between the spectral domain electric field components on the patch and the far-zone radiation field in spherical coordinates. We can express the relation as

$$E_\theta \simeq \tilde{E}_x \cos\phi + \tilde{E}_y \sin\phi, \tag{3.27}$$

$$E_\phi \simeq (\tilde{E}_y \cos\phi - \tilde{E}_x \sin\phi)\cos\theta. \tag{3.28}$$

Fig. 3.8 presents the variation of the radiation pattern, when we have considered isotropic, negative uniaxial electric anisotropic and positive uniaxial electric anisotropic substrates for $\phi = 0°$. The data used for the analysis are $\varepsilon_x = \varepsilon_z = 5$ (for isotropic), $\varepsilon_x = 5$, $\varepsilon_z = 3.6$ (negative uniaxial), $\varepsilon_x = 5$, $\varepsilon_z = 6.4$ (positive uniaxial) and $\mu_x = \mu_z = 1$. We have taken the antenna element with $P_a = 15$ mm, $P_b = 10$ mm, $d = 2$ mm, $S_a = 4P_a$ and $S_b = 4P_b$. The figure shows the influence of anisotropy present in the substrate on the radiation pattern. It follows the same pattern as previously presented for the resonant frequency in Fig. 3.6. It is in good agreement with the results published by Boufrioua [2011] which says that the radiated power increases with negative uniaxial electric anisotropy and decreases with positive one [Barkat et al., 2017].

3.2.1.3 Input Impedance

We have calculated the input impedance of the antenna by the method explained in [Heckler, 2010]. We feed the microstrip patch with the transmission line and use a δ-gap generator for the voltage to excite the transmission line [Davidovitz and Lo, 1989]. We present the geometry of the analyzed structure in Fig. 3.9. From the figure, it is clear that we consider the isolated segment of transmission line to be twice of the feeding line and feed it in the middle. In this way, the impedance of the stub becomes half of the input impedance of the whole transmission line. Therefore on subtracting the stub impedance from the

whole structure impedance, we get the actual input impedance of the antenna fed with the microstrip transmission line.

We have done the DMM computations on considering only half of the structure using H-wall symmetry as shown in Fig. 3.9. We have taken the electric anisotropic substrate with $\varepsilon_x = 2.33$, $\varepsilon_z = 4$, $\mu_x{=}\mu_z = 1$ and $d = 1.57$ mm. We have fed the patch antenna element with $P_a = 7.6$ mm and $P_b = 9.6$ mm with transmission line of length $l_f = 7.04$ mm and width $w = 1.52$ mm. We have placed the ABC walls along the substrate with $S_a = P_a{+}2{\times}9$ mm, $S_b = P_b{+}2{\times}9$ mm and have used 4 e-lines in x-direction and 8 e-lines in y-direction on patch while analyzing the structure. Fig. 3.10 gives the comparison between the results from DMM and ANSYS HFSS. We have observed good agreement between the predictions from both methodologies.

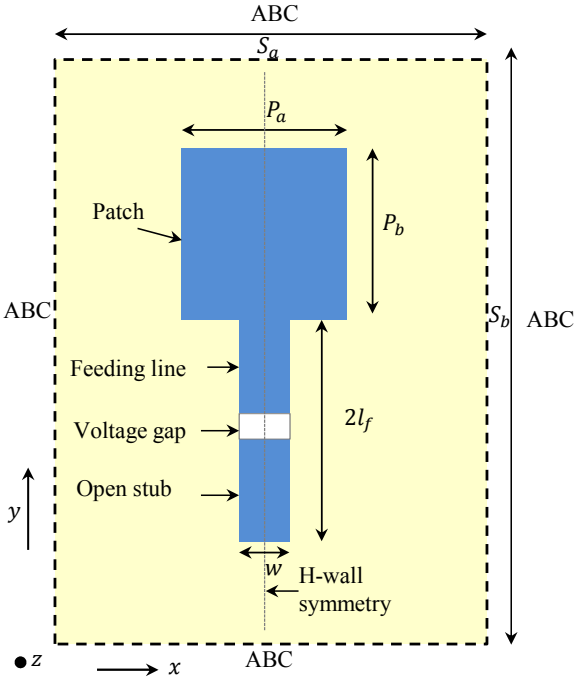

Figure 3.9: Geometry for the computation of input impedance.

3.2.2 Patch Antenna with Metamaterial Substrate

Metamaterials are built with periodic structures of unit cells which have average size smaller than the influenced wavelength. The dispersive properties of the substrate change due to the presence of metallic structures in the material [Weng et al., 2008]. Therefore, we have further applied the DMM method to analyze a patch antenna with 2×2 cells metal grid in the substrate. We place the metal grid, which consists of square lattices, in the middle of the two dielectric layers. The analyzed structure is in accordance with Fig. 3.11. We place the radiating element on the top layer and the ground plane below the bottom layer. We also provide the general idea of 2D discretization for the proposed structure in the figure. The location of the field and current components has a shift of half discretization distance, i.e., $\Delta x/2$ or $\Delta y/2$.

The structure consists of three dielectric layers with two metallized interfaces. After using the FWEC and simple network analysis techniques, we obtain the system equation

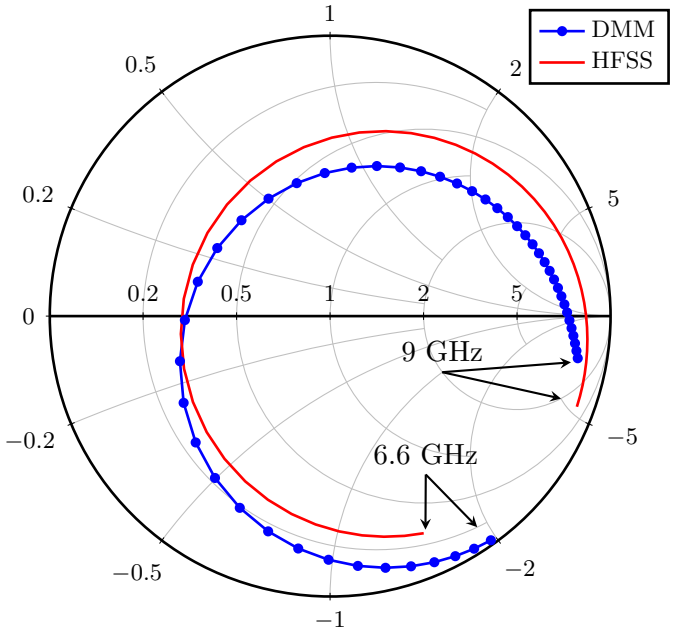

Figure 3.10: Input impedance of a microstrip patch antenna.

in the form

$$\begin{bmatrix} \widetilde{\boldsymbol{J}}_1 \\ \widetilde{\boldsymbol{J}}_2 \end{bmatrix} = \begin{bmatrix} \widetilde{\boldsymbol{L}}_{11} & \widetilde{\boldsymbol{L}}_{12} \\ \widetilde{\boldsymbol{L}}_{21} & \widetilde{\boldsymbol{L}}_{22} \end{bmatrix} \begin{bmatrix} \widetilde{\boldsymbol{E}}_1 \\ \widetilde{\boldsymbol{E}}_2 \end{bmatrix} \text{ or } \widetilde{\boldsymbol{J}} = \widetilde{\boldsymbol{L}}\widetilde{\boldsymbol{E}}. \tag{3.29}$$

We must then convert the obtained equation into the spatial domain as given in (3.12) using (3.13), since we know $\widetilde{\boldsymbol{L}} = \widetilde{\boldsymbol{G}}^{-1}$.

We have analyzed the proposed antenna with $P_a = P_b = 45$ mm, $a = 72$ mm, $b = 63$ mm, $S_a = S_b = 165$ mm, $d_1 = d_2 = 2$ mm, $\varepsilon_{r1} = 2.65$ and $\varepsilon_{r2} = 1$ for 1 to 6 GHz frequency band. The structure is open from the top. Table 3.3 compares the obtained results from DMM and ANSYS HFSS. For DMM, we have analyzed only one quarter of the structure with limited number of discretization lines to obtain the resonant frequency. We have used 4 e-lines in x-direction and 6 e-lines in y-direction on the patch for the analysis. From the table, it is clear that presence of metal-grid in the substrate changes the properties of antenna and makes it suitable for multi-band systems.

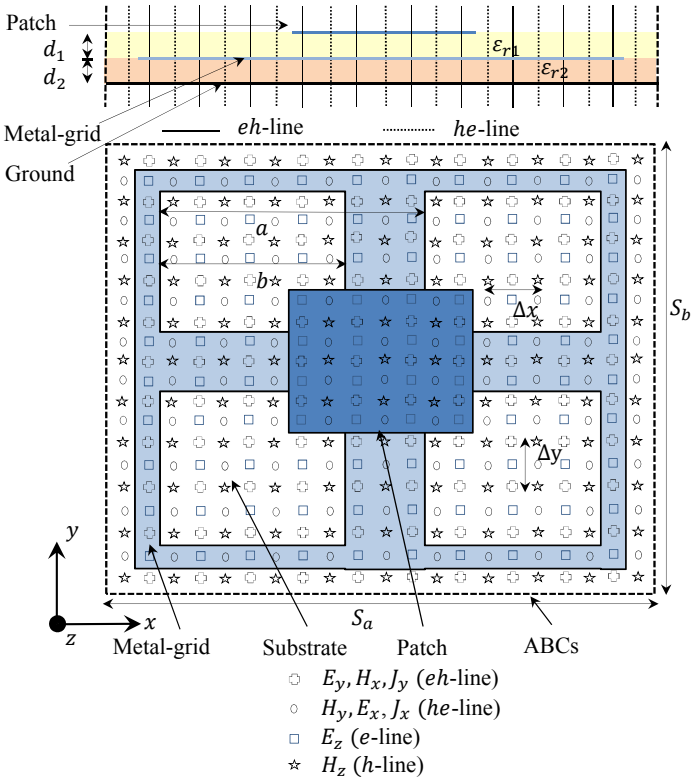

Figure 3.11: Side and top view of antenna with discretization.

Table 3.3: Resonant frequency.

Method	Resonant Frequency (GHz)	
	Conventional antenna	Antenna with metagrid
HFSS	2.45, 4.95, 5.40	2.03, 2.27, 2.60, 2.69, 3.09, 3.42, 3.98, 4.62, 5.23, 5.62
DMM	2.40, 5.52	2.22, 3.38, 3.93, 4.52, 5.21, 5.81

4 Analysis of Transmission Lines with Anisotropic Quasi-planar Dielectric Layers

Microstrip structures are very widely used in antennas and microwave devices for navigation and communication systems in transport, aeronautics and space. Often there is a need to integrate them into the surface of aircrafts, satellites and vehicles, which leads to the structures to be conformal [Yinusa, 2018]. New, lightweight materials (e.g., CFRP), exhibiting multilayers with anisotropic behavior, are used more widely. Since the substrate material strongly affects the properties of the structures, the microwave circuit elements need to be modeled very precisely and fast numerical procedures are required to predict their characteristics.

In the literature, we can find work done for analyzing waveguides with arbitrary cross-section using different methods. For example, Horikis [2013] used the finite difference technique, Yee and Audeh [1965] used the point matching technique, She [1989] used the iterated moment method and Yang and Pregla [1996] used the method of lines (MoL) to analyze conformal structures.

The conformal transmission lines with quasi-planar substrate were examined earlier using the discrete mode matching (DMM) method but with isotropic media [Dreher and Ioffe, 2000]. Ioffe et al. [2003] employed the method to 3D structures with non-planar layers. The present chapter extends this method to analyze quasi-planar transmission line structures with anisotropic materials. The shape of the interfaces can be defined by a suitable equation, from which the slope at each discretization point can be calculated. Consequently, the field components are determined for each sampling point in the interfaces with varying slope. Then the Green's function (or system equation) is derived using a full-wave equivalent circuit (FWEC) in the spatial domain.

Chapter 1 has already discussed the formation of hybrid-matrices for uniaxial anisotropic layers. In this chapter, we derive the hybrid-matrix elements for biaxial anisotropic dielectric layers. For a biaxial medium, there are two optical axes in different directions and two polarized propagating waves. Both waves are extraordinary waves and have orientation perpendicular to each other [Zhang and Li, 1998].

We demonstrate the application by computing propagation constants for a quasi-planar waveguide and a stripline having uniaxial or biaxial anisotropic dielectric layers and verify the results from DMM with those obtained with commercial software, ANSYS HFSS. This chapter is based on [Kamra and Dreher, 2018e, 2019d].

4.1 Formulation in the Spatial Domain

4.1.1 Field Relations

We depict the general cross-section of the microwave structure with arbitrarily shaped dielectric layers in Fig. 4.1. Here we consider several microstrip lines in the interfaces of the dielectric layers. For the present analysis, we take the stratification of the structure

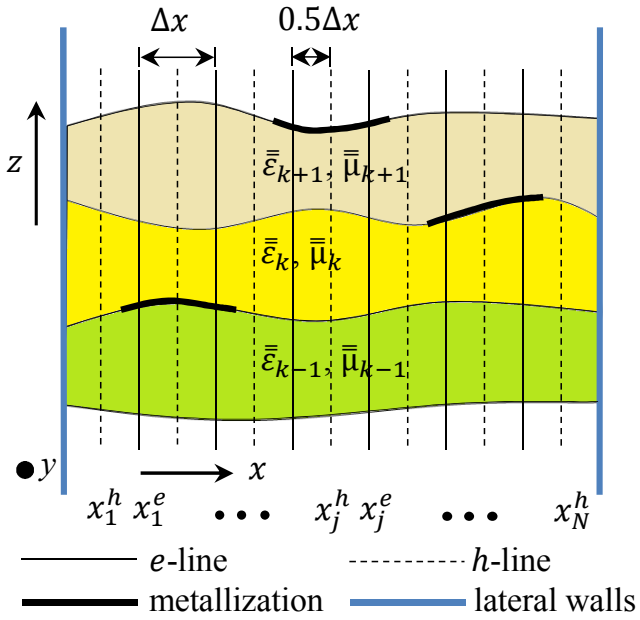

Figure 4.1: Quasi-planar multilayered microwave structure with anisotropic media.

in z-direction and the wave propagation ($\exp(-jk_y y)$) in y-direction. The permittivity ($\bar{\bar{\varepsilon}} = \varepsilon_0 \bar{\bar{\varepsilon}}_r$) and permeability ($\bar{\bar{\mu}} = \mu_0 \bar{\bar{\mu}}_r$) tensor of the biaxial anisotropic dielectric layer can be written with

$$\bar{\bar{\varepsilon}}_r = \begin{pmatrix} \varepsilon_x & 0 & 0 \\ 0 & \varepsilon_y & 0 \\ 0 & 0 & \varepsilon_z \end{pmatrix}, \tag{4.1}$$

$$\bar{\bar{\mu}}_r = \begin{pmatrix} \mu_x & 0 & 0 \\ 0 & \mu_y & 0 \\ 0 & 0 & \mu_z \end{pmatrix}. \tag{4.2}$$

It is mentioned by Krowne [1984] that we should begin our analysis by taking any two independent field components. Hence, we start our analysis with two scalar fields E_y and H_y. From the source-free Maxwell's equations normalized by the free-space wave number k_0, the relations between the field components can be written as

$$\left(\frac{\partial^2}{\partial y^2} + \varepsilon_x \mu_z\right) \begin{bmatrix} E_x \\ H_z \end{bmatrix} = \begin{bmatrix} \frac{\partial}{\partial x}\frac{\partial}{\partial y} & j\mu_z \frac{\partial}{\partial z} \\ j\varepsilon_x \frac{\partial}{\partial x} & \frac{\partial}{\partial y}\frac{\partial}{\partial z} \end{bmatrix} \begin{bmatrix} E_y \\ H_y \end{bmatrix}, \tag{4.3}$$

$$\left(\frac{\partial^2}{\partial y^2} + \varepsilon_z \mu_x\right) \begin{bmatrix} E_z \\ H_x \end{bmatrix} = \begin{bmatrix} \frac{\partial}{\partial y}\frac{\partial}{\partial z} & -j\mu_x \frac{\partial}{\partial x} \\ -j\varepsilon_z \frac{\partial}{\partial z} & \frac{\partial}{\partial x}\frac{\partial}{\partial y} \end{bmatrix} \begin{bmatrix} E_y \\ H_y \end{bmatrix}, \tag{4.4}$$

where $\eta_0 H_{x,y,z}$ is replaced by $H_{x,y,z}$ with $\eta_0 = \sqrt{\mu_0 \varepsilon_0}$. After applying the Fourier transform, we obtain two coupled second-order differential equations

$$\frac{d^2}{dz^2}\tilde{E}_y + a\tilde{E}_y + b\frac{d}{dz}\tilde{H}_y = 0 \tag{4.5}$$

$$\frac{d^2}{dz^2}\tilde{H}_y + c\tilde{H}_y + d\frac{d}{dz}\tilde{E}_y = 0 \tag{4.6}$$

where

$$a = q\varepsilon_y\mu_x - \frac{q\mu_x}{p\mu_z}k_x^2 \tag{4.7a}$$

$$b = jk_xk_y\left(\frac{q\mu_x}{p\varepsilon_x\mu_z} - \frac{1}{\varepsilon_z}\right) \tag{4.7b}$$

$$c = p\varepsilon_x\mu_y - \frac{p\varepsilon_x}{q\varepsilon_z}k_x^2 \tag{4.7c}$$

$$d = jk_xk_y\left(\frac{1}{\mu_z} - \frac{p\varepsilon_x}{q\varepsilon_z\mu_x}\right) \tag{4.7d}$$

$$p = 1 - \frac{k_y^2}{\varepsilon_x\mu_z} \tag{4.7e}$$

$$q = 1 - \frac{k_y^2}{\varepsilon_z\mu_x}. \tag{4.7f}$$

From (4.5) and (4.6), we can conclude that TE^y and TM^y modes cannot exist for the biaxial case. On elimination of the other coupled field component $\tilde{H}_y$ or $\tilde{E}_y$ from (4.5) or (4.6), respectively, we get a fourth-order differential equation

$$\left(\frac{d^4}{dz^4} + (a + c - bd)\frac{d^2}{dz^2} + ac\right)\tilde{\psi} = 0, \tag{4.8}$$

with $\tilde{\psi} = \tilde{E}_y$ or $\tilde{H}_y$. The four analytical solutions ($\pm k_{z(1,2)}$) can be computed from (4.8) with

$$k_{z(1,2)}^2 = -(\frac{a + c - bd}{2}) \pm \frac{1}{2}\sqrt{(a + c - bd)^2 - 4ac}, \tag{4.9}$$

where the field solution is with $d^2/dz^2 = k_z^2$. When we take $\tilde{\psi} = \tilde{H}_y$, then the solution can be written as

$$\tilde{H}_y = Ae^{k_{z1}z} + Be^{-k_{z1}z} + Ce^{k_{z2}z} + De^{-k_{z2}z}. \tag{4.10}$$

From (4.6), we can write

$$\tilde{E}_y = -\frac{1}{d}\int\left[\frac{d^2\tilde{H}_y}{dz^2} + c\tilde{H}_y\right]dz. \tag{4.11}$$

Therefore combining (4.10) and (4.11), we get

$$\tilde{E}_y = -\frac{PA}{k_{z1}d}e^{k_{z1}z} + \frac{PB}{k_{z1}d}e^{-k_{z1}z} - \frac{QC}{k_{z2}d}e^{k_{z2}z} + \frac{QD}{k_{z2}d}e^{-k_{z2}z}, \tag{4.12}$$

where $P = k_{z1}^2 + c$ and $Q = k_{z2}^2 + c$.

For the uniaxial case with optical axis in y-direction, the variables b and d become zero in (4.5) and (4.6), respectively. Therefore, we get two uncoupled differential equations which can be solved as explained in Chapter 2 and in [Kamra and Dreher, 2018d]. Similarly, the independent field components should be E_x, H_x and E_z, H_z for the optical axis in x- and z-directions, respectively. The isotropic case can be solved with either pair of the independent field components.

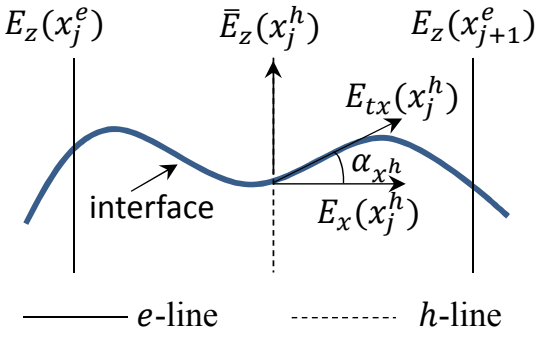

Figure 4.2: Field components at quasi-planar interface.

4.1.2 The Discrete Mode Matching Method

We assume the structure to be infinite in the propagation direction, so we need just 1D discretization along x for the analysis of a multilayered microstrip line as shown in Fig. 4.1. We sample the field components at N equidistant points x_j between the lateral walls. In the figure, e-lines show the position of the E_y and h-lines the position of the H_y field component. The modal expansion of field components having N modes discretized by N samples is given by

$$\psi_j(x_j, z) = \sum_{i=1}^{N} \tau_x(k_{xi}x_j)\tilde{\psi}_i(k_{xi}, z) \qquad \text{or} \qquad \boldsymbol{\psi} = \boldsymbol{T}\widetilde{\boldsymbol{\psi}}. \tag{4.13}$$

Here $\boldsymbol{T}$ is the transformation matrix (Fourier series elements) using the exact eigensolutions $\tau_x(k_{xi}x_j)$ (Table 2.1) of the Helmholtz equation which are dependent on the lateral boundary conditions and i denotes the index of the modes while j denotes the index of the samples.

We assume that for an arbitrary layer k the cross-section is constant in the y-direction. Therefore E_y and H_y are tangential to the interfaces along the whole x-direction. The quasi planar nature of the layers at the interfaces is in x-direction. Therefore the other tangential fields become E_{tx} and H_{tx}. Fig. 4.2 clarifies the tangential field component calculation and the components are represented as

$$E_{tx_k} = E_{x_k}\cos\alpha_{x^h} + \bar{E}_{z_k}\sin\alpha_{x^h}, \tag{4.14a}$$
$$H_{tx_k} = H_{x_k}\cos\alpha_{x^e} + \bar{H}_{z_k}\sin\alpha_{x^e}. \tag{4.14b}$$

Here $\alpha_{x^{(e,h)}} = \arctan(df(x)/dx)$ is the inclination angle at the interface with the x-axis at e- or h-line, with $f(x)$ representing the interface. From (4.3)-(4.4), we can say that for 1D discretization the E_z, E_y and H_x (or H_z, H_y and E_x) components are sampled at the same position. To determine E_{tx}, we must calculate E_x and E_z at the same location. Therefore, we use $\bar{E}_z$ in (4.14a) which is the mean of the adjacent sampled values of E_z. Similarly, we calculate $\bar{H}_z$ from the mean of the adjacent sampled values of H_z.

We can determine the hybrid matrix of the dielectric layer in a similar way as explained in Chapter 2, but for quasi planar structures, we should deal with the equations in spatial domain (4.3)-(4.4) rather than in spectral domain. Therefore, we obtain the discretized

field relations for layer k in matrix form as

$$\begin{bmatrix} \boldsymbol{E}_{tx_k} \\ \boldsymbol{H}_{tx_k} \\ \boldsymbol{E}_{y_k} \\ \boldsymbol{H}_{y_k} \end{bmatrix} = \begin{bmatrix} \boldsymbol{Q}^A_{tx_k} & \boldsymbol{Q}^B_{tx_k} & \boldsymbol{Q}^C_{tx_k} & \boldsymbol{Q}^D_{tx_k} \\ \boldsymbol{G}^A_{tx_k} & \boldsymbol{G}^B_{tx_k} & \boldsymbol{G}^C_{tx_k} & \boldsymbol{G}^D_{tx_k} \\ \boldsymbol{Q}^A_{y_k} & \boldsymbol{Q}^B_{y_k} & \boldsymbol{Q}^C_{y_k} & \boldsymbol{Q}^D_{y_k} \\ \boldsymbol{G}^A_{y_k} & \boldsymbol{G}^B_{y_k} & \boldsymbol{G}^C_{y_k} & \boldsymbol{G}^D_{y_k} \end{bmatrix} \begin{bmatrix} \boldsymbol{A}_k \\ \boldsymbol{B}_k \\ \boldsymbol{C}_k \\ \boldsymbol{D}_k \end{bmatrix}. \tag{4.15}$$

Now to obtain the relation between the tangential fields at the interfaces $k-1$ and k bounding the layer k, we write

$$\begin{bmatrix} \boldsymbol{E}_{k-1} \\ \boldsymbol{H}_{k-1} \end{bmatrix} = \boldsymbol{M}_{k-1}\boldsymbol{F}, \quad \begin{bmatrix} \boldsymbol{E}_{k} \\ \boldsymbol{H}_{k} \end{bmatrix} = \boldsymbol{M}_{k}\boldsymbol{F}, \tag{4.16}$$

$$\boldsymbol{M}_k = \begin{bmatrix} \boldsymbol{Q}^A_{tx_k} & \boldsymbol{Q}^B_{tx_k} & \boldsymbol{Q}^C_{tx_k} & \boldsymbol{Q}^D_{tx_k} \\ \boldsymbol{Q}^A_{y_k} & \boldsymbol{Q}^B_{y_k} & \boldsymbol{Q}^C_{y_k} & \boldsymbol{Q}^D_{y_k} \\ -\boldsymbol{G}^A_{y_k} & -\boldsymbol{G}^B_{y_k} & -\boldsymbol{G}^C_{y_k} & -\boldsymbol{G}^D_{y_k} \\ \boldsymbol{G}^A_{tx_k} & \boldsymbol{G}^B_{tx_k} & \boldsymbol{G}^C_{tx_k} & \boldsymbol{G}^D_{tx_k} \end{bmatrix}, \tag{4.17}$$

and take the notations of the fields and coefficients in the matrix form as

$$\boldsymbol{E}_k = \begin{bmatrix} \boldsymbol{E}_{tx_k} \\ \boldsymbol{E}_{y_k} \end{bmatrix}, \ \boldsymbol{H}_k = \begin{bmatrix} -\boldsymbol{H}_{y_k} \\ \boldsymbol{H}_{tx_k} \end{bmatrix}, \ \boldsymbol{F} = \begin{bmatrix} \boldsymbol{A}_k \\ \boldsymbol{B}_k \\ \boldsymbol{C}_k \\ \boldsymbol{D}_k \end{bmatrix}. \tag{4.18}$$

The full expressions of the terms in (4.17) are given in Appendix B. After eliminating the unknown coefficient column matrix $\boldsymbol{F}$, this results in

$$\begin{bmatrix} \boldsymbol{E}_{k-1} \\ \boldsymbol{H}_{k-1} \end{bmatrix} = \boldsymbol{K}_k \begin{bmatrix} \boldsymbol{E}_{k} \\ \boldsymbol{H}_{k} \end{bmatrix}. \tag{4.19}$$

The hybrid matrix ($\boldsymbol{K}_k$) for layer k can be represented as

$$\boldsymbol{K}_k = \boldsymbol{M}_{k-1}\boldsymbol{M}_k^{-1} = \begin{bmatrix} \boldsymbol{V}_k & \boldsymbol{Z}_k \\ \boldsymbol{Y}_k & \boldsymbol{B}_k \end{bmatrix}. \tag{4.20}$$

As shown in Fig. 4.3, the matrix $\boldsymbol{K}_k$ relates the tangential fields at the top and bottom of the interfaces of the layer k in the spatial domain. The system equation can be formed by using this FWEC, network analysis techniques and the continuity equations on the interfaces to match the fields. Then the boundary conditions which state that the tangential electric

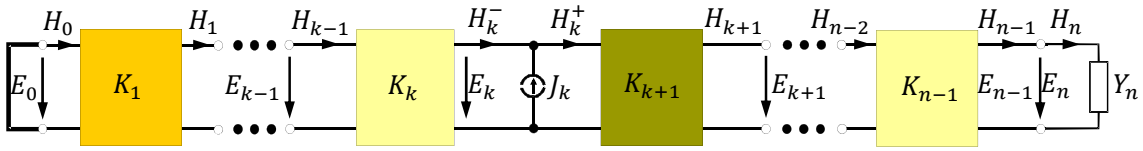

Figure 4.3: Full-wave equivalent circuit of a general planar microwave structure in spatial domain.

field components must vanish on the metallizations and the electric currents outside that region must be applied. We obtain the reduced system equation as

$$\boldsymbol{G}_{\text{red}}\boldsymbol{J}_{\text{red}} = 0 \qquad \text{or} \qquad \boldsymbol{L}_{\text{red}}\boldsymbol{E}_{\text{red}} = 0, \tag{4.21}$$

which can be solved as an indirect eigenvalue problem ($\det(\boldsymbol{G}_{\text{red}}) = 0$ or $\det(\boldsymbol{L}_{\text{red}}) = 0$) to find the propagation constants for the transmission lines. Here $\boldsymbol{G} = \boldsymbol{L}^{-1}$ denotes the Green's function and $\boldsymbol{L}_{\text{red}}$ is equivalent to $\boldsymbol{L}$ in waveguides without metallizations, as there are no currents on the interfaces.

4.2 Numerical Results

4.2.1 Waveguides

First, we have applied the DMM formulation to analyze a partially filled waveguide whose inner layer is taken to be in triangular shape. The schematic is shown in the inset of Fig. 4.4. The data used for the analysis are $b = 6.35$ mm, $a = 2b$, $d = 0.5b$, $\bar{\bar{\varepsilon}}_{r1} = 9.4$ or (9.4, 9.4, 11.6) or (9.4, 13, 11.6) and $\varepsilon_{r2} = 1$. Fig. 4.5 gives the FWEC obtained from the structure where $\boldsymbol{K}_1$ and $\boldsymbol{K}_2$ represent the hybrid matrices for the layer 1 and 2, respectively. From the circuit, we can deduce the system equation as

$$(\boldsymbol{Z}_1^{-1}\boldsymbol{V}_1 + \boldsymbol{B}_2\boldsymbol{Z}_2^{-1})\boldsymbol{E}_1 = \boldsymbol{0} \qquad \text{or} \qquad \boldsymbol{L}\boldsymbol{E}_1 = \boldsymbol{0}, \tag{4.22}$$

where $\boldsymbol{E}_1$ represents the tangential electric fields at the interface between the two dielectric layers.

Fig. 4.4 shows the dispersion curves, normalized by k_0, obtained after solving the eigenvalue problem. For the present computation, we have analyzed only half of the structure due to symmetry and have used 17 e-lines to discretize it. The results agree well with the results obtained from ANSYS HFSS. Then, Fig. 4.6 demonstrates six higher order modes computed for the biaxial case of the waveguide shown in the inset of Fig. 4.4. The figure validates the DMM results with the commercial software.

Then, we have changed the inner interface within the waveguide with the function

$$f(x) = 0.05b(1 + \exp(-u^2(x/a - 0.5)^2)), \tag{4.23}$$

and have analyzed the structure with the following parameters: $b = 7.5$ mm, $a = 2b$, $\bar{\bar{\varepsilon}}_{r1} = 8.875$ or (8.875, 8.875, 15) or (8.875, 10, 15) and $\varepsilon_{r2} = 1$. The shape of the interface varies with the different model parameters u as shown in Fig. 4.7. Fig. 4.8 gives the computed values of the normalized propagation constant with varying u. We have used 22 e-lines for discretizing half of the structure. The figure compares the DMM results for the isotropic, uniaxial and biaxial anisotropic medium with the results from the HFSS. We have computed the results at 30 GHz frequency.

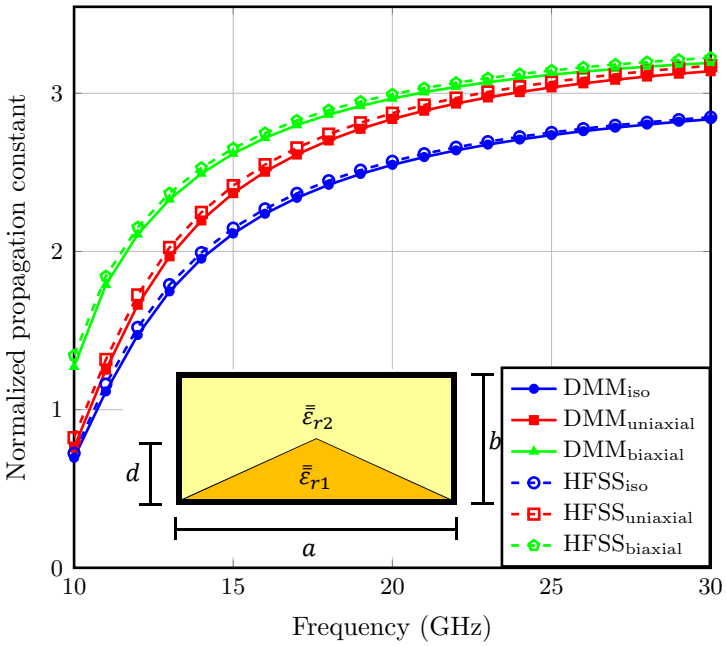

Figure 4.4: Dispersion curve for the partially filled waveguide with triangular dielectric layer.

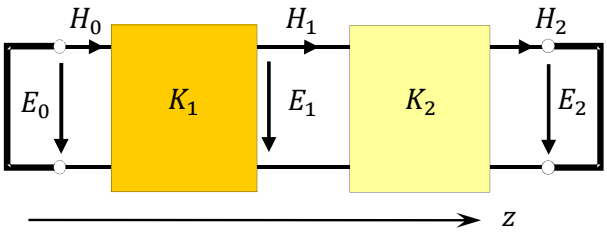

Figure 4.5: Full-wave equivalent circuit for the quasi-planar waveguide.

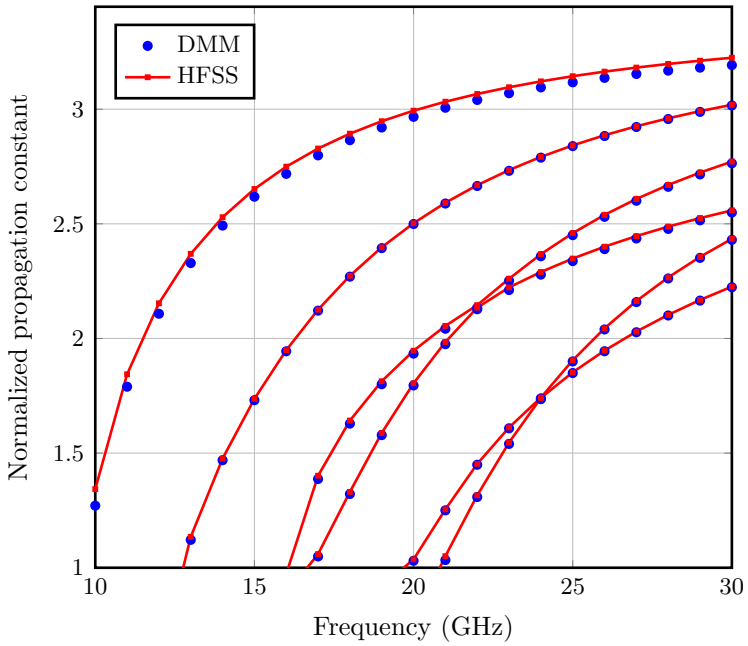

Figure 4.6: Dispersion curve for the higher order modes.

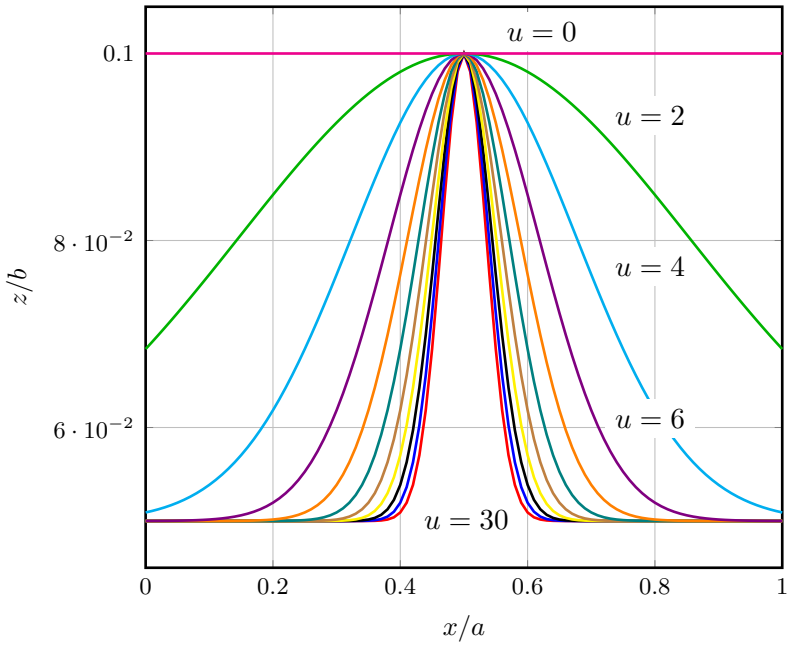

Figure 4.7: Variation of the interface present within partially filled waveguide for different model parameters u.

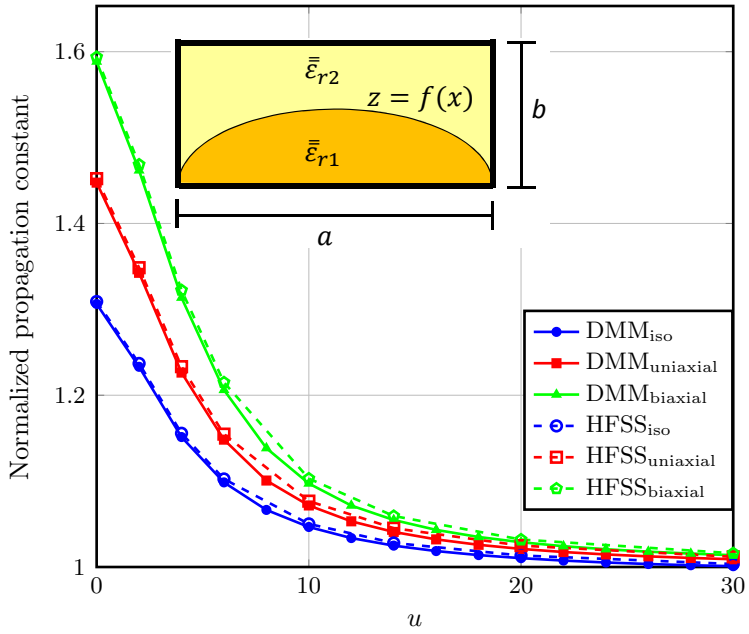

Figure 4.8: Normalized propagation constant as a function of the model parameter u of the interface present in the quasi-planar waveguide shown in inset.

4.2.2 Microstrip Line

Next, we have analyzed a microstrip line where the strip is placed on the inner interface of the structure shown in Fig. 4.8. The inner layers of the structure are taken with relative permittivity $\bar{\bar{\varepsilon}}_{r1} = 8.875$ or (8.875, 8.875, 10) or (8.875, 9, 11) and $\varepsilon_{r2} = 1$. The cross section of the structure is with $b = 7.5$ mm, $a = 2b$, and has a strip width $w = 0.25a$. Fig. 4.9 clearly shows the variation of the strip with the interface. We obtain the FWEC of the quasi-planar stripline as depicted in Fig. 4.10. The system equation for the two-layer microstrip line takes the form

$$(\boldsymbol{Z}_1^{-1}\boldsymbol{V}_1 + \boldsymbol{B}_2\boldsymbol{Z}_2^{-1})\boldsymbol{E}_1 = \boldsymbol{J}_1 \qquad \text{or} \qquad \boldsymbol{L}\boldsymbol{E}_1 = \boldsymbol{J}_1, \tag{4.24}$$

where $\boldsymbol{J}_1$ gives the currents on the strip.

Fig. 4.11 shows the computed results at 30 GHz frequency with DMM and HFSS. For the DMM computation, we have used 12 e-lines on half of the strip for the isotropic and uniaxial case and 6 e-lines for the biaxial case. In HFSS, the consumed time span for the analysis at each u-point varied between 26 seconds to 1 hour, while with the DMM formulation it was between 10 to 12 seconds. We have used the same number of segments for all values of u in HFSS and also the same number of discretization lines in DMM to clearly interpret the curvy interface. However, HFSS needs more mesh elements and computation time to smoothly analyze the interface with higher value of u, while for DMM, the computation time does not vary much for different values of u. With the same number of discretization lines, it depends only on how much time is needed to calculate the roots of the eigenvalue problem.

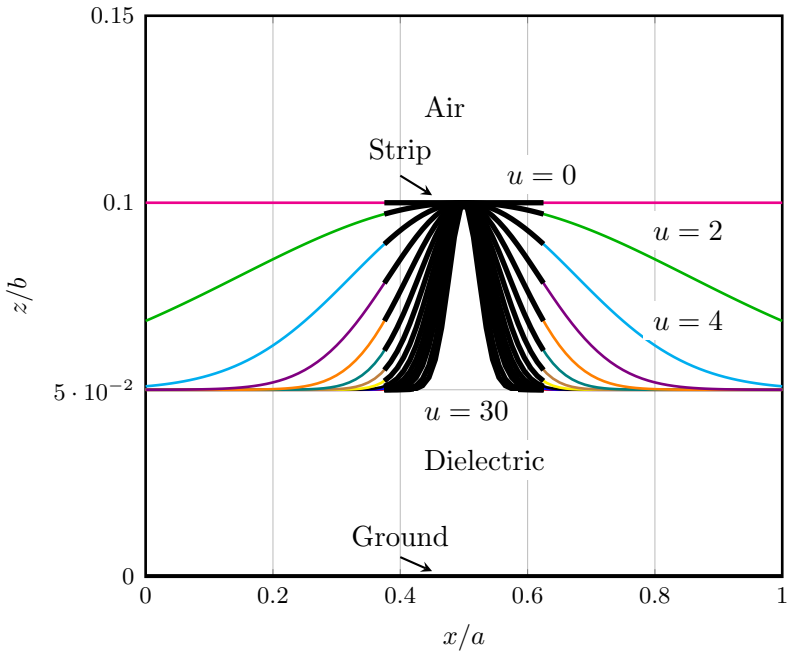

Figure 4.9: Quasi-planar stripline structure.

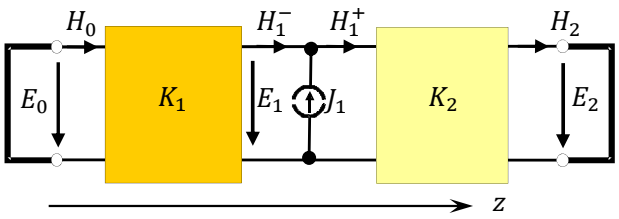

Figure 4.10: Full-wave equivalent circuit for the quasi-planar stripline.

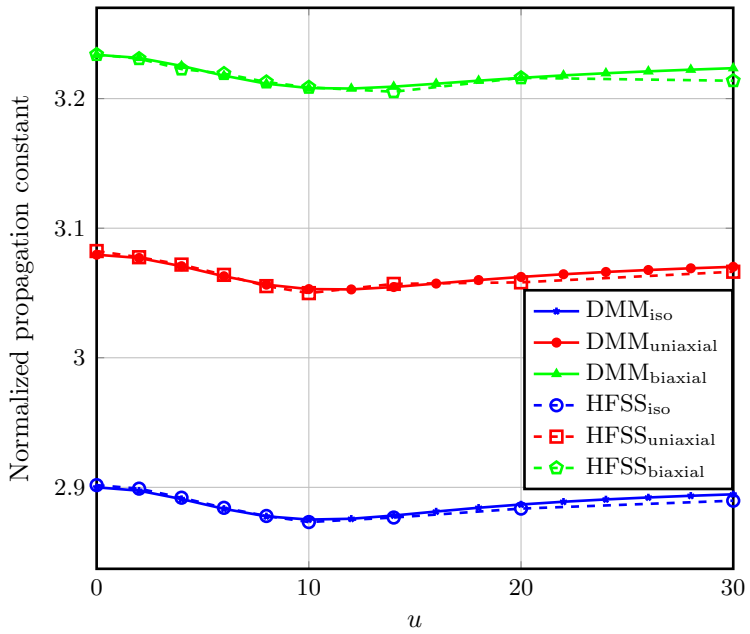

Figure 4.11: Normalized propagation constant as a function of the model parameter u of the interface present in the quasi-planar stripline shown in Fig. 4.9.

5 Analysis of Cylindrical and Quasi-cylindrical Structures with Uniaxial Anisotropy

In the former chapters, we have discussed the analysis of planar structures and quasi-planar structures with Cartesian coordinate system. Our next goal is to deal with a cylindrical coordinate system which helps us to easily deal with conformal structures.

In the field of navigation and communication systems, we need to integrate transmission lines on circular, elliptical or any quasi-circular surfaces of aircrafts, satellites and vehicles, or to feed conformal antennas [Yinusa, 2018; Naser-Moghaddasi et al., 2010], which leads to the development of conformal transmission line structures. Over the past few decades, anisotropic materials have widely been used in the field of microwave and optical engineering due to the technological advancements, which is also evident from the fact that several authors have stressed the use of anisotropy in the material [Tonning, 1982; Lindell and Oksanen, 1984; Oksanen and Lindell, 1989] for conformal structures. Hence, it is important to exactly characterize the anisotropic material profile and to develop efficient techniques to model the conformal microwave circuit elements precisely.

In this chapter, the focus is on analyzing cylindrical or quasi-cylindrical structures with numerous anisotropic thin layers as shown in Fig. 5.1, where $\widetilde{\boldsymbol{F}}$ denotes the field components at the interfaces. Different approaches to analyze conformal structures have been discussed in the open literature [Oksanen and Lindell, 1989; Medina and Horno, 1990; Shibayama et al., 2000; Pregla and Conradi, 2003; Kusiek et al., 2015]. Here, we make use of the full-wave equivalent circuit (FWEC) to model the conformal multilayered structure with electrically or magnetically, or both, uniaxial anisotropic material, where each dielectric layer is represented by a hybrid block (or $\boldsymbol{K}$-matrix). This matrix relates all the tangential field components at the interfaces of the layer (Fig. 5.2). We describe the general derivation of the hybrid-matrix elements for anisotropic dielectric layers in a cylindrical coordinate system, which gives the flexibility to analyze different conformal interfaces not just circular or elliptical.

To deal with cylindrical interfaces, it is sufficient to begin the analysis in spectral domain as explained for planar structures in Chapter 2. For quasi-cylindrical interfaces, we should however adopt spatial domain analysis to calculate the field components on the exact shape of the interfaces. Therefore, in the following sections the method is explained in both spectral and spatial domain for the analysis of cylindrical and non-cylindrical structures, respectively.

First we demonstrate the application of this extended equivalent circuit by analyzing graded-index fibers and finding their propagation constants with different profiles. Here, we model the graded-index core by a stratified structure which consists of several layers with varying indices of refraction like staircases following the base profile. Then we discuss the application of the DMM method to elliptical transmission lines with 1D discretization. Lastly, we demonstrate the application for 2D discretization by analyzing a microstrip patch over the most common quasi-circular cylinder, i.e., elliptical cylinder. We validate the numerical results obtained from DMM by comparing them with the ones obtained with

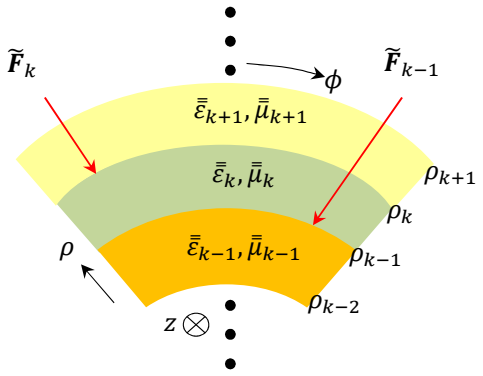

Figure 5.1: Schematic view of the anisotropic stratified dielectric for cylindrical structures.

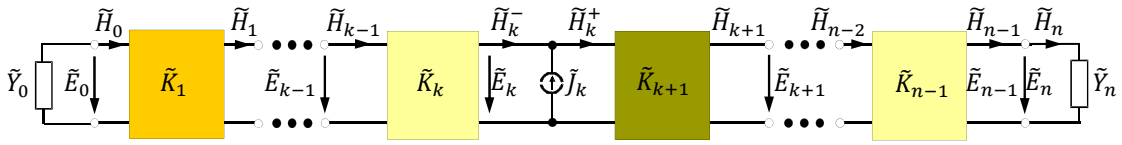

Figure 5.2: Full-wave equivalent circuit of a general microwave structure with stratified dielectric. The structure is considered to be open from bottom and top both.

commercial software, i.e., ANSYS HFSS and/or CST Microwave Studio. This chapter is based on [Kamra and Dreher, 2019b,c].

5.1 Formulation for the Transmission Line Structures

5.1.1 Field Relation

To characterize the anisotropic medium, the analysis starts from the permittivity ($\bar{\bar{\varepsilon}} = \varepsilon_0 \bar{\bar{\varepsilon}}_r$) and permeability ($\bar{\bar{\mu}} = \mu_0 \bar{\bar{\mu}}_r$) tensor with optical axis in z-direction, where

$$\bar{\bar{\varepsilon}}_r = \begin{pmatrix} \varepsilon_t & 0 & 0 \\ 0 & \varepsilon_t & 0 \\ 0 & 0 & \varepsilon_z \end{pmatrix}, \quad \bar{\bar{\mu}}_r = \begin{pmatrix} \mu_t & 0 & 0 \\ 0 & \mu_t & 0 \\ 0 & 0 & \mu_z \end{pmatrix}. \tag{5.1}$$

We write the Maxwell's equations in cylindrical coordinates and for a source-free and homogeneous medium in their differential form by

$$\nabla \times \vec{E}(\rho, \phi, z) = -j\omega\mu_0 \bar{\bar{\mu}}_r \cdot \vec{H}(\rho, \phi, z), \tag{5.2a}$$

$$\nabla \times \vec{H}(\rho, \phi, z) = j\omega\varepsilon_0 \bar{\bar{\varepsilon}}_r \cdot \vec{E}(\rho, \phi, z), \tag{5.2b}$$

where $\vec{E}$ and $\vec{H}$ are electric and magnetic field vectors, ω is the angular frequency, μ_0 the free-space permeability and ε_0 the free-space permittivity. In cylindrical coordinates, we write

$$\vec{E}(\rho, \phi, z) = E_\rho(\rho, \phi, z)\hat{\rho} + E_\phi(\rho, \phi, z)\hat{\phi} + E_z(\rho, \phi, z)\hat{z}, \tag{5.3}$$

with $\hat{\rho}$, $\hat{\phi}$ and $\hat{z}$ denoting the unit vectors along ρ, ϕ and z coordinates, respectively. To simplify the analysis, space variables are normalized by the free-space wave number k_0, and

$\eta_0\vec{H}$ is replaced by $\vec{H}$, where $\eta_0 = \sqrt{\mu_0/\varepsilon_0}$, is the intrinsic impedance of the free space. So in the extended form, Faraday's law (5.2a) gives the field relations as

$$\frac{1}{\rho}\frac{\partial}{\partial\phi}E_z - \frac{\partial}{\partial z}E_\phi = -j\mu_t H_\rho, \tag{5.4a}$$

$$\frac{\partial}{\partial z}E_\rho - \frac{\partial}{\partial\rho}E_z = -j\mu_t H_\phi, \tag{5.4b}$$

$$\frac{1}{\rho}\frac{\partial}{\partial\rho}(\rho E_\phi) - \frac{1}{\rho}\frac{\partial}{\partial\phi}E_\rho = -j\mu_z H_z. \tag{5.4c}$$

Next on taking Ampere's law (5.2b), the expressions are

$$\frac{1}{\rho}\frac{\partial}{\partial\phi}H_z - \frac{\partial}{\partial z}H_\phi = j\varepsilon_t E_\rho, \tag{5.5a}$$

$$\frac{\partial}{\partial z}H_\rho - \frac{\partial}{\partial\rho}H_z = j\varepsilon_t E_\phi, \tag{5.5b}$$

$$\frac{1}{\rho}\frac{\partial}{\partial\rho}(\rho H_\phi) - \frac{1}{\rho}\frac{\partial}{\partial\phi}H_\rho = j\varepsilon_z E_z. \tag{5.5c}$$

As the optical axis is in z-direction, we can assume E_z and H_z as two independent field components. Therefore on rearranging (5.4)-(5.5), the other field components can be calculated using the relation

$$\left(\frac{\partial^2}{\partial z^2} + \varepsilon_t\mu_t\right)\begin{bmatrix} E_\rho \\ H_\rho \\ E_\phi \\ H_\phi \end{bmatrix} = \begin{bmatrix} \frac{\partial}{\partial\rho}\frac{\partial}{\partial z} & -\frac{j\mu_t}{\rho}\frac{\partial}{\partial\phi} \\ \frac{j\varepsilon_t}{\rho}\frac{\partial}{\partial\phi} & \frac{\partial}{\partial\rho}\frac{\partial}{\partial z} \\ \frac{1}{\rho}\frac{\partial}{\partial\phi}\frac{\partial}{\partial z} & j\mu_t\frac{\partial}{\partial\rho} \\ -j\varepsilon_t\frac{\partial}{\partial\rho} & \frac{1}{\rho}\frac{\partial}{\partial\phi}\frac{\partial}{\partial z} \end{bmatrix}\begin{bmatrix} E_z \\ H_z \end{bmatrix}. \tag{5.6}$$

5.1.2 Interface Condition

Consider a dielectric where the layers are stratified in ρ-direction as shown in Fig. 5.1, in which the arbitrary layer k is bounded by the interfaces $k-1$ and k. The pertinent source-free differential equation can be written as

$$\nabla^2\psi - \nabla(\nabla\cdot\psi) + \bar{\bar{\mu}}_r\cdot\bar{\bar{\varepsilon}}_r\cdot\psi = 0, \tag{5.7a}$$

or

$$\nabla^2\psi + K^2\psi = 0. \tag{5.7b}$$

In cylindrical coordinates we obtain

$$\left(\rho\frac{\partial}{\partial\rho}\left(\rho\frac{\partial}{\partial\rho}\right) + \frac{\partial^2}{\partial\phi^2} + \rho^2\left(\frac{\partial^2}{\partial z^2} + K^2\right)\right)\psi(\rho,\phi,z) = 0, \tag{5.8}$$

where ψ represents each of the independent electromagnetic field components, i.e., E_z and H_z and K represents propagation constant of the medium. We assume the propagation in z-direction and the cross-section does not vary in this direction. Therefore, we write

$$\psi(\rho,\phi,z) = \psi(\rho,\phi)e^{-jk_z z}. \tag{5.9}$$

After introducing (5.9) in (5.8) and taking the derivative with respect to z, we get

$$\left(\rho\frac{\partial}{\partial\rho}\left(\rho\frac{\partial}{\partial\rho}\right)+\frac{\partial^2}{\partial\phi^2}+(k_\rho\rho)^2\right)\psi(\rho,\phi)=0. \tag{5.10}$$

Using Fourier transformation, we can write the differential equation (5.10) with derivatives with respect to one coordinate only. Therefore, transforming (5.10) into spectral domain using modal expansion of the field components as in [Thiel and Dreher, 2002], leads to the classic Bessel differential equation

$$\left(\rho\frac{\partial}{\partial\rho}\left(\rho\frac{\partial}{\partial\rho}\right)-{\nu_i}^2+(k_\rho\rho)^2\right)\tilde{\psi}(\rho,\nu_i)=0, \tag{5.11}$$

with $k_\rho^2=(K^2-k_z^2)$ and ν_i denotes the spectral variable in ϕ-direction for mode i. Here, in the anisotropic case the propagation constant K has two roots [Li et al., 2001], which have to be taken into consideration. One represents TE waves (ordinary waves) and the other represents TM waves (extraordinary waves). Therefore the dispersion relation for E_z or TM mode is obtained as

$$k_{\rho e}=\sqrt{\frac{\varepsilon_z}{\varepsilon_t}(\mu_t\varepsilon_t-k_z^2)}, \tag{5.12}$$

and for H_z or TE mode as

$$k_{\rho h}=\sqrt{\frac{\mu_z}{\mu_t}(\mu_t\varepsilon_t-k_z^2)}. \tag{5.13}$$

5.1.2.1 Spectral Domain

As $\widetilde{\boldsymbol{\psi}}$ represents column matrices of two independent field components (with all the modal values), i.e., $\widetilde{\boldsymbol{E}}_z, \widetilde{\boldsymbol{H}}_z$, the solution of (5.11) within an arbitrary layer k can be written in the form

$$\widetilde{\boldsymbol{E}}_{z_k}=\boldsymbol{A}_k\mathbf{J}_{\boldsymbol{\nu}}(k_{\rho e_k}\rho)+\boldsymbol{B}_k\mathbf{Y}_{\boldsymbol{\nu}}(k_{\rho e_k}\rho), \tag{5.14a}$$

$$\widetilde{\boldsymbol{H}}_{z_k}=\boldsymbol{C}_k\mathbf{J}_{\boldsymbol{\nu}}(k_{\rho h_k}\rho)+\boldsymbol{D}_k\mathbf{Y}_{\boldsymbol{\nu}}(k_{\rho h_k}\rho), \tag{5.14b}$$

or

$$\tilde{E}_{z_k}(\rho,\nu_i)=A_{k_i}\mathrm{J}_{\nu_i}(k_{\rho e_k}\rho)+B_{k_i}\mathrm{Y}_{\nu_i}(k_{\rho e_k}\rho), \tag{5.15a}$$

$$\tilde{H}_{z_k}(\rho,\nu_i)=C_{k_i}\mathrm{J}_{\nu_i}(k_{\rho h_k}\rho)+D_{k_i}\mathrm{Y}_{\nu_i}(k_{\rho h_k}\rho). \tag{5.15b}$$

Here $\mathbf{J}_{\boldsymbol{\nu}}$ and $\mathbf{Y}_{\boldsymbol{\nu}}$ denote the matrices of Bessel functions of first and second kind, i.e., J_ν and Y_ν respectively, after modal expansion. Now, take the field relations and their derivatives at the interfaces k and $k-1$. Then, on eliminating the unknowns $\boldsymbol{A}_k$, $\boldsymbol{B}_k$, $\boldsymbol{C}_k$ and $\boldsymbol{D}_k$, the relation for the field components at the interfaces of the layer k with normalized thickness d_k can be written as

$$\frac{\partial}{\partial\rho}\begin{bmatrix}\widetilde{\boldsymbol{\psi}}_{k-1}\\ \widetilde{\boldsymbol{\psi}}_k\end{bmatrix}=\hat{\boldsymbol{p}}_{\boldsymbol{\nu}_k}\begin{bmatrix}\bar{\boldsymbol{r}}_{\boldsymbol{\nu}_k} & \frac{2}{\pi}\boldsymbol{I}\\ -\frac{2}{\pi}\boldsymbol{I} & \bar{\boldsymbol{q}}_{\boldsymbol{\nu}_k}\end{bmatrix}\begin{bmatrix}\widetilde{\boldsymbol{\psi}}_{k-1}\\ \widetilde{\boldsymbol{\psi}}_k\end{bmatrix}. \tag{5.16}$$

On transforming (5.6) using Fourier transformation, we get the other field components in spectral domain in matrix form as

$$\widetilde{\boldsymbol{E}}_\rho = -\frac{jk_z}{\varepsilon_{dt}}\frac{\partial}{\partial\rho}\widetilde{\boldsymbol{E}}_z - \frac{j\mu_t\boldsymbol{\nu}}{\rho\varepsilon_{dt}}\widetilde{\boldsymbol{H}}_z, \tag{5.17a}$$

$$\widetilde{\boldsymbol{H}}_\rho = \frac{j\varepsilon_t\boldsymbol{\nu}}{\rho\varepsilon_{dt}}\widetilde{\boldsymbol{E}}_z - \frac{jk_z}{\varepsilon_{dt}}\frac{\partial}{\partial\rho}\widetilde{\boldsymbol{H}}_z, \tag{5.17b}$$

$$\widetilde{\boldsymbol{E}}_\phi = -\frac{k_z\boldsymbol{\nu}}{\rho\varepsilon_{dt}}\widetilde{\boldsymbol{E}}_z + \frac{j\mu_t}{\varepsilon_{dt}}\frac{\partial}{\partial\rho}\widetilde{\boldsymbol{H}}_z, \tag{5.17c}$$

$$\widetilde{\boldsymbol{H}}_\phi = -\frac{j\varepsilon_t}{\varepsilon_{dt}}\frac{\partial}{\partial\rho}\widetilde{\boldsymbol{E}}_z - \frac{k_z\boldsymbol{\nu}}{\rho\varepsilon_{dt}}\widetilde{\boldsymbol{H}}_z, \tag{5.17d}$$

where $\varepsilon_{dt} = \varepsilon_t\mu_t - k_z^2$.

Using (5.14) - (5.17), we can find the relation between the fields which are tangential to the interfaces $k-1$ (bottom) and k (top) of the dielectric layer k as

$$\begin{bmatrix}\widetilde{\boldsymbol{E}}_{k-1}\\ \widetilde{\boldsymbol{H}}_{k-1}\end{bmatrix} = \widetilde{\boldsymbol{K}}_k \begin{bmatrix}\widetilde{\boldsymbol{E}}_k\\ \widetilde{\boldsymbol{H}}_k\end{bmatrix}, \tag{5.18}$$

with the hybrid matrix

$$\widetilde{\boldsymbol{K}}_k = \begin{bmatrix}\widetilde{\boldsymbol{V}}_k & \widetilde{\boldsymbol{Z}}_k\\ \widetilde{\boldsymbol{Y}}_k & \widetilde{\boldsymbol{B}}_k\end{bmatrix} \tag{5.19}$$

and

$$\widetilde{\boldsymbol{E}}_k = j\begin{bmatrix}\rho_k\widetilde{\boldsymbol{E}}_{\phi k}\\ \widetilde{\boldsymbol{E}}_{zk}\end{bmatrix},\ \widetilde{\boldsymbol{H}}_k = -\begin{bmatrix}-\widetilde{\boldsymbol{H}}_{zk}\\ \rho_k\widetilde{\boldsymbol{H}}_{\phi k}\end{bmatrix}. \tag{5.20}$$

The components of the $\widetilde{\boldsymbol{K}}$-matrix are given as

$$\widetilde{\boldsymbol{V}}_k = \frac{\pi}{2}\begin{bmatrix}-\bar{\boldsymbol{r}}_{\boldsymbol{\nu}h} & -k_z\boldsymbol{\nu}\varepsilon_{dt}^{-1}(\bar{\boldsymbol{r}}_{\boldsymbol{\nu}h} + \bar{\boldsymbol{q}}_{\boldsymbol{\nu}e})\\ 0 & \bar{\boldsymbol{q}}_{\boldsymbol{\nu}e}\end{bmatrix}_k, \tag{5.21a}$$

$$\widetilde{\boldsymbol{Z}}_k = \frac{\pi}{2\varepsilon_t}\begin{bmatrix}-\varepsilon_{dt}^{-1}(k_z^2\boldsymbol{\nu}^2\boldsymbol{p}_{\boldsymbol{\nu}e} + \mu_t\varepsilon_t\bar{\boldsymbol{s}}_{\boldsymbol{\nu}h}) & k_z\boldsymbol{\nu}\boldsymbol{p}_{\boldsymbol{\nu}e}\\ k_z\boldsymbol{\nu}\boldsymbol{p}_{\boldsymbol{\nu}e} & -\boldsymbol{p}_{\boldsymbol{\nu}e}\varepsilon_{dt}\end{bmatrix}_k, \tag{5.21b}$$

$$\widetilde{\boldsymbol{Y}}_k = \frac{\pi}{2\mu_t}\begin{bmatrix}\boldsymbol{p}_{\boldsymbol{\nu}h}\varepsilon_{dt} & k_z\boldsymbol{\nu}\boldsymbol{p}_{\boldsymbol{\nu}h}\\ k_z\boldsymbol{\nu}\boldsymbol{p}_{\boldsymbol{\nu}h} & \varepsilon_{dt}^{-1}(\varepsilon_t\mu_t\bar{\boldsymbol{s}}_{\boldsymbol{\nu}e} + k_z^2\boldsymbol{\nu}^2\boldsymbol{p}_{\boldsymbol{\nu}h})\end{bmatrix}_k, \tag{5.21c}$$

$$\widetilde{\boldsymbol{B}}_k = \frac{\pi}{2}\begin{bmatrix}\bar{\boldsymbol{q}}_{\boldsymbol{\nu}h} & 0\\ k_z\boldsymbol{\nu}\varepsilon_{dt}^{-1}(\bar{\boldsymbol{q}}_{\boldsymbol{\nu}h} + \bar{\boldsymbol{r}}_{\boldsymbol{\nu}e}) & -\bar{\boldsymbol{r}}_{\boldsymbol{\nu}e}\end{bmatrix}_k, \tag{5.21d}$$

where the subscript e is for a TM mode while h is for a TE mode. The explanation of other terms are presented in the Appendix C.

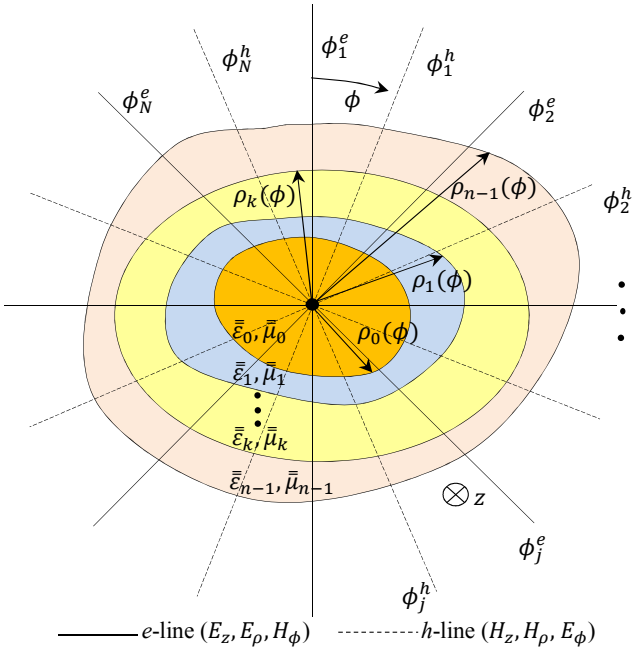

Figure 5.3: Discretization scheme for the non-circular transmission lines.

5.1.2.2 Spatial Domain with 1D Discretization

When the layers are not in perfect circular shape, then there is a need to apply the method in spatial domain to determine the field components at the interfaces with varying slope. It is assumed that the cross-section is constant in the z-direction, so there is a need of only 1D discretization in ϕ-direction (Fig. 5.3). In terms of modal expansion, the general solution of the Maxwell's equations in the layer k can be written as

$$E_{z_k}(\rho,\phi,z) = \sum_i^{\infty} [A_{k_i} \mathrm{J}_{\nu_i}(k_{\rho e_k}\rho) + B_{k_i} \mathrm{Y}_{\nu_i}(k_{\rho e_k}\rho)] \tau_\phi^e(\nu_i,\phi) e^{-jk_z z}, \tag{5.22a}$$

$$H_{z_k}(\rho,\phi,z) = \sum_i^{\infty} [C_{k_i} \mathrm{J}_{\nu_i}(k_{\rho h_k}\rho) + D_{k_i} \mathrm{Y}_{\nu_i}(k_{\rho h_k}\rho)] \tau_\phi^h(\nu_i,\phi) e^{-jk_z z}, \tag{5.22b}$$

where ν_i represents the eigenvalues (spectral variable in ϕ-direction) and $\tau_\phi^{e,h}$ represent the eigensolutions depending on the lateral walls bounding the domain. The eigensolutions are well explained in [Heckler, 2010]. For convenience, we have summarized them in Appendix C.

We discretize the structure with two-line systems as shown in Fig. 5.3, where e-lines show the position of E_z and h-lines show the position of H_z field components. When the closed structure is discretized with N^e e-lines and N^h h-lines in ϕ-direction, then according to the sampling theorem we should truncate the expansion of the field component E_z with N^e modes and H_z with N^h modes. Therefore, (5.22) can be written in truncated form as

$$E_{z_k}(\rho,\phi^e,z) = \sum_{i=N_i}^{N_f} [A_{k_i} \mathrm{J}_{\nu_i}(k_{\rho e_k}\rho) + B_{k_i} \mathrm{Y}_{\nu_i}(k_{\rho e_k}\rho)] \tau_\phi^e(\nu_i,\phi^e) e^{-jk_z z}, \tag{5.23a}$$

$$H_{z_k}(\rho,\phi^h,z)=\sum_{i=N_i}^{N_f}[C_{k_i}\mathrm{J}_{\nu_i}(k_{\rho h_k}\rho)+D_{k_i}\mathrm{Y}_{\nu_i}(k_{\rho h_k}\rho)]\tau_\phi^h(\nu_i,\phi^h)e^{-jk_z z}, \tag{5.23b}$$

where N_i and N_f are $-0.5(N^{e,h}-1)$ and $0.5(N^{e,h}-1)$, respectively, for odd $N^{e,h}$. When we bound the computational domain with electric or magnetic walls then N_i becomes 0 or 1 and N_f becomes $N^{e,h}$.

Because the quasi circular nature of the layers at the interfaces is in the ϕ-direction, the field components (E_z and H_z) in z-direction remain tangential to the interfaces along the whole ϕ-direction while the other tangential fields become $E_{t\phi}$ and $H_{t\phi}$, and are represented as

$$E_{t\phi_k}=E_{\phi_k}\cos\alpha_{\phi^h}+\bar{E}_{\rho_k}\sin\alpha_{\phi^h}, \tag{5.24a}$$

$$H_{t\phi_k}=H_{\phi_k}\cos\alpha_{\phi^e}+\bar{H}_{\rho_k}\rho\sin\alpha_{\phi^e}. \tag{5.24b}$$

Here, $\alpha_\phi=\arctan(f(\phi)^{-1}df(\phi)/d\phi)$ is the inclination angle at the interface with the ϕ-axis, with $f(\phi)$ representing the interface. From (5.6), we can say that for 1D discretization (Fig. 5.3) E_z, E_ρ and H_ϕ (or H_z, H_ρ and E_ϕ) components are sampled at the same point. As E_ρ and E_ϕ are located on different lines, therefore $\bar{E}_\rho$ is calculated from the mean of the adjacent values to get the field component in the same position as E_ϕ. Similarly, $\bar{H}_\rho$ is calculated.

On combining (5.6), (5.23) and (5.24), the tangential field components can be written in matrix form as

$$\begin{bmatrix}\boldsymbol{E}_{t\phi_k}\\ \boldsymbol{H}_{t\phi_k}\\ \boldsymbol{E}_{z_k}\\ \boldsymbol{H}_{z_k}\end{bmatrix}=\begin{bmatrix}\boldsymbol{Q}^A_{t\phi_k} & \boldsymbol{Q}^B_{t\phi_k} & \boldsymbol{Q}^C_{t\phi_k} & \boldsymbol{Q}^D_{t\phi_k}\\ \boldsymbol{G}^A_{t\phi_k} & \boldsymbol{G}^B_{t\phi_k} & \boldsymbol{G}^C_{t\phi_k} & \boldsymbol{G}^D_{t\phi_k}\\ \boldsymbol{Q}^A_{z_k} & \boldsymbol{Q}^B_{z_k} & \boldsymbol{Q}^C_{z_k} & \boldsymbol{Q}^D_{z_k}\\ \boldsymbol{G}^A_{z_k} & \boldsymbol{G}^B_{z_k} & \boldsymbol{G}^C_{z_k} & \boldsymbol{G}^D_{z_k}\end{bmatrix}\begin{bmatrix}\boldsymbol{A}_k\\ \boldsymbol{B}_k\\ \boldsymbol{C}_k\\ \boldsymbol{D}_k\end{bmatrix}. \tag{5.25}$$

The full expressions of the terms in (5.27) are given in Appendix C. Using (5.27), we write the discretized field relations at the interfaces $k-1$ and k bounding the layer k in the form

$$\begin{bmatrix}\boldsymbol{E}_{k-1}\\ \boldsymbol{H}_{k-1}\end{bmatrix}=\boldsymbol{M}_{k-1}\boldsymbol{F},\quad \begin{bmatrix}\boldsymbol{E}_{k}\\ \boldsymbol{H}_{k}\end{bmatrix}=\boldsymbol{M}_{k}\boldsymbol{F}, \tag{5.26}$$

where

$$\boldsymbol{M}_k=\begin{bmatrix}\boldsymbol{Q}^A_{t\phi_k} & \boldsymbol{Q}^B_{t\phi_k} & \boldsymbol{Q}^C_{t\phi_k} & \boldsymbol{Q}^D_{t\phi_k}\\ \boldsymbol{Q}^A_{z_k} & \boldsymbol{Q}^B_{z_k} & \boldsymbol{Q}^C_{z_k} & \boldsymbol{Q}^D_{z_k}\\ \boldsymbol{G}^A_{z_k} & \boldsymbol{G}^B_{z_k} & \boldsymbol{G}^C_{z_k} & \boldsymbol{G}^D_{z_k}\\ -\boldsymbol{G}^A_{t\phi_k} & -\boldsymbol{G}^B_{t\phi_k} & -\boldsymbol{G}^C_{t\phi_k} & -\boldsymbol{G}^D_{t\phi_k}\end{bmatrix}, \tag{5.27}$$

and take the notations of the fields and coefficients in matrix form as

$$\boldsymbol{E}_k=\begin{bmatrix}\boldsymbol{E}_{t\phi_k}\\ \boldsymbol{E}_{z_k}\end{bmatrix},\ \boldsymbol{H}_k=\begin{bmatrix}\boldsymbol{H}_{z_k}\\ -\boldsymbol{H}_{t\phi_k}\end{bmatrix},\ \boldsymbol{F}=\begin{bmatrix}\boldsymbol{A}_k\\ \boldsymbol{B}_k\\ \boldsymbol{C}_k\\ \boldsymbol{D}_k\end{bmatrix}. \tag{5.28}$$

After eliminating the unknown coefficient column matrix $\boldsymbol{F}$, it results in

$$\begin{bmatrix} \boldsymbol{E}_{k-1} \\ \boldsymbol{H}_{k-1} \end{bmatrix} = \boldsymbol{K}_k \begin{bmatrix} \boldsymbol{E}_k \\ \widetilde{\boldsymbol{H}}_k \end{bmatrix}. \tag{5.29}$$

Therefore, the hybrid matrix ($\boldsymbol{K}_k$) for layer k can be represented as

$$\boldsymbol{K}_k = \boldsymbol{M}_{k-1}\boldsymbol{M}_k^{-1} = \begin{bmatrix} \boldsymbol{V}_k & \boldsymbol{Z}_k \\ \boldsymbol{Y}_k & \boldsymbol{B}_k \end{bmatrix}. \tag{5.30}$$

5.1.3 System Equation

In order to derive the system equation for the multilayered cylindrical structures, we set up an FWEC which consists of hybrid blocks ($\widetilde{\boldsymbol{K}}_k$) as shown in Fig. 5.2. Each block represents a corresponding dielectric layer in the structure. The inner and outer layers are terminated with admittances $\widetilde{\boldsymbol{Y}}_0$ and $\widetilde{\boldsymbol{Y}}_n$, respectively, whose expressions are given in Appendix C. Several inner layers (without metallic strip) can be taken into account simultaneously by simple matrix multiplication. From this we get the equivalent hybrid matrix as

$$\boldsymbol{K}_{eq} = \prod_{k=1}^{n-1} \boldsymbol{K}_k, \tag{5.31}$$

representing all the cascaded $\boldsymbol{K}_k$ matrices (Fig. 5.4). After applying the continuity equations in the interface k to match the fields we get the system equation in the form

$$\boldsymbol{G}\boldsymbol{J} = \boldsymbol{E}. \tag{5.32}$$

There is no current on the interfaces of the waveguides, therefore the system equation becomes

$$\boldsymbol{L}\boldsymbol{E} = 0. \tag{5.33}$$

The propagation constant can be found on solving the indirect eigenvalue equation

$$\det(\boldsymbol{L}) = 0, \tag{5.34}$$

where the elements of the matrix $\boldsymbol{L} = \boldsymbol{G}^{-1}$ for multilayered structures can be calculated from (2.42)-(2.43).

For stripline structures, after applying the network analysis technique and the boundary conditions that the tangential electric field components must vanish on the metallizations and the electric currents outside that region, we obtain the reduced matrix as

$$\boldsymbol{G}_{\mathrm{red}}\boldsymbol{J}_{\mathrm{red}} = 0 \qquad \text{or} \qquad \boldsymbol{L}_{\mathrm{red}}\boldsymbol{E}_{\mathrm{red}} = 0. \tag{5.35}$$

It can be solved as indirect eigenvalue problem $\det(\boldsymbol{G}_{\mathrm{red}}) = 0$ or $\det(\boldsymbol{L}_{\mathrm{red}}) = 0$ to find the propagation constant for the microstrip line.

For structures with circular interfaces, spectral domain equations should be used to simplify the calculations. For waveguides, (5.33) must be solved in spectral domain using

(5.21). While for stripline structures, (5.35) must be solved, where the spectral domain Green's function is converted into spatial domain using

$$\begin{bmatrix} \boldsymbol{G}_{\phi\phi} & \boldsymbol{G}_{\phi z} \\ \boldsymbol{G}_{z\phi} & \boldsymbol{G}_{zz} \end{bmatrix} = \begin{bmatrix} \boldsymbol{T}_h & 0 \\ 0 & \boldsymbol{T}_e \end{bmatrix} \begin{bmatrix} \widetilde{\boldsymbol{G}}_{\phi\phi} & \widetilde{\boldsymbol{G}}_{\phi z} \\ \widetilde{\boldsymbol{G}}_{z\phi} & \widetilde{\boldsymbol{G}}_{zz} \end{bmatrix} \begin{bmatrix} \boldsymbol{T}_h^{-1} & 0 \\ 0 & \boldsymbol{T}_e^{-1} \end{bmatrix}. \tag{5.36}$$

Here, the transformation matrices $\boldsymbol{T}_e$ and $\boldsymbol{T}_h$ are formed from τ_ϕ^e and τ_ϕ^h, respectively.

5.2 Numerical Results

5.2.1 Graded-Index Fibers

We apply the developed procedure of multilayered cylindrical structures to analyze graded-index fibers. Fig. 5.5 shows the schematic of the fiber. We approximate the core of the structure by a step-index profile. After deciding on the number of layers (M_{core}) taken to model the profile, we calculate the outer radius of each layer from

$$\rho_k = \frac{\rho_{\text{core}}}{M_{\text{core}}}(k+1). \tag{5.37}$$

Here, k represents the integer number which varies from 0 to $M_{\text{core}}-1$ and ρ_{core} represents the radius of the core. We take the index profile in the same way as given by Heckler and Dreher [2007a],

$$f(\rho) = n_{\max}^2\left[1 - 2\Delta\left(\frac{\rho}{\rho_{\text{core}}}\right)^q\right],\ 0 \le \rho \le \rho_{\text{core}}, \tag{5.38}$$

where Δ is the profile height and the value of q is 1 or 2 for linear and parabolic profiles, respectively. We calculate the refractive index for each layer k as

$$n_k^2 = f(\rho_{n_k}), \tag{5.39}$$

where

$$\rho_{n_k} = \frac{\rho_{\text{core}}}{2M_{\text{core}}}(2k+1) \tag{5.40}$$

represents the radius at the middle of the layer.

Fig. 5.4 represents the reduced FWEC of the fiber after matrix multiplication of all the inner layers. Thus, we obtain the total admittance ($\widetilde{\boldsymbol{L}}$) of the structure by simple circuit analysis as

$$\widetilde{\boldsymbol{L}} = (\widetilde{\boldsymbol{Y}}_0\widetilde{\boldsymbol{Z}}_{eq} + \widetilde{\boldsymbol{B}}_{eq})^{-1}(\widetilde{\boldsymbol{Y}}_0\widetilde{\boldsymbol{V}}_{eq} + \widetilde{\boldsymbol{Y}}_{eq}) + \widetilde{\boldsymbol{Y}}_n, \tag{5.41}$$

where $\widetilde{\boldsymbol{Y}}_0$ denotes the innermost layer (core) admittance, $\widetilde{\boldsymbol{Y}}_n$ denotes the top open layer admittance and $\widetilde{\boldsymbol{B}}_{eq}$, $\widetilde{\boldsymbol{V}}_{eq}$, $\widetilde{\boldsymbol{Y}}_{eq}$, and $\widetilde{\boldsymbol{Z}}_{eq}$ are the elements of the equivalent hybrid matrix $\widetilde{\boldsymbol{K}}_{eq}$ of the inner layers. The propagation constant of the fiber can be found on solving the indirect eigenvalue problem

$$\det(\widetilde{\boldsymbol{L}}) = 0. \tag{5.42}$$

First, we have analyzed the fiber with both linear and parabolic profile with $n_{\max} = (3.098, 3.098, 3.098\sqrt{\alpha})$ and $n_{\text{clad}} = (1.52, 1.52, 1.52\sqrt{\alpha})$, where α is the anisotropy ratio in the material. Therefore, we define the material by $\varepsilon_r = n^2$ and $\mu_r = 1$. We take the structure open at the top, so we can model it by an air layer extending to ∞. Fig. 5.6

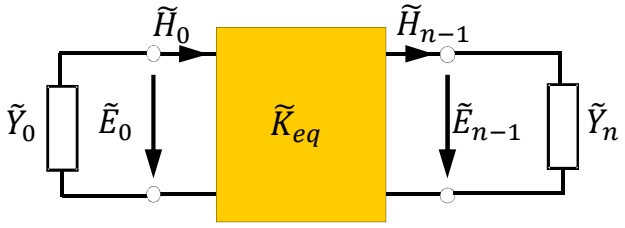

Figure 5.4: Full-wave equivalent circuit of a stratified structure after matrix multiplication.

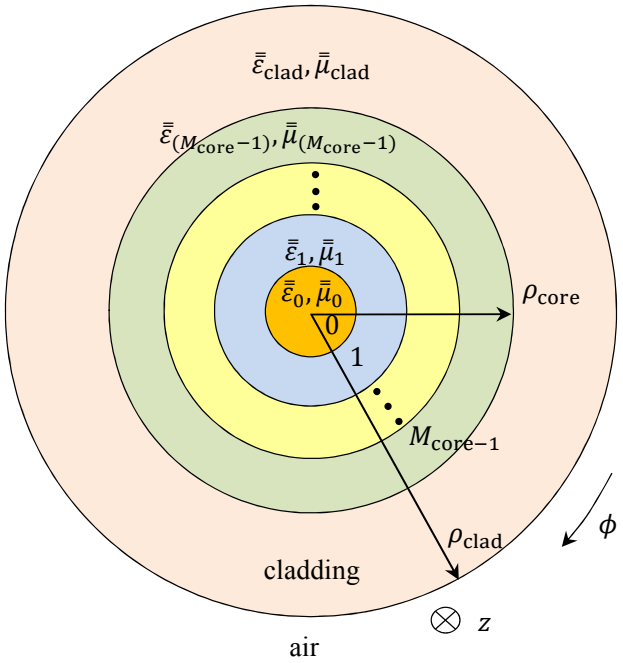

Figure 5.5: Schematic view of the equivalent model for a graded-index fiber with anisotropic material.

shows the normalized propagation constants of the HE_{11} mode for both linear and parabolic profiles with normalized $\rho_{\text{core}} = 0.45$ and $\rho_{\text{clad}} = 7\rho_{\text{core}}$. The figure compares the results with ANSYS HFSS and CST for $M_{\text{core}} = 2$, 5, and 10. The results from HFSS are slightly below from the ones with our code and the results from CST are slightly above, but in very good agreement. However, the commercial codes were not able to handle significantly more than 10 layers in a reasonable time.

We have done the programming of the code in MATLAB and have performed all the simulations on Intel i7-6600U CPU @2.6 GHz processor. When we have modeled the fiber core with 10 layers, the computation time with the FWEC was 0.16 seconds, whereas the same simulation took 25 seconds with HFSS (port mode calculation) and 27 seconds with CST (time-domain solver with port modes only). We have used open boundary conditions in CST and waveguide port excitation for both HFSS and CST. With $M_{\text{core}} = 10{,}000$ in the fiber, the elapsed time with FWEC computation was 12.16 seconds.

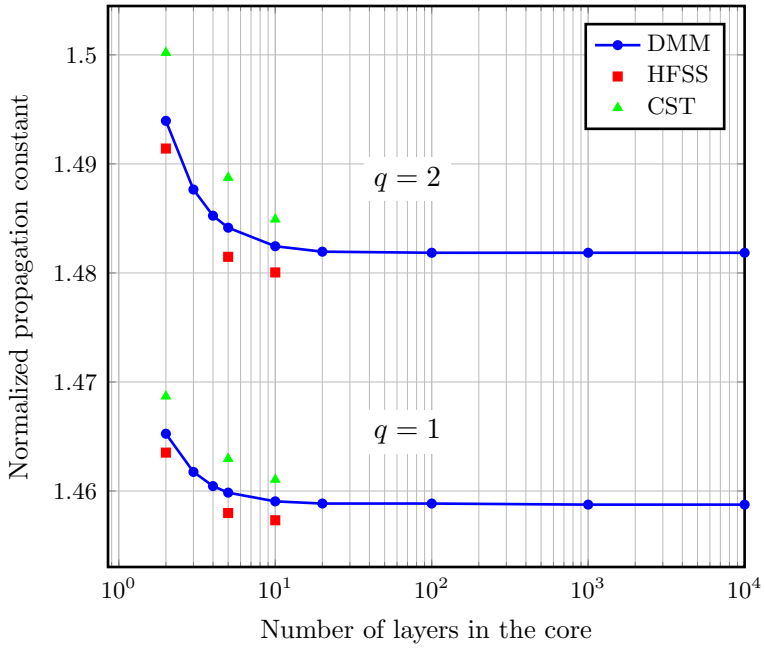

Figure 5.6: Normalised propagation constants of the first mode (HE_{11}) for different number of layers used to model the core of graded-index fiber with anisotropic material ($\alpha = 2$).

5.2.2 Elliptical Waveguide

To verify the DMM formulations for non-circular interfaces of the stratified dielectric in microwave structures, we have started with analyzing a simple elliptical waveguide. The waveguide comprises 2 layers, one is an elliptical core and the other is air surrounding that core. Fig. 5.7 presents the schematic view of the analysed waveguide, with different values of the normalized frequency $V_B = Bk_0\sqrt{\varepsilon_{r,\text{core}} - \varepsilon_{r,\text{air}}}$. We have taken the material of the core with $\varepsilon_{r,\text{core}} = (1.539)^2$ for the isotropic and $\bar{\bar{\varepsilon}}_{r,\text{core}} = ((1.539)^2, (1.539)^2, (1.25)^2)$ for the anisotropic case. We have assumed the normalized frequency for both cases with $\varepsilon_{r,\text{core}} = (1.539)^2$. We have done the analysis with axial ratio ($\text{AR} = B/A$) of the waveguide at 0.5 for the isotropic case and 0.5 and 0.8 for the anisotropic case. We obtain the total admittance of the structure as

$$\boldsymbol{L} = \boldsymbol{Y}_0 + \boldsymbol{Y}_1, \tag{5.43}$$

where $\boldsymbol{Y}_0$ denotes the admittance of the core and $\boldsymbol{Y}_1$ denotes the admittance of the air surrounding the core.

Fig. 5.8 plots the dispersion curve for the first two modes i.e. oHE_{11} and eHE_{11} at 2 GHz frequency. The figure shows very good agreement with the various approaches shown in Heckler and Dreher [2007b] for the isotropic case and also with the ANSYS HFSS and CST for both the isotropic and the anisotropic case. Fig. 5.9 and Fig. 5.10 show the electric and magnetic field distribution for both modes at the cross section of the waveguide at $V_B = 1.6$ and $\text{AR} = 0.8$ for the anisotropic case.

5.2.3 Elliptical Stripline

Here, the DMM formulation is used to analyze conformal stripline structures. First we consider the case of a stripline, where the top ground is taken to be in elliptical shape. We

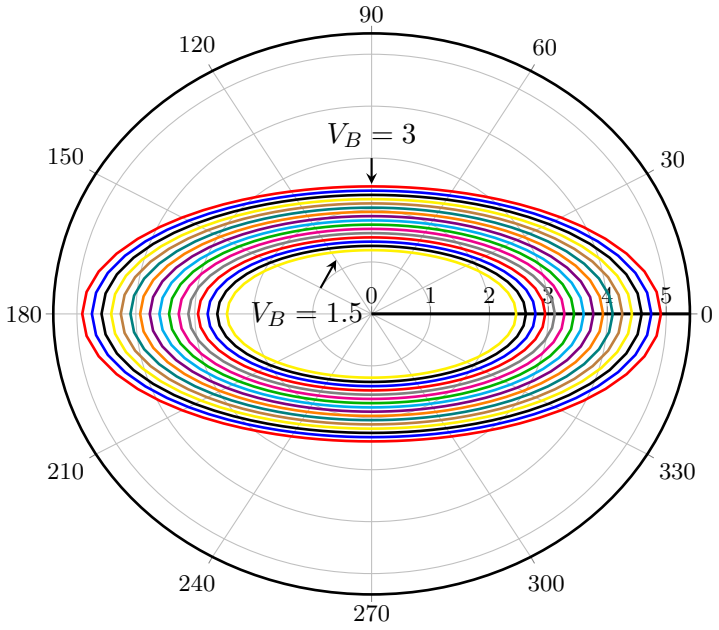

Figure 5.7: Elliptical waveguide structure.

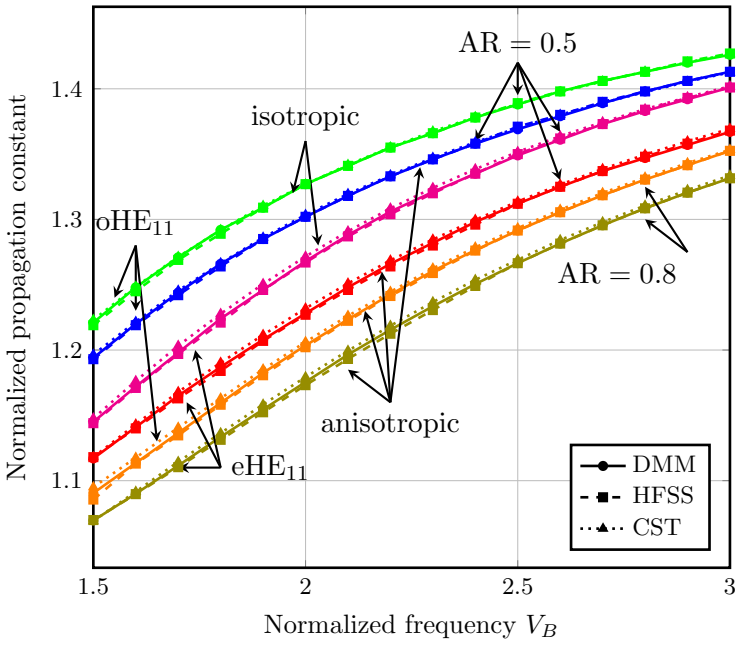

Figure 5.8: Dispersion curve of elliptical waveguide.

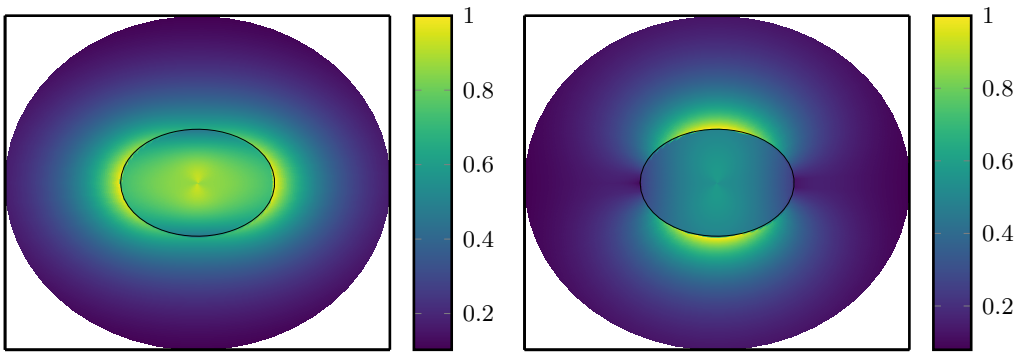

(a) oHE_{11} **(b)** eHE_{11}

Figure 5.9: Distribution of the total electric field for the elliptical waveguide.

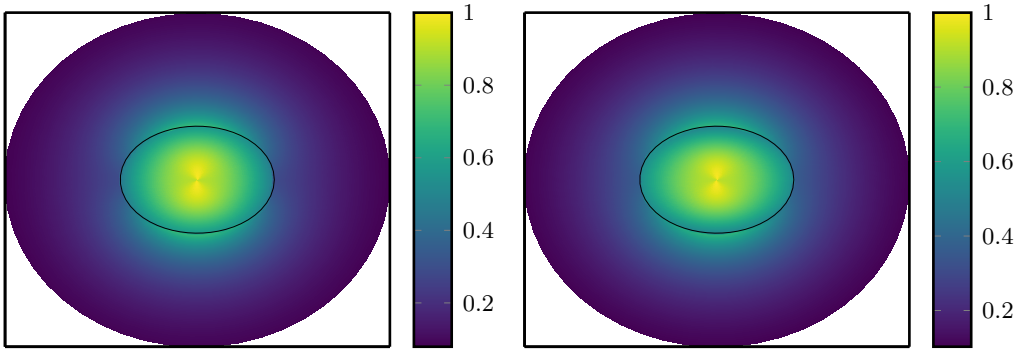

(a) oHE_{11} **(b)** eHE_{11}

Figure 5.10: Distribution of the total magnetic field for the elliptical waveguide.

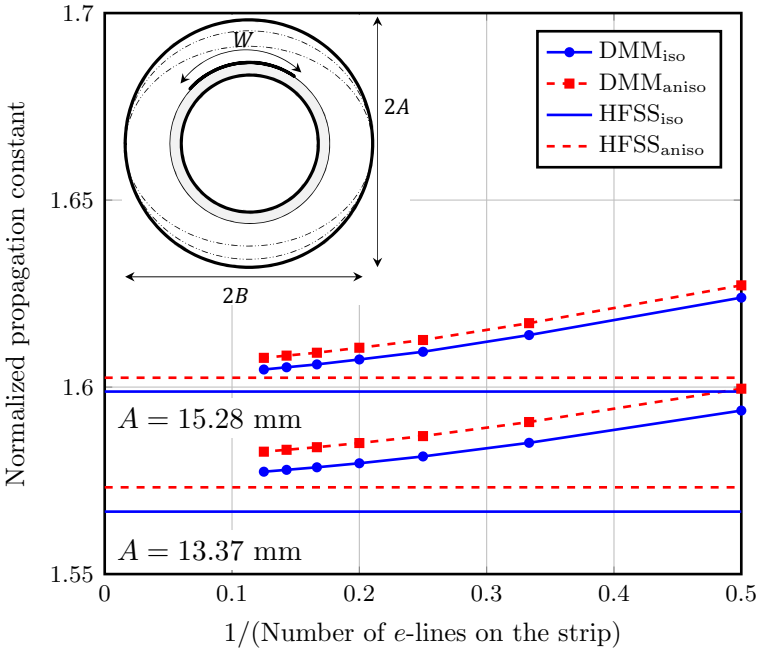

Figure 5.11: Propagation constants of striplines with elliptical top ground.

have done the simulations with the parameters: $\rho_1 = 11.72$ mm $\rho_0 = 10.98$ mm, $B = 16.23$ mm, $W = 5.37(\rho_1 - \rho_0)$, $\varepsilon_{r2} = 1$, $\mu_{r2} = 1$, $\varepsilon_{r1} = 3$ and $\mu_{r1} = 1$ for the isotropic case, while $\bar{\bar{\mu}}_{r1} = (1, 1, 2)$ for the anisotropic case. From network analysis technique, we obtain the system equation as

$$\left(\boldsymbol{Z}_1^{-1}\boldsymbol{V}_1 + \boldsymbol{B}_2\boldsymbol{Z}_2^{-1}\right)\boldsymbol{E}_1 = \boldsymbol{J}_1. \tag{5.44}$$

Fig. 5.11 shows the computed propagation constants for different cases of A. We have achieved a very good agreement with the predictions from DMM and ANSYS HFSS.

Then, we have analyzed the microstrip line where the strip is coated on the elliptical interface between substrate and air. We have done the computations with the same parameters as above with the elliptical top ground, while we have taken $B = 11.72$ mm and $\phi = 20°$ for the microstrip line. Here, we obtain the system equation as

$$\left(\boldsymbol{Z}_1^{-1}\boldsymbol{V}_1 + \boldsymbol{Y}_2\right)\boldsymbol{E}_1 = \boldsymbol{J}_1, \tag{5.45}$$

where the first term $\boldsymbol{Z}_1^{-1}\boldsymbol{V}_1$ denotes that the structure is grounded at the bottom and the second term $\boldsymbol{Y}_2$ gives the admittance of the open top. Again the propagation constants are computed for different values of A, as shown in Fig. 5.12. We can see from the graphs that the DMM obtains smooth convergence. Fig. 5.13 shows the electric and magnetic field distribution over the cross-section of the stripline at $A = 12.18$ mm for the anisotropic case.

Also, we have analyzed the microstrip line bounded by E-walls along the azimuth as shown in Fig. 5.14. We have done the analysis with $\rho_0 = 11$ mm, $A = 1.2B$ and B varies from 12 to 18 mm. Fig. 5.14 shows the dispersion curve of the structure with anisotropic material ($\varepsilon_{r1} = 3$, $\bar{\bar{\mu}}_{r1} = (1, 1, 2)$). We have done all the calculations at 5 GHz frequency. The HFSS time span was between 4 to 7.5 minutes for full structure simulation, while DMM took between 9 to 11 seconds for analyzing half of the structure due to symmetry. We have obtained very good results with only 4 e-lines on half of the strip.

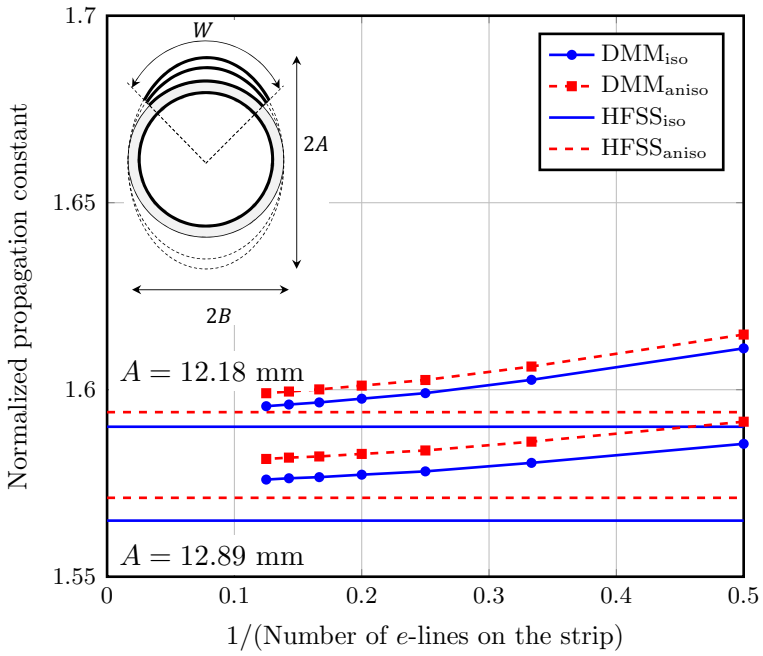

Figure 5.12: Propagation constants of microstrip lines with non-circular cross-section.

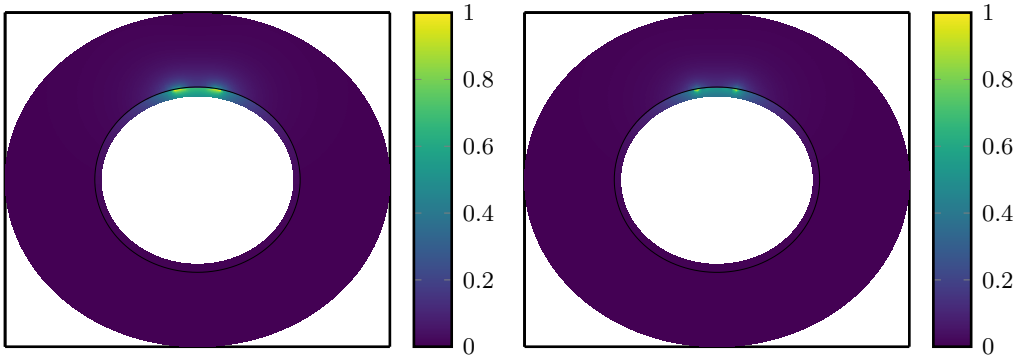

(a) Electric field **(b)** Magnetic field

Figure 5.13: Distribution of the total electric and magnetic field for the microstrip line with non-circular cross-section.

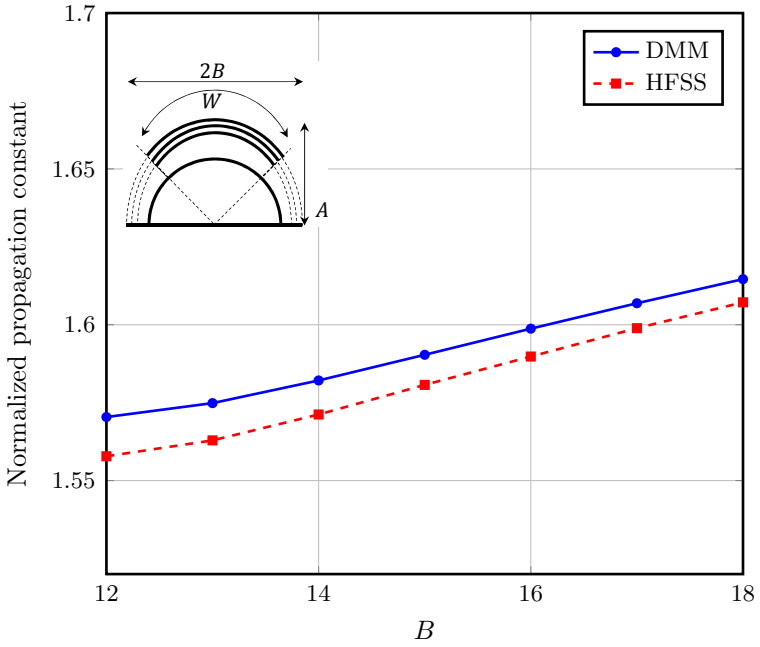

Figure 5.14: Variation of the propagation constants with the dimension of the microstrip line with non-circular cross-section.

5.3 Formulation for the 2D Discretization

Fig. 5.15 shows a multilayered structure with varying interfaces in both ϕ- and z-directions. There is a need to apply lateral boundary conditions in two directions to enclose the domain. Therefore, we can represent the general solution of Maxwell's equations as

$$E_{z_k}(\rho,\phi,z) = \sum_{i}^{\infty}\sum_{l}^{\infty}[A_{k_{il}}\mathrm{J}_{\nu_{il}}(k_{\rho e_k}\rho) + B_{k_{il}}\mathrm{Y}_{\nu_{il}}(k_{\rho e_k}\rho)]\tau_{\phi}^{e}(\nu_i,\phi)\tau_{z}^{e}(k_{zl},z), \tag{5.46a}$$

$$H_{z_k}(\rho,\phi,z) = \sum_{i}^{\infty}\sum_{l}^{\infty}[C_{k_{il}}\mathrm{J}_{\nu_{il}}(k_{\rho h_k}\rho) + D_{k_{ij}}\mathrm{Y}_{\nu_{il}}(k_{\rho h_k}\rho)]\tau_{\phi}^{h}(\nu_i,\phi)\tau_{z}^{h}(k_{zl},z), \tag{5.46b}$$

where ν_i and k_{zl} are the eigenvalues and $\tau_{\phi}^{e,h}$ and $\tau_{z}^{e,h}$ are the eigenfunctions depending on the lateral walls bounding the domain. Here, $k_{\rho e}$ is for TE waves and $k_{\rho h}$ for TM waves and can be represented as

$$k_{\rho e} = \sqrt{\frac{\varepsilon_z}{\varepsilon_t}(\mu_t\varepsilon_t - k_z^2)} \text{ and } k_{\rho h} = \sqrt{\frac{\mu_z}{\mu_t}(\mu_t\varepsilon_t - k_z^2)}. \tag{5.47}$$

Fig. 5.16 gives the two-dimensional discretization scheme for the cylindrical coordinate system. We take the position of the independent field components as e-lines and h-lines for E_z and H_z, respectively, which are shifted with half discretization distance (($\Delta\phi/2$ or $\Delta z/2$)) in ϕ- and z-direction. We bound the computational domain with N_{ϕ}^{e} and N_{z}^{e} number of e-lines in ϕ- and z-directions and N_{ϕ}^{h} and N_{z}^{h} number of h-lines in ϕ- and z-directions by placing some E-, H- or ABC-walls. Therefore, $N_{\phi}^{e,h}$ and $N_{z}^{e,h}$ should be the number of modes included in the modal expansion in ϕ- and z-directions, respectively. Then (5.46) in

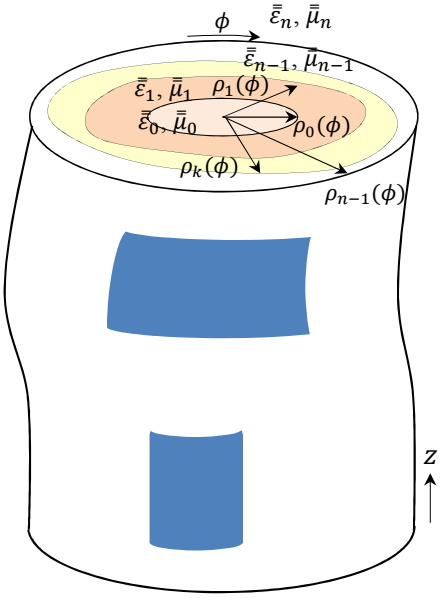

Figure 5.15: Multilayered structure with quasi-cylindrical interfaces.

truncated form becomes

$$E_{z_k}(\rho, \phi^e, z^e) = \sum_{i}^{N_\phi^e} \sum_{l}^{N_z^e} [A_{k_{il}} \mathrm{J}_{\nu_{il}}(k_{\rho e_k}\rho) + B_{k_{il}} \mathrm{Y}_{\nu_{il}}(k_{\rho e_k}\rho)] \tau_\phi^e(\nu_i, \phi^e) \tau_z^e(k_{zl}, z^e), \tag{5.48a}$$

$$H_{z_k}(\rho, \phi^h, z^h) = \sum_{i}^{N_\phi^h} \sum_{l}^{N_z^h} [C_{k_{il}} \mathrm{J}_{\nu_{il}}(k_{\rho h_k}\rho) + D_{k_{ij}} \mathrm{Y}_{\nu_{il}}(k_{\rho h_k}\rho)] \tau_\phi^h(\nu_i, \phi^h) \tau_z^h(k_{zl}, z^h). \tag{5.48b}$$

The positions of the other field components can be identified using the relation given in (5.6). A detailed study about positioning of the discretization lines on the metallization is done in [Heckler and Dreher, 2016]. In case of symmetry in the metallization, there is a need to only examine half or quarter of the structure. Appendix D covers the possible cases with the positions of the field components.

Since the deformations in the structure can happen in both ϕ- and z-direction, we can calculate the tangential field components at the interfaces by combining the field components. We can write the obtained relation as

$$E_{t\phi_k} = E_{\phi_k} \cos\alpha_{\phi^h} + \bar{E}_{\rho_k} \sin\alpha_{\phi^h}, \tag{5.49a}$$

$$H_{t\phi_k} = H_{\phi_k} \cos\alpha_{\phi^e} + \bar{H}_{\rho_k} \sin\alpha_{\phi^e}, \tag{5.49b}$$

$$E_{tz_k} = E_{z_k} \cos\alpha_{z^e} + \bar{E}_{\rho_k} \sin\alpha_{z^e}, \tag{5.49c}$$

$$H_{tz_k} = H_{z_k} \cos\alpha_{z^h} + \bar{H}_{\rho_k} \sin\alpha_{z^h}. \tag{5.49d}$$

Here, α_ϕ and α_z are the inclination angles at the interface with the ϕ- and z-axes, respectively. The tangential field components are sampled at the same points as E_z and H_z. From Fig. 5.16 it is clear that the position of E_ρ (eh-line) and H_ρ (he-line) is different from the position of E_z (e-line) and H_z (h-line) or E_ϕ ((h-line)) and H_ϕ (e-line), respectively. Therefore, we take the average of the adjacent sampled values of E_ρ and H_ρ and represent the average as $\bar{E}_\rho$ and $\bar{H}_\rho$.

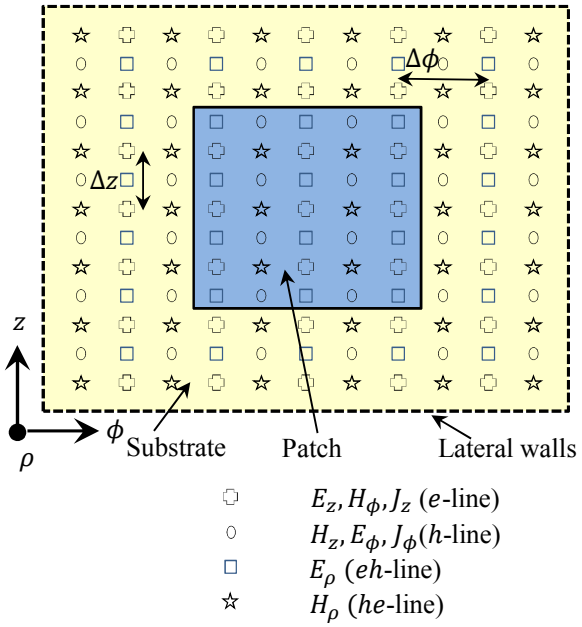

Figure 5.16: 2D discretization scheme for the interfaces of the structure.

After calculating the tangential field components at the interfaces and doing some analytical work, we can calculate the admittance/hyrid matrix for each layer. Then, on using the FWEC and network analysis techniques we get the system equation in the form

$$\begin{bmatrix} \boldsymbol{G}_{t\phi} & \boldsymbol{G}_{t\phi tz} \\ \boldsymbol{G}_{tzt\phi} & \boldsymbol{G}_{tz} \end{bmatrix} \begin{bmatrix} \boldsymbol{J}_{t\phi} \\ \boldsymbol{J}_{tz} \end{bmatrix} = \begin{bmatrix} \boldsymbol{E}_{t\phi} \\ \boldsymbol{E}_{tz} \end{bmatrix} \quad \text{or} \quad \boldsymbol{GJ} = \boldsymbol{E}. \tag{5.50}$$

5.4 Numerical Results for Microstrip Patch with Elliptical Substrate

We have applied the extended DMM method to analyze a microstrip patch with elliptical substrate. We have fed the antenna with a conformal microstrip line as shown in Fig. 5.17. Fig. 5.18 gives the FWEC obtained of the analyzed structure. The method to analyze conformal antennas with voltage gap generators is well discussed in [Heckler and Dreher, 2011] and is similar to what is explained in Chapter 3. The dimensions used for the analysis are $B_0 = 28.43$ mm, $B_1 = 30$ mm, $A_0 = B_0/\text{AR}$, $A_1 = B_1/\text{AR}$, $P_a = 105°$, $P_b = 52.78$ mm and $W_f = 4.71$ mm. Here the axial ratio $\text{AR} = B/A$ represents the ratio between the minor and major axes of the ellipse. We have taken the material properties of the substrate as $\varepsilon_{r1} = 2.2$ and $\mu_{r1} = 1$ for the isotropic case, while $\bar{\bar{\varepsilon}}_{r1} = (2.2, 2.2, 1.5)$ and $\bar{\bar{\mu}}_{r1} = (1, 1, 2)$ for the anisotropic case.

Due to symmetry, we have analyzed only half of the structure with DMM. We have calculated the absorbing boundary conditions using Higdon's operator [Higdon, 1987] to bound the structure in z-direction. We have discretized the structure with a limited number of lines: 9 e-lines to discretize the patch in ϕ-direction, and 8 and 7 h-lines to discretize the patch in z-direction, for AR = 1 and 0.833, respectively. The cross-section of the substrate

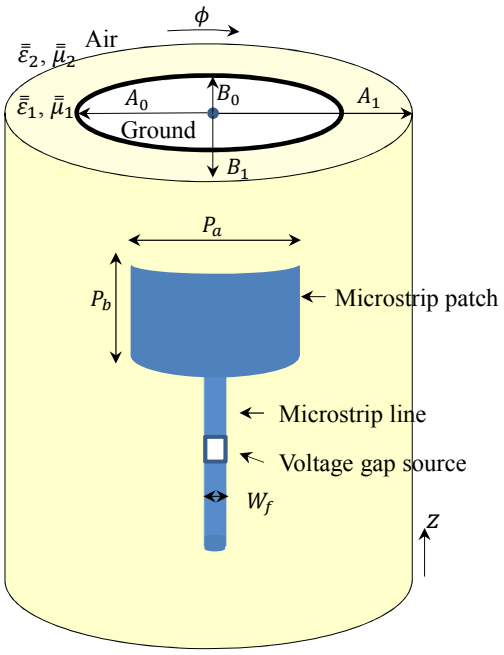

Figure 5.17: Microstrip patch antenna with elliptical substrate.

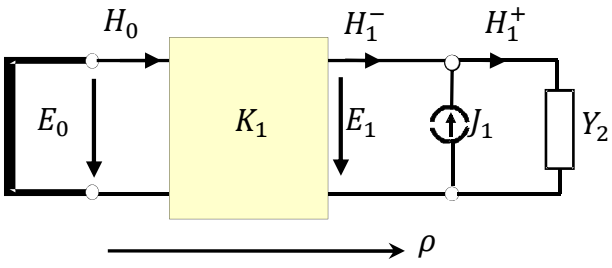

Figure 5.18: Full-wave equivalent circuit for microstrip patch antenna with elliptical substrate.

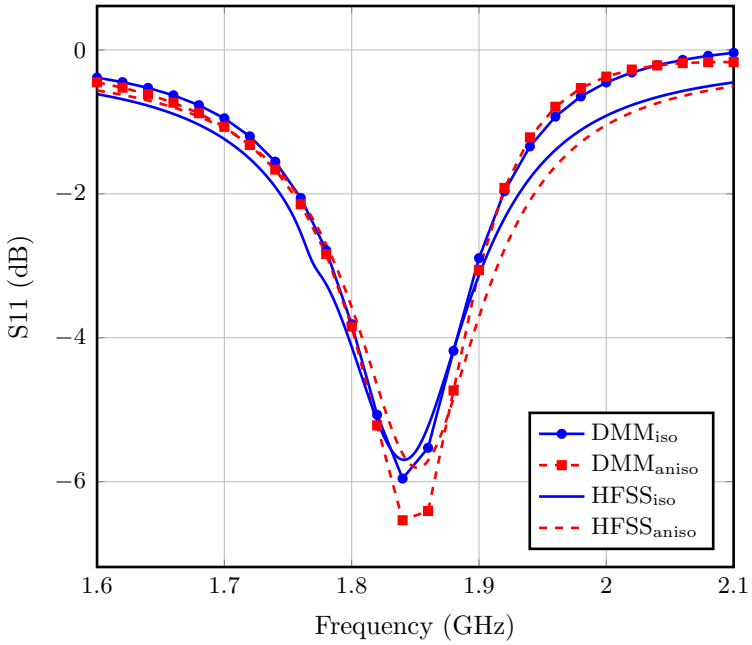

Figure 5.19: S-parameters for the microstrip patch antenna with cylindrical substrate.

becomes cylindrical with AR = 1, therefore the system equation appears as

$$\begin{bmatrix} \boldsymbol{G}_{\phi} & \boldsymbol{G}_{\phi z} \\ \boldsymbol{G}_{z} & \boldsymbol{G}_{z} \end{bmatrix} \begin{bmatrix} \boldsymbol{J}_{\phi} \\ \boldsymbol{J}_{z} \end{bmatrix} = \begin{bmatrix} \boldsymbol{E}_{\phi} \\ \boldsymbol{E}_{z} \end{bmatrix}. \tag{5.51}$$

The cross-section is elliptical with AR = 0.833 and there are no variations in z-direction. We obtain the system equation as

$$\begin{bmatrix} \boldsymbol{G}_{t\phi} & \boldsymbol{G}_{t\phi z} \\ \boldsymbol{G}_{zt\phi} & \boldsymbol{G}_{z} \end{bmatrix} \begin{bmatrix} \boldsymbol{J}_{t\phi} \\ \boldsymbol{J}_{z} \end{bmatrix} = \begin{bmatrix} \boldsymbol{E}_{t\phi} \\ \boldsymbol{E}_{z} \end{bmatrix} \tag{5.52}$$

or

$$\left(\boldsymbol{Z}_1^{-1}\boldsymbol{V}_1 + \boldsymbol{B}_2\boldsymbol{Z}_2^{-1}\right)^{-1}\boldsymbol{J}_1 = \boldsymbol{E}_1. \tag{5.53}$$

Figures 5.19 and 5.20 show the S-parameters for the structure with AR = 1 and 0.833, respectively. The figures compare the results computed from the DMM formulation with the ones obtained from HFSS. A very good agreement has been obtained between them. Figures 5.21 and 5.22 compare the computed input impedances for these antennas.

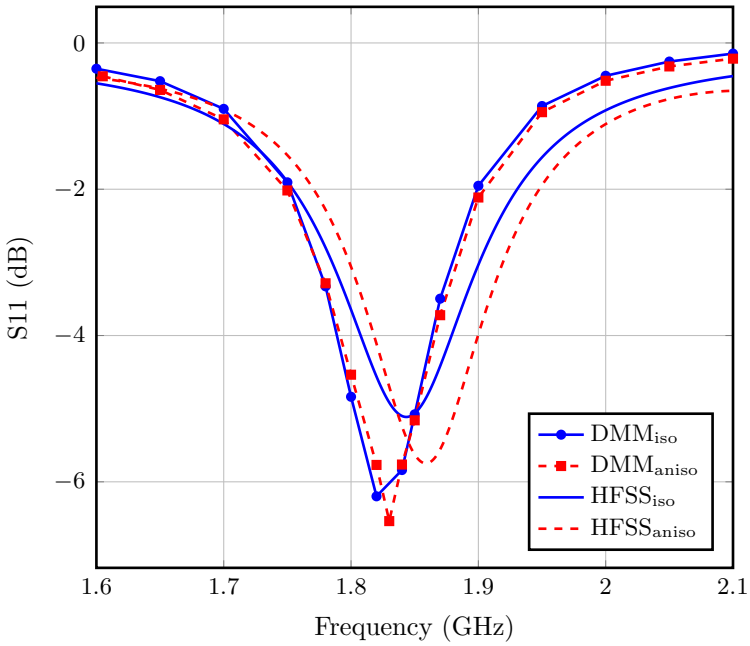

Figure 5.20: S-parameters for the microstrip patch antenna with elliptical substrate.

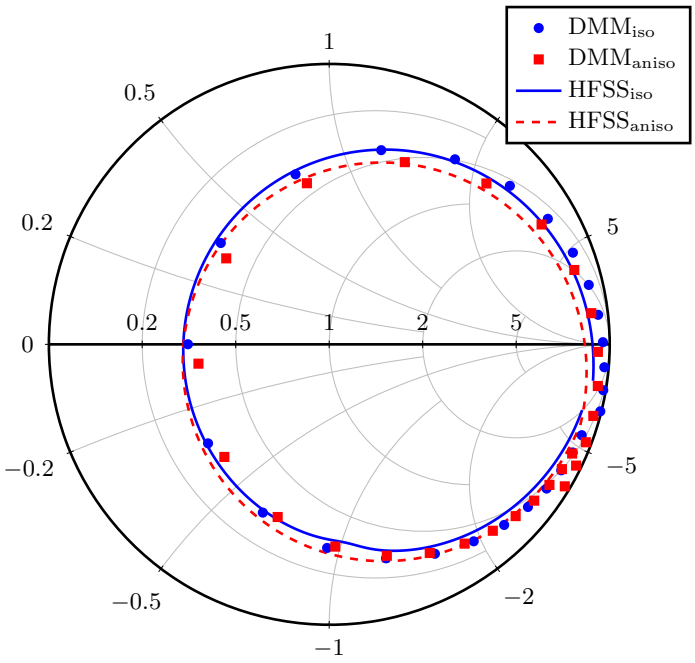

Figure 5.21: Input impedance of the patch with cylindrical substrate

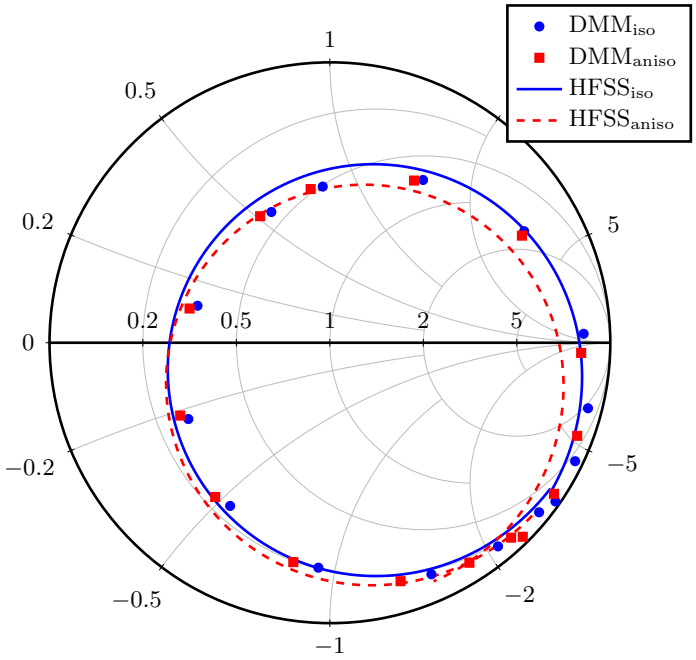

Figure 5.22: Input impedance of the patch with elliptical substrate.

6 Analysis of Anisotropic Inhomogeneous Transmission Lines

Planar dielectric waveguides are widely used in microwave and millimeter-wave circuits using non-radiative dielectric (NRD) waveguide integrated technology [Wu and Han, 1997], substrate integrated technology [Cassivi et al., 2002], and also in modern integrated optics [Bulla et al., 2002]. The focus of this chapter is on inhomogeneous dielectric structures. Various hybrid waveguides are shown in Fig. 6.1. These inhomogeneities are fabricated in the fibers or optical waveguides to provide the desired confinement. Here the problem is to characterize the media where the permittivity and/or permeability are space dependent. It is desired by the design engineers that the dielectric waveguides must be accurately modeled with efficient numerical procedures so that they have precise values of propagation constants for these complex multilayered structures.

Several approaches are already used to precisely compute the propagation constants of inhomogeneous waveguides, like Fourier decomposition in [Pashaie, 2007], method of lines (MoL) in [Berini and Wu, 1996; Pregla et al., 1987], finite element method in [Lu and Fernandez, 1993], variational method in [Akiba and Haus, 1982] and plane wave expansion method in [Eti and Kurt, 2016].

This chapter extends the DMM method and explains the derivation of the hybrid-matrix elements for the inhomogeneous dielectric layers. The formulation is then used to compute the system equation of the structure under analysis. The method is applied to various inhomogeneous dielectric waveguides for validation. It also considers metallization between the dielectric layers.

First, we introduce the detailed theory for the analysis of inhomogeneous dielectric layers. The full-wave analysis is obtained using summation of both kinds of modes, transversal electric and transversal magnetic modes. Then, we discuss the various cases where the derived hybrid matrices can be useful. At the end, we discuss various numerical results and validate them with open literature and/or commercial software ANSYS HFSS. This chapter is based on [Kamra and Dreher, 2019a, 2020b].

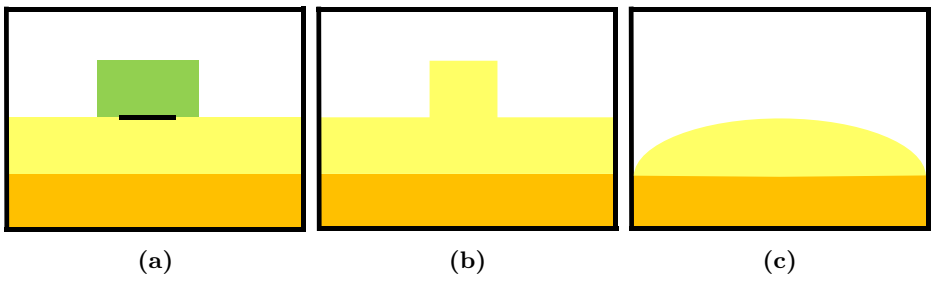

Figure 6.1: Hybrid waveguide structures: (a) Dielectric waveguide with microstrip, (b) Dielectric waveguide (c) Dielectric waveguide with quasi-planar interface.

6.1 Formulation for the Full-Wave Equivalent Circuit

6.1.1 Field Relations

We consider an arbitrary planar multilayered structure with homogeneous and inhomogeneous dielectric layers. The direction of the wave propagation is taken along the z-axis and the cross-section in the xy-plane as shown in Fig. 6.2. The inhomogeneous layer contains an abrupt transition in the material properties. Therefore, the space dependent permittivity ($\bar{\bar{\varepsilon}} = \varepsilon_0 \bar{\bar{\varepsilon}}_r$) and permeability ($\bar{\bar{\mu}} = \mu_0 \bar{\bar{\mu}}_r$) tensors of the dielectric layer can be written with

$$\bar{\bar{\varepsilon}}_r = \begin{pmatrix} \varepsilon_x(x,y) & 0 & 0 \\ 0 & \varepsilon_y(x,y) & 0 \\ 0 & 0 & \varepsilon_z(x,y) \end{pmatrix}, \tag{6.1}$$

$$\bar{\bar{\mu}}_r = \begin{pmatrix} \mu_x(x,y) & 0 & 0 \\ 0 & \mu_y(x,y) & 0 \\ 0 & 0 & \mu_z(x,y) \end{pmatrix}. \tag{6.2}$$

The source-free second order curl-curl equations are obtained for electric and magnetic fields as

$$\nabla \times \bar{\bar{\mu}}_r^{-1} \cdot \nabla \times \vec{E}(x,y,z) - \bar{\bar{\varepsilon}}_r \cdot \vec{E}(x,y,z) = 0, \tag{6.3}$$

$$\nabla \times \bar{\bar{\varepsilon}}_r^{-1} \cdot \nabla \times \vec{H}(x,y,z) - \bar{\bar{\mu}}_r \cdot \vec{H}(x,y,z) = 0. \tag{6.4}$$

Here, all the space variables are normalized by the free space wave number k_0, the time factor is suppressed and $\eta_0 \vec{H}$ is replaced by $\vec{H}$, where $\eta_0 = \sqrt{\mu_0/\varepsilon_0}$ is the intrinsic impedance of the free space. We can take a large number of layers in y-direction, which removes the y-dependance of the material properties.

We know that each scalar differential equation obtained from (6.3) and (6.4) is at least coupled to another one. It is a well-known fact that hybrid modes are a combination of TE and TM modes. Therefore, we consider TE^x ($E_x^{\mathrm{TE}} = 0$) and TM^x ($H_x^{\mathrm{TM}} = 0$) modes to obtain the uncoupled scalar differential equations and take $\psi = E_y^{\mathrm{TE}},\ H_y^{\mathrm{TM}}$ to be the two independent field components. We obtain the differential equation for the TE^x modes as

$$\frac{\partial^2}{\partial y^2} E_y^{\mathrm{TE}} + \mu_x \frac{\varepsilon_z}{\varepsilon_y} \frac{\partial}{\partial x} \frac{1}{\mu_z} \frac{\partial}{\partial x} E_y^{\mathrm{TE}} + \mu_x \varepsilon_z E_y^{\mathrm{TE}} - \frac{\varepsilon_z}{\varepsilon_y} k_z^2 E_y^{\mathrm{TE}} = 0. \tag{6.5}$$

Similarly, we obtain the differential equation for the TM^x modes as

$$\frac{\partial^2}{\partial y^2} H_y^{\mathrm{TM}} + \varepsilon_x \frac{\mu_z}{\mu_y} \frac{\partial}{\partial x} \frac{1}{\varepsilon_z} \frac{\partial}{\partial x} H_y^{\mathrm{TM}} + \mu_z \varepsilon_x H_y^{\mathrm{TM}} - \frac{\mu_z}{\mu_y} k_z^2 H_y^{\mathrm{TM}} = 0. \tag{6.6}$$

We can calculate all the electric and magnetic field components with the following set of equations:

$$E_x = \frac{1}{k_z} \left(\frac{\partial}{\partial x} \frac{1}{\varepsilon_z} \frac{\partial}{\partial x} H_y^{\mathrm{TM}} + \mu_y H_y^{\mathrm{TM}} \right) \tag{6.7}$$

$$H_x = -\frac{1}{k_z} \left(\frac{\partial}{\partial x} \frac{1}{\mu_z} \frac{\partial}{\partial x} E_y^{\mathrm{TE}} + \varepsilon_y E_y^{\mathrm{TE}} \right) \tag{6.8}$$

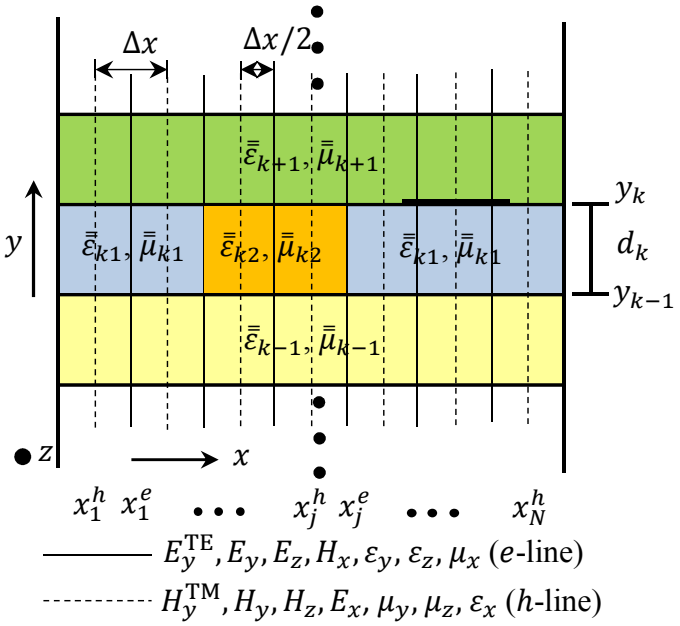

Figure 6.2: Discretization scheme for the waveguide structure with inhomogeneous dielectric layers.

$$E_z = -\frac{j}{k_z}\frac{\varepsilon_y}{\varepsilon_z}\frac{\partial}{\partial y}E_y^{\mathrm{TE}} - \frac{j}{\varepsilon_z}\frac{\partial}{\partial x}H_y^{\mathrm{TM}} \tag{6.9}$$

$$H_z = \frac{j}{\mu_z}\frac{\partial}{\partial x}E_y^{\mathrm{TE}} - \frac{j}{k_z}\frac{\mu_y}{\mu_z}\frac{\partial}{\partial y}H_y^{\mathrm{TM}} \tag{6.10}$$

$$E_y = E_y^{\mathrm{TE}} + \frac{1}{\varepsilon_z k_z}\frac{\partial}{\partial y}\frac{\partial}{\partial x}H_y^{\mathrm{TM}} \tag{6.11}$$

$$H_y = H_y^{\mathrm{TM}} - \frac{1}{\mu_z k_z}\frac{\partial}{\partial y}\frac{\partial}{\partial x}E_y^{\mathrm{TE}}. \tag{6.12}$$

6.1.2 The Discrete Mode Matching Method

We consider that the transmission lines are infinite in the propagation direction. Therefore, the method employs only 1D discretization along the horizontal tangential direction (x-axis) for the analysis and takes the analytical solution in the perpendicular direction (y-axis). The structure is discretized using e- and h-lines, which give the position of E_y^{TE} and H_y^{TM}, respectively. Fig. 6.2 shows the equidistant discretization scheme used for the inhomogeneous dielectric layers bounded with electric walls. We take the distance between the edge of the metallization and the e-line to be $0.25\Delta x$. We can relate the spatial domain field components in the spectral domain using the relation in matrix form

$$\boldsymbol{\psi} = \boldsymbol{T}\boldsymbol{S}\widetilde{\boldsymbol{\psi}} \tag{6.13}$$

or we write

$$\boldsymbol{E}_y^{\mathrm{TE}} = \boldsymbol{T}_e\boldsymbol{S}_e\widetilde{\boldsymbol{E}}_y^{\mathrm{TE}} \tag{6.14}$$

$$\boldsymbol{H}_y^{\mathrm{TM}} = \boldsymbol{T}_h\boldsymbol{S}_h\widetilde{\boldsymbol{H}}_y^{\mathrm{TM}}. \tag{6.15}$$

Here $\widetilde{\boldsymbol{\psi}}$ represents the column matrix of the independent field components in spectral domain containing all the modal values, $\boldsymbol{\psi}$ represents the column matrix of the independent field components in spatial domain, $\boldsymbol{T}_{e,h}$ gives the transformation matrices and $\boldsymbol{S}_{e,h}$ denotes additional matrices which account for inhomogeneity in the dielectric layer (subscript e is for e-lines and subscript h is for h-lines). We calculate the transformation matrices depending on the conditions used to bound the lateral domain which consists of eigensolutions with exact eigenvalues as mentioned in Chapter 2.

We can easily identify the locations of the other field components with the help of the field relations (6.7)-(6.10). Fig. 6.2 describes the positions of all the field components and material properties. Therefore, the relation of the other field components between the spatial domain and the spectral domain in matrix form can be summarized as

$$\boldsymbol{E}_x = \boldsymbol{T}_h \widetilde{\boldsymbol{E}}_x \tag{6.16}$$

$$\boldsymbol{E}_y = \boldsymbol{T}_e \widetilde{\boldsymbol{E}}_y \tag{6.17}$$

$$\boldsymbol{E}_z = \boldsymbol{T}_e \widetilde{\boldsymbol{E}}_y \tag{6.18}$$

$$\boldsymbol{H}_x = \boldsymbol{T}_e \widetilde{\boldsymbol{H}}_x \tag{6.19}$$

$$\boldsymbol{H}_y = \boldsymbol{T}_h \widetilde{\boldsymbol{H}}_y \tag{6.20}$$

$$\boldsymbol{H}_z = \boldsymbol{T}_h \widetilde{\boldsymbol{H}}_z. \tag{6.21}$$

On using the continuity equation of magnetic fields on the interface, we get the relation for the current densities as

$$\boldsymbol{J}_x = \boldsymbol{T}_h \widetilde{\boldsymbol{J}}_x \tag{6.22}$$

$$\boldsymbol{J}_z = \boldsymbol{T}_e \widetilde{\boldsymbol{J}}_z. \tag{6.23}$$

The discontinuities in layer k are aligned with the e-lines, therefore the material properties on these lines change accordingly:

$$\varepsilon_y = \frac{\varepsilon_{y1} + \varepsilon_{y2}}{2} \tag{6.24}$$

$$\varepsilon_z = \frac{\varepsilon_{z1} + \varepsilon_{z2}}{2} \tag{6.25}$$

$$\mu_x = \frac{\mu_{x1} + \mu_{x2}}{2}. \tag{6.26}$$

The reason for taking the arithmetic mean of the material properties at the discontinuities is well explained in [Pregla et al., 1987]. Due to inhomogeneity in the dielectric layer, we get the diagonal matrix of varying material properties along the discretization in x-direction. These matrices can be converted into spectral domain using the relation

$$\bar{\boldsymbol{\varepsilon}}_{e,h} = \boldsymbol{T}_{e,h}^{-1} \boldsymbol{\varepsilon}_{e,h} \boldsymbol{T}_{e,h} \tag{6.27}$$

$$\bar{\boldsymbol{\mu}}_{e,h} = \boldsymbol{T}_{e,h}^{-1} \boldsymbol{\mu}_{e,h} \boldsymbol{T}_{e,h}. \tag{6.28}$$

On transforming (6.5) and (6.6) using (6.13), we get the relations

$$\boldsymbol{Q}_e = \bar{\boldsymbol{\mu}}_{xe} \bar{\boldsymbol{\varepsilon}}_{ze} \bar{\boldsymbol{\varepsilon}}_{ye}^{-1} \boldsymbol{k}_x \bar{\boldsymbol{\mu}}_{zh}^{-1} \boldsymbol{k}_x - \bar{\boldsymbol{\mu}}_{xe} \bar{\boldsymbol{\varepsilon}}_{ze} + \bar{\boldsymbol{\varepsilon}}_{ze} \bar{\boldsymbol{\varepsilon}}_{ye}^{-1} k_z^2, \tag{6.29}$$

$$\boldsymbol{Q}_h = \bar{\boldsymbol{\varepsilon}}_{xh} \bar{\boldsymbol{\mu}}_{zh} \bar{\boldsymbol{\mu}}_{yh}^{-1} \boldsymbol{k}_x \bar{\boldsymbol{\varepsilon}}_{ze}^{-1} \boldsymbol{k}_x - \bar{\boldsymbol{\mu}}_{zh} \bar{\boldsymbol{\varepsilon}}_{xh} + \bar{\boldsymbol{\mu}}_{zh} \bar{\boldsymbol{\mu}}_{yh}^{-1} k_z^2, \tag{6.30}$$

where $\boldsymbol{k}_x$ denotes the eigenvalues.

Now, there is a need to solve the eigenvalue problems

$$\boldsymbol{Q}_e\boldsymbol{S}_e = \boldsymbol{S}_e\boldsymbol{k}_{ye}^2 \text{ and } \boldsymbol{Q}_h\boldsymbol{S}_h = \boldsymbol{S}_h\boldsymbol{k}_{yh}^2, \tag{6.31}$$

to obtain the ordinary differential equation

$$\left(\frac{d^2}{dy^2} - \boldsymbol{k}_{ye,h}^2\right)\widetilde{\boldsymbol{\psi}}_{e,h} = 0. \tag{6.32}$$

On solving the separated equation (6.32), we get the solution within the arbitrary layer k as

$$\widetilde{\boldsymbol{E}}_{y_k}^{\mathrm{TE}} = \boldsymbol{A}_k e^{-\boldsymbol{k}_{ye_k}y} + \boldsymbol{B}e^{\boldsymbol{k}_{ye_k}y}, \tag{6.33a}$$

$$\widetilde{\boldsymbol{H}}_{y_k}^{\mathrm{TM}} = \boldsymbol{C}_k e^{-\boldsymbol{k}_{yh_k}y} + \boldsymbol{D}_k e^{\boldsymbol{k}_{yh_k}y}. \tag{6.33b}$$

After discretizing the structure and transforming the field components (6.7)-(6.10) according to (6.14)-(6.21), we get the tangential field components in spectral domain as

$$\widetilde{\boldsymbol{E}}_x = \frac{1}{k_z}\left((-j\boldsymbol{k}_x)\bar{\boldsymbol{\varepsilon}}_{ze}^{-1}(-j\boldsymbol{k}_x) + \bar{\boldsymbol{\mu}}_{yh}\right)\boldsymbol{S}_h\widetilde{\boldsymbol{H}}_y^{\mathrm{TM}} \tag{6.34}$$

$$\widetilde{\boldsymbol{H}}_x = -\frac{1}{k_z}\left((-j\boldsymbol{k}_x)\bar{\boldsymbol{\mu}}_{zh}^{-1}(-j\boldsymbol{k}_x) + \bar{\boldsymbol{\varepsilon}}_{ye}\right)\boldsymbol{S}_e\widetilde{\boldsymbol{E}}_y^{\mathrm{TE}} \tag{6.35}$$

$$\widetilde{\boldsymbol{E}}_z = -\frac{j}{k_z}\bar{\boldsymbol{\varepsilon}}_{ye}\bar{\boldsymbol{\varepsilon}}_{ze}^{-1}\frac{\partial}{\partial y}\boldsymbol{S}_e\widetilde{\boldsymbol{E}}_y^{\mathrm{TE}} - j\bar{\boldsymbol{\varepsilon}}_{ze}^{-1}(-j\boldsymbol{k}_x)\boldsymbol{S}_h\widetilde{\boldsymbol{H}}_y^{\mathrm{TM}} \tag{6.36}$$

$$\widetilde{\boldsymbol{H}}_z = j\bar{\boldsymbol{\mu}}_{zh}^{-1}(-j\boldsymbol{k}_x)\boldsymbol{S}_e\widetilde{\boldsymbol{E}}_y^{\mathrm{TE}} - \frac{j}{k_z}\bar{\boldsymbol{\mu}}_{yh}\bar{\boldsymbol{\mu}}_{zh}^{-1}\frac{\partial}{\partial y}\boldsymbol{S}_h\widetilde{\boldsymbol{H}}_y^{\mathrm{TM}}. \tag{6.37}$$

On using (6.33a)-(6.37), we rewrite the tangential field components for the layer k in matrix form as

$$\begin{bmatrix}\widetilde{\boldsymbol{E}}_{x_k}\\ \widetilde{\boldsymbol{H}}_{x_k}\\ \widetilde{\boldsymbol{E}}_{z_k}\\ \widetilde{\boldsymbol{H}}_{z_k}\end{bmatrix} = \begin{bmatrix}\widetilde{\boldsymbol{Q}}_{x_k}^A & \widetilde{\boldsymbol{Q}}_{x_k}^B & \widetilde{\boldsymbol{Q}}_{x_k}^C & \widetilde{\boldsymbol{Q}}_{x_k}^D\\ \widetilde{\boldsymbol{G}}_{x_k}^A & \widetilde{\boldsymbol{G}}_{x_k}^B & \widetilde{\boldsymbol{G}}_{x_k}^C & \widetilde{\boldsymbol{G}}_{x_k}^D\\ \widetilde{\boldsymbol{Q}}_{z_k}^A & \widetilde{\boldsymbol{Q}}_{z_k}^B & \widetilde{\boldsymbol{Q}}_{z_k}^C & \widetilde{\boldsymbol{Q}}_{z_k}^D\\ \widetilde{\boldsymbol{G}}_{z_k}^A & \widetilde{\boldsymbol{G}}_{z_k}^B & \widetilde{\boldsymbol{G}}_{z_k}^C & \widetilde{\boldsymbol{G}}_{z_k}^D\end{bmatrix}\begin{bmatrix}\boldsymbol{A}_k\\ \boldsymbol{B}_k\\ \boldsymbol{C}_k\\ \boldsymbol{D}_k\end{bmatrix}. \tag{6.38}$$

Now to obtain the relation between the fields at the interfaces $k-1$ and k bounding the layer k, we write

$$\begin{bmatrix}\widetilde{\boldsymbol{E}}_{k-1}\\ \widetilde{\boldsymbol{H}}_{k-1}\end{bmatrix} = \widetilde{\boldsymbol{M}}_{k-1}\boldsymbol{F}, \quad \begin{bmatrix}\widetilde{\boldsymbol{E}}_k\\ \widetilde{\boldsymbol{H}}_k\end{bmatrix} = \widetilde{\boldsymbol{M}}_k\boldsymbol{F}, \tag{6.39}$$

$$\widetilde{\boldsymbol{M}}_k = \begin{bmatrix}\widetilde{\boldsymbol{Q}}_{x_k}^A & \widetilde{\boldsymbol{Q}}_{x_k}^B & \widetilde{\boldsymbol{Q}}_{x_k}^C & \widetilde{\boldsymbol{Q}}_{x_k}^D\\ \widetilde{\boldsymbol{Q}}_{z_k}^A & \widetilde{\boldsymbol{Q}}_{z_k}^B & \widetilde{\boldsymbol{Q}}_{z_k}^C & \widetilde{\boldsymbol{Q}}_{z_k}^D\\ \widetilde{\boldsymbol{G}}_{z_k}^A & \widetilde{\boldsymbol{G}}_{z_k}^B & \widetilde{\boldsymbol{G}}_{z_k}^C & \widetilde{\boldsymbol{G}}_{z_k}^D\\ -\widetilde{\boldsymbol{G}}_{x_k}^A & -\widetilde{\boldsymbol{G}}_{x_k}^B & -\widetilde{\boldsymbol{G}}_{x_k}^C & -\widetilde{\boldsymbol{G}}_{x_k}^D\end{bmatrix}, \tag{6.40}$$

and take the notation of the fields and coefficients in matrix form as

$$\widetilde{\boldsymbol{E}}_k = \begin{bmatrix} \widetilde{\boldsymbol{E}}_{x_k} \\ \widetilde{\boldsymbol{E}}_{z_k} \end{bmatrix}, \; \widetilde{\boldsymbol{H}}_k = \begin{bmatrix} \widetilde{\boldsymbol{H}}_{z_k} \\ -\widetilde{\boldsymbol{H}}_{x_k} \end{bmatrix}, \; \boldsymbol{F} = \begin{bmatrix} \boldsymbol{A}_k \\ \boldsymbol{B}_k \\ \boldsymbol{C}_k \\ \boldsymbol{D}_k \end{bmatrix}. \tag{6.41}$$

On eliminating the unknown column matrix $\boldsymbol{F}$ from (6.39), we get the relation for the field components at the interfaces of the layer k with normalized thickness d_k as

$$\begin{bmatrix} \widetilde{\boldsymbol{E}}_{k-1} \\ \widetilde{\boldsymbol{H}}_{k-1} \end{bmatrix} = \widetilde{\boldsymbol{K}}_k \begin{bmatrix} \widetilde{\boldsymbol{E}}_k \\ \widetilde{\boldsymbol{H}}_k \end{bmatrix}, \tag{6.42}$$

with the hybrid matrix

$$\widetilde{\boldsymbol{K}}_k = \widetilde{\boldsymbol{M}}_{k-1} \widetilde{\boldsymbol{M}}_k^{-1} = \begin{bmatrix} \widetilde{\boldsymbol{V}}_k & \widetilde{\boldsymbol{Z}}_k \\ \widetilde{\boldsymbol{Y}}_k & \widetilde{\boldsymbol{B}}_k \end{bmatrix}. \tag{6.43}$$

We can take into account the multiple dielectric layers by simple matrix multiplication. After getting hybrid matrices for each layer, we must apply continuity equations to match the fields at the interfaces. Then the Green's function ($\widetilde{\boldsymbol{G}}$) can be found in spectral domain after applying the theory of full-wave equivalent circuit and network analysis technique according to [Kamra and Dreher, 2018d]. The system equation takes the form

$$\widetilde{\boldsymbol{G}} \widetilde{\boldsymbol{J}} = \widetilde{\boldsymbol{E}}, \tag{6.44}$$

where $\widetilde{\boldsymbol{J}}$ and $\widetilde{\boldsymbol{E}}$ represent surface current density and electric field in the interfaces respectively. By applying the boundary conditions at the interface in the waveguides, we can write $\widetilde{\boldsymbol{J}} = 0$. Therefore, the propagation constant can be found on solving the indirect eigenvalue problem

$$\det(\widetilde{\boldsymbol{L}}) = 0 \quad \text{where} \quad \widetilde{\boldsymbol{L}} = \widetilde{\boldsymbol{G}}^{-1}. \tag{6.45}$$

6.1.2.1 Interface with Metallization

Now consider the case when metallization is present on the interfaces of the structure. We take the metallization to be infinitely thin. The system matrix with several metallized interfaces (M) can be represented by (2.43). After that, we transform the field components and current densities in (6.44) into the spatial domain using (6.16)-(6.23) and get

$$\begin{bmatrix} \boldsymbol{G}_{xx} & \boldsymbol{G}_{xz} \\ \boldsymbol{G}_{zx} & \boldsymbol{G}_{zz} \end{bmatrix} \begin{bmatrix} \boldsymbol{J}_x \\ \boldsymbol{J}_z \end{bmatrix} = \begin{bmatrix} \boldsymbol{E}_x \\ \boldsymbol{E}_z \end{bmatrix} \quad \text{or} \quad \boldsymbol{G}\boldsymbol{J} = \boldsymbol{E} \tag{6.46}$$

where

$$\begin{bmatrix} \boldsymbol{G}_{xx} & \boldsymbol{G}_{xz} \\ \boldsymbol{G}_{zx} & \boldsymbol{G}_{zz} \end{bmatrix} = \begin{bmatrix} \boldsymbol{T}_h & 0 \\ 0 & \boldsymbol{T}_e \end{bmatrix} \begin{bmatrix} \widetilde{\boldsymbol{G}}_{xx} & \widetilde{\boldsymbol{G}}_{xz} \\ \widetilde{\boldsymbol{G}}_{zx} & \widetilde{\boldsymbol{G}}_{zz} \end{bmatrix} \begin{bmatrix} \boldsymbol{T}_h^{-1} & 0 \\ 0 & \boldsymbol{T}_e^{-1} \end{bmatrix}. \tag{6.47}$$

Here $\boldsymbol{G} = \boldsymbol{L}^{-1}$ denotes the Green's function in spatial domain.

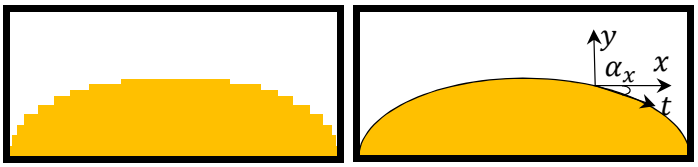

Figure 6.3: Waveguide with quasi-planar interface.

After obtaining the system equation, the boundary conditions must be applied. The conditions state that the tangential electric field components must vanish on the metallizations and the electric currents outside that region. We obtain the reduced system equation as

$$\boldsymbol{G}_{\text{red}}\boldsymbol{J}_{\text{red}} = 0 \qquad \text{or} \qquad \boldsymbol{L}_{\text{red}}\boldsymbol{E}_{\text{red}} = 0, \tag{6.48}$$

where $\boldsymbol{J}_{\text{red}}$ contains the tangential surface current density components located on the metallizations, while $\boldsymbol{E}_{\text{red}}$ contains the tangential electric field components located outside the metallization. We can solve it as an indirect eigenvalue problem

$$\det(\boldsymbol{G}_{\text{red}}) = 0 \qquad \text{or} \qquad \det(\boldsymbol{L}_{\text{red}}) = 0 \tag{6.49}$$

to find the propagation constants for the transmission lines with metallization in the interfaces. $\boldsymbol{L}_{\text{red}}$ is equivalent to $\boldsymbol{L}$ in waveguides, as there are no currents on the interfaces.

6.1.2.2 Quasi-planar Interface

When the interfaces between the layers are not constant according to the coordinate system then there are two ways to deal with such types of problems. One way is to divide the non-planar dielectric layer into several layers with changing rib width as shown in Fig. 6.3a. This will lead us to deal with inhomogeneous layers which has been explained in earlier sections. The other way is to calculate tangential field components at the actual interface as shown in Fig. 6.3b.

In the second way we deal with non-planar interfaces within the dielectric, therefore the whole analysis should be done in spatial domain. We assume that the quasi planar nature of the layers at the interfaces is in x-direction and the cross-section is constant in z-direction. We need to calculate the tangential field components at the interfaces. In this case, the components no longer remain in the x-direction as in the previous case, but E_z and H_z are tangential to the interfaces along the whole x-direction. Therefore the other tangential fields become E_{tx} and H_{tx} and are represented as

$$E_{tx_k} = E_{x_k}\cos\alpha_{x^h} + \bar{E}_{y_k}\sin\alpha_{x^h}, \tag{6.50a}$$
$$H_{tx_k} = H_{x_k}\cos\alpha_{x^e} + \bar{H}_{y_k}\sin\alpha_{x^e}. \tag{6.50b}$$

Here $\alpha_{x^{(e,h)}}$ represents the inclination angle at the interface with the x-axis. From Fig. 6.2, we can say that for 1D discretization E_y^{TE}, E_z, E_y and H_x (or H_y^{TM}, H_z, H_y and E_x) components are sampled at the same position. To determine E_{tx}, we must calculate E_x and E_y at the same point. Therefore, $\bar{E}_y$ is used in (6.50a) which is the mean of the adjacent sampled values of E_y. Similarly, $\bar{H}_y$ is calculated from the mean of the adjacent values of

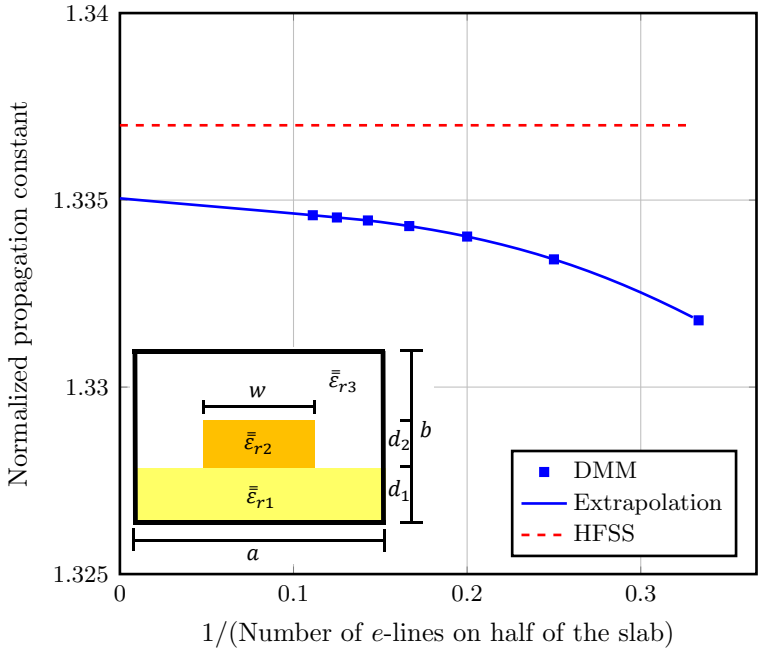

Figure 6.4: Convergence behavior of normalized propagation constant for rib waveguide.

H_y. Then, (6.41) changes according to

$$\boldsymbol{E}_k = \begin{bmatrix} \boldsymbol{E}_{tx_k} \\ \boldsymbol{E}_{z_k} \end{bmatrix}, \quad \boldsymbol{H}_k = \begin{bmatrix} \boldsymbol{H}_{z_k} \\ -\boldsymbol{H}_{tx_k} \end{bmatrix}. \tag{6.51}$$

6.2 Numerical Results

6.2.1 Convergence for Rib Waveguide

First, we have taken the rib waveguide, shown in the inset of Fig 6.4, for the analysis. It is widely used for optical communication. We have analyzed the waveguide with $\varepsilon_{r1} = 1.5$, $\varepsilon_{r2} = 3.8$, $\varepsilon_{r3} = 1$, $a/d_2 = 13.5$, $b/d_2 = 8$, $d_1/d_2 = 0.5$ and $d_2 = 1.5$. The two bottom layers are combined together and the resultant hybrid matrix is obtained as

$$\widetilde{\boldsymbol{K}}_{eq} = \widetilde{\boldsymbol{K}}_1 \widetilde{\boldsymbol{K}}_2 = \begin{bmatrix} \widetilde{\boldsymbol{V}}_{eq} & \widetilde{\boldsymbol{Z}}_{eq} \\ \widetilde{\boldsymbol{Y}}_{eq} & \widetilde{\boldsymbol{B}}_{eq} \end{bmatrix}. \tag{6.52}$$

From network analysis techniques, we simply obtain the system equation as

$$\widetilde{\boldsymbol{L}}\widetilde{\boldsymbol{E}} = 0, \text{ where } \widetilde{\boldsymbol{L}} = \widetilde{\boldsymbol{Z}}_{eq}^{-1}\widetilde{\boldsymbol{V}}_{eq} + \widetilde{\boldsymbol{B}}_3\widetilde{\boldsymbol{Z}}_3^{-1}. \tag{6.53}$$

The first term of the admittance ($\widetilde{\boldsymbol{Z}}_{eq}^{-1}\widetilde{\boldsymbol{V}}_{eq}$) denotes the admittance of the grounded bottom layer and the second term ($\widetilde{\boldsymbol{B}}_3\widetilde{\boldsymbol{Z}}_3^{-1}$) denotes the admittance of the closed top layer.

Fig. 6.4 shows the convergence of the propagation constant (normalized by k_0) of the fundamental mode with increasing number of e-lines used for discretization of half of the

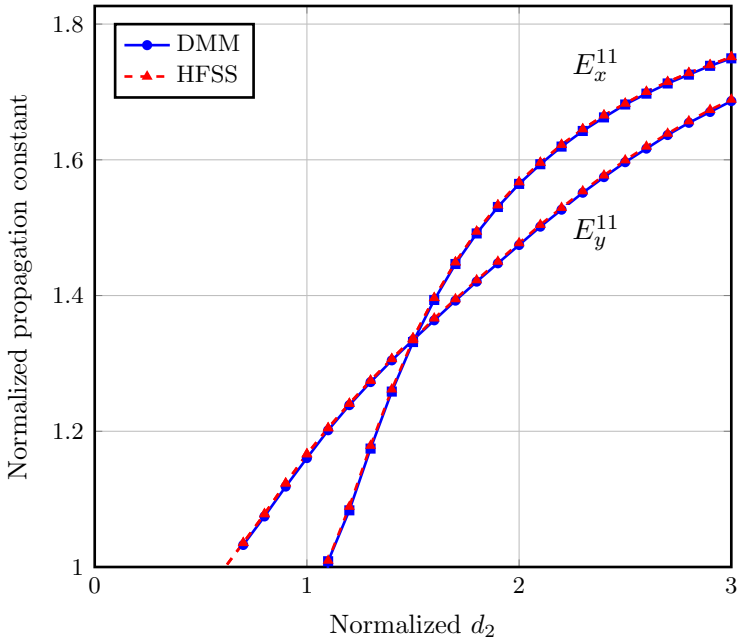

Figure 6.5: Dispersion curve for rib waveguide.

slab with ε_{r2}. The increase in the discretization lines is equivalent to the increasing number of modes used for the field expansion due to the Nyquist–Shannon sampling theorem. We have computed the values for up to 9 e-lines because the results do not vary much with increment in discretization lines after a certain limit. We can see from the figure that the results with 7, 8 and 9 e-lines are very close to each other and within a small number of discretization lines we can reach a high level of accuracy. An extrapolation to the exact value given by an infinite number of lines and modes (1/(Number of e-lines) $\rightarrow$ 0) is also possible. Therefore there is no need to do very fine discretization of the structure which saves our memory and time.

Fig. 6.5 shows the dispersion curve for two fundamental modes of the same rib waveguide over normalized d_2. We have validated the results with the predicted results from ANSYS HFSS. The results also agree well with the results presented in [Pregla et al., 1987] for MoL and finite difference technique. Fig. 6.6 shows the variation of the electric field along the horizontal direction at various heights of the waveguide cross-section. It shows that the field is concentrated mainly over the rib region and is maximum below the rib.

6.2.2 Lossy Anisotropic Image Waveguide

We have then applied the DMM formulation on a shielded lossy anisotropic image waveguide, as shown in Fig. 6.7a. We have analyzed only half of the structure by placing a magnetic wall along the centre due to symmetry. The relative permittivities of the dielectric structure are $\varepsilon_{x1} = \varepsilon_{z1} = 1.5 - j1.5$, $\varepsilon_{y1} = \varepsilon'_{y1} - j1.5$ (where $\varepsilon'_{y1} = 1, 1.5$ or 2) and $\varepsilon_{r2} = 1$. The system equation of the structure becomes same as the two-layer waveguide, which is

$$\left(\widetilde{\boldsymbol{Z}}_1^{-1}\widetilde{\boldsymbol{V}}_1 + \widetilde{\boldsymbol{B}}_2\widetilde{\boldsymbol{Z}}_2^{-1}\right)\widetilde{\boldsymbol{E}}_1 = 0. \tag{6.54}$$

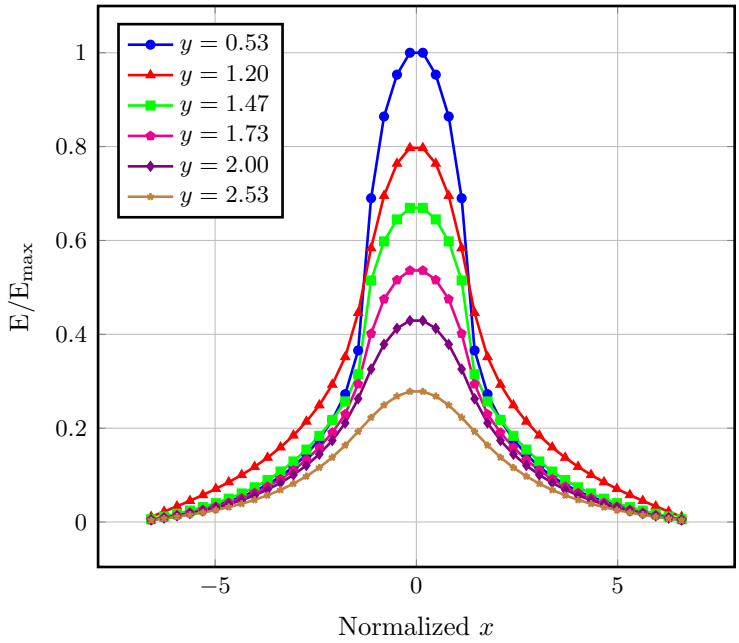

Figure 6.6: Normalized electric field variation along x-direction in rib waveguide ($d_2 = 1$).

Fig. 6.7 shows the obtained attenuation and phase constant (normalized by k_0) for E_y^{11} mode from the DMM method with only 5 e-lines placed on the inner slab of the structure. It also compares the results with different numerical techniques, i.e., FEM [Lu and Fernandez, 1993] and MoL [Berini and Wu, 1996], and shows good agreement with them. The MATLAB simulation was done on an Intel i7-6600U CPU @2.6 GHz processor and took 0.3 to 0.5 seconds to compute the propagation constants at each b-point.

6.2.3 Anisotropic Dielectric Waveguide

Second, we have analyzed the open dielectric waveguide, as shown in Fig. 6.8. We can enclose the computational domain with absorbing boundary conditions (ABCs) or electric walls placed at far distance from the guide. Here we have considered the waveguide to be bounded by ABC walls with a distance of $6b$ in the lateral sides and open from both top and bottom sides. We have calculated the required eigenvalues using Higdon's operator. We can divide the structure into 3 layers, i.e., 0, 1, 2, where 0^{th} and 2^{nd} layers are with ε_{r2} and 1^{st} layer is with $\bar{\bar{\varepsilon}}_{r1}$. From network analysis technique, we simply obtain the system equation as

$$\left((\widetilde{\boldsymbol{B}}_1 + \widetilde{\boldsymbol{Y}}_0\widetilde{\boldsymbol{Z}}_1)^{-1}(\widetilde{\boldsymbol{Y_0}}\widetilde{\boldsymbol{V_1}} + \widetilde{\boldsymbol{Y}}_1) + \widetilde{\boldsymbol{Y}}_2\right)\widetilde{\boldsymbol{E}}_1 = 0. \tag{6.55}$$

The relative permittivities of the structure are $\bar{\bar{\varepsilon}}_{r1} = (2.31, 2.19, 2.31)$ and $\varepsilon_{r2} = 2.05$. The normalized electric field distribution of the E_x^{11} mode at normalized $b = 4$ is presented in Fig. 6.9. We can see from Fig. 6.8 that the computed results from DMM agree well with fourier decomposition [Pashaie, 2007], MoL and FEM.

6.2.4 $LiNbO_3$ Optical Waveguide

Next, we have taken the $LiNbO_3$ anisotropic optical waveguide. We have analyzed only half of the structure by placing a vertical magnetic wall along the centre. The material properties

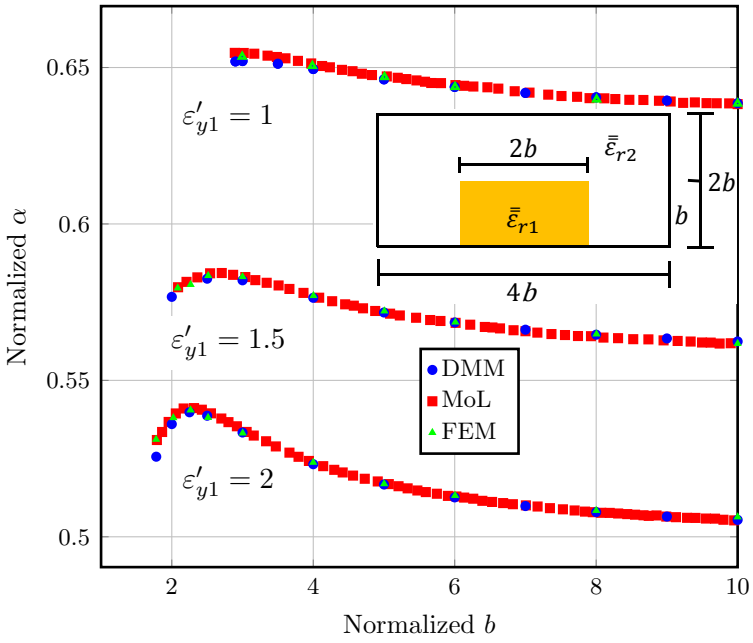

(a)

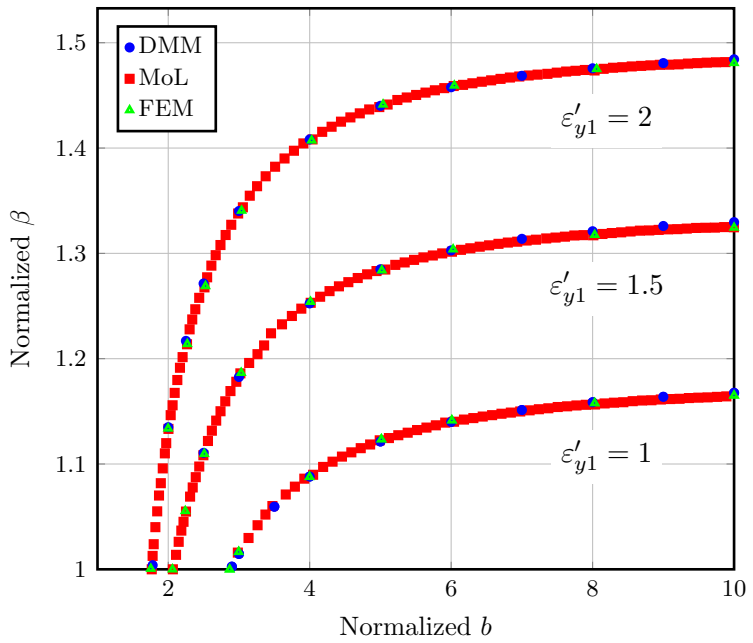

(b)

Figure 6.7: Dispersion characteristics of the lossy image waveguide as illustrated: (a) Normalized attenuation constant, (b) Normalized phase constant.

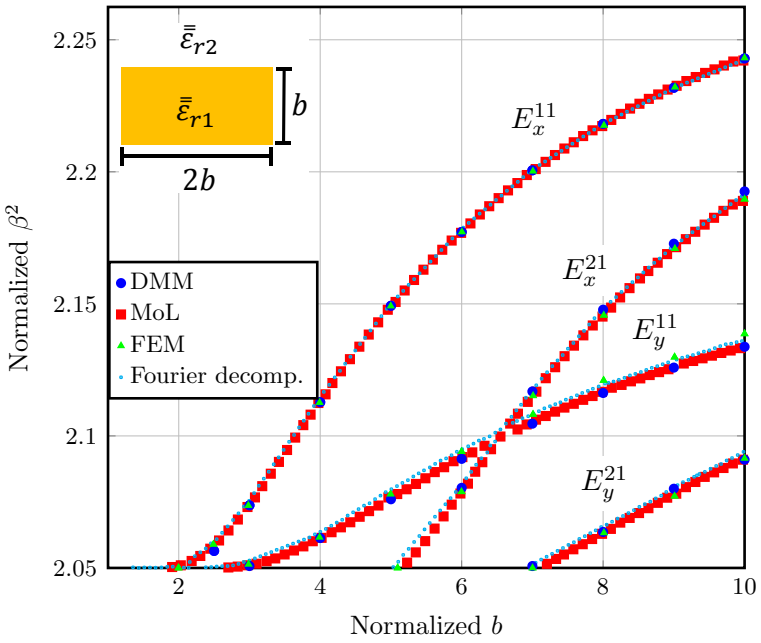

Figure 6.8: Normalized dispersion characteristics of the illustrated anisotropic dielectric waveguide.

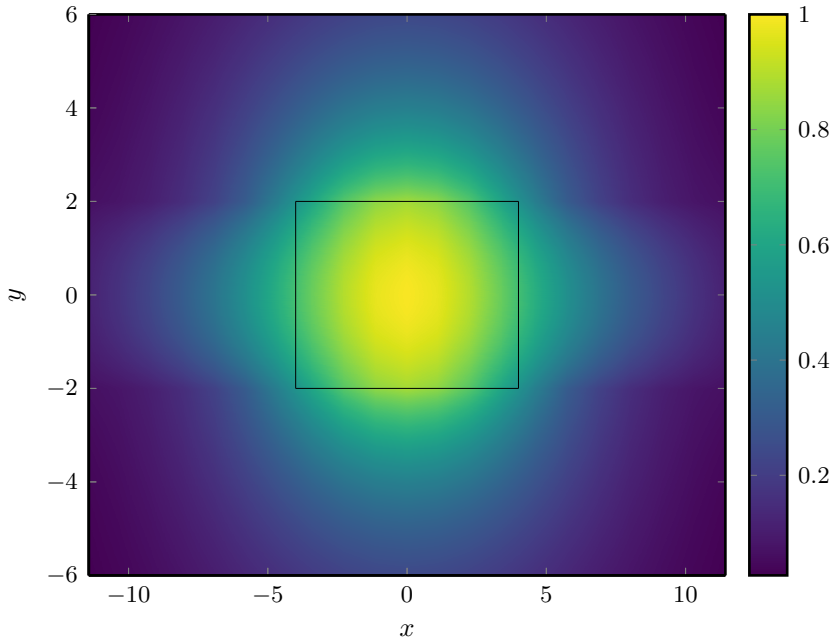

Figure 6.9: Normalized electric field distribution of the first mode in the anisotropic dielectric waveguide for $b = 4$.

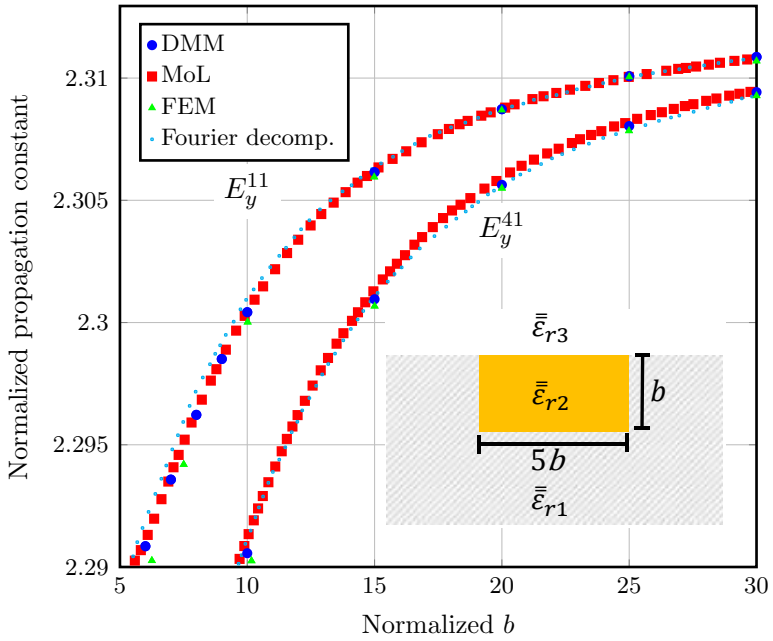

Figure 6.10: Normalized dispersion characteristics of the illustrated optical waveguide.

of the structure are $\bar{\bar{\varepsilon}}_{r1} = ((2.2)^2, (2.29)^2, (2.29)^2)$, $\bar{\bar{\varepsilon}}_{r2} = ((2.22)^2, (2.3129)^2, (2.3129)^2)$ and $\varepsilon_{r3} = 1$. Fig. 6.10 depicts the structure of the optical waveguide, which is open from the top and bottom both. Therefore, we get a similar system equation as in the case of the anisotropic dielectric waveguide (6.55).

The figure presents the normalized propagation constants of the guided modes E_y^{11} and E_y^{41} and validates the DMM results with the results from other methods.

6.2.5 Effect of Anisotropy in Dielectric Waveguide

Then we have taken a case study, where we have examined the effect of different permittivity and permeability tensors on the dielectric waveguide as given in Table 6.1. The background material has the relative permittivity $\varepsilon_{r2} = 2$ and the relative permeability $\mu_{r2} = 1$. We have done the analysis for two guided modes, i.e., E_x^{11} and E_y^{11}. Fig. 6.11 gives the dispersion curves and shows the good agreement between the obtained results from DMM and the results from other literature.

Table 6.1: Material tensors for the structure shown in Fig. 6.11.

	Case 1	**Case 2**	**Case 3**
$\bar{\bar{\varepsilon}}_{r1}$	$\varepsilon_{x1} = 2.6$	$\varepsilon_{x1} = 2.4$	$\varepsilon_{x1} = 2.8$
	$\varepsilon_{y1} = 2.6$	$\varepsilon_{y1} = 2.8$	$\varepsilon_{y1} = 2.4$
	$\varepsilon_{z1} = 2.6$	$\varepsilon_{z1} = 2.6$	$\varepsilon_{z1} = 2.6$
$\bar{\bar{\mu}}_{r1}$	$\mu_{x1} = 1.10$	$\mu_{x1} = 1.15$	$\mu_{x1} = 1.05$
	$\mu_{y1} = 1.10$	$\mu_{y1} = 1.05$	$\mu_{y1} = 1.15$
	$\mu_{z1} = 1.10$	$\mu_{z1} = 1.10$	$\mu_{z1} = 1.10$

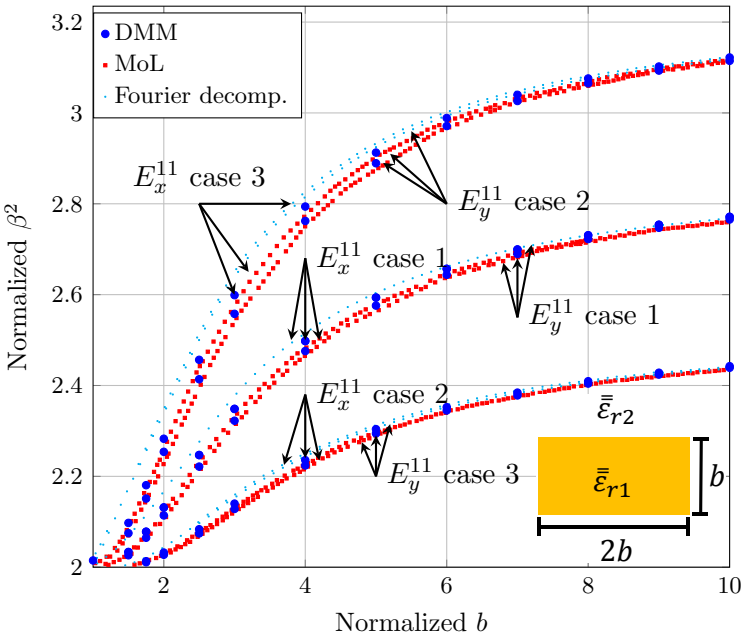

Figure 6.11: Normalized dispersion characteristics of the illustrated dielectric waveguide with different material tensors.

6.2.6 Hybrid Waveguide

To understand the coupling between the microstrip and the dielectric waveguide, we have examined the hybrid waveguide which consists of an inhomogeneous dielectric waveguide with microstrip, as shown in Fig. 6.12. The analysis gives the results for the coupled waveguide and microstrip (CG) when we move the dielectric slab from the side wall to the center. We have also computed the results for the dielectric waveguide without microstrip (WG), and microstrip line without dielectric slab with $\bar{\bar{\varepsilon}}_{r3}$ (MS). We can divide the structure into four dielectric layers with three homogeneous layers and one inhomogeneous layer. The system matrix obtained for the coupled hybrid waveguide is

$$\left(\widetilde{\boldsymbol{Z}}_{eq_d}^{-1}\widetilde{\boldsymbol{V}}_{eq_d} + \widetilde{\boldsymbol{B}}_{eq_u}\widetilde{\boldsymbol{Z}}_{eq_u}^{-1}\right)\widetilde{\boldsymbol{E}}_m = \widetilde{\boldsymbol{J}}_m, \tag{6.56}$$

where

$$\widetilde{\boldsymbol{K}}_{eq_d} = \widetilde{\boldsymbol{K}}_1\widetilde{\boldsymbol{K}}_2 \qquad \text{and} \qquad \widetilde{\boldsymbol{K}}_{eq_u} = \widetilde{\boldsymbol{K}}_3\widetilde{\boldsymbol{K}}_4 \tag{6.57}$$

and $\widetilde{\boldsymbol{E}}_m$ and $\widetilde{\boldsymbol{J}}_m$ denote the electric field distribution and surface current density, respectively, over the interface with metallization.

Fig. 6.13 and 6.14 show the effective dielectric constants with respect to the shift between microstrip and dielectric slab for isotropic and anisotropic dielectric layers, respectively. The data used for the analysis are $\varepsilon_{r1} = 1$, $\bar{\bar{\varepsilon}}_{r2} = 9.6$ or (9.6, 9, 9.6), $\bar{\bar{\varepsilon}}_{r3} = 16$ or (16, 15, 16), $\varepsilon_{r4} = 1$, $a = 7.112$ mm, $w = 1.6$ mm, $t = 1.422$ mm and $d_1 = d_2 = d_3 = d_4 = 0.729$ mm. The computation was done at 30 GHz frequency and with 5 e-lines on the strip. The DMM results agree well with the results obtained from the ANSYS HFSS for both isotropic and anisotropic medium. The isotropic results also validate with the results from the method of lines presented in [Pregla et al., 1987].

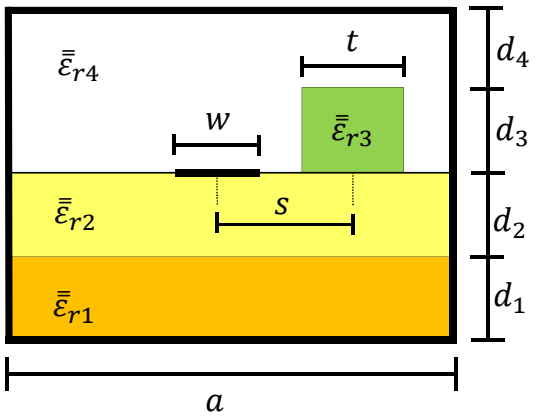

Figure 6.12: Coupled microstrip and dielectric waveguide.

The simulation for the coupled dielectric waveguide and microstrip at $s/a = -0.05$ using the DMM formulation took around 1 second and HFSS took 17 seconds with port mode calculation.

6.2.7 Comparison between Waveguides with Different Interfaces

Next, we have done a comparison between the results obtained from different kinds of shielded waveguides. We have analyzed the conventional two-layer homogeneous dielectric waveguide, the quasi-planar waveguide with varying interface and the rib waveguide, as shown in Fig. 6.15.

Again, we have considered only half of the structure for the analysis by placing a magnetic wall along the center due to symmetry. The material properties of the structure are $\bar{\bar{\varepsilon}}_{r1} = 1.5$ or (1.5, 2, 1), $\varepsilon_{r2} = 1$ and $\mu_{r1} = \mu_{r2} = 1$. The structure has width $4b$ and height $2b$. The width of the rib is taken to be $2b$. For a quasi-planar waveguide, we can use any equation which can determine the shape of the interface. Here, we have used the function

$$f(x) = 0.001b + (0.999d/(1 + \exp(B(x - A)))), \tag{6.58}$$

with $A = (x_1 + x_2)/2$, $B = 2/|x_1 - x_2|$, $x_1 = 0.95b$ and $x_2 = 1.2b$.

Fig. 6.16 and 6.17 give the normalized propagation constants computed from DMM with varying value of normalized b. The figures also compare the DMM results with the results obtained from HFSS. They show very good agreement between the results. It is clear from the figures that the results from the quasi-planar interface very well approximate the results from the rib structure.

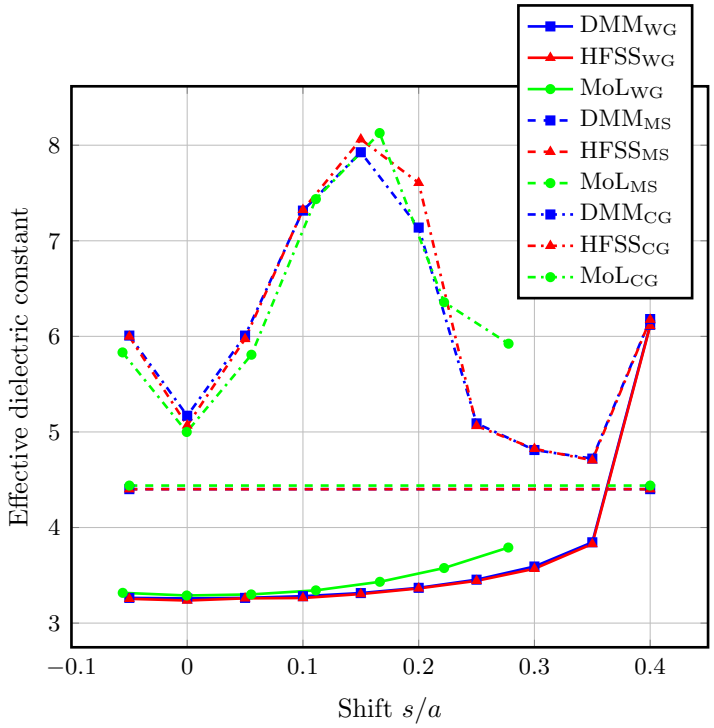

Figure 6.13: Effective dielectric constant versus shift for isotropic waveguides (WG: dielectric waveguide only, MS: microstrip only, CG: coupled guide).

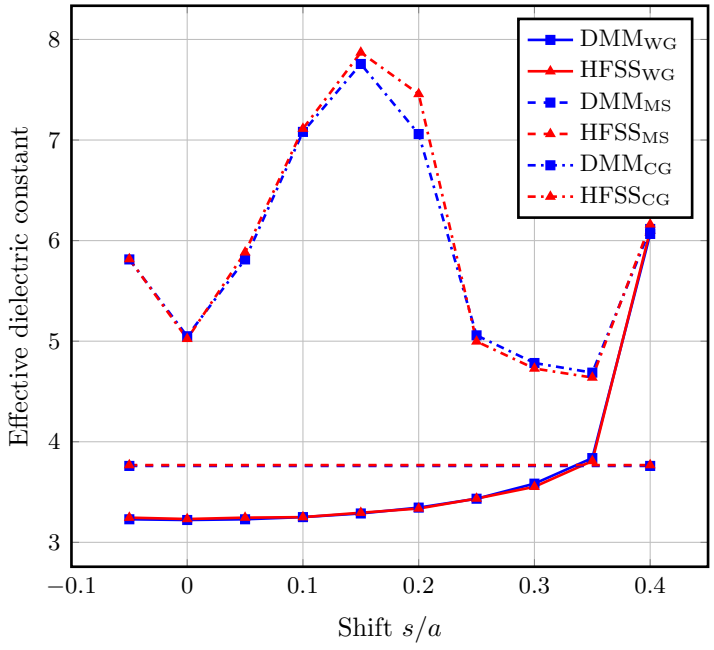

Figure 6.14: Effective dielectric constant versus shift for anisotropic waveguides..

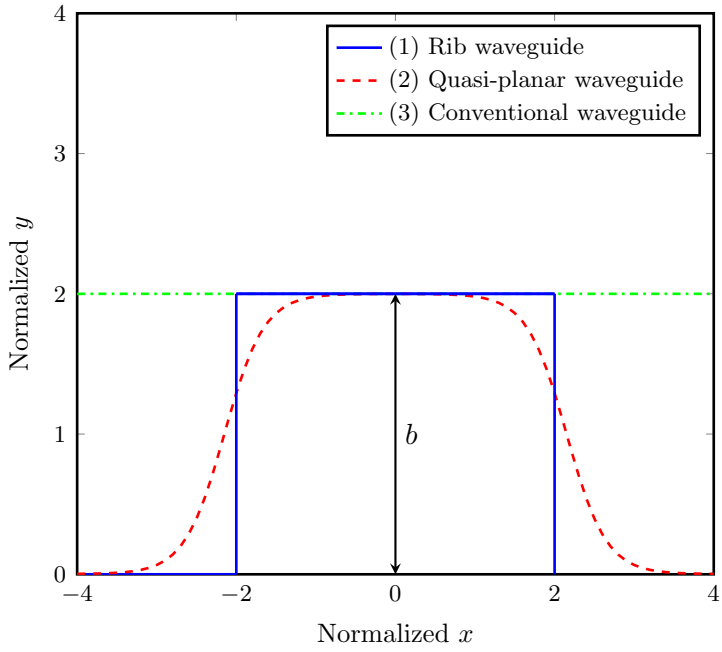

Figure 6.15: Cross-section of different analyzed waveguides (with $b = 2$).

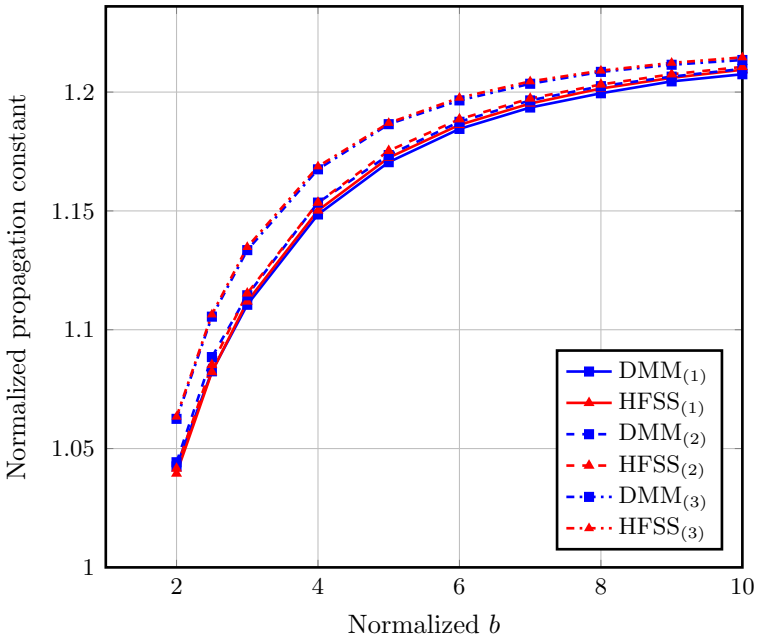

Figure 6.16: Dispersion curves for waveguides with isotropic medium. The different cases are shown in Fig. 6.15.

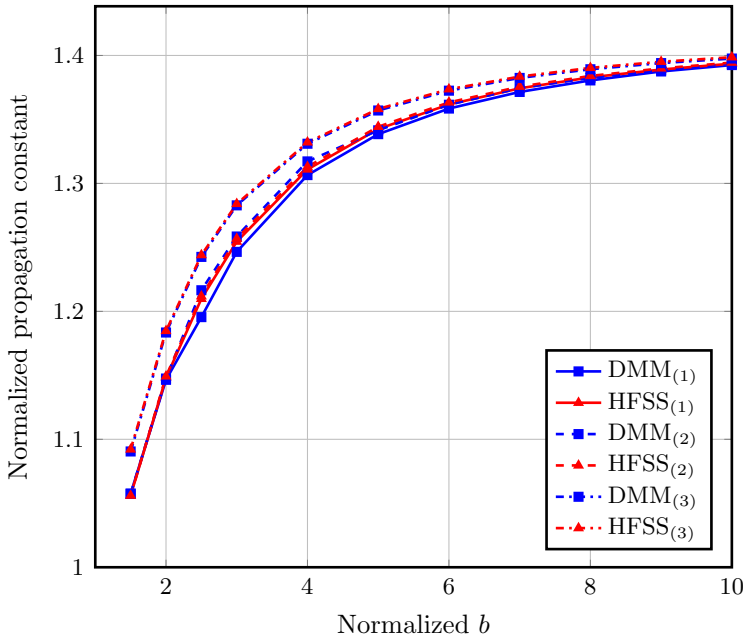

Figure 6.17: Dispersion curves for waveguides with anisotropic medium.

7 Analysis of Transmission Lines with Anisotropic Elliptical Dielectric Layers

During the past decades, a considerable amount of attention has been paid to the analysis of optical fibers or dielectric waveguides for fast data transmission. The fibers exhibit ellipticity due to fabrication imperfections or purposely, due to manufacturing convenience. Also, the elliptical fibers have the interesting feature that their higher order modes are azimuthally stable, in contrast to circular fibers.

In Chapter 5, we have dealt with elliptical structures using a cylindrical coordinate system. The goal of this chapter is to extend the DMM method to directly deal with an elliptical coordinate system. We consider the problem of electromagnetic wave propagation along a dielectric cylinder of elliptical cross-section. We use elliptic cylinder functions, known as Mathieu functions to find the solution of the Helmholtz equation. The whole analysis is done in spatial domain.

Several authors have analyzed elliptical waveguides in the literature, for example propagating modes are determined using ellipse transformation perturbation method (ETPM) in [Antikainen et al., 2017]. The cutoff wavelength is solved using the method of fundamental solutions (MFS) along with the singular value decomposition (SVD) technique in [Young et al., 2005] and higher order mode cutoff is investigated in [Rengarajan, 1989]. Conradi and Pregla [2001] explain the analysis of elliptical fibers using method of lines (MoL) in elliptical coordinates but the angular Mathieu functions are approximated with a Fourier expansion. Dyott collated lot of information on several approaches used to analyze elliptical fibers in the book [Dyott, 1995]. Yeh and Shimabukuro [2008] also discussed in detail the fundamental theory of wave propagation in elliptical dielectric rods and several results in Chapter 6 of the book.

This chapter first describes the solution of the Helmholtz equation in elliptical coordinates. Then, it explains the derivation of the hybrid-matrix elements for elliptical dielectric layers. We demonstrate the application by computing propagation constants for elliptical dielectric waveguides with isotropic and uniaxial anisotropic layers. Finally, we validate the computed results with the open literature and/or results obtained from the commercial software ANSYS HFSS. This chapter is based on [Kamra and Dreher, 2020a].

7.1 Formulation in the Elliptical Coordinate System

Let us consider the elliptical coordinate system (ξ, η, z) as shown in Fig. 7.1. In the figure, we describe the elliptical cylinder by the coordinate ξ and the hyperbolic cylinder by the coordinate η. We locate the two foci of the elliptical cylinder at $-f$ and $+f$ on the x-axis. We can write the relation between the Cartesian and the elliptical coordinate system as

$$x = f \cosh\xi \cos\eta = A \cos\eta, \tag{7.1}$$

$$y = f \sinh\xi \sin\eta = B \sin\eta, \tag{7.2}$$

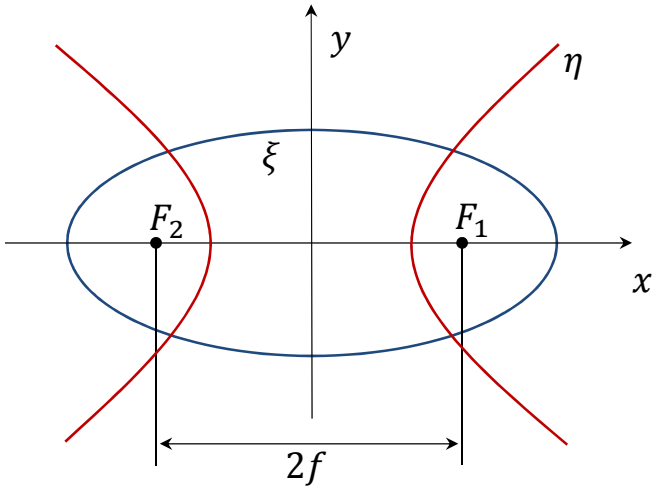

Figure 7.1: Elliptical cylindrical coordinates with semifocal length f.

where A and B represent the semi-major and the semi-minor axes of the elliptical cylinder. The range of the coordinates is specified as

$$\xi \geq 0, \qquad 0 \leq \eta \leq 2\pi, \qquad -\inf \leq z \leq \inf\,. \tag{7.3}$$

7.1.1 Solution of the Maxwell's Equations

We write the Maxwell's equations in elliptical coordinates and for a source-free and homogeneous medium in their differential form as

$$\nabla \times \vec{E}(\xi,\eta,z) = -j\omega\bar{\bar{\mu}} \cdot \vec{H}(\xi,\eta,z), \tag{7.4a}$$

$$\nabla \times \vec{H}(\xi,\eta,z) = j\omega\bar{\bar{\varepsilon}} \cdot \vec{E}(\xi,\eta,z). \tag{7.4b}$$

We take the permittivity ($\bar{\bar{\varepsilon}} = \varepsilon_0\bar{\bar{\varepsilon}}_r$) and permeability ($\bar{\bar{\mu}} = \mu_0\bar{\bar{\mu}}_r$) tensors with optical axis in z-direction with

$$\bar{\bar{\varepsilon}}_r = \begin{pmatrix} \varepsilon_t & 0 & 0 \\ 0 & \varepsilon_t & 0 \\ 0 & 0 & \varepsilon_z \end{pmatrix}, \quad \bar{\bar{\mu}}_r = \begin{pmatrix} \mu_t & 0 & 0 \\ 0 & \mu_t & 0 \\ 0 & 0 & \mu_z \end{pmatrix}. \tag{7.5}$$

In the extended form, Faraday's law (7.4a) gives the field relations as

$$\frac{1}{h}\left\{\frac{\partial}{\partial\eta}E_z - \frac{\partial}{\partial z}(hE_\eta)\right\} = -j\omega\mu_0\mu_t H_\xi, \tag{7.6a}$$

$$\frac{1}{h}\left\{\frac{\partial}{\partial z}(hE_\xi) - \frac{\partial}{\partial\xi}E_z\right\} = -j\omega\mu_0\mu_t H_\eta, \tag{7.6b}$$

$$\frac{1}{h^2}\left\{\frac{\partial}{\partial\xi}(hE_\eta) - \frac{\partial}{\partial\eta}(hE_\xi)\right\} = -j\omega\mu_0\mu_z H_z. \tag{7.6c}$$

Next on taking Ampere's law (7.4b), the expressions are

$$\frac{1}{h}\left\{\frac{\partial}{\partial\eta}H_z - \frac{\partial}{\partial z}(hH_\eta)\right\} = -j\omega\varepsilon_0\varepsilon_t E_\xi, \tag{7.7a}$$

$$\frac{1}{h}\left\{\frac{\partial}{\partial z}(hH_\xi) - \frac{\partial}{\partial \xi}H_z\right\} = -j\omega\varepsilon_0\varepsilon_t E_\eta, \tag{7.7b}$$

$$\frac{1}{h^2}\left\{\frac{\partial}{\partial \xi}(hH_\eta) - \frac{\partial}{\partial \eta}(hH_\xi)\right\} = -j\omega\varepsilon_0\varepsilon_z E_z. \tag{7.7c}$$

As the optical axis is in z-direction, we assume E_z and H_z as the two independent field components. Then, we calculate the other field components using the relations

$$\left(\frac{\partial^2}{\partial z^2} + \omega^2\varepsilon_0\mu_0\varepsilon_t\mu_t\right)E_\xi = \frac{1}{h}\frac{\partial}{\partial z}\frac{\partial}{\partial \xi}E_z - \frac{j\omega\mu_0\mu_t}{h}\frac{\partial}{\partial \eta}H_z \tag{7.8a}$$

$$\left(\frac{\partial^2}{\partial z^2} + \omega^2\varepsilon_0\mu_0\varepsilon_t\mu_t\right)H_\xi = \frac{j\omega\varepsilon_0\varepsilon_t}{h}\frac{\partial}{\partial \eta}E_z + \frac{1}{h}\frac{\partial}{\partial z}\frac{\partial}{\partial \xi}H_z \tag{7.8b}$$

$$\left(\frac{\partial^2}{\partial z^2} + \omega^2\varepsilon_0\mu_0\varepsilon_t\mu_t\right)E_\eta = \frac{1}{h}\frac{\partial}{\partial z}\frac{\partial}{\partial \eta}E_z + \frac{j\omega\mu_0\mu_t}{h}\frac{\partial}{\partial \xi}H_z \tag{7.8c}$$

$$\left(\frac{\partial^2}{\partial z^2} + \omega^2\varepsilon_0\mu_0\varepsilon_t\mu_t\right)H_\eta = \frac{-j\omega\varepsilon_0\varepsilon_t}{h}\frac{\partial}{\partial \xi}E_z + \frac{1}{h}\frac{\partial}{\partial z}\frac{\partial}{\partial \eta}H_z. \tag{7.8d}$$

Here the scale factor $h = f\sqrt{\cosh^2\xi - \cos^2\eta}$ and f is the semifocal length of the ellipse.

We write the source free differential equation for the electric field E_z in elliptical coordinates as

$$\left(\frac{\partial^2}{\partial \xi^2} + \frac{\partial^2}{\partial \eta^2} + h^2\frac{\varepsilon_z}{\varepsilon_t}\frac{\partial^2}{\partial z^2} + h^2\omega^2\varepsilon_0\mu_0\mu_t\varepsilon_z\right)E_z = 0, \tag{7.9}$$

and for the magnetic field H_z as

$$\left(\frac{\partial^2}{\partial \xi^2} + \frac{\partial^2}{\partial \eta^2} + h^2\frac{\mu_z}{\mu_t}\frac{\partial^2}{\partial z^2} + h^2\omega^2\varepsilon_0\mu_0\varepsilon_t\mu_z\right)H_z = 0. \tag{7.10}$$

On assuming that the propagation is in z-direction then the equations lead to

$$\left(\frac{\partial^2}{\partial \xi^2} + \frac{\partial^2}{\partial \eta^2} + h^2\varepsilon_{d(e,h)}\right)\psi = 0, \tag{7.11}$$

where ψ represents each of the independent electromagnetic field components, i.e., E_z and H_z and $\varepsilon_{de} = \omega^2\varepsilon_0\mu_0\mu_t\varepsilon_z - k_z^2\varepsilon_z/\varepsilon_t$ and $\varepsilon_{dh} = \omega^2\varepsilon_0\mu_0\varepsilon_t\mu_z - k_z^2\mu_z/\mu_t$ for E_z and H_z, respectively. Similar to the procedure explained in [Yeh and Shimabukuro, 2008], we apply next the rule of separation of variables on the field component and set

$$\psi = R(\xi)S(\eta). \tag{7.12}$$

Then we obtain two ordinary differential equations

$$\frac{\partial^2 S(\eta)}{\partial \eta^2} + (a - 2q\cos 2\eta)S(\eta) = 0, \tag{7.13}$$

$$\frac{\partial^2 R(\xi)}{\partial \xi^2} - (a - 2q\cosh 2\xi)R(\xi) = 0. \tag{7.14}$$

Here, a represents the separation constant and q equals $\varepsilon_{de}f^2/4$ and $\varepsilon_{dh}f^2/4$ for E_z and H_z, respectively. These equations are known as Mathieu differential equation and modified Mathieu differential equation, respectively.

We express the solution of the differential equation (7.9) as linear combination of products of angular and radial Mathieu functions:

$$\begin{aligned} E_{z_0} =& \sum_{i=0}^{\infty} A_{0_i} \mathrm{Je}_i(q_{e_{0,0}}, \xi) \mathrm{Ce}_i(q_{e_{0,0}}, \eta) \\ &+ \sum_{i=1}^{\infty} B_{0_i} \mathrm{Jo}_i(q_{e_{0,0}}, \xi) \mathrm{So}_i(q_{e_{0,0}}, \eta) \qquad (0 \leq \xi \leq \xi_0), \end{aligned} \tag{7.15}$$

$$\begin{aligned} E_{z_k} =& \sum_{i=0}^{\infty} [A_{k1_i} \mathrm{Je}_i(q_{e_{k,int}}, \xi) + A_{k2_i} \mathrm{Ne}_i(q_{e_{k,int}}, \xi)] \mathrm{Ce}_i(q_{e_{k,int}}, \eta) \\ &+ \sum_{i=1}^{\infty} [B_{k1_i} \mathrm{Jo}_i(q_{e_{k,int}}, \xi) + B_{k2_i} \mathrm{No}_i(q_{e_{k,int}}, \xi)] \mathrm{So}_i(q_{e_{k,int}}, \eta) \qquad (\xi_{k-1} \leq \xi \leq \xi_k), \end{aligned} \tag{7.16}$$

$$\begin{aligned} E_{z_n} =& \sum_{i=0}^{\infty} A_{n_i} \mathrm{He}_i^{(2)}(q_{e_{n,n-1}}, \xi) \mathrm{Ce}_i(q_{e_{n,n-1}}, \eta) \\ &+ \sum_{i=1}^{\infty} B_{n_i} \mathrm{Ho}_i^{(2)}(q_{e_{n,n-1}}, \xi) \mathrm{So}_i(q_{e_{n,n-1}}, \eta) \qquad (\xi_{n-1} \leq \xi < \infty). \end{aligned} \tag{7.17}$$

The field component in (7.15) is for innermost layer 0 extending from $\xi = 0$ to ξ_0, (7.16) is for arbitrary layer k extending from $\xi = \xi_{k-1}$ to ξ_k and (7.17) is for top layer n extending from $\xi = \xi_{n-1}$ to ∞. Similarly, we write the solution of the differential equation (7.10) as

$$\begin{aligned} H_{z_0} =& \sum_{i=0}^{\infty} C_{0_i} \mathrm{Je}_i(q_{h_{0,0}}, \xi) \mathrm{Ce}_i(q_{h_{0,0}}, \eta) \\ &+ \sum_{i=1}^{\infty} D_{0_i} \mathrm{Jo}_i(q_{h_{0,0}}, \xi) \mathrm{So}_i(q_{h_{0,0}}, \eta) \qquad (0 \leq \xi \leq \xi_0), \end{aligned} \tag{7.18}$$

$$\begin{aligned} H_{z_k} =& \sum_{i=0}^{\infty} [C_{k1_i} \mathrm{Je}_i(q_{h_{k,int}}, \xi) + C_{k2_i} \mathrm{Ne}_i(q_{h_{k,int}}, \xi)] \mathrm{Ce}_i(q_{h_{k,int}}, \eta) \\ &+ \sum_{i=1}^{\infty} [D_{k1_i} \mathrm{Jo}_i(q_{h_{k,int}}, \xi) + D_{k2_i} \mathrm{No}_i(q_{h_{k,int}}, \xi)] \mathrm{So}_i(q_{h_{k,int}}, \eta) \qquad (\xi_{k-1} \leq \xi \leq \xi_k), \end{aligned} \tag{7.19}$$

$$\begin{aligned} H_{z_n} =& \sum_{i=0}^{\infty} C_{n_i} \mathrm{He}_i^{(2)}(q_{h_{n,n-1}}, \xi) \mathrm{Ce}_i(q_{h_{n,n-1}}, \eta) \\ &+ \sum_{i=1}^{\infty} D_{n_i} \mathrm{Ho}_i^{(2)}(q_{h_{n,n-1}}, \xi) \mathrm{So}_i(q_{h_{n,n-1}}, \eta) \qquad (\xi_{n-1} \leq \xi < \infty). \end{aligned} \tag{7.20}$$

The even and odd angular Mathieu functions, represented with Ce and So, respectively, are solutions of the Mathieu differential equation (7.13). The functions Je, Jo and Ne, No are radial Mathieu functions of the first and second kind which come from the solution of the modified Mathieu differential equation (7.14). They play a similar role as Bessel functions in the circular coordinate system. Eqs. (7.17) and (7.20) contain He and Ho, which represent even and odd Mathieu-Hankel functions of the second kind, respectively,

which are analogous to the Hankel functions. Mathieu-Hankel functions come from the solution of the modified Mathieu differential equation (7.14) in an unbounded domain. The angular Mathieu functions are expressed with Fourier series and the radial Mathieu functions as series of Bessel functions. Here the terms $q_{e_{k,int}}$ and $q_{h_{k,int}}$ are dependent on medium parameters with k denoting the dielectric layers and *int* denoting the interfaces between the layers. For example, layer 0 has only top interface 0 with $\xi = \xi_0$, layer k has both bottom and top interfaces represented by $k-1$ with $\xi = \xi_{k-1}$ and k with $\xi = \xi_k$, respectively, and layer n has bottom interface $n-1$ with $\xi = \xi_{n-1}$. Therefore, the Mathieu functions are not only functions of η or ξ coordinates, but also depend on the medium parameters, i.e., $\bar{\bar{\varepsilon}}$, $\bar{\bar{\mu}}$. The definitions of these Mathieu functions are given in McLachlan [1951]. The coefficients are represented by A_{k1_i}, A_{k2_i}, A_{0_i}, A_{n_i}, B_{k1_i}, B_{k2_i}, B_{0_i}, B_{n_i}, C_{k1_i}, C_{k2_i}, C_{0_i}, C_{n_i}, D_{k1_i}, D_{k2_i}, D_{0_i} and D_{n_i} for mode i.

7.1.2 Mode Classification

We know that the coexistence of TE and TM modes happens when the fields are dependent on the angular coordinate. They give rise to the hybrid modes which are also the case in the cylindrical coordinate system. The modes are known as HE if the cross-sectional field pattern is similar to the TE mode or H mode, and EH if the cross-sectional field pattern is similar to the TM mode or E mode. However, there exists an asymmetry in the elliptical cylinder, which generates two types of field configurations. Thus, we have even or odd types of hybrid modes which are denoted with prescript e or o, i.e., e,oHE or e,oEH.

7.1.2.1 Even Modes eHE or eEH

The expressions for the independent electric and magnetic field components for even modes are

$$E_{z_0} = \sum_{i=1}^{\infty} B_{0_i} \mathrm{Jo}_i(q_{e_{0,0}}, \xi)\mathrm{So}_i(q_{e_{0,0}}, \eta) \qquad (0 \le \xi \le \xi_0), \tag{7.21}$$

$$E_{z_k} = \sum_{i=1}^{\infty} [B_{k1_i} \mathrm{Jo}_i(q_{e_{k,int}}, \xi) + B_{k2_i}\mathrm{No}_i(q_{e_{k,int}}, \xi)]\mathrm{So}_i(q_{e_{k,int}}, \eta) \qquad (\xi_{k-1} \le \xi \le \xi_k), \tag{7.22}$$

$$E_{z_n} = \sum_{i=1}^{\infty} B_{n_i} \mathrm{Ho}_i^{(2)}(q_{e_{n,n-1}}, \xi)\mathrm{So}_i(q_{e_{n,n-1}}, \eta) \qquad (\xi_{n-1} \le \xi < \infty), \tag{7.23}$$

$$H_{z_0} = \sum_{i=0}^{\infty} C_{0_i} \mathrm{Je}_i(q_{h_{0,0}}, \xi)\mathrm{Ce}_i(q_{h_{0,0}}, \eta) \qquad (0 \le \xi \le \xi_0), \tag{7.24}$$

$$H_{z_k} = \sum_{i=0}^{\infty} [C_{k1_i} \mathrm{Je}_i(q_{h_{k,int}}, \xi) + C_{k2_i}\mathrm{Ne}_i(q_{h_{k,int}}, \xi)]\mathrm{Ce}_i(q_{h_{k,int}}, \eta) \qquad (\xi_{k-1} \le \xi \le \xi_k), \tag{7.25}$$

$$H_{z_n} = \sum_{i=0}^{\infty} C_{n_i} \mathrm{He}_i^{(2)}(q_{h_{n,n-1}}, \xi)\mathrm{Ce}_i(q_{h_{n,n-1}}, \eta) \qquad (\xi_{n-1} \le \xi < \infty). \tag{7.26}$$

7.1.2.2 Odd Modes oHE or oEH

Similarly, the expressions for the independent electric and magnetic field components for odd modes are

$$E_{z_0} = \sum_{i=0}^{\infty} A_{0_i} \mathrm{Je}_i(q_{e_{0,0}}, \xi)\mathrm{Ce}_i(q_{e_{0,0}}, \eta) \qquad (0 \le \xi \le \xi_0), \tag{7.27}$$

$$E_{z_k} = \sum_{i=0}^{\infty} [A_{k1_i} \mathrm{Je}_i(q_{e_{k,int}}, \xi) + A_{k2_i} \mathrm{Ne}_i(q_{e_{k,int}}, \xi)]\mathrm{Ce}_i(q_{e_{k,int}}, \eta) \qquad (\xi_{k-1} \le \xi \le \xi_k), \tag{7.28}$$

$$E_{z_n} = \sum_{i=0}^{\infty} A_{n_i} \mathrm{He}_i^{(2)}(q_{e_{n,n-1}}, \xi)\mathrm{Ce}_i(q_{e_{n,n-1}}, \eta) \qquad (\xi_{n-1} \le \xi < \infty), \tag{7.29}$$

$$H_{z_0} = \sum_{i=1}^{\infty} D_{0_i} \mathrm{Jo}_i(q_{h_{0,0}}, \xi)\mathrm{So}_i(q_{h_{0,0}}, \eta) \qquad (0 \le \xi \le \xi_0), \tag{7.30}$$

$$H_{z_k} = \sum_{i=1}^{\infty} [D_{k1_i} \mathrm{Jo}_i(q_{h_{k,int}}, \xi) + D_{k2_i} \mathrm{No}_i(q_{h_{k,int}}, \xi)]\mathrm{So}_i(q_{h_{k,int}}, \eta) \qquad (\xi_{k-1} \le \xi \le \xi_k), \tag{7.31}$$

$$H_{z_n} = \sum_{i=1}^{\infty} D_{n_i} \mathrm{Ho}_i^{(2)}(q_{h_{n,n-1}}, \xi)\mathrm{So}_i(q_{h_{n,n-1}}, \eta) \qquad (\xi_{n-1} \le \xi < \infty). \tag{7.32}$$

7.1.3 The Discrete Mode Matching Method

We assume that the structure is infinite in the propagation direction, i.e., in z-direction. From (7.21)-(7.26) and (7.27)-(7.32), it is clear that the wave solution for every elliptical cylinder ξ is dependent on each and every point on the η-axis. Therefore we do 1D discretization in the η-direction (see Fig. 7.2). For every value of q, there exists an infinite sequence of eigenvalues a and for each value of a exists a corresponding infinite sequence of eigenvectors (expansion coefficients). The important step in the algorithm is to compute the eigenvalues and the corresponding eigenvectors. Here, we consider a number of 25 expansion coefficients for all categories of Mathieu functions. In our code, we calculate exact expansion coefficients without any approximations.

We take E_z and H_z to be the two independent field components. We assume that E_z is sampled on e-lines and H_z on h-lines. We discretize the structure with N_η^e e-lines and N_η^h h-lines in the η-direction and include the same number of modes in the field expansion. Therefore, we write (7.21)-(7.26) in discretized form as

$$E_{z_0}(\xi, \eta_j^e) = \sum_{i=1}^{N_\eta^e} B_{0_i} \mathrm{Jo}_i(q_{e_{0,0}}, \xi)\mathrm{So}_i(q_{e_{0,0}}, \eta_j^e) \qquad (0 \le \xi \le \xi_0), \tag{7.33}$$

$$E_{z_k}(\xi, \eta_j^e) = \sum_{i=1}^{N_\eta^e} [B_{k1_i} \mathrm{Jo}_i(q_{e_{k,int}}, \xi) + B_{k2_i} \mathrm{No}_i(q_{e_{k,int}}, \xi)]\mathrm{So}_i(q_{e_{k,int}}, \eta_j^e) \qquad (\xi_{k-1} \le \xi \le \xi_k), \tag{7.34}$$

$$E_{z_n}(\xi, \eta_j^e) = \sum_{i=1}^{N_\eta^e} B_{n_i} \mathrm{Ho}_i^{(2)}(q_{e_{n,n-1}}, \xi)\mathrm{So}_i(q_{e_{n,n-1}}, \eta_j^e) \qquad (\xi_{n-1} \le \xi < \infty), \tag{7.35}$$

$$H_{z_0}(\xi,\eta_j^h)=\sum_{i=0}^{N_\eta^h} C_{0_i}\mathrm{Je}_i(q_{h_{0,0}},\xi)\mathrm{Ce}_i(q_{h_{0,0}},\eta_j^h) \qquad (0\le\xi\le\xi_0), \tag{7.36}$$

$$H_{z_k}(\xi,\eta_j^h)=\sum_{i=0}^{N_\eta^h}[C_{k1_i}\mathrm{Je}_i(q_{h_{k,int}},\xi)+C_{k2_i}\mathrm{Ne}_i(q_{h_{k,int}},\xi)]\mathrm{Ce}_i(q_{h_{k,int}},\eta_j^h) \qquad (\xi_{k-1}\le\xi\le\xi_k), \tag{7.37}$$

$$H_{z_n}(\xi,\eta_j^h)=\sum_{i=0}^{N_\eta^h} C_{n_i}\mathrm{He}_i^{(2)}(q_{h_{n,n-1}},\xi)\mathrm{Ce}_i(q_{h_{n,n-1}},\eta_j^h) \qquad (\xi_{n-1}\le\xi<\infty). \tag{7.38}$$

Similarly we write (7.27)-(7.32) in discretized form as

$$E_{z_0}(\xi,\eta_j^e,z)=\sum_{i=0}^{N_\eta^e} A_{0_i}\mathrm{Je}_i(q_{e_{0,0}},\xi)\mathrm{Ce}_i(q_{e_{0,0}},\eta_j^e) \qquad (0\le\xi\le\xi_0), \tag{7.39}$$

$$E_{z_k}(\xi,\eta_j^e,z)=\sum_{i=0}^{N_\eta^e}[A_{k1_i}\mathrm{Je}_i(q_{e_{k,int}},\xi)+A_{k2_i}\mathrm{Ne}_i(q_{e_{k,int}},\xi)]\mathrm{Ce}_i(q_{e_{k,int}},\eta_j^e) \qquad (\xi_{k-1}\le\xi\le\xi_k), \tag{7.40}$$

$$E_{z_n}(\xi,\eta_j^e,z)=\sum_{i=0}^{N_\eta^e} A_{n_i}\mathrm{He}_i^{(2)}(q_{e_{n,n-1}},\xi)\mathrm{Ce}_i(q_{e_{n,n-1}},\eta_j^e) \qquad (\xi_{n-1}\le\xi\le\infty), \tag{7.41}$$

$$H_{z_0}(\xi,\eta_j^h,z)=\sum_{i=1}^{N_\eta^h} D_{0_i}\mathrm{Jo}_i(q_{h_{0,0}},\xi)\mathrm{So}_i(q_{h_{0,0}},\eta_j^h) \qquad (0\le\xi\le\xi_0), \tag{7.42}$$

$$H_{z_k}(\xi,\eta_j^h,z)=\sum_{i=1}^{N_\eta^h}[D_{k1_i}\mathrm{Jo}_i(q_{h_{k,int}},\xi)+D_{k2_i}\mathrm{No}_i(q_{h_{k,int}},\xi)]\mathrm{So}_i(q_{h_{k,int}},\eta_j^h) \qquad (\xi_{k-1}\le\xi\le\xi_k), \tag{7.43}$$

$$H_{z_n}(\xi,\eta_j^h,z)=\sum_{i=1}^{N_\eta^h} D_{n_i}Ho_i^{(2)}(q_h,\xi)So_i(q_{h_{n,n-1}},\eta_j^h) \qquad (\xi_{n-1}\le\xi\le\infty). \tag{7.44}$$

From (7.8), we can identify the location of the other field components. Therefore, we say that for 1D discretization E_z, E_ξ and H_η (or H_z, H_ξ and E_η) components are sampled at the same locations. Using (7.34), (7.37) and the field relations from Maxwell's equations, we write the discretized tangential field components for even modes in layer k in matrix form as

$$\begin{bmatrix}\boldsymbol{E}_{\eta_k}\\ \boldsymbol{H}_{\eta_k}\\ \boldsymbol{E}_{z_k}\\ \boldsymbol{H}_{z_k}\end{bmatrix}=\begin{bmatrix}\boldsymbol{Q}_{\eta_k}^{B_1} & \boldsymbol{Q}_{\eta_k}^{B_2} & \boldsymbol{Q}_{\eta_k}^{C_1} & \boldsymbol{Q}_{\eta_k}^{C_2}\\ \boldsymbol{G}_{\eta_k}^{B_1} & \boldsymbol{G}_{\eta_k}^{B_2} & \boldsymbol{G}_{\eta_k}^{C_1} & \boldsymbol{G}_{\eta_k}^{C_2}\\ \boldsymbol{Q}_{z_k}^{B_1} & \boldsymbol{Q}_{z_k}^{B_2} & \boldsymbol{0} & \boldsymbol{0}\\ \boldsymbol{0} & \boldsymbol{0} & \boldsymbol{G}_{z_k}^{C_1} & \boldsymbol{G}_{z_k}^{C_2}\end{bmatrix}\begin{bmatrix}\boldsymbol{B}_{k1}\\ \boldsymbol{B}_{k2}\\ \boldsymbol{C}_{k1}\\ \boldsymbol{C}_{k2}\end{bmatrix}. \tag{7.45}$$

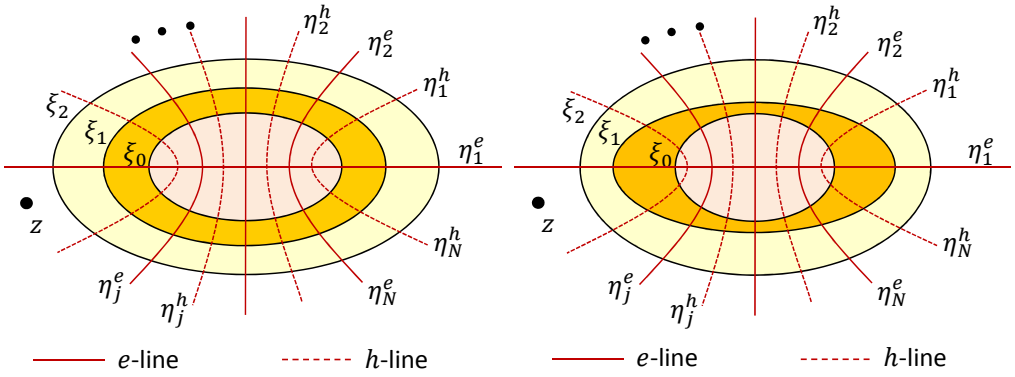

(a) Layers with equal ellipticities. **(b)** Layers with different ellipticities.

Figure 7.2: Discretization scheme for the elliptical transmission lines.

Similarly, for odd modes

$$\begin{bmatrix} \boldsymbol{E}_{\eta_k} \\ \boldsymbol{H}_{\eta_k} \\ \boldsymbol{E}_{z_k} \\ \boldsymbol{H}_{z_k} \end{bmatrix} = \begin{bmatrix} \boldsymbol{Q}_{\eta_k}^{A_1} & \boldsymbol{Q}_{\eta_k}^{A_2} & \boldsymbol{Q}_{\eta_k}^{D_1} & \boldsymbol{Q}_{\eta_k}^{D_2} \\ \boldsymbol{G}_{\eta_k}^{A_1} & \boldsymbol{G}_{\eta_k}^{A_2} & \boldsymbol{G}_{\eta_k}^{D_1} & \boldsymbol{G}_{\eta_k}^{D_2} \\ \boldsymbol{Q}_{z_k}^{A_1} & \boldsymbol{Q}_{z_k}^{A_2} & \boldsymbol{0} & \boldsymbol{0} \\ \boldsymbol{0} & \boldsymbol{0} & \boldsymbol{G}_{z_k}^{D_1} & \boldsymbol{G}_{z_k}^{D_2} \end{bmatrix} \begin{bmatrix} \boldsymbol{A}_{k1} \\ \boldsymbol{A}_{k2} \\ \boldsymbol{D}_{k1} \\ \boldsymbol{D}_{k2} \end{bmatrix}. \tag{7.46}$$

Therefore, we write the relations for layer k in the form

$$\begin{bmatrix} \boldsymbol{E}_{k-1} \\ \boldsymbol{H}_{k-1} \end{bmatrix} = \boldsymbol{M}_{k-1}\boldsymbol{F}, \quad \begin{bmatrix} \boldsymbol{E}_{k} \\ \boldsymbol{H}_{k} \end{bmatrix} = \boldsymbol{M}_{k}\boldsymbol{F}, \tag{7.47}$$

where

$$\boldsymbol{M}_k = \begin{bmatrix} \boldsymbol{Q}_{\eta_k}^{B_1} & \boldsymbol{Q}_{\eta_k}^{B_2} & \boldsymbol{Q}_{\eta_k}^{C_1} & \boldsymbol{Q}_{\eta_k}^{C_2} \\ \boldsymbol{Q}_{z_k}^{B_1} & \boldsymbol{Q}_{z_k}^{B_2} & \boldsymbol{0} & \boldsymbol{0} \\ \boldsymbol{0} & \boldsymbol{0} & \boldsymbol{G}_{z_k}^{C_1} & \boldsymbol{G}_{z_k}^{C_2} \\ \boldsymbol{G}_{\eta_k}^{B_1} & \boldsymbol{G}_{\eta_k}^{B_2} & \boldsymbol{G}_{\eta_k}^{C_1} & \boldsymbol{G}_{\eta_k}^{C_2} \end{bmatrix} \tag{7.48}$$

for even modes and

$$\boldsymbol{M}_k = \begin{bmatrix} \boldsymbol{Q}_{\eta_k}^{A_1} & \boldsymbol{Q}_{\eta_k}^{A_2} & \boldsymbol{Q}_{\eta_k}^{D_1} & \boldsymbol{Q}_{\eta_k}^{D_2} \\ \boldsymbol{Q}_{z_k}^{A_1} & \boldsymbol{Q}_{z_k}^{A_2} & \boldsymbol{0} & \boldsymbol{0} \\ \boldsymbol{0} & \boldsymbol{0} & \boldsymbol{G}_{z_k}^{D_1} & \boldsymbol{G}_{z_k}^{D_2} \\ \boldsymbol{G}_{\eta_k}^{A_1} & \boldsymbol{G}_{\eta_k}^{A_2} & \boldsymbol{G}_{\eta_k}^{D_1} & \boldsymbol{G}_{\eta_k}^{D_2} \end{bmatrix} \tag{7.49}$$

for odd modes. We take the notations of the fields and coefficients in the matrix form as

$$\boldsymbol{E}_k = \begin{bmatrix} \boldsymbol{E}_{\eta_k} \\ \boldsymbol{E}_{z_k} \end{bmatrix}, \quad \boldsymbol{H}_k = \begin{bmatrix} \boldsymbol{H}_{z_k} \\ \boldsymbol{H}_{\eta_k} \end{bmatrix}, \tag{7.50}$$

$$\boldsymbol{F} = \begin{bmatrix} \boldsymbol{B}_{k1} \\ \boldsymbol{B}_{k2} \\ \boldsymbol{C}_{k1} \\ \boldsymbol{C}_{k2} \end{bmatrix} \text{ or } \begin{bmatrix} \boldsymbol{A}_{k1} \\ \boldsymbol{A}_{k2} \\ \boldsymbol{D}_{k1} \\ \boldsymbol{D}_{k2} \end{bmatrix}. \tag{7.51}$$

After eliminating the unknown coefficient column matrix $\boldsymbol{F}$, it results in

$$\begin{bmatrix} \boldsymbol{E}_{k-1} \\ \boldsymbol{H}_{k-1} \end{bmatrix} = \boldsymbol{K}_k \begin{bmatrix} \boldsymbol{E}_k \\ \widetilde{\boldsymbol{H}}_k \end{bmatrix}. \tag{7.52}$$

Therefore, we represent the hybrid matrix ($\boldsymbol{K}_k$) for layer k as

$$\boldsymbol{K}_k = \boldsymbol{M}_{k-1}\boldsymbol{M}_k^{-1}. \tag{7.53}$$

Next on using (7.33), (7.36), (7.35) and (7.38), we write the discretized tangential field components present in the inner layer extending from $\xi = 0$ to $\xi = \xi_0$ or outer bounded layer for even modes as

$$\begin{bmatrix} \boldsymbol{E}_{\eta_\chi} \\ \boldsymbol{E}_{z_\chi} \end{bmatrix} = \begin{bmatrix} \boldsymbol{Q}^B_{\eta_\chi} & \boldsymbol{Q}^C_{\eta_\chi} \\ \boldsymbol{Q}^B_{z_\chi} & \boldsymbol{0} \end{bmatrix} \begin{bmatrix} \boldsymbol{B}_\chi \\ \boldsymbol{C}_\chi \end{bmatrix}, \tag{7.54}$$

$$\begin{bmatrix} \boldsymbol{H}_{z_\chi} \\ \boldsymbol{H}_{\eta_\chi} \end{bmatrix} = \begin{bmatrix} \boldsymbol{0} & \boldsymbol{G}^C_{z_\chi} \\ \boldsymbol{G}^B_{\eta_\chi} & \boldsymbol{G}^C_{\eta_\chi} \end{bmatrix} \begin{bmatrix} \boldsymbol{B}_\chi \\ \boldsymbol{C}_\chi \end{bmatrix}. \tag{7.55}$$

For odd modes, we write

$$\begin{bmatrix} \boldsymbol{E}_{\eta_\chi} \\ \boldsymbol{E}_{z_\chi} \end{bmatrix} = \begin{bmatrix} \boldsymbol{Q}^A_{\eta_\chi} & \boldsymbol{Q}^D_{\eta_\chi} \\ \boldsymbol{Q}^A_{z_\chi} & \boldsymbol{0} \end{bmatrix} \begin{bmatrix} \boldsymbol{A}_\chi \\ \boldsymbol{D}_\chi \end{bmatrix}, \tag{7.56}$$

$$\begin{bmatrix} \boldsymbol{H}_{z_\chi} \\ \boldsymbol{H}_{\eta_\chi} \end{bmatrix} = \begin{bmatrix} \boldsymbol{0} & \boldsymbol{G}^D_{z_\chi} \\ \boldsymbol{G}^A_{\eta_\chi} & \boldsymbol{G}^D_{\eta_\chi} \end{bmatrix} \begin{bmatrix} \boldsymbol{A}_\chi \\ \boldsymbol{D}_\chi \end{bmatrix}, \tag{7.57}$$

where $\chi = 0$ for inner layer and $\chi = n$ for the outer unbounded medium. We calculate the admittance by

$$\boldsymbol{Y}_\chi = \boldsymbol{M}_{H_\chi}\boldsymbol{M}_{E_\chi}^{-1}, \tag{7.58}$$

where

$$\boldsymbol{M}_{E_\chi} = \begin{bmatrix} \boldsymbol{Q}^B_{\eta_\chi} & \boldsymbol{Q}^C_{\eta_\chi} \\ \boldsymbol{Q}^B_{z_\chi} & \boldsymbol{0} \end{bmatrix} \quad \text{and} \quad \boldsymbol{M}_{H_\chi} = \begin{bmatrix} \boldsymbol{0} & \boldsymbol{G}^C_{z_\chi} \\ \boldsymbol{G}^B_{\eta_\chi} & \boldsymbol{G}^C_{\eta_\chi} \end{bmatrix} \tag{7.59}$$

for even modes and

$$\boldsymbol{M}_{E_\chi} = \begin{bmatrix} \boldsymbol{Q}^A_{\eta_\chi} & \boldsymbol{Q}^D_{\eta_\chi} \\ \boldsymbol{Q}^A_{z_\chi} & \boldsymbol{0} \end{bmatrix} \quad \text{and} \quad \boldsymbol{M}_{H_\chi} = \begin{bmatrix} \boldsymbol{0} & \boldsymbol{G}^D_{z_\chi} \\ \boldsymbol{G}^A_{\eta_\chi} & \boldsymbol{G}^D_{\eta_\chi} \end{bmatrix} \tag{7.60}$$

for odd modes.

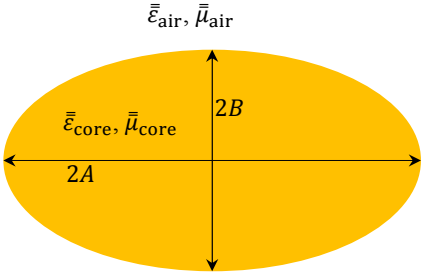

Figure 7.3: Schematic of elliptical waveguide cross-section.

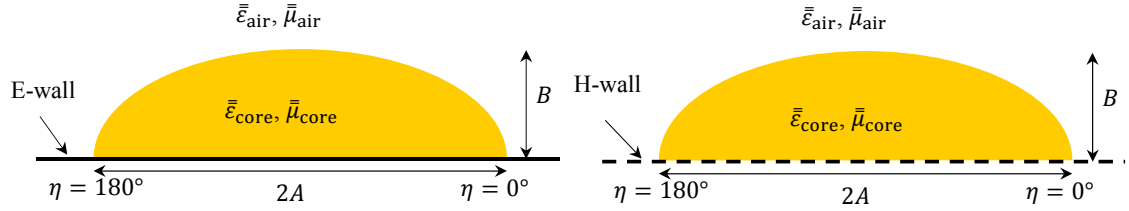

(a) $\text{eHE}_{il}/\text{eEH}_{il}$ **(b)** $\text{oHE}_{il}/\text{oEH}_{il}$

Figure 7.4: Half of the elliptical waveguide cross-section.

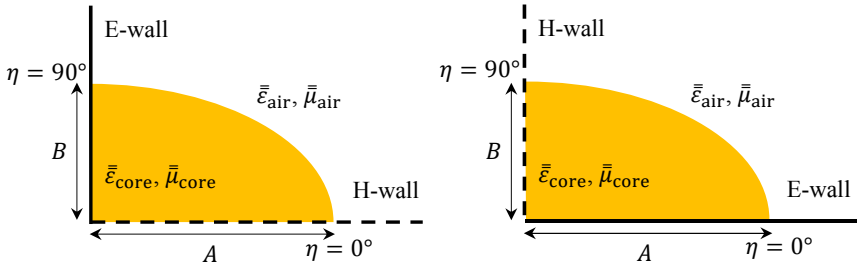

(a) $\text{eHE}_{il}/\text{eEH}_{il}$ **(b)** $\text{oHE}_{il}/\text{oEH}_{il}$

Figure 7.5: One quarter of the elliptical waveguide cross-section (i as odd index).

Table 7.1: Value of modes for different boundary combinations

Boundary combination (left/right)	i (integers)
E/E	all(i)
M/M	all(i)
M/E	odd(i)

Let us consider a two-layer dielectric waveguide as shown in Fig. 7.3. We need to analyze only half of the structure due to symmetry. We get even modes by placing electric walls (E-wall) on the bounding domain while we get odd modes by placing magnetic walls (H-wall) on the boundary, as represented in Fig. 7.4. We can also analyze only a quarter of the structure to get odd or even modes with odd subscript, e.g., eHE$_{il}$ with i as odd index. Fig 7.5 gives the position of E- and H-walls to get suitable modes. Here the coordinate η discretization starts from the horizontal line, as given in Fig. 7.2. Table 7.1 defines the suitable values for mode i in the modal expansion for various boundary conditions.

After calculating the hybrid or admittance matrices for each dielectric layer, we calculate the system equation using a full-wave equivalent circuit. Then, we find the propagation constant after using the boundary conditions and solving the eigenvalue problem as explained in the previous chapters.

7.2 Numerical Results

7.2.1 Elliptical Waveguide

To validate the DMM formulations in elliptical coordinates, we have analyzed the same dielectric elliptical waveguide as taken for analysis in Chapter 5. The waveguide comprises two layers, one is the elliptical core and the other is air surrounding the core as given in Fig. 7.3. The analysis is performed with an axial ratio $B/A = 0.5$, where B is the minor axis and A is the major axis. The material of the elliptical core is taken as $\varepsilon_{r,\text{core}} = (1.539)^2$ for the isotropic and $\bar{\bar{\varepsilon}}_{r,\text{core}} = ((1.539)^2, (1.539)^2, (1.25)^2)$ for the anisotropic case. The dispersion curves, as shown in Fig. 7.6 and 7.7, are plotted against the normalized frequency $V_B = Bk_0\sqrt{\varepsilon_{r,\text{core}} - \varepsilon_{r,\text{air}}}$. Here V_B is calculated using isotropic values for both the isotropic and the anisotropic case. The computed propagation constants are normalized with the free-space wave number k_0.

The computed results agree very well with the open literature [Pregla and Conradi, 2003; Conradi and Pregla, 2001; Dyott, 1995] and predicted results from ANSYS HFSS. The results from Pregla and Conradi [2003] (MoL$_{\text{cyl}}$) are based on a cylindrical coordinate system while the results from Conradi and Pregla [2001] (MoL+Fourier) are calculated in an elliptical coordinate system but with Fourier approximation. We have also compared the results with those shown in Chapter 5 using a cylindrical coordinate system.

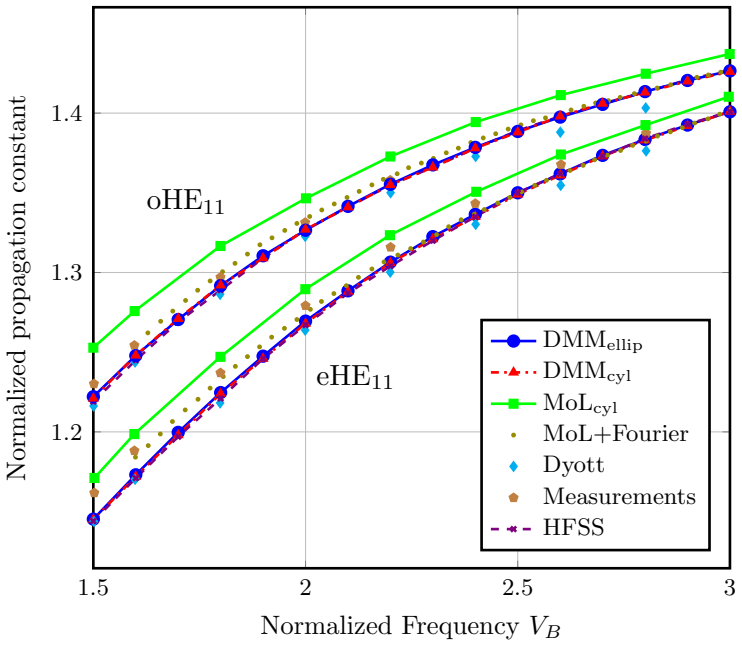

Figure 7.6: Dispersion curve of elliptical waveguide with isotropic material. (DMM_{cyl}: [Kamra and Dreher, 2019b], MoL_{cyl}: [Pregla and Conradi, 2003], MoL+Fourier: [Conradi and Pregla, 2001], Dyott, Measurements: [Dyott, 1995])

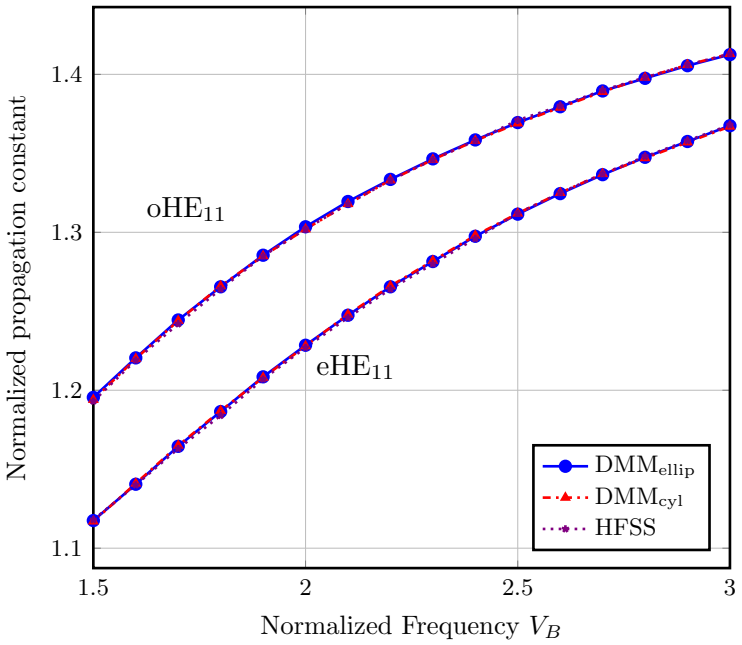

Figure 7.7: Dispersion curve of elliptical waveguide with anisotropic material.

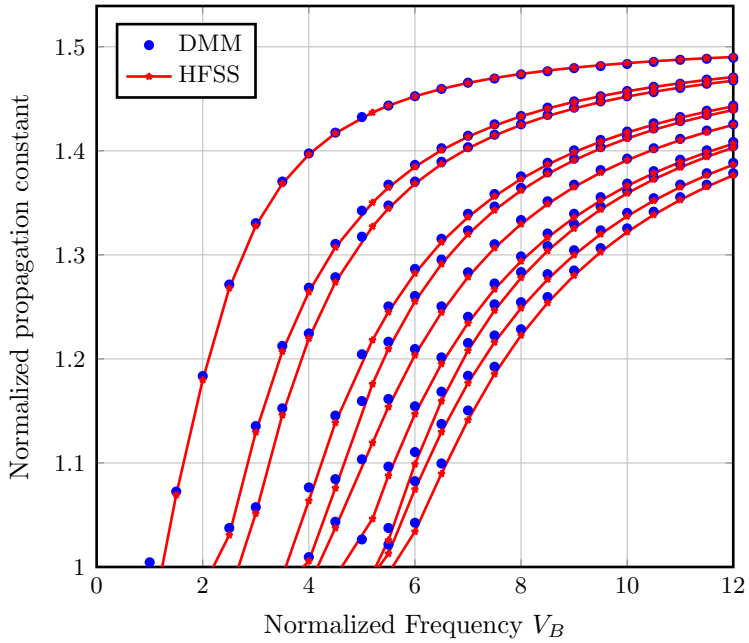

Figure 7.8: Higher order even modes of a dielectric rod.

7.2.2 Investigation of Higher Order Modes

Further to investigate higher order modes, we have analyzed a polythene rod as elliptical core with $\varepsilon_r = 2.26$ and surrounded by air. We have done the computation with an axial ratio $B/A = 0.9$. Fig. 7.8 and 7.9 show the results for the even and odd fundamental modes, respectively, and the first nine higher order modes. We have again plotted the dispersion curves against the normalized frequency V_B. They show very good agreement with the results computed from ANSYS HFSS. They are also in order with the results shown in [Dyott, 1995].

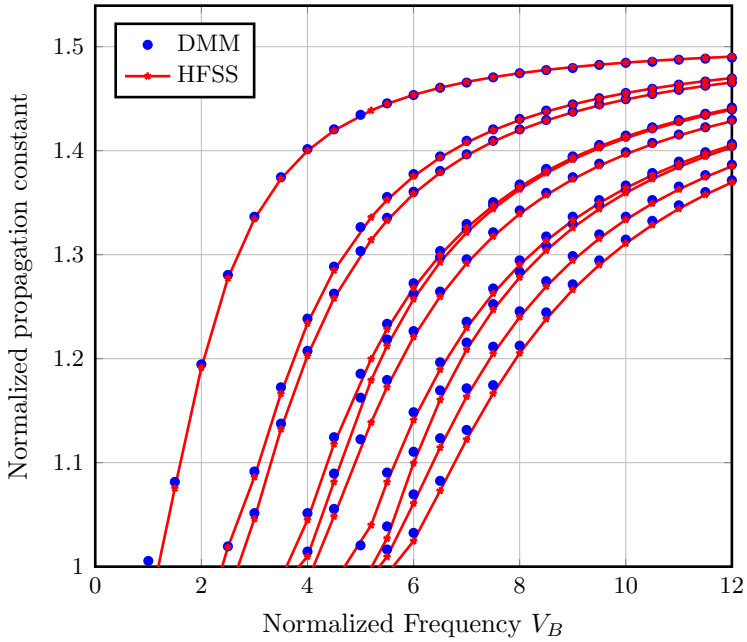

Figure 7.9: Higher order odd modes of a dielectric rod.

8 Conclusion & Outlook

In the present work, we have extended the discrete mode matching method (DMM) for the analysis of multilayered microstrip transmission lines and printed antennas with different kinds of dielectric layers whether in terms of anisotropy or homogeneity, or with metamaterial substrate. It has involved a generalized relation of the field components of the multilayered structure, which can be represented by a full-wave hybrid matrix for each layer. Thus, for stratified structures, we have obtained the system equation by using a full-wave equivalent circuit (FWEC). We have used straightforward circuit analysis techniques and matrix multiplications to take into account several dielectric layers. The accuracy of the DMM could be inferred from the monotonic convergence curves, which allow the extrapolation to the value that would be obtained for an infinite number of discretization lines. The DMM method of analysis has been proven very efficient to analyze a variety of structures. The codes are written in MATLAB for the whole analysis procedure.

First, we have presented a simple formalism as a basis to analyze planar microwave structures with uniaxial anisotropic materials having either electric or magnetic anisotropy or both. This formulation is based on the Fourier transformation of electromagnetic field components on the interfaces of stratified structures. The application was demonstrated by analyzing the well-known example of a two-layer waveguide filled with uniaxial anisotropic dielectric material. Then, we have presented the application of the discrete mode matching method to analyze a microstrip line filled with anisotropic dielectric material. We have validated the numerical results with the finite-element based software ANSYS HFSS and the open literature.

We can conclude that the proposed method provides convincible results in a shorter computing time with few lines on the strip. Moreover, we can analyze the transmission lines with any number of metallic strips accurately using the DMM method with only 1D discretization. Therefore, we have validated the method with a multilayered microstrip line with multiple strips and coupled waveguides. The method can also be used to analyze slotlines and coupled microstrip lines. We have bounded the structures used for the verification by electric walls. However, absorbing boundary conditions can also be used to deal with open and radiating structures in more practical situations.

Then we have presented the method to analyze microstrip patch antennas with anisotropic substrate. We have used a 2D discretization scheme for the analysis of radiators which reduces the computation time and memory. It can easily deal with multilayered substrate present in the structure. Accurate results have been achieved with the proposed method and have been validated with the open literature. For antennas, we have employed absorbing boundary conditions (ABCs) to deal with open and radiating phenomena as in more practical situations. It has removed the need of 3D meshes and provides accurate results.

We have also dealt with the application of the DMM method to analyze microstrip antennas based on metamaterial substrates. We have seen the advantage of including metamaterial in the substrate which provides multiple resonant frequencies in the selected band. The method can easily deal with multilayered structures with metallizations in

different interfaces which gives the flexibility to include more complex unit cells in the structure.

Another contribution of the present work was to deal with conformal structures and biaxial anisotropy. The derivation of the mathematical formulation for the FWEC in spatial domain has been given to analyze quasi-planar transmission lines with biaxial anisotropic stratified media. We have analyzed both waveguides and stripline structures with good agreement to commercial software. We can also extend the method for the analysis of microstrip patch antennas on quasi-planar anisotropic substrates with 2D discretization.

Next to analyze circular or quasi-circular uniaxial anisotropic dielectric layers, we have derived the FWEC formulation with a cylindrical coordinate system. A general procedure for the fast and efficient full-wave analysis of stratified conformal anisotropic structures has been presented. It involved the tangential field relations on the interfaces of each layer in spectral domain or spatial domain. The method has been successfully applied and verified with commercial software whereby a gain in computing time by a factor of more than 100 has been achieved for optical fibers. Besides optical fibers, we have efficiently analyzed other microwave structures like elliptical waveguides, and striplines with metallic strips at the non-circular interfaces. The method is not limited to elliptical structures, it can analyze any conformal interface represented by a suitable function. For analyzing microstrip antennas on quasi-cylindrical substrates, we have extended the method to 2D discretization. For the analysis, we have calculated the angle of inclination with the regular coordinate system using the slope of the interface. We have presented the numerical results for the microstrip patch antenna with elliptical substrate and validated with the commercial software.

Then, we have presented an extension of the discrete mode matching (DMM) method which enables us to analyze the multilayered planar structures with inhomogeneous dielectric layers. The presented algorithm enabled us to deal with different hybrid waveguides very accurately and efficiently. The formulation is capable to deal with electric as well as magnetic anisotropy in the structure. Various examples have been analyzed and presented. The obtained results have shown good validation with the results available in the open literature and/or results from commercial software.

Motivated with the conformal structures, we have also discussed the DMM method with the elliptical coordinate system in the last chapter. The derivation of the hybrid matrix elements for anisotropic elliptical dielectric layers has been done. The formulation has been validated well with the quasi-cylindrical approach. The elliptical fibers have been analyzed with good agreement with the commercial software and open literature.

In short, we can write the advantages of the DMM method as:

- It easily deals with multilayered structures with just matrix multiplications.
- It uses sampling of the field components in only one or two dimensions.
- It uses exact eigenvalues which are dependent on lateral boundary conditions.
- It removes the need of 3D meshes and reduces time and memory requirements.
- It provides smooth convergence, hence extrapolation is possible and gives accurate results.

Till now, we have used only uniform discretization everywhere in the structure. In future, there is a scope to apply non-uniform discretization or subgridding technique to the

structures. We can put more lines in the region where field variations are significant. The non-uniform discretization has been done efficiently in method of lines [Greda and Pregla, 2002, 2004]. This can further reduce the computation time. Also there is a possibility to further extend the work to periodic structures. This can enable us to deal with unit cells in metamaterials more efficiently.

A Admittances with Terminations

We write the tangential field relations between the interfaces $k-1$ and k of the layer k as

$$\begin{bmatrix} \widetilde{\boldsymbol{E}}_{k-1} \\ \widetilde{\boldsymbol{H}}_{k-1} \end{bmatrix} = \begin{bmatrix} \widetilde{\boldsymbol{V}}_k & \widetilde{\boldsymbol{Z}}_k \\ \widetilde{\boldsymbol{Y}}_k & \widetilde{\boldsymbol{B}}_k \end{bmatrix} \begin{bmatrix} \widetilde{\boldsymbol{E}}_k \\ \widetilde{\boldsymbol{H}}_k \end{bmatrix} \quad \text{with} \quad \widetilde{\boldsymbol{K}}_k = \begin{bmatrix} \widetilde{\boldsymbol{V}}_k & \widetilde{\boldsymbol{Z}}_k \\ \widetilde{\boldsymbol{Y}}_k & \widetilde{\boldsymbol{B}}_k \end{bmatrix}. \tag{A.1}$$

The FWEC shown in Fig. A.1 includes the terminated bottom and top layer of the stratified dielectric. Both bottom and top layers can be closed (grounded) or open. In the figure, a grounded bottom layer is shown by the short circuit and an open top layer is represented by the admittance. It also gives the resultant equivalent circuit after the cascading of the matrices. To calculate the terminations, we write the tangential field components on the lower (-) and the upper (+) side of the interface k with metallization as

$$\widetilde{\boldsymbol{H}}_k^- = -\widetilde{\boldsymbol{Y}}^{(d)} \widetilde{\boldsymbol{E}}_k^-, \tag{A.2}$$

$$\widetilde{\boldsymbol{H}}_k^+ = \widetilde{\boldsymbol{Y}}^{(u)} \widetilde{\boldsymbol{E}}_k^+. \tag{A.3}$$

For open bottom, the field relation becomes

$$\begin{bmatrix} \widetilde{\boldsymbol{E}}_0 \\ \widetilde{\boldsymbol{H}}_0 \end{bmatrix} = \begin{bmatrix} \widetilde{\boldsymbol{V}}_d & \widetilde{\boldsymbol{Z}}_d \\ \widetilde{\boldsymbol{Y}}_d & \widetilde{\boldsymbol{B}}_d \end{bmatrix} \begin{bmatrix} \widetilde{\boldsymbol{E}}_k^- \\ \widetilde{\boldsymbol{H}}_k^- \end{bmatrix} \tag{A.4}$$

and

$$\widetilde{\boldsymbol{H}}_0 = -\widetilde{\boldsymbol{Y}}_0 \widetilde{\boldsymbol{E}}_0 \tag{A.5}$$

for the bottom layer 0. Here hybrid matrix $\widetilde{\boldsymbol{K}}_d$ represents the cascading of the hybrid matrices of the inner layers from 1 to k. We obtain the lower admittance

$$\widetilde{\boldsymbol{Y}}^{(d)} = (\widetilde{\boldsymbol{B}}_d + \widetilde{\boldsymbol{Y}}_0 \widetilde{\boldsymbol{Z}}_d)^{-1} (\widetilde{\boldsymbol{Y}}_0 \widetilde{\boldsymbol{V}}_d + \widetilde{\boldsymbol{Y}}_d). \tag{A.6}$$

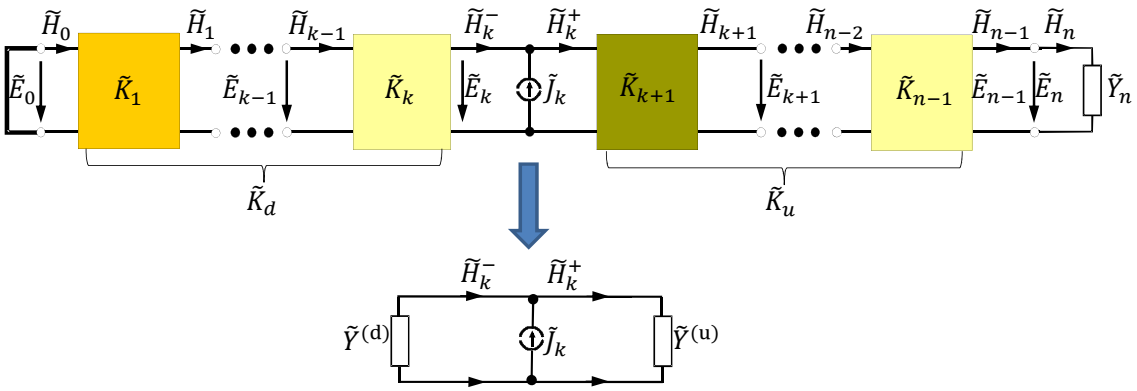

Figure A.1: Equivalent circuit of a stratified dielectric.

For closed bottom ($\widetilde{\boldsymbol{E}}_0 = 0$), we obtain the admittance

$$\widetilde{\boldsymbol{Y}}^{(d)} = \widetilde{\boldsymbol{Z}}_d^{-1}\widetilde{\boldsymbol{V}}_{\boldsymbol{d}}. \tag{A.7}$$

For open top layer, the field relation becomes

$$\begin{bmatrix} \widetilde{\boldsymbol{E}}_k^+ \\ \widetilde{\boldsymbol{H}}_k^+ \end{bmatrix} = \begin{bmatrix} \widetilde{\boldsymbol{V}}_u & \widetilde{\boldsymbol{Z}}_u \\ \widetilde{\boldsymbol{Y}}_u & \widetilde{\boldsymbol{B}}_u \end{bmatrix} \begin{bmatrix} \widetilde{\boldsymbol{E}}_n \\ \widetilde{\boldsymbol{H}}_n \end{bmatrix}. \tag{A.8}$$

and

$$\widetilde{\boldsymbol{H}}_n = \widetilde{\boldsymbol{Y}}_n\widetilde{\boldsymbol{E}}_n \tag{A.9}$$

for the top layer n. Here hybrid matrix $\widetilde{\boldsymbol{K}}_u$ represents the cascading of the hybrid matrices of the outer layers from $(k+1)$ to $(n-1)$. We obtain the upper admittance

$$\widetilde{\boldsymbol{Y}}^{(u)} = (\widetilde{\boldsymbol{Y}}_u + \widetilde{\boldsymbol{B}}_u\widetilde{\boldsymbol{Y}}_n)(\widetilde{\boldsymbol{V}}_u + \widetilde{\boldsymbol{Z}}_u\widetilde{\boldsymbol{Y}}_n)^{-1}. \tag{A.10}$$

For closed top layer ($\widetilde{\boldsymbol{E}}_n = 0$), we obtain the admittance

$$\widetilde{\boldsymbol{Y}}^{(u)} = \widetilde{\boldsymbol{B}}_u\widetilde{\boldsymbol{Z}}_u^{-1}. \tag{A.11}$$

B Expressions in Rectangular Coordinates

B.1 z-Dependence of Field Components

Generally we calculate tangential field components at the interfaces of the dielectric layers, i.e., E_x, E_y, H_x and H_y. To see the field variation along the cross-section of the structure, we need to find out the field dependency on the perpendicular coordinate (z) [Dreher and Pregla, 1993]. The normal field components E_z and H_z can be written as

$$E_z = \frac{1}{j\varepsilon_z}\big(\frac{\partial}{\partial x}H_y - \frac{\partial}{\partial y}H_x\big), \tag{B.1}$$

$$H_z = -\frac{1}{j\mu_z}\big(\frac{\partial}{\partial x}E_y - \frac{\partial}{\partial y}E_x\big). \tag{B.2}$$

On transforming into spectral domain, we write them in matrix form as

$$\widetilde{\boldsymbol{E}}_z = \frac{1}{j\varepsilon_z}\big((-j\boldsymbol{k}_x)\widetilde{\boldsymbol{H}}_y - (-j\boldsymbol{k}_y)\widetilde{\boldsymbol{H}}_x\big), \tag{B.3}$$

$$\widetilde{\boldsymbol{H}}_z = -\frac{1}{j\mu_z}\big((-jk_x)\widetilde{\boldsymbol{E}}_y - (-j\boldsymbol{k}_y)\widetilde{\boldsymbol{E}}_x\big). \tag{B.4}$$

To get the z-dependence of all the field components in spectral domain, we eliminate the coefficients of the wave solution at $k-1$ and k interface of the arbitrary layer k and obtain

$$\widetilde{\boldsymbol{\psi}}(z) = \hat{\boldsymbol{\alpha}}(\hat{\boldsymbol{S}}_1\widetilde{\boldsymbol{\psi}}_{k-1} + \hat{\boldsymbol{S}}_2\widetilde{\boldsymbol{\psi}}_k), \tag{B.5}$$

where

$$\hat{\boldsymbol{\alpha}} = (\boldsymbol{k}_{ze,h}\sinh\boldsymbol{k}_{ze,h}d_k)^{-1} \tag{B.6}$$

$$\hat{\boldsymbol{S}}_1 = \boldsymbol{k}_{ze,h}\sinh\boldsymbol{k}_{ze,h}(z_k - z) \tag{B.7}$$

$$\hat{\boldsymbol{S}}_2 = \boldsymbol{k}_{ze,h}\sinh\boldsymbol{k}_{ze,h}(z - z_{k-1}). \tag{B.8}$$

When there is metallization at the bottom layer, then

$$\widetilde{\boldsymbol{\psi}}(z) = \hat{\boldsymbol{S}}\widetilde{\boldsymbol{\psi}}_1, \tag{B.9}$$

where

$$\hat{\boldsymbol{S}} = \sinh\boldsymbol{k}_{ze,h}z(\sinh\boldsymbol{k}_{ze,h}d_1)^{-1} \tag{B.10}$$

for $\widetilde{\boldsymbol{\psi}} = \widetilde{\boldsymbol{E}}_x$, $\widetilde{\boldsymbol{E}}_y$ or $\widetilde{\boldsymbol{H}}_z$, and

$$\hat{\boldsymbol{S}} = \cosh\boldsymbol{k}_{ze,h}z(\cosh\boldsymbol{k}_{ze,h}d_1)^{-1} \tag{B.11}$$

for $\widetilde{\boldsymbol{\psi}} = \widetilde{\boldsymbol{E}}_z$, $\widetilde{\boldsymbol{H}}_x$ or $\widetilde{\boldsymbol{H}}_y$ with dielectric height d_1. When the structure is open at the top, then

$$\widetilde{\boldsymbol{\psi}}(z) = \hat{\boldsymbol{S}}\widetilde{\boldsymbol{\psi}}_n, \tag{B.12}$$

where

$$\hat{\boldsymbol{S}} = e^{-\boldsymbol{k}_{ze,h}(z-z_n)}. \tag{B.13}$$

B.2 Equations for Spatial Domain

In Chapter 4, we assume the cross-section of the structure in xz-plane and the wave propagation in y-direction. For any arbitrary layer k, we obtain the equations for 1D discretization in x-direction as

$$E_{y_k}(x^e, y, z) = \sum_i^{N^e} (A_{k_i} S_i^A + B_{k_i} S_i^B + C_{k_i} S_i^C + D_{k_i} S_i^D)$$
$$H_{y_k}(x^h, y, z) = \sum_i^{N^h} (A_{k_i} R_i^A + B_{k_i} R_i^B + C_{k_i} R_i^C + D_{k_i} R_i^D), \tag{B.14}$$

where

$$S_i^A = -\frac{P}{k_{z1} d} \tau_x^e(k_{xi}, x^e) e^{k_{z1} z} e^{-jk_y y} \tag{B.15}$$
$$S_i^B = \frac{P}{k_{z1} d} \tau_x^e(k_{xi}, x^e) e^{-k_{z1} z} e^{-jk_y y} \tag{B.16}$$
$$S_i^C = -\frac{Q}{k_{z2} d} \tau_x^e(k_{xi}, x^e) e^{k_{z2} z} e^{-jk_y y} \tag{B.17}$$
$$S_i^D = \frac{Q}{k_{z2} d} \tau_x^e(k_{xi}, x^e) e^{-k_{z2} z} e^{-jk_y y}. \tag{B.18}$$

$$R_i^A = \tau_x^h(k_{xi}, x^h) e^{k_{z1} z} e^{-jk_y y} \tag{B.19}$$
$$R_i^B = \tau_x^h(k_{xi}, x^h) e^{-k_{z1} z} e^{-jk_y y} \tag{B.20}$$
$$R_i^C = \tau_x^h(k_{xi}, x^h) e^{k_{z2} z} e^{-jk_y y} \tag{B.21}$$
$$R_i^D = \tau_x^h(k_{xi}, x^h) e^{-k_{z2} z} e^{-jk_y y}. \tag{B.22}$$

We write the expressions used in Chapter 4 as

$$Q_{tx} = Q_x \cos \alpha_x^h + \bar{Q}_z \sin \alpha_x^h \tag{B.23}$$
$$Q_x^A = \frac{D_x D_y S^A}{p \varepsilon_x \mu_z} + \frac{j D_z R^A}{p \varepsilon_x} \tag{B.24}$$
$$Q_x^B = \frac{D_x D_y S^B}{p \varepsilon_x \mu_z} + \frac{j D_z R^B}{p \varepsilon_x} \tag{B.25}$$
$$Q_x^C = \frac{D_x D_y S^C}{p \varepsilon_x \mu_z} + \frac{j D_z R^C}{p \varepsilon_x} \tag{B.26}$$
$$Q_x^D = \frac{D_x D_y S^D}{p \varepsilon_x \mu_z} + \frac{j D_z R^D}{p \varepsilon_x} \tag{B.27}$$
$$Q_z^A = \frac{D_y D_z S^A}{q \varepsilon_z \mu_x} - \frac{j D_x R^A}{q \varepsilon_z} \tag{B.28}$$
$$Q_z^B = \frac{D_y D_z S^B}{q \varepsilon_z \mu_x} - \frac{j D_x R^B}{q \varepsilon_z} \tag{B.29}$$
$$Q_z^C = \frac{D_y D_z S^C}{q \varepsilon_z \mu_x} - \frac{j D_x R^C}{q \varepsilon_z} \tag{B.30}$$

$$Q_z^D = \frac{D_y D_z S^D}{q\varepsilon_z \mu_x} - \frac{jD_x R^D}{q\varepsilon_z} \tag{B.31}$$

$$\bar{Q}_z(x_j^h) = \frac{1}{2}(Q_z(x_j^e) + Q_z(x_{j+1}^e)) \tag{B.32}$$

$$Q_y^A = S^A \tag{B.33}$$

$$Q_y^B = S^B \tag{B.34}$$

$$Q_y^C = S^C \tag{B.35}$$

$$Q_y^D = S^D \tag{B.36}$$

$$G_{tx} = G_x \cos\alpha_x^e + \bar{G}_z \sin\alpha_x^e \tag{B.37}$$

$$G_x^A = -\frac{jD_z S^A}{q\mu_x} + \frac{D_x D_y R^A}{q\varepsilon_z \mu_x} \tag{B.38}$$

$$G_x^B = -\frac{jD_z S^B}{q\mu_x} + \frac{D_x D_y R^B}{q\varepsilon_z \mu_x} \tag{B.39}$$

$$G_x^C = -\frac{jD_z S^C}{q\mu_x} + \frac{D_x D_y R^C}{q\varepsilon_z \mu_x} \tag{B.40}$$

$$G_x^D = -\frac{jD_z S^D}{q\mu_x} + \frac{D_x D_y R^D}{q\varepsilon_z \mu_x} \tag{B.41}$$

$$G_z^A = \frac{jD_x S^A}{p\mu_z} + \frac{D_y D_z R^A}{p\varepsilon_x \mu_z} \tag{B.42}$$

$$G_z^B = \frac{jD_x S^B}{p\mu_z} + \frac{D_y D_z R^B}{p\varepsilon_x \mu_z} \tag{B.43}$$

$$G_z^C = \frac{jD_x S^C}{p\mu_z} + \frac{D_y D_z R^C}{p\varepsilon_x \mu_z} \tag{B.44}$$

$$G_z^D = \frac{jD_x S^D}{p\mu_z} + \frac{D_y D_z R^D}{p\varepsilon_x \mu_z} \tag{B.45}$$

$$\bar{G}_z(x_j^h) = \frac{1}{2}(G_z(x_j^e) + G_z(x_{j+1}^e)) \tag{B.46}$$

$$G_y^A = R^A \tag{B.47}$$

$$G_y^B = R^B \tag{B.48}$$

$$G_y^C = R^C \tag{B.49}$$

$$G_y^D = R^D \tag{B.50}$$

with $D_y = -jk_y$.

C Expressions in Cylindrical Coordinates

C.1 Equations for Spectral Domain

We write the expressions for E_z or TM mode by

$$\hat{\boldsymbol{p}}_{\boldsymbol{\nu}e_k} = \operatorname{diag}\big((\boldsymbol{p}_{\boldsymbol{\nu}e_k}\rho_{k-1})^{-1}, (\boldsymbol{p}_{\boldsymbol{\nu}e_k}\rho_k)^{-1}\big) \tag{C.1}$$

$$\bar{\boldsymbol{q}}_{\boldsymbol{\nu}e_k} = k_{\rho e_k}\rho_k \boldsymbol{q}_{\boldsymbol{\nu}\boldsymbol{e}_k} \tag{C.2}$$

$$\bar{\boldsymbol{r}}_{\boldsymbol{\nu}e_k} = k_{\rho e_k}\rho_{k-1} \boldsymbol{r}_{\boldsymbol{\nu}\boldsymbol{e}_k} \tag{C.3}$$

$$\bar{\boldsymbol{s}}_{\boldsymbol{\nu}e_k} = k^2_{\rho e_k}\rho_k\rho_{k-1} \boldsymbol{s}_{\boldsymbol{\nu}\boldsymbol{e}_k} \tag{C.4}$$

$$\begin{aligned}\boldsymbol{p}_{\boldsymbol{\nu}e_k} = {} & \boldsymbol{J}_{\boldsymbol{\nu}}(k_{\rho e_k}\rho_{k-1})\boldsymbol{Y}_{\boldsymbol{\nu}}(k_{\rho e_k}\rho_k) \\ & - \boldsymbol{J}_{\boldsymbol{\nu}}(k_{\rho e_k}\rho_k)\boldsymbol{Y}_{\boldsymbol{\nu}}(k_{\rho e_k}\rho_{k-1})\end{aligned} \tag{C.5}$$

$$\begin{aligned}\boldsymbol{q}_{\boldsymbol{\nu}e_k} = {} & \boldsymbol{J}_{\boldsymbol{\nu}}(k_{\rho e_k}\rho_{k-1})\boldsymbol{Y}'_{\boldsymbol{\nu}}(k_{\rho e_k}\rho_k) \\ & -\boldsymbol{J}'_{\boldsymbol{\nu}}(k_{\rho e_k}\rho_k)\boldsymbol{Y}_{\boldsymbol{\nu}}(k_{\rho e_k}\rho_{k-1})\end{aligned} \tag{C.6}$$

$$\begin{aligned}\boldsymbol{r}_{\boldsymbol{\nu}e_k} = {} & \boldsymbol{J}'_{\boldsymbol{\nu}}(k_{\rho e_k}\rho_{k-1})\boldsymbol{Y}_{\boldsymbol{\nu}}(k_{\rho e_k}\rho_k) \\ & -\boldsymbol{J}_{\boldsymbol{\nu}}(k_{\rho e_k}\rho_k)\boldsymbol{Y}'_{\boldsymbol{\nu}}(k_{\rho e_k}\rho_{k-1})\end{aligned} \tag{C.7}$$

$$\begin{aligned}\boldsymbol{s}_{\boldsymbol{\nu}e_k} = {} & \boldsymbol{J}'_{\boldsymbol{\nu}}(k_{\rho e_k}\rho_{k-1})\boldsymbol{Y}'_{\boldsymbol{\nu}}(k_{\rho e_k}\rho_k) \\ & -\boldsymbol{J}'_{\boldsymbol{\nu}}(k_{\rho e_k}\rho_k)\boldsymbol{Y}'_{\boldsymbol{\nu}}(k_{\rho e_k}\rho_{k-1}).\end{aligned} \tag{C.8}$$

We can model the inner layer by the admittance matrix $\widetilde{\boldsymbol{Y}}_0$ and the outer unbounded medium surrounding the structure by $\widetilde{\boldsymbol{Y}}_n$. We write the expression as

$$\widetilde{\boldsymbol{Y}}_{0,n} = \frac{-1}{\mu_t}\begin{bmatrix} -\varepsilon_{dt}\boldsymbol{u}^{-1}_{\boldsymbol{\nu}h} & -k_z\nu\boldsymbol{u}^{-1}_{\boldsymbol{\nu}h} \\ -k_z\nu\boldsymbol{u}^{-1}_{\boldsymbol{\nu}h} & \varepsilon^{-1}_{dt}(-k_z^2\nu^2\boldsymbol{u}^{-1}_{\boldsymbol{\nu}h} + \varepsilon_t\mu_t\boldsymbol{u}_{\boldsymbol{\nu}e}) \end{bmatrix}_{0,n}, \tag{C.9}$$

where

$$\boldsymbol{u}_{\boldsymbol{\nu}e_0} = k_{\rho e_0}\rho_0\frac{\boldsymbol{J}'_{\boldsymbol{\nu}}(k_{\rho e_0}\rho_0)}{\boldsymbol{J}_{\boldsymbol{\nu}}(k_{\rho e_0}\rho_0)}, \tag{C.10}$$

$$\boldsymbol{u}_{\boldsymbol{\nu}e_n} = k_{\rho e_n}\rho_n\frac{\boldsymbol{H}'^{(2)}_{\boldsymbol{\nu}}(k_{\rho e_n}\rho_n)}{\boldsymbol{H}^{(2)}_{\boldsymbol{\nu}}(k_{\rho e_n}\rho_n)}. \tag{C.11}$$

Similar equations follow for H_z or TE mode, whereby the subscript e is replaced by h (or $k_{\rho e} \to k_{\rho h}$).

C.2 Equations for Spatial Domain

For any arbitrary layer k, we obtain the equations for 1D discretization as

$$\begin{aligned} E_{z_k}(\rho, \phi^e, z) &= \sum_{i}^{N^e} (A_{k_i} P_i^A + B_{k_i} P_i^B) \\ H_{z_k}(\rho, \phi^e, z) &= \sum_{i}^{N^h} (C_{k_i} P_i^C + D_{k_i} P_i^D), \end{aligned} \tag{C.12}$$

where

$$\begin{aligned} P_i^A &= J_{\nu_i}(k_{\rho e}\rho)\tau_\phi^e(\nu_i, \phi^e)e^{-jk_z z} \\ P_i^B &= Y_{\nu_i}(k_{\rho e}\rho)\tau_\phi^e(\nu_i, \phi^e)e^{-jk_z z} \\ P_i^C &= J_{\nu_i}(k_{\rho h}\rho)\tau_\phi^h(\nu_i, \phi^h)e^{-jk_z z} \\ P_i^D &= Y_{\nu_i}(k_{\rho h}\rho)\tau_\phi^h(\nu_i, \phi^h)e^{-jk_z z}. \end{aligned} \tag{C.13}$$

For 2D discretization

$$\begin{aligned} E_{z_k}(\rho, \phi^e, z^e) &= \sum_{i}^{N_\phi^e} \sum_{l}^{N_z^e} (A_{k_{il}} P_{il}^A + B_{k_{il}} P_{il}^B) \\ H_{z_k}(\rho, \phi^h, z^h) &= \sum_{i}^{N_\phi^h} \sum_{l}^{N_z^h} (C_{k_{il}} P_{il}^C + D_{k_{il}} P_{il}^D), \end{aligned} \tag{C.14}$$

where

$$\begin{aligned} P_{il}^A &= J_{\nu_{il}}(k_{\rho e}\rho)\tau_\phi^e(\nu_i, \phi^e)\tau_z^e(k_{zl}, z^e) \\ P_{il}^B &= Y_{\nu_{il}}(k_{\rho e}\rho)\tau_\phi^e(\nu_i, \phi^e)\tau_z^e(k_{zl}, z^e) \\ P_{il}^C &= J_{\nu_{il}}(k_{\rho h}\rho)\tau_\phi^h(\nu_i, \phi^h)\tau_z^h(k_{zl}, z^h) \\ P_{il}^D &= Y_{\nu_{il}}(k_{\rho h}\rho)\tau_\phi^h(\nu_i, \phi^h)\tau_z^h(k_{zl}, z^h). \end{aligned} \tag{C.15}$$

We write the expressions used in Chapter 5 as

$$Q_{t\phi} = Q_\phi \cos\alpha_\phi^h + \bar{Q}_\rho \sin\alpha_\phi^h \tag{C.16}$$

$$Q_\phi^A = \frac{D_\phi D_z P^A}{e_{dt}\rho} \tag{C.17}$$

$$Q_\phi^B = \frac{D_\phi D_z P^B}{e_{dt}\rho} \tag{C.18}$$

$$Q_\phi^C = \frac{j\mu_t D_\rho P^C}{e_{dt}} \tag{C.19}$$

$$Q_\phi^D = \frac{j\mu_t D_\rho P^D}{e_{dt}} \tag{C.20}$$

$$Q_\rho^A = \frac{D_\rho D_z P^A}{e_{dt}} \tag{C.21}$$

$$Q_\rho^B = \frac{D_\rho D_z P^B}{e_{dt}} \tag{C.22}$$
$$Q_\rho^C = -\frac{j\mu_t D_\phi P^C}{e_{dt}\rho} \tag{C.23}$$
$$Q_\rho^D = -\frac{j\mu_t D_\phi P^D}{e_{dt}\rho} \tag{C.24}$$
$$Q_{tz} = Q_z \cos\alpha_z^e + \bar{Q}_\rho \sin\alpha_z^e \tag{C.25}$$
$$Q_z^A = P^A \tag{C.26}$$
$$Q_z^B = P^B \tag{C.27}$$
$$Q_z^C = 0 \tag{C.28}$$
$$Q_z^D = 0 \tag{C.29}$$

$$G_{t\phi} = G_\phi \cos\alpha_\phi^e + \bar{G}_\rho \sin\alpha_\phi^e \tag{C.30}$$
$$G_\phi^A = \frac{j\varepsilon_t D_\rho P^A}{e_{dt}} \tag{C.31}$$
$$G_\phi^B = \frac{j\varepsilon_t D_\rho P^B}{e_{dt}} \tag{C.32}$$
$$G_\phi^C = \frac{D_\phi D_z P^C}{e_{dt}\rho} \tag{C.33}$$
$$G_\phi^D = \frac{D_\phi D_z P^D}{e_{dt}\rho} \tag{C.34}$$
$$G_\rho^A = \frac{j\varepsilon_t D_\phi P^A}{e_{dt}\rho} \tag{C.35}$$
$$G_\rho^B = \frac{j\varepsilon_t D_\phi P^B}{e_{dt}\rho} \tag{C.36}$$
$$G_\rho^C = \frac{D_\rho D_z P^C}{e_{dt}} \tag{C.37}$$
$$G_\rho^D = \frac{D_\rho D_z P^D}{e_{dt}} \tag{C.38}$$
$$G_{tz} = G_z \cos\alpha_z^h + \bar{G}_\rho \sin\alpha_z^h \tag{C.39}$$
$$G_z^A = 0 \tag{C.40}$$
$$G_z^B = 0 \tag{C.41}$$
$$G_z^C = P^C \tag{C.42}$$
$$G_z^D = P^D, \tag{C.43}$$

where $e_{dt} = \varepsilon_t\mu_t - k_z^2$.

For inner layer extending from 0 to ρ_0 (denoted by 0) and outer unbounded layer (denoted by n), we obtain the equations for 1D discretization as

$$E_{z_{0,n}}(\rho, \phi^e, z) = \sum_i^{N^e} A_{0,n_i} P_{0,n_i}^A$$

$$H_{z_{0,n}}(\rho, \phi^h, z) = \sum_{i}^{N^h} C_{0,n_i} P^C_{0,n_i}, \tag{C.44}$$

where

$$\begin{aligned} P^A_{0_i} &= J_{\nu_i}(k_{\rho e_0}\rho)\tau^e_\phi(\nu_i, \phi^e)e^{-jk_z z} \\ P^C_{0_i} &= J_{\nu_i}(k_{\rho h_0}\rho)\tau^h_\phi(\nu_i, \phi^h)e^{-jk_z z} \end{aligned} \tag{C.45}$$

and

$$\begin{aligned} P^A_{n_i} &= H^{(2)}_{\nu_i}(k_{\rho e_n}\rho)\tau^e_\phi(\nu_i, \phi^e)e^{-jk_z z} \\ P^C_{n_i} &= H^{(2)}_{\nu_i}(k_{\rho h_n}\rho)\tau^h_\phi(\nu_i, \phi^h)e^{-jk_z z}. \end{aligned} \tag{C.46}$$

For 2D discretization

$$\begin{aligned} E_{z_{0,n}}(\rho, \phi^e, z^e) &= \sum_{i}^{N^e_\phi}\sum_{l}^{N^e_z} A_{0,n_{il}} P^A_{0,n_{il}} \\ H_{z_{0,n}}(\rho, \phi^h, z^h) &= \sum_{i}^{N^h_\phi}\sum_{l}^{N^h_z} C_{0,n_{il}} P^C_{0,n_{il}}, \end{aligned} \tag{C.47}$$

where

$$\begin{aligned} P^A_{0_{il}} &= J_{\nu_{il}}(k_{\rho e_0}\rho)\tau^e_\phi(\nu_i, \phi^e)\tau^e_z(k_{zl}, z^e) \\ P^C_{0_{il}} &= J_{\nu_{il}}(k_{\rho h_0}\rho)\tau^h_\phi(\nu_i, \phi^h)\tau^h_z(k_{zl}, z^h) \end{aligned} \tag{C.48}$$

and

$$\begin{aligned} P^A_{n_{il}} &= H^{(2)}_{\nu_{il}}(k_{\rho e_n}\rho)\tau^e_\phi(\nu_i, \phi^e)\tau^e_z(k_{zl}, z^e) \\ P^C_{n_{il}} &= H^{(2)}_{\nu_{il}}(k_{\rho h_n}\rho)\tau^h_\phi(\nu_i, \phi^h)\tau^h_z(k_{zl}, z^h). \end{aligned} \tag{C.49}$$

C.3 Eigensolutions of the Helmholtz Equation

The eigensolutions in both ϕ- and z-directions are summarized in the Table C.1 and C.2, respectively, where ϕ_0 is the angular distance between walls along azimuth (ϕ) and a is the distance between walls in the axial direction (z).

Table C.1: Eigensolutions of the Helmholtz equation in azimuth direction for different boundary combinations

Boundary combination along azimuth	$\tau^e_{\phi i}$	$\tau^h_{\phi i}$	ν_i
E-wall/E-wall	$-j\sin(\nu_i\phi^e)$	$\cos(\nu_i\phi^h)$	$\frac{i\pi}{\phi_0}$
H-wall/H-wall	$\cos(\nu_i\phi^e)$	$-j\sin(\nu_i\phi^h)$	$\frac{i\pi}{\phi_0}$
H-wall/E-wall	$\cos(\nu_i\phi^e)$	$-j\sin(\nu_i\phi^h)$	$\frac{(i-\frac{1}{2})\pi}{\phi_0}$
Closed Cylinder	$\exp^{-j\nu_i\phi^e}$	$\exp^{-j\nu_i\phi^h}$	i

Table C.2: Eigensolutions of the Helmholtz equation in axial direction for different boundary combinations

Boundary combination (left/right)	τ^e_{zl}	τ^h_{zl}	k_{zl}
E-wall/E-wall	$\cos(k_{zl}z^e)$	$-j\sin(k_{zl}z^h)$	$\frac{l\pi}{a}$
H-wall/H-wall	$-j\sin(k_{zl}z^e)$	$\cos(k_{zl}z^h)$	$\frac{l\pi}{a}$
H-wall/E-wall	$-j\sin(k_{zl}z^e)$	$\cos(k_{zl}z^h)$	$\frac{(l-\frac{1}{2})\pi}{a}$
ABC/ABC	$\cos(k_{zl}z^e)$ $-j\sin(k_{z(l+1)}z^e)$ $\vdots$ (alternating)	$-j\sin(k_{zl}z^h)$ $\cos(k_{z(l+1)}z^h)$ $\vdots$ (alternating)	k_{zl} satisfying B_z=+A_z $k_{z(l+1)}$ satisfying B_z=-A_z $\vdots$ (alternating)
E-wall/ABC	$\cos(k_{zl}z^e)$	$-j\sin(k_{zl}z^h)$	k_{zl} satisfying B_z=+A_z
H-wall/ABC	$-j\sin(k_{zl}z^e)$	$\cos(k_{zl}z^h)$	k_{zl} satisfying B_z=-A_z

D Discretization with Symmetry

D.1 Cartesian Coordinate System

D.1.1 1D Discretization

When the microstrip transmission line presents a symmetry, then only half of the structure needs to be analyzed. Fig. D.1a shows the discretization when structure is truncated in half by the H-wall in the middle and Fig. D.1b shows when the structure is truncated by the E-wall in the middle. Let us assume that the number of e-lines present on half of the strip in x-direction is N_{es} with discretization distance of Δx between the lines. Then the width of the strip becomes

$$W = 2(N_{es} - 0.25)\Delta x \tag{D.1}$$

for an H-wall in the middle and

$$W = 2(N_{es} + 0.25)\Delta x \tag{D.2}$$

for an E-wall in the middle.

D.1.2 2D Discretization

We take a microstrip patch antenna surrounded by E-walls in x-direction and H-walls in y-direction. Let us assume that the number of eh-lines present on half of the patch in x-direction is N_{ehp_x} and in y-direction is N_{ehp_y}. The discretization distance between lines in x-direction is Δx and in y-direction is Δy. When we truncate the patch by placing an H-wall in the center in x-direction (Fig. D.2a), then the patch dimensions become

$$P_a = 2(N_{ehp_x} - 0.25)\Delta x, \tag{D.3}$$

$$P_b = (N_{ehp_y} + 0.5)\Delta y. \tag{D.4}$$

In case of symmetry with E-wall in the middle of the structure (Fig. D.2b), the patch dimensions become

$$P_a = 2(N_{ehp_x} + 0.25)\Delta x, \tag{D.5}$$

$$P_b = (N_{ehp_y} + 0.5)\Delta y. \tag{D.6}$$

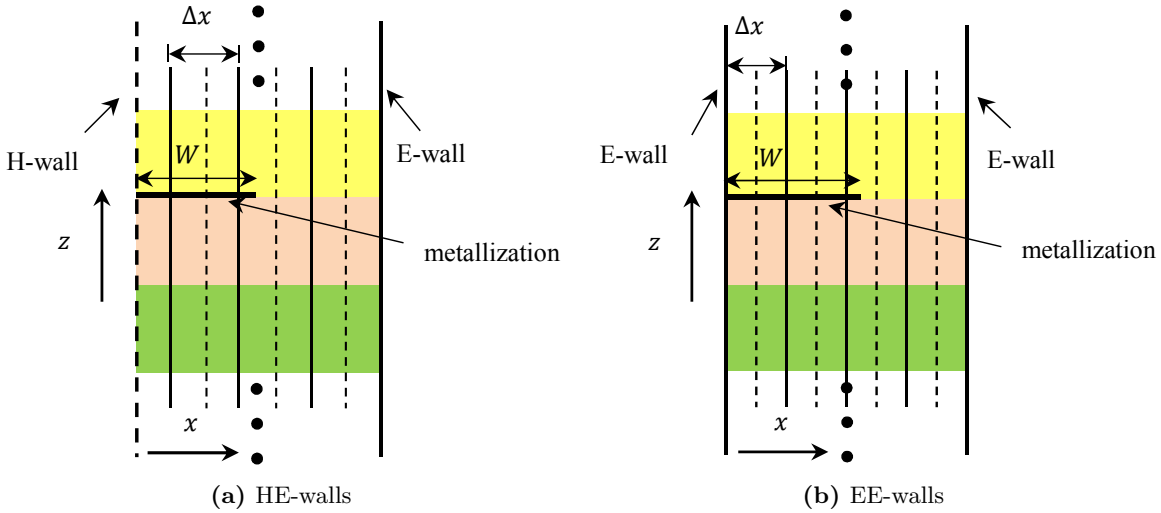

(a) HE-walls **(b)** EE-walls

Figure D.1: 1D discretization scheme for half of the microstrip structure in Cartesian coordinate system. (— e-line (E_z, E_y, H_x), - - - h-line (H_z, H_y, E_x))

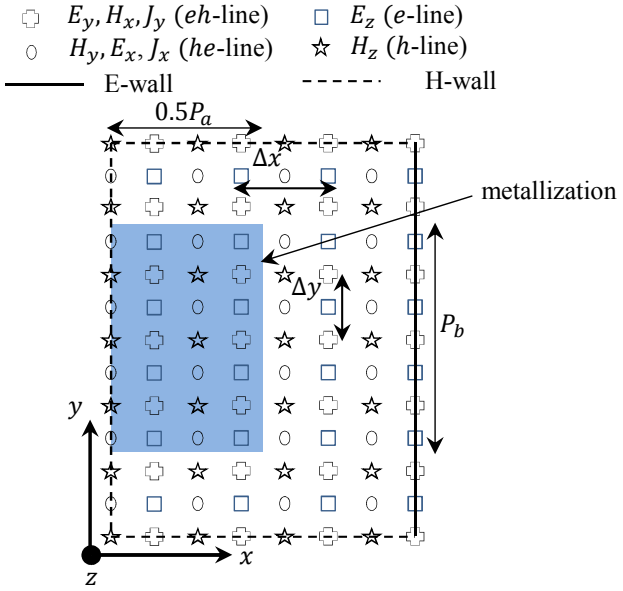

(a) HE/HH-walls

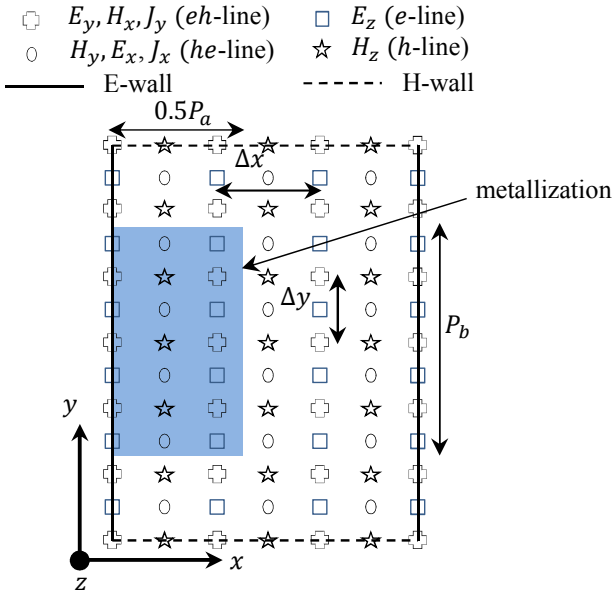

(b) EE/HH-walls

Figure D.2: 2D discretization scheme for half of the microstrip patch in Cartesian coordinate system.

For resonance along y, we need to analyze only a quarter of the structure with the symmetry conditions shown in Fig. D.3a. Here we truncate the microstrip patch with H-wall in x-direction and E-wall in y-direction. In short, the structure is bounded by HE-walls in x-direction and EH-walls in y-direction. The number of eh-lines placed on quarter of the patch are N_{ehp_x} and N_{ehp_y} in x- and y-directions, respectively. The patch dimensions in this case become

$$P_a = 2(N_{ehp_x} - 0.25)\Delta x, \tag{D.7}$$

$$P_b = 2(N_{ehp_y} + 0.25)\Delta y. \tag{D.8}$$

For resonance along x, we also need to analyze only a quarter of the structure with the symmetry conditions shown in Fig. D.3b. Here we truncate the microstrip patch with E-wall in x-direction and H-wall in y-direction. In short, the structure is bounded by EE-walls in x-direction and HH-walls in y-direction. The patch dimensions in this case become

$$P_a = 2(N_{ehp_x} + 0.25)\Delta x, \tag{D.9}$$

$$P_b = 2(N_{ehp_y} + 0.75)\Delta y. \tag{D.10}$$

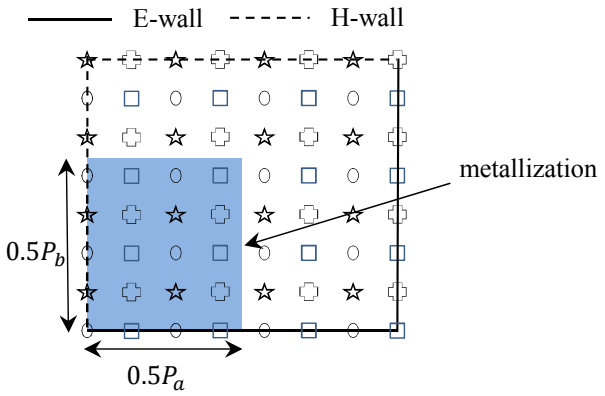

(a) HE/EH-walls

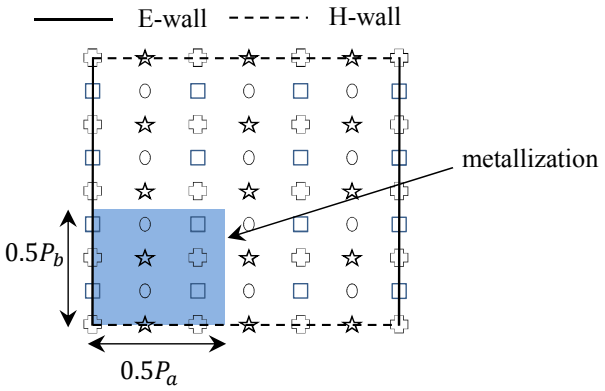

(b) EE/HH-walls

Figure D.3: 2D discretization scheme for a quarter of the microstrip patch.

D.2 Cylindrical Coordinate System

D.2.1 1D Discretization

Similar discretization happens in cylindrical structures as in planar structures. The difference comes in the location of the field components. Fig. D.4 gives the discretization of the cross-section of cylindrical microstrip lines. The computational domain of the structure can be truncated by placing E-walls or H-walls as given in Fig. D.4a and D.4b respectively. When there are N_{es} number of e-lines present on the strip in ϕ-direction, then the strip width becomes

$$W = (N_{es} - 0.5)\Delta\phi, \tag{D.11}$$

where $\Delta\phi$ is the discretization distance between the lines. A quarter sector can also be analyzed using H-wall symmetry in the middle of the strip as shown in Fig. D.4c. The total width of the microstrip is equal to

$$W = 2(N_{es} - 0.25)\Delta\phi, \tag{D.12}$$

with N_{es} e-lines placed on half of the strip.

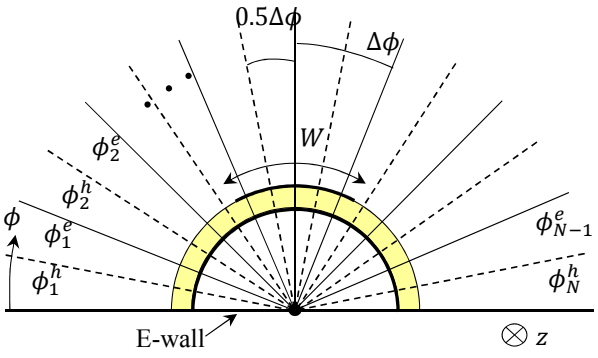

(a) EE-walls

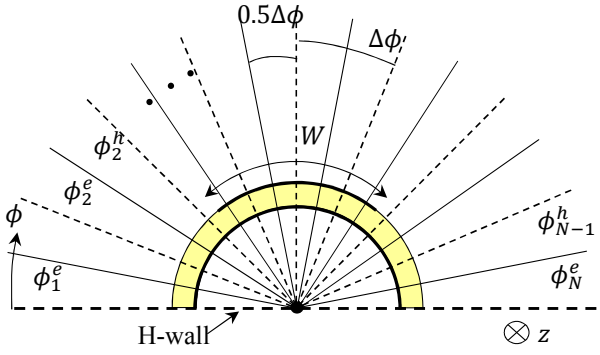

(b) HH-walls

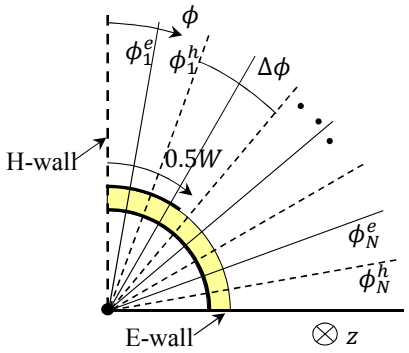

(c) HE-walls

Figure D.4: 1D discretization scheme for half of the microstrip structure in a cylindrical coordinate system. (— e-line (E_z, E_ρ, H_ϕ), - - - h-line (H_z, H_ρ, E_ϕ))

D.2.2 2D Discretization

We take the microstrip patch present on the cylindrical substrate. We bound the domain of the cylinder with EE-walls in ϕ-direction and HH-walls in z-direction. Similar to the Cartesian coordinate system, here also we need to analyze only half of the domain due to the symmetry present in the patch structure. The top half view of the rectangular microstrip patch present on the cylindrical structure is depicted in Fig. D.5. We consider that the number of e-lines present on half of the patch along ϕ and z is N_{ep_ϕ} and N_{ep_z}, respectively. When we truncate the patch by placing an H-wall in the center in ϕ-direction (Fig. D.5a), then the patch dimensions become

$$P_a = 2(N_{ep_\phi} - 0.25)\Delta\phi, \tag{D.13}$$

$$P_b = (N_{ep_z} + 0.5)\Delta z, \tag{D.14}$$

where $\Delta\phi$ and Δz are the discretization distances in ϕ- and z-directions, respectively. In case of symmetry with E-wall in the middle of the structure (Fig. D.5b), the patch dimensions become

$$P_a = 2(N_{ep_\phi} + 0.25)\Delta\phi, \tag{D.15}$$

$$P_b = (N_{ep_z} + 0.5)\Delta z. \tag{D.16}$$

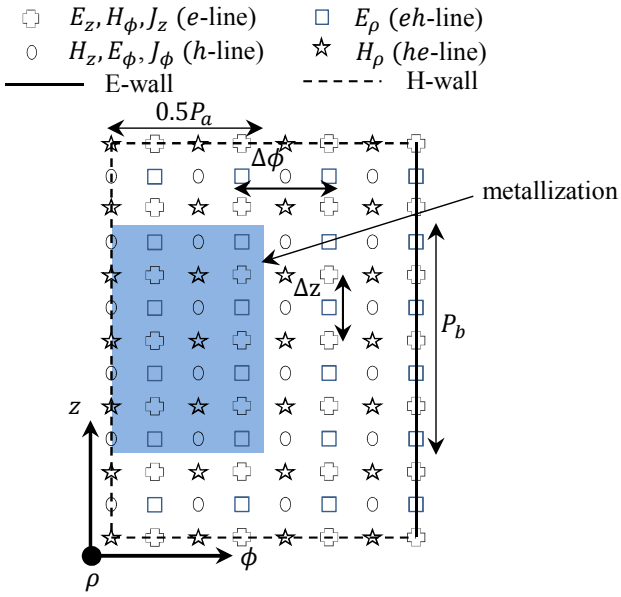

(a) HE/HH-walls

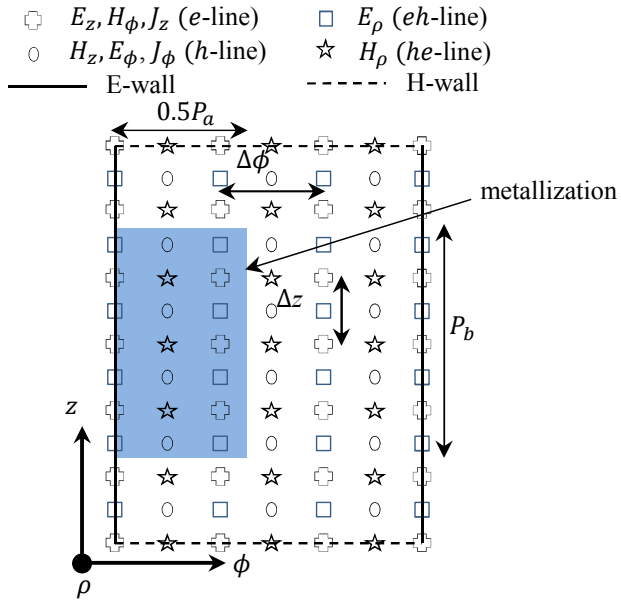

(b) EE/HH-walls

Figure D.5: 2D discretization scheme for half of the microstrip patch in a cylindrical coordinate system.

The discretization for a quarter of the patch for resonance in z- or ϕ-direction follows the same pattern as shown in Fig. D.3a and D.3b, respectively. The field locations are the same as in Fig. D.5. The patch dimensions for first case in Fig. D.3a become

$$P_a = 2(N_{ep_\phi} - 0.25)\Delta\phi, \tag{D.17}$$

$$P_b = 2(N_{ep_z} + 0.25)\Delta z, \tag{D.18}$$

while the patch dimensions for second case in Fig. D.3b become

$$P_a = 2(N_{ep_\phi} + 0.25)\Delta\phi, \tag{D.19}$$

$$P_b = 2(N_{ep_z} + 0.75)\Delta z. \tag{D.20}$$

List of Symbols

Latin Symbols

Symbol	Description	Unit
A	major axis of the elliptical cross-section	m
B	minor axis of the elliptical cross-section	m
$\vec{B}$	magnetic flux density vector	V s m^{-2}
$\boldsymbol{B}_k$	submatrix of $\boldsymbol{K}_k$	
$\widetilde{\boldsymbol{B}}_k$	submatrix of $\widetilde{\boldsymbol{K}}_k$	
$\vec{D}$	electric displacement vector	A s m^{-2}
$\vec{E}$	electric field vector	V m^{-1} or $V^{\#}$
$\boldsymbol{E}$	electric field column matrix of system of equations in spatial domain	V
$\widetilde{\boldsymbol{E}}$	electric field column matrix of system of equations in spectral domain	V
$\boldsymbol{E}_k$	column matrix of FWEC that represents the electric field tangential to the k^{th} interface in spatial domain	V
$\boldsymbol{E}_k^+$	column matrix of FWEC that represents the tangential electric field above the k^{th} interface in spatial domain	V
$\boldsymbol{E}_k^-$	column matrix of FWEC that represents the tangential electric field below the k^{th} interface in spatial domain	V
$\widetilde{\boldsymbol{E}}_k$	column matrix of FWEC that represents the electric field tangential to the k^{th} interface in spectral domain	V
$\widetilde{\boldsymbol{E}}_k^+$	column matrix of FWEC that represents the tangential electric field above the k^{th} interface in spectral domain	V
$\widetilde{\boldsymbol{E}}_k^-$	column matrix of FWEC that represents the tangential electric field below the k^{th} interface in spectral domain	V
$\boldsymbol{E}_{\text{red}}$	reduced form of $\boldsymbol{E}$	V
$\vec{E}(x, y, z)$	electric field vector in rectangular coordinate system	V m^{-1}
$\vec{E}(\rho, \phi, z)$	electric field vector in cylindrical coordinate system	V m^{-1}

Symbol	Description	Unit
$\vec{E}(\xi, \eta, z)$	electric field vector in elliptical coordinate system	V m^{-1}
E_{tx}	electric field along x tangential to the k^{th} interface	V
$\boldsymbol{E}_{tx}$	column matrix containing the sampled E_{tx}	V
E_{tz}	electric field along z tangential to the k^{th} interface	V
$\boldsymbol{E}_{tz}$	column matrix containing the sampled E_{tz}	V
$E_{t\phi}$	electric field along ϕ tangential to the k^{th} interface	V
$\boldsymbol{E}_{t\phi}$	column matrix containing the sampled $E_{t\phi}$	V
E_x	x-oriented electric field component	V
$\boldsymbol{E}_x$	column matrix containing the sampled E_x in spatial domain	V
$\tilde{E}_x$	field component E_x in spectral domain	V
$\widetilde{\boldsymbol{E}}_x$	column matrix containing the modal values of $\tilde{E}_x$	V
$\widetilde{\boldsymbol{E}}_{x_k}$	column matrix containing the modal values of $\tilde{E}_x$ in the k^{th} interface	V
E_y	y-oriented electric field component	V
$\boldsymbol{E}_y$	column matrix containing the sampled E_y in spatial domain	V
$\tilde{E}_y$	field component E_y in spectral domain	V
$\widetilde{\boldsymbol{E}}_y$	column matrix containing the modal values of $\tilde{E}_z$	V
$\widetilde{\boldsymbol{E}}_{y_k}$	column matrix containing the modal values of $\tilde{E}_y$ in the k^{th} interface	V
E_z	z-oriented electric field component	V m^{-1}** or V
$\boldsymbol{E}_z$	column matrix containing the sampled E_z in spatial domain	V
$\tilde{E}_z$	field component E_z in spectral domain	V
$\widetilde{\boldsymbol{E}}_z$	column matrix containing the modal values of $\tilde{E}_z$	V
E_{z_k}	z-oriented electric field component in the k^{th} layer	V
$\boldsymbol{E}_{z_k}$	column matrix containing the sampled E_z in the k^{th} interface	V
$\widetilde{\boldsymbol{E}}_{z_k}$	column matrix containing the modal values of $\tilde{E}_z$ in the k^{th} interface	V
$\bar{E}_{z_k}$	interpolated E_{z_k}	V
E_ϕ	ϕ-oriented electric field component	V
$\boldsymbol{E}_\phi$	column matrix containing the sampled E_ϕ in spatial domain	V
$\tilde{E}_\phi$	field component E_ϕ in spectral domain	V

Symbol	Description	Unit
$\widetilde{\boldsymbol{E}}_\phi$	column matrix containing the modal values of $\tilde{E}_\phi$	V
E_{ϕ_k}	ϕ-oriented electric field component in the k^{th} layer	V
$\widetilde{\boldsymbol{E}}_{\phi_k}$	column matrix containing the modal values of $\tilde{E}_\phi$ in the k^{th} interface	V
E_ρ	ρ-oriented electric field component	V
$\tilde{E}_\rho$	field component E_ρ in spectral domain	V
$\widetilde{\boldsymbol{E}}_\rho$	column matrix containing the modal values of $\tilde{E}_\rho$	V
E_{ρ_k}	ρ-oriented electric field component in the k^{th} layer	V
$\bar{E}_{\rho_k}$	interpolated E_{ρ_k}	V
E_ξ	ξ-oriented electric field component	V m^{-1}
E_η	η-oriented electric field component	V m^{-1}
$\boldsymbol{E}_{\eta_k}$	column matrix containing the sampled E_η in the k^{th} interface	V m^{-1}
$\boldsymbol{E}_\theta$	column matrix containing electric field along θ	V
$\boldsymbol{E}_\phi$	column matrix containing electric field along ϕ	V
$\boldsymbol{G}$	matrix of the system of equations in the spatial domain whose elements are according to the Green's function of the structure	
$\widetilde{\boldsymbol{G}}$	matrix of the system of equations in the spectral domain whose elements are according to the Green's function of the structure	
$\boldsymbol{G}_{\text{red}}$	reduced form of $\boldsymbol{G}$	
$\boldsymbol{G}_{xx}$	submatrix of $\boldsymbol{G}$	
$\widetilde{\boldsymbol{G}}_{xx}$	submatrix of $\widetilde{\boldsymbol{G}}$	
$\boldsymbol{G}_{xy}$	submatrix of $\boldsymbol{G}$	
$\widetilde{\boldsymbol{G}}_{xy}$	submatrix of $\widetilde{\boldsymbol{G}}$	
$\boldsymbol{G}_{yx}$	submatrix of $\boldsymbol{G}$	
$\widetilde{\boldsymbol{G}}_{yx}$	submatrix of $\widetilde{\boldsymbol{G}}$	
$\boldsymbol{G}_{yy}$	submatrix of $\boldsymbol{G}$	
$\widetilde{\boldsymbol{G}}_{yy}$	submatrix of $\widetilde{\boldsymbol{G}}$	
$\vec{H}$	magnetic field vector	A m^{-1} or A Ω*
$\boldsymbol{H}_k$	column matrix of FWEC that represents the magnetic field tangential to the k^{th} interface in spatial domain	A Ω

Symbol	Description	Unit
$\boldsymbol{H}_k^+$	column matrix of FWEC that represents the tangential magnetic field above the k^{th} interface in spatial domain	A Ω
$\boldsymbol{H}_k^-$	column matrix of FWEC that represents the tangential magnetic field below the k^{th} interface in spatial domain	A Ω
$\widetilde{\boldsymbol{H}}_k$	column matrix of FWEC that represents the magnetic field tangential to the k^{th} interface in spectral domain	A Ω
$\widetilde{\boldsymbol{H}}_k^+$	column matrix of FWEC that represents the tangential magnetic field above the k^{th} interface in spectral domain	A Ω
$\widetilde{\boldsymbol{H}}_k^-$	column matrix of FWEC that represents the tangential magnetic field below the k^{th} interface in spectral domain	A Ω
$\vec{H}(x,y,z)$	magnetic field vector in rectangular coordinate system	A m^{-1}
$\vec{H}(\rho,\phi,z)$	magnetic field vector in cylindrical coordinate system	A m^{-1}
$\vec{H}(\xi,\eta,z)$	magnetic field vector in elliptical coordinate system	A m^{-1}
H_{tx}	magnetic field along x tangential to the k^{th} interface	A Ω
$\boldsymbol{H}_{tx}$	column matrix containing the sampled H_{tx} in the k^{th} interface	A Ω
H_{tz}	magnetic field along z tangential to the k^{th} interface	A Ω
$\boldsymbol{H}_{tz}$	column matrix containing the sampled H_{tz} in the k^{th} interface	A Ω
$H_{t\phi}$	magnetic field along ϕ tangential to the k^{th} interface	A Ω
$\boldsymbol{H}_{t\phi}$	column matrix containing the sampled $H_{t\phi}$ in the k^{th} interface	A Ω
H_x	x-oriented magnetic field component	A Ω
$\boldsymbol{H}_x$	column matrix containing the sampled H_x in spatial domain	A Ω
$\tilde{H}_x$	field component H_x in spectral domain	A Ω
$\widetilde{\boldsymbol{H}}_x$	column matrix containing the modal values of $\tilde{H}_x$	A Ω
$\widetilde{\boldsymbol{H}}_{x_k}$	column matrix containing the modal values of $\tilde{H}_x$ in the k^{th} interface	A Ω
H_y	y-oriented magnetic field component	A Ω
$\boldsymbol{H}_y$	column matrix containing the sampled H_y in spatial domain	A Ω
$\tilde{H}_y$	field component H_y in spectral domain	A Ω
$\widetilde{\boldsymbol{H}}_y$	column matrix containing the modal values of $\tilde{H}_y$	A Ω
$\widetilde{\boldsymbol{H}}_{y_k}$	column matrix containing the modal values of $\tilde{H}_y$ in the k^{th} interface	A Ω
H_z	z-oriented magnetic field component	A m^{-1}** or A Ω

Symbol	Description	Unit
$\boldsymbol{H}_z$	column matrix containing the sampled H_z in spatial domain	A Ω
$\tilde{H}_z$	field component H_z in spectral domain	A Ω
$\widetilde{\boldsymbol{H}}_z$	column matrix containing the modal values of $\tilde{H}_z$	A Ω
H_{z_k}	z-oriented magnetic field component in the k^{th} layer	A Ω
$\boldsymbol{H}_{z_k}$	column matrix containing the sampled H_z in the k^{th} interface	A Ω
$\widetilde{\boldsymbol{H}}_{z_k}$	column matrix containing the modal values of $\tilde{H}_z$ in the k^{th} interface	A Ω
$\bar{H}_{z_k}$	interpolated H_{z_k}	A Ω
H_ϕ	ϕ-oriented magnetic field component	A Ω
$\tilde{H}_\phi$	field component H_ϕ in spectral domain	A Ω
$\widetilde{\boldsymbol{H}}_\phi$	column matrix containing the modal values of $\tilde{H}_\phi$	A Ω
H_{ϕ_k}	ϕ-oriented magnetic field component in the k^{th} layer	A Ω
$\widetilde{\boldsymbol{H}}_{\phi_k}$	column matrix containing the modal values of $\tilde{H}_\phi$ in the k^{th} interface	A Ω
H_ρ	ρ-oriented magnetic field component	A Ω
$\tilde{H}_\rho$	field component H_ρ in spectral domain	A Ω
$\widetilde{\boldsymbol{H}}_\rho$	column matrix containing the modal values of $\tilde{H}_\rho$	A Ω
H_{ρ_k}	ρ-oriented magnetic field component in the k^{th} layer	A Ω
$\bar{H}_{\rho_k}$	interpolated H_{ρ_k}	A Ω
H_ξ	ξ-oriented magnetic field component	A m^{-1}
H_η	η-oriented magnetic field component	A m^{-1}
$\boldsymbol{H}_{\eta_k}$	column matrix containing the sampled H_η in the k^{th} interface	A m^{-1}
$\boldsymbol{J}$	surface current density column matrix of system of equations in spatial domain	A Ω
$\widetilde{\boldsymbol{J}}$	surface current density column matrix of system of equations in spectral domain	A Ω
$\widetilde{\boldsymbol{J}}_k$	column matrix of FWEC that represents the surface current density tangential to the k^{th} interface in spectral domain	A Ω
$\boldsymbol{J}_{\text{red}}$	reduced form of $\boldsymbol{J}$	A Ω
J_{tz}	surface current density along z tangential to the k^{th} interface	A Ω
$\boldsymbol{J}_{tz}$	column matrix containing the sampled J_{tz} in the k^{th} interface	A Ω
$J_{t\phi}$	surface current density along z tangential to the k^{th} interface	A Ω

Symbol	Description	Unit
$\boldsymbol{J}_{t\phi}$	column matrix containing the sampled J_{tz} in the k^{th} interface	A Ω
$\boldsymbol{J}_x$	column matrix containing the sampled surface current density along x in spatial domain	A Ω
$\widetilde{\boldsymbol{J}}_x$	column matrix containing the modal values of surface current density along x in spectral domain	A Ω
$\boldsymbol{J}_y$	column matrix containing the sampled surface current density along y in spatial domain	A Ω
$\widetilde{\boldsymbol{J}}_y$	column matrix containing the modal values of surface current density along y in spectral domain	A Ω
$\boldsymbol{J}_z$	column matrix containing the sampled surface current density along z in spatial domain	A Ω
$\widetilde{\boldsymbol{J}}_z$	column matrix containing the modal values of surface current density along z in spectral domain	A Ω
$\boldsymbol{J}_\phi$	column matrix containing the sampled surface current density along ϕ in spatial domain	A Ω
k	index for the sequence of the dielectric layer in stratified media	
K	propagation constant	
k_0	propagation constant in the vacuum	m^{-1}
$\widetilde{\boldsymbol{K}}_{eq}$	equivalent hybrid matrix obtained after multiplications of cascaded $\widetilde{\boldsymbol{K}}_k$ matrices	
$\boldsymbol{K}_k$	hybrid matrix of the k^{th} layer in FWEC in the spatial domain	
$\widetilde{\boldsymbol{K}}_k$	hybrid matrix of the k^{th} layer in FWEC in the spectral domain	
k_x	spectral variable in x-direction	
k_y	spectral variable in y-direction	
k_{xi}	spectral variable in x-direction of order i	
k_{yi}	spectral variable in y-direction of order i	
k_z	spectral variable/wave number in z-direction	
k_{zi}	spectral variable in z-direction of order i	
k_{ze}	wave number in z-direction for e-lines	
k_{zh}	wave number in z-direction for h-lines	
k_ρ	wave number in ρ-direction	
$k_{\rho e}$	wave number in ρ-direction for e-lines	
$k_{\rho h}$	wave number in ρ-direction for h-lines	

Symbol	Description	Unit
n	total number of layers	
N_x	number of modes in x-direction	
N_y	number of modes in y-direction	
N_z	number of modes in z-direction	
N_ϕ	number of modes in ϕ-direction	
$\boldsymbol{L}$	matrix of the admittance as given by system of equations in the spatial domain	
$\widetilde{\boldsymbol{L}}$	matrix of the admittance as given by system of equations in the spectral domain	
$\boldsymbol{L}_{\mathrm{red}}$	reduced form of $\boldsymbol{L}$	
$\widetilde{\boldsymbol{L}}_{k,k}$	submatrix of $\widetilde{\boldsymbol{L}}$	
P_a	patch width	m
P_b	patch length	m
S_a	substrate width	m
S_b	substrate length	m
$\boldsymbol{T}_e$	transformation matrix for e-lines	
$\boldsymbol{T}_{ee}$	transformation matrix for e, e-lines in 2D discretization	
$\boldsymbol{T}_{eh}$	transformation matrix for e, h-lines in 2D discretization	
$\boldsymbol{T}_h$	transformation matrix for h-lines	
$\boldsymbol{T}_{he}$	transformation matrix for h, e-lines in 2D discretization	
$\boldsymbol{T}_{hh}$	transformation matrix for h, h-lines in 2D discretization	
$\boldsymbol{V}_k$	submatrix of $\boldsymbol{K}_k$	
$\widetilde{\boldsymbol{V}}_k$	submatrix of $\widetilde{\boldsymbol{K}}_k$	
x	coordinate of rectangular coordinate system (normalized by k_0)	
x'	x-coordinate of a point source	
y	coordinate of rectangular coordinate system (normalized by k_0)	
y'	y-coordinate of a point source	
$\boldsymbol{Y}_0$	admittance of inner layer in the spatial domain	
$\widetilde{\boldsymbol{Y}}_0$	admittance of inner layer with $0 \leq \rho \leq \rho_0$ in the spectral domain	

Symbol	Description	Unit
$\boldsymbol{Y}_k$	submatrix of $\boldsymbol{K}_k$	
$\widetilde{\boldsymbol{Y}}_k$	submatrix of $\widetilde{\boldsymbol{K}}_k$	
$\boldsymbol{Y}_n$	admittance of unbounded medium around the multilayered structure in the spatial domain	
$\widetilde{\boldsymbol{Y}}_n$	admittance of unbounded medium around the multilayered structure in the spectral domain	
z	coordinate of rectangular coordinate system (normalized by k_0)	
Z_0	characteristic impedance	Ω
z_k	height of z coordinate at k^{th} interface	
$\boldsymbol{Z}_k$	submatrix of $\boldsymbol{K}_k$	
$\widetilde{\boldsymbol{Z}}_k$	submatrix of $\widetilde{\boldsymbol{K}}_k$	

Greek Symbols

Symbol	Description	Unit
α_x	angle at the interface with the x-axis	
α_z	angle at the interface with the z-axis	
α_ϕ	angle at the interface with the ϕ-axis	
Δx	distance between two adjacent e-/h-lines along x	
Δy	distance between two adjacent e-/h-lines along y	
Δz	distance between two adjacent e-/h-lines along z	
$\Delta\phi$	distance between two adjacent e-/h-lines along ϕ	m^{-1}
$\bar{\bar{\varepsilon}}$	permittivity tensor	$\mathrm{F\ m}^{-1}$
$\bar{\bar{\varepsilon}}_k$	permittivity tensor of layer k	$\mathrm{F\ m}^{-1}$
$\bar{\bar{\varepsilon}}_r$	relative permittivity tensor	
$\bar{\bar{\varepsilon}}_{rk}$	relative permittivity tensor of layer k	
ε_0	permittivity of vacuum	$\mathrm{F\ m}^{-1}$
ε_{air}	relative permittivity of air	
$\varepsilon_{\text{core}}$	relative permittivity of core of the fiber	
ε_m	relative permittivity of medium where ABCs are placed	
ε_{de}	$= k_x^2 + k_y^2$ for e-line field component	

Symbol	Description	Unit
ε_{dh}	$= k_x^2 + k_y^2$ for h-line field component	
ε_r	relative permittivity	
ε_{rk}	relative permittivity of layer k	
ε_t	relative permittivity in ρ- and ϕ-directions	
ε_x	relative permittivity in x-direction	
ε_y	relative permittivity in y-direction	
ε_z	relative permittivity in z-direction	
ξ	coordinate of elliptical coordinate system	
ξ_k	ξ coordinate at k^{th} interface	
η	coordinate of elliptical coordinate system	
η_0	intrinsic impedance of vacuum	Ω
η_j^e	η coordinate of the j^{th} e-line	
η_j^h	η coordinate of the j^{th} h-line	
θ	coordinate of spherical coordinate system	
θ	angle of incidence	
$\bar{\bar{\mu}}$	permeability tensor	H m^{-1}
$\bar{\bar{\mu}}_k$	permeability tensor of layer k	H m^{-1}
$\bar{\bar{\mu}}_r$	relative permeability tensor	
$\bar{\bar{\mu}}_{rk}$	relative permeability tensor of layer k	
μ_0	permeability of vacuum	H m^{-1}
μ_m	relative permeability of medium where ABCs are placed	
μ_r	relative permeability	
μ_{rk}	relative permeability of layer k	
μ_t	relative permittivity in ρ- and ϕ-directions	
μ_x	relative permeability in x-direction	
μ_y	relative permeability in y-direction	
μ_z	relative permeability in z-direction	
ν	spectral variable along ϕ	m
ρ	coordinate of cylindrical coordinate system (normalized by k_0)	
τ_x	eigensolutions along x	

Symbol	Description	Unit
τ_y	eigensolutions along y	
τ_x^e	eigensolutions along x related to e-lines	
τ_x^h	eigensolutions along x related to h-lines	
τ_y^e	eigensolutions along y related to e-lines	
τ_y^h	eigensolutions along y related to h-lines	
τ_ϕ^e	eigensolutions along ϕ related to e-lines	
τ_ϕ^h	eigensolutions along ϕ related to h-lines	
τ_z^e	eigensolutions along z related to e-lines	
τ_z^h	eigensolutions along z related to h-lines	
ϕ	coordinate of cylindrical coordinate system (normalized by k_0)	m^{-1}
ϕ	coordinate of spherical coordinate system	
ϕ_n^e	ϕ coordinate of the n^{th} e-line	m^{-1}
ϕ_n^h	ϕ coordinate of the n^{th} h-line	m^{-1}
ψ	variable that represents fields or field component	
$\boldsymbol{\psi}$	column matrix containing the sampled ψ in the spatial domain	
$\tilde{\psi}$	variable that represents fields or field component in the spectral domain	
$\widetilde{\boldsymbol{\psi}}$	column matrix containing the modal values of $\tilde{\psi}$	
ω	angular frequency	s^{-1}

normalized by k_0
* $\eta_0\vec{H}$ is replaced by $\vec{H}$ and normalized by k_0
** in elliptical coordinate system

List of Abbreviations

1D	one-dimentional
2D	two-dimentional
3D	three-dimentional
ABC	absorbing boundary condition
AR	axial ratio
CFRP	carbon fiber reinforced polymer / carbonfaserverstärkte Kunststoffe (CFK)
CST	Computer Simulation Technology
DMM	discrete mode matching
E-wall	electric wall
FDTD	finite-difference time domain
FEM	finite element method
FWEC	full-wave equivalent circuit
FTD	fourier transform domain
H-wall	magnetic wall
HFSS	High-Frequency Structure Simulator
LH	left-handed
MoL	method of lines
MoM	method of moments
MSP	method of stationary phase
TE	transversal electric
TM	transversal magnetic

Bibliography

Akan, V. and Yazgan, E. (2005). Quasi-static solutions of multilayer elliptical, cylindrical coplanar striplines and multilayer coplanar striplines with finite dielectric dimensions - asymmetrical case. *IEEE Transactions on Microwave Theory and Techniques*, 53(12):3681–3686.

Akiba, S. and Haus, H. A. (1982). Variational analysis of optical waveguides with rectangular cross section. *Applied Optics*, 21(5):804–808.

Antikainen, A., Essiambre, R.-J., and Agrawal, G. P. (2017). Determination of modes of elliptical waveguides with ellipse transformation perturbation theory. *Optica*, 4(12):1510–1513.

Aouabdia, N., Belhadj-Tahar, N.-E., Alquie, G., and Benabdelaziz, F. (2011). Theoretical and experimental evaluation of superstrate effect on rectangular patch resonator parameters. *Progress In Electromagnetics Research B*, 32:129–147.

Aouiche, A., Djellid, A., and Bouttout, F. (2015). Fuzzy neuroconformal analysis of multilayer elliptical cylindrical and asymmetrical coplanar striplines. *AEU - International Journal of Electronics and Communications*, 69(9):1151 – 1166.

Balanis, C. A. (1997). *Antenna Theory: Analysis and Design,* 2^{nd} *edition.* John Wiley & Sons, New York.

Barkat, L., Bedra, S., Fortaki, T., and Bedra, R. (2017). Neurospectral computation for the resonant characteristics of microstrip patch antenna printed on uniaxially anisotropic substrates. *International Journal of Microwave and Wireless Technologies*, 9(3):613–620.

Berini, P. and Wu, K. (1996). Modeling lossy anisotropic dielectric waveguides with the method of lines. *IEEE Transactions on Microwave Theory and Techniques*, 44(5):749–759.

Boufrioua, A. (2011). Analysis of a rectangular microstrip antenna on a uniaxial substrate. In Nasimuddin, N., editor, *Microstrip Antennas*, chapter 2. IntechOpen, Rijeka.

Bulla, D. A. P., Borges, B.-H. V., Romero, M. A., Morimoto, N. I., and Neto, L. G. (2002). Design and fabrication of sio/sub 2//si/sub 3/n/sub 4/ integrated-optics waveguides on silicon substrates. *IEEE Transactions on Microwave Theory and Techniques*, 50(1):9–12.

Caizzone, S. (2017). Miniaturized E5a/E1 antenna array for robust GNSS navigation. *IEEE Antennas and Wireless Propagation Letters*, 16:485–488.

Caloz, C. and Itoh, T. (2006). *Electromagnetic Metamaterials: Transmission Line Theory and Microwave Applications.* John Wiley & Sons, New Jersey.

Cassivi, Y., Perregrini, L., Arcioni, P., Bressan, M., Wu, K., and Conciauro, G. (2002). Dispersion characteristics of substrate integrated rectangular waveguide. *IEEE Microwave and Wireless Components Letters*, 12(9):333–335.

Chen, Y. P., Chew, W. C., and Jiang, L. (2012). A new Green's function formulation for modeling homogeneous objects in layered medium. *IEEE Transactions on Antennas and Propagation*, 60(10):4766–4776.

Clemens, M. and Weiland, T. (2002). Magnetic field simulation using conformal FIT formulations. *IEEE Transactions on Magnetics*, 38(2):389–392.

Coifman, R., Rokhlin, V., and Wandzura, S. (1993). The fast multipole method for the wave equation: a pedestrian prescription. *IEEE Antennas and Propagation Magazine*, 35(3):7–12.

Collin, R. E. and Zucker, F. J. (1969). *Antenna Theory, Part 1.* McGraw-Hill, New York.

Conradi, O. and Pregla, R. (2001). Analysis of fibers with elliptical cross section. In *Proceedings of 3rd International Conference on Transparent Optical Networks (IEEE Cat. No.01EX488)*, pages 12–15.

Courant, R. (1943). Variational methods for the solution of problems of equilibrium and vibrations. *Bulletin of the American Mathematical Society*, 49(1):1–23.

Davidovitz, M. and Lo, Y. T. (1989). Rigorous analysis of a circular patch antenna excited by a microstrip transmission line. *IEEE Transactions on Antennas and Propagation*, 37(8):949–958.

Dietrich, F. J., Metzen, P., and Monte, P. (1998). The globalstar cellular satellite system. *IEEE Transactions on Antennas and Propagation*, 46(6):935–942.

Dreher, A. (1995). A new approach to dyadic Green's function in spectral domain. *IEEE Transactions on Antennas and Propagation*, 43(11):1297–1302.

Dreher, A. (1996). Discrete mode matching for the full-wave analysis of planar waveguide structures. In *IEEE MTT-S International Microwave Symposium Digest*, volume 1, pages 193–196 vol.1.

Dreher, A. and Ioffe, A. (2000). Analysis of microstrip lines in multilayer structures of arbitrarily varying thickness. *IEEE Microwave and Guided Wave Letters*, 10(2):52–54.

Dreher, A. and Pregla, R. (1993). Full-wave analysis of radiating planar resonators with the method of lines. *IEEE Transactions on Microwave Theory and Techniques*, 41(8):1363–1368.

Dreher, A. and Rother, T. (1995). New aspects of the method of lines. *IEEE Microwave and Guided Wave Letters*, 5(11):408–410.

Du, Z., Gong, K., Fu, J. S., Feng, Z., and Gao, B. (2000). CAD models for asymmetrical, elliptical, cylindrical, and elliptical cone coplanar strip lines. *IEEE Transactions on Microwave Theory and Techniques*, 48(2):312–316.

Dyott, R. B. (1995). *Elliptical Fiber Waveguides.* Artech House, London, U.K.

Eibert, T. F. (2005). A diagonalized multilevel fast multipole method with spherical harmonics expansion of the k-space integrals. *IEEE Transactions on Antennas and Propagation*, 53(2):814–817.

Enoch, S., Tayeb, G., Sabouroux, P., Guérin, N., and Vincent, P. (2002). A metamaterial for directive emission. *Physical Review Letters*, 89:213902.

Eti, N. and Kurt, H. (2016). Model analysis of ridge and rib types of silicon waveguides with void compositions. *IEEE Journal of Quantum Electronics*, 52(10):1–7.

Garg, R., Bhartia, P., Bahl, I., and Ittipiboon, A. (2001). *Microstrip Antenna Design Handbook.* Artech House, Nordwood.

Greda, L. A. and Pregla, R. (2002). Hybrid analysis of three-dimensional structures by the method of lines using novel nonequidistant discretization. In *2002 IEEE MTT-S International Microwave Symposium Digest (Cat. No.02CH37278).*

Greda, L. A. and Pregla, R. (2004). New high-accuracy subgridding technique for the method of lines. In *2004 IEEE MTT-S International Microwave Symposium Digest (IEEE Cat. No.04CH37535).*

Harrington, R. F. (1968). *Field Computation by Moment Methods.* Macmillan, New York.

Hassad, M., Boughrara, A. S., and Fortaki, T. (2014). Full-wave analysis of rectangular microstrip antenna printed on electric-magnetic uniaxial anisotropic substrates. *International Journal of Future Generation Communication and Networking*, 7(4):183–194.

Heckler, M. V. T. (2010). *Discrete Mode Matching Method for Conformal Microstrip Antennas.* Doctoral thesis, Technical University of Munich.

Heckler, M. V. T. and Dreher, A. (2006). Analysis of cylindrical microstrip lines using the discrete mode matching method. *IEEE Microwave and Wireless Components Letters*, 16(7):392–394.

Heckler, M. V. T. and Dreher, A. (2007a). Analysis of graded-index fibers using a full-wave equivalent circuit. *Journal of Lightwave Technology*, 25(1):346–349.

Heckler, M. V. T. and Dreher, A. (2007b). The application of the discrete mode matching method to noncircular dielectric waveguides. *IEEE Microwave and Wireless Components Letters*, 17(9):628–630.

Heckler, M. V. T. and Dreher, A. (2011). Analysis of conformal microstrip antennas with the discrete mode matching method. *IEEE Transactions on Antennas and Propagation*, 59(3):784–792.

Heckler, M. V. T. and Dreher, A. (2016). On the discretization for the discrete mode matching method for conformal microstrip structures. In *10th European Conference on Antennas and Propagation (EuCAP)*, pages 1–4.

Higdon, R. L. (1987). Numerical absorbing boundary conditions for the wave equation. *Mathematics of Computation*, 49(179):65–90.

Hiptmair, R. (1999). Multigrid method for Maxwell's equations. *Society for Industrial and Applied Mathematics (SIAM)*, 36.

Horikis, T. P. (2013). Dielectric waveguides of arbitrary cross sectional shape. *Applied Mathematical Modelling*, 37(7):5080 – 5091.

Hsu, C. J. (2001). Coplanar-waveguide dispersion characteristics including anisotropic substrates. *IEEE Transactions on Microwave Theory and Techniques*, 49(2):362–368.

Huang, J. (1995). Microstrip antennas for commercial applications. In Pozar, D. M. and Schaubert, D., editors, *Microstrip Antennas*, pages 371–379. IEEE Press, Piscataway.

Ioffe, A. and Dreher, A. (1999). Verwendung von absorbierenden randbedingungen hoher ordnung für die discrete mode matching methode. In *Kleinheubacher Berichte*, pages 133–140.

Ioffe, A., Thiel, M., and Dreher, A. (2003). Analysis of microstrip patch antennas on arbitrarily shaped multilayers. *IEEE Transactions on Antennas and Propagation*, 51(8):1929–1935.

Itoh, T. (1989). *Numerical Techniques for Microwave and Millimeter-Wave Passive Structures*. John Wiley & Sons, Newyork.

Kamra, V. and Dreher, A. (2017). Discrete mode matching method for the analysis of microstrip lines on uniaxial anisotropic substrates. In *International Applied Computational Electromagnetics Society Symposium - Italy (ACES)*, pages 1–2, Florence, Italy.

Kamra, V. and Dreher, A. (2018a). Analysis of microstrip antennas on metamaterial substrate using discrete mode matching method. In *IEEE International Symposium on Antennas and Propagation USNC/URSI National Radio Science Meeting*, pages 649–650, Boston, US.

Kamra, V. and Dreher, A. (2018b). Analysis of microstrip antennas on multilayer uniaxial anisotropic substrate with discrete mode matching method. In *12th European Conference on Antennas and Propagation (EuCAP 2018)*, pages 1–5, London, UK.

Kamra, V. and Dreher, A. (2018c). Efficient analysis of multiple microstrip transmission lines with anisotropic substrates. *IEEE Microwave and Wireless Components Letters*, 28(8):636–638.

Kamra, V. and Dreher, A. (2018d). Full-wave equivalent circuit for the analysis of multilayered microwave structures with anisotropic layers. *Electronics Letters*, 54(3):153–155.

Kamra, V. and Dreher, A. (2018e). Multilayered transmission lines on quasi-planar substrates with anisotropy. In *Kleinheubacher Tagung*, Miltenberg, Germany.

Kamra, V. and Dreher, A. (2019a). Analysis of anisotropic inhomogeneous dielectric waveguides with discrete mode matching method. In *IEEE International Microwave Symposium*, Boston, US.

Kamra, V. and Dreher, A. (2019b). Analysis of circular and noncircular waveguides and striplines with multilayered uniaxial anisotropic medium. *IEEE Transactions on Microwave Theory and Techniques*, 67(2):584–591.

Kamra, V. and Dreher, A. (2019c). Analysis of conformal antennas with quasi-cylindrical substrates using discrete mode matching method. In *URSI Electromagnetic Theory Symposium*, San Diego, US.

Kamra, V. and Dreher, A. (2019d). Multilayered transmission lines on quasi-planar substrates with anisotropic medium. *Advances in Radio Science*, 17:77–82.

Kamra, V. and Dreher, A. (2020a). Analysis of elliptical waveguides with anisotropic dielectric layers. *IEEE Access*, 8:31444–31452.

Kamra, V. and Dreher, A. (2020b). Efficient analysis of inhomogeneous dielectric waveguides with dielectric strips and microstrips using discrete mode matching method. *IEEE Journal on Multiscale and Multiphysics Computational Techniques*, 5:19–27.

Karahan, M., Aksoy, E., and Sahinkaya, D. S. A. (2015). Design of wideband conformal antenna array at X-band for satellite applications. In *7th International Conference on Recent Advances in Space Technologies (RAST)*, pages 397–400.

Ko, W. L. and Mittra, R. (1991). A combination of FD-TD and prony's methods for analyzing microwave integrated circuits. *IEEE Transactions on Microwave Theory and Techniques*, 39(12):2176–2181.

Kretch, B. E. and Collin, R. E. (1987). Microstrip dispersion including anisotropic substrates. *IEEE Transactions on Microwave Theory and Techniques*, 35(8):710–718.

Krowne, C. (1984). Green's function in the spectral domain for biaxial and uniaxial anisotropic planar dielectric structures. *IEEE Transactions on Antennas and Propagation*, 32(12):1273–1281.

Krowne, C. (1986). Determination of the Green's function in the spectral domain using a matrix method: Application to radiators or resonators immersed in a complex anisotropic layered medium. *IEEE Transactions on Antennas and Propagation*, 34(2):247–253.

Kusiek, A., Lech, R., Marynowski, W., and Mazur, J. (2015). An analysis of multistrip line configuration on elliptical cylinder. *IEEE Transactions on Microwave Theory and Techniques*, 63(6):1800–1808.

Lee, J., Lee, R., and Cangellaris, A. (1997). Time-domain finite-element methods. *IEEE Transactions on Antennas and Propagation*, 45(3):430–442.

Lee, J. F., Palandech, R., and Mittra, R. (1992). Modeling three-dimensional discontinuities in waveguides using nonorthogonal FDTD algorithm. *IEEE Transactions on Microwave Theory and Techniques*, 40(2):346–352.

Li, L.-W., Liu, S., Leong, M.-S., and Yeo, T.-S. (2001). Circular cylindrical waveguide filled with uniaxial anisotropic media electromagnetic fields and dyadic Green's functions. *IEEE Transactions on Microwave Theory and Techniques*, 49(7):1361–1364.

Lindell, I. V. and Oksanen, M. I. (1984). Asymptotic analysis of weakly guiding anisotropic optical fibers. *Journal of the Optical Society of America A*, 1(1):87–95.

Liu, Y., Shi, D., Zhang, S., and Gao, Y. (2016). Multiband antenna for satellite navigation system. *IEEE Antennas and Wireless Propagation Letters*, 15:1329–1332.

Lu, Y. and Fernandez, F. A. (1993). An efficient finite element solution of inhomogeneous anisotropic and lossy dielectric waveguides. *IEEE Transactions on Microwave Theory and Techniques*, 41(6):1215–1223.

Mao, K. (2007). *Finite element analysis of multilayer transmission line and circuit components.* Doctoral thesis, University of Illinois, UrbanaChampaign.

McLachlan, N. W. (1951). *Theory and Application of Mathieu Functions.* Clarendon.

Medina, F. and Horno, M. (1990). Spectral and variational analysis of generalized cylindrical and elliptical strip and microstrip lines. *IEEE Transactions on Microwave Theory and Techniques*, 38(9):1287–1293.

Mesa, F., Marques, R., and Horno, M. (1998). On the computation of the complete spectral Green's dyadic for layered bianisotropic structures. *IEEE Transactions on Microwave Theory and Techniques*, 46(8):1158–1164.

Naser-Moghaddasi, M., Sadeghzadeh, R. A., Ghiamy, M., Neyestanak, A. A. L., and Virdee, B. S. (2010). An elliptical cylindrical FDTD algorithm for modeling conformal patch antenna. *IEEE Transactions on Antennas and Propagation*, 58(12):3990–3996.

Oksanen, M. I. and Lindell, I. V. (1989). Variational analysis of anisotropic graded-index optical fibers. *Journal of Lightwave Technology*, 7(1):87–91.

Ozdemir, T. and Volakis, J. L. (1997). Triangular prisms for edge-based vector finite element analysis of conformal antennas. *IEEE Transactions on Antennas and Propagation*, 45(5):788–797.

Pashaie, R. (2007). Fourier decomposition analysis of anisotropic inhomogeneous dielectric waveguide structures. *IEEE Transactions on Microwave Theory and Techniques*, 55(8):1689–1696.

Pozar, D. (1983). Considerations for millimeter wave printed antennas. *IEEE Transactions on Antennas and Propagation*, 31(5):740–747.

Pozar, D. (1987). Radiation and scattering from a microstrip patch on a uniaxial substrate. *IEEE Transactions on Antennas and Propagation*, 35(6):613–621.

Pozar, D. M. and Schaubert, D. H. (1995). *Microstrip Antennas: The Analysis and Design of Microstrip Antennas and Arrays.* IEEE Press, Piscataaway.

Pregla, R. (2008). *Analysis of Electromagnetic Fields and Waves: The Method of Lines.* John Wiley & Sons, Chichester, UK.

Pregla, R. and Conradi, O. (2003). Modeling of uniaxial anisotropic fibers with noncircular cross section by the method of lines. *Journal of Lightwave Technology*, 21(5):1294–1299.

Pregla, R., Koch, M., and Pascher, W. (1987). Analysis of hybrid waveguide structures consisting of microstrips and dielectric waveguides. In *17th European Microwave Conference*, pages 927–932.

Rengarajan, S. R. (1989). On higher order mode cutoff frequencies in elliptical step index fibers. *IEEE Transactions on Microwave Theory and Techniques*, 37(8):1244–1248.

She, S. X. (1989). Iterated-moment method for the analysis of optical waveguides of arbitrary cross section. *Journal of the Optical Society of America A*, 6(7):1031–1037.

Shibayama, J., Takahashi, T., Yamauchi, J., and Nakano, H. (2000). Efficient time-domain finite-difference beam propagation methods for the analysis of slab and circularly symmetric waveguides. *Journal of Lightwave Technology*, 18(3):437–442.

Smith, D. R., Padilla, W. J., Vier, D. C., Nemat-Nasser, S. C., and Schultz, S. (2000). Composite medium with simultaneously negative permeability and permittivity. *Physics Review Letters*, 84:4184–4187.

Sullivan, P. and Schaubert, D. (1986). Analysis of an aperture coupled microstrip antenna. *IEEE Transactions on Antennas and Propagation*, 34(8):977–984.

Taflove, A. (2007). A perspective on the 40-year history of FDTD computational electrodynamics. *ACES Journal*, 22(1):1–21.

Talbi, A., Nedil, M., and Hettak, K. (2018). Conformal continuous tanrsverse stub antenna based on SIW technology for 5G applications. In *IEEE International Symposium on Antennas and Propagation USNC/URSI National Radio Science Meeting*, pages 1829–1830.

Thiel, M. and Dreher, A. (2002). Dyadic Green's function of multilayer cylindrical closed and sector-structures for waveguide, microstrip-antenna, and network analysis. *IEEE Transactions on Microwave Theory and Techniques*, 50(11):2576–2579.

Tonning, A. (1982). Circularly symmetric optical waveguide with strong anisotropy. *IEEE Transactions on Microwave Theory and Techniques*, 30(5):790–794.

Verma, A. K., Singh, P., and Matekovits, L. (2014). Strip-width and slot-gap dependent equivalent isotropic substrate and dispersion characteristics of asymmetric coplanar waveguide, symmetric coplanar waveguide and micro-coplanar strip line on anisotropic substrates. *IEEE Transactions on Microwave Theory and Techniques*, 62(10):2232–2241.

Veselago, V. G. (1968). The electrodynamics of substances with simultaneously negative values of ε and μ. *Soviet Physics Uspekhi*, 10(4):509–514.

Wei, C., Harrington, R. F., Mautz, J. R., and Sarkar, T. K. (1984). Multiconductor transmission lines in multilayered dielectric media. *IEEE Transactions on Microwave Theory and Techniques*, 32(4):439–450.

Weiland, T. (1977). A discretization model for the solution of Maxwell's equations for six-component fields. *Archiv Elektronik und Uebertragungstechnik*, 31:116–120.

Weng, Z.-B., Jiao, Y.-C., Zhang, F.-S., Song, Y., and Zhao, G. (2008). A multi-band patch antenna on metamaterial substrate. *Journal of Electromagnetic Waves and Applications*, 22(2-3):445–452.

Wong, K.-L., Row, J.-S., Kuo, C.-W., and Huang, K.-C. (1993). Resonance of a rectangular microstrip patch on a uniaxial substrate. *IEEE Transactions on Microwave Theory and Techniques*, 41(4):698–701.

Wu, B.-I., Wang, W., Pacheco, J., Chen, X., Grzegorczyk, T. M., and Kong, J. A. (2005). A study of using metamaterials as antenna substrate to enhance gain. *Progress In Electromagnetics Research*, 51:295–328.

Wu, K. and Han, L. (1997). Hybrid integration technology of planar circuits and NRD-guide for cost-effective microwave and millimeter-wave applications. *IEEE Transactions on Microwave Theory and Techniques*, 45(6):946–954.

Yang, W. D. and Pregla, R. (1996). The method of lines for analysis of integrated optical waveguide structures with arbitrary curved interfaces. *Journal of Lightwave Technology*, 14(5):879–884.

Yee, H. Y. and Audeh, N. F. (1965). Uniform waveguides with arbitrary cross-section considered by the point-matching method. *IEEE Transactions on Microwave Theory and Techniques*, 13(6):847–851.

Yee, K. S. (1966). Numerical solution of initial boundary value problems involving Maxwell's equations in isotropic media. *IEEE Transactions on Antennas and Propagation*, 14(3):302–307.

Yeh, C. and Shimabukuro, F. I. (2008). *The Essence of Dielectric Waveguides*. Springer, Boston, MA.

Yijiang, C. (1988). Anisotropic fibers with elliptical deformed core. *Applied Physics B*, 47(1):21–25.

Yinusa, K. A. (2018). A dual-band conformal antenna for GNSS applications in small cylindrical structures. *IEEE Antennas and Wireless Propagation Letters*, 17(6):1056–1059.

Yinusa, K. A., Marcos, E. P., and Caizzone, S. (2018). Robust satellite navigation by means of a spherical cap conformal antenna array. In *18th International Symposium on Antenna Technology and Applied Electromagnetics (ANTEM)*, pages 1–2.

Young, D. L., Hu, S. P., Chen, C. W., Fan, C. M., and Murugesan, K. (2005). Analysis of elliptical waveguides by the method of fundamental solutions. *Microwave and Optical Technology Letters*, 44(6):552–558.

Zhang, K. and Li, D. (1998). *Electromagnetic Theory for Microwaves and Optoelectronics*. Speinger, Berlin Heidelberg Newyork.

Publications of the Author

Journal Articles

Kamra, V. and Dreher, A. (2018a). Efficient analysis of multiple microstrip transmission lines with anisotropic substrates. *IEEE Microwave and Wireless Components Letters*, 28(8):636–638.

Kamra, V. and Dreher, A. (2018b). Full-wave equivalent circuit for the analysis of multilayered microwave structures with anisotropic layers. *Electronics Letters*, 54(3):153–155.

Kamra, V. and Dreher, A. (2019a). Analysis of circular and noncircular waveguides and striplines with multilayered uniaxial anisotropic medium. *IEEE Transactions on Microwave Theory and Techniques*, 67(2):584–591.

Kamra, V. and Dreher, A. (2019b). Multilayered transmission lines on quasi-planar substrates with anisotropic medium. *Advances in Radio Science*, 17:77–82.

Kamra, V. and Dreher, A. (2020a). Analysis of elliptical waveguides with anisotropic dielectric layers. *IEEE Access*, 8:31444–31452.

Kamra, V. and Dreher, A. (2020b). Efficient analysis of inhomogeneous dielectric waveguides with dielectric strips and microstrips using discrete mode matching method. *IEEE Journal on Multiscale and Multiphysics Computational Techniques*, 5:19–27.

Conference Proceedings

Kamra, V. and Dreher, A. (2017). Discrete mode matching method for the analysis of microstrip lines on uniaxial anisotropic substrates. In *International Applied Computational Electromagnetics Society Symposium - Italy (ACES)*, pages 1–2, Florence, Italy.

Kamra, V. and Dreher, A. (2018a). Analysis of microstrip antennas on metamaterial substrate using discrete mode matching method. In *IEEE International Symposium on Antennas and Propagation USNC/URSI National Radio Science Meeting*, pages 649–650, Boston, US.

Kamra, V. and Dreher, A. (2018b). Analysis of microstrip antennas on multilayer uniaxial anisotropic substrate with discrete mode matching method. In *12th European Conference on Antennas and Propagation (EuCAP)*, pages 1–5, London, UK.

Kamra, V. and Dreher, A. (2018c). Multilayered transmission lines on quasi-planar substrates with anisotropy. In *Kleinheubacher Tagung*, Miltenberg, Germany.

Kamra, V. and Dreher, A. (2019a). Analysis of anisotropic inhomogeneous dielectric waveguides with discrete mode matching method. In *IEEE International Microwave Symposium*, Boston, US.

Kamra, V. and Dreher, A. (2019b). Analysis of conformal antennas with quasi-cylindrical substrates using discrete mode matching method. In *URSI Electromagnetic Theory Symposium*, San Diego, US.

Kamra, V. and Dreher, A. (2019c). Efficient analysis of transmission lines with anisotropic elliptical dielectric layers. In *Kleinheubacher Tagung*, Miltenberg, Germany.